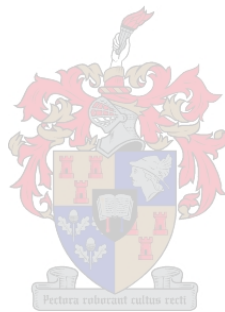


An In-Situ System For PV Module Performance Monitoring

by

Tashriq Pandy



*Thesis presented in partial fulfilment of the requirements for
the degree of Master of Engineering (Electrical and
Electronic) in the Faculty of Engineering at Stellenbosch
University*

Supervisor: Dr. Johann M. Strauss

April 2019

Declaration

By submitting this thesis electronically, I declare that the entirety of the work contained therein is my own, original work, that I am the sole author thereof (save to the extent explicitly otherwise stated), that reproduction and publication thereof by Stellenbosch University will not infringe any third party rights and that I have not previously in its entirety or in part submitted it for obtaining any qualification.

Date: March 2019

Copyright © 2019 Stellenbosch University
All rights reserved.

Abstract

An In-Situ System For PV Module Performance Monitoring

T. Pandy

*Department of Electrical and Electronic Engineering,
University of Stellenbosch,
Private Bag X1, Matieland 7602, South Africa.*

Thesis: MEng (E&E)

March 2019

There is a global pursuit to improve the efficiency of energy generation due to the increasing global demand for energy, limited resources and the global trend towards alternative energy. While the photovoltaic (PV) industry is experiencing continuous growth, there are many challenges that come with effectively managing PV systems. Various studies have shown that increasing levels of PV plant monitoring can increase energy yield and lower downtime. However, at the same time this significantly increases the initial capital cost that in turn could detrimentally influence cost competitiveness and feasibility.

In this thesis, an in-situ PV monitoring system using perturbation techniques to effectively monitor PV systems is proposed. The monitoring system consists of a PV module monitoring device, a perturbation device (incorporated in the monitoring device) and a data acquisition device. The PV monitoring device captures PV module temperature and I-V data simultaneously during perturbation at a pre-set interval. A wireless sensor network is then used to send the captured data to the data acquisition device.

The perturbation device utilises two techniques. These perturbation techniques temporarily apply different intensity levels of oscillation by applying two different switching topologies of an inductor and a capacitor. The oscillations temporarily perturb the operating point of the PV module to shift back and forth along the characteristic I-V curve at a fast-enough rate to not influence the PV system operation. If the intensity of the oscillations is enough to pass the knee point on the I-V curve, then the maximum power point of the PV module can be determined.

The effectiveness of the monitoring system was firstly simulated and then experimentally verified while operating the PV modules at different operating points on the I-V curve. It is concluded that the one perturbation approach that introduces greater oscillations can best identify the maximum power point of the PV module, including when the PV module is operated far away from the maximum power point.

Uittreksel

In situ stelsel vir fotovoltaïese module werkverrigtingsmonitering

(“An In-Situ System For PV Module Performance Monitoring”)

T. Pandy

*Departement Elektriese en Elektroniese Ingenieurswese,
Universiteit van Stellenbosch,
Privaatsak X1, Matieland 7602, Suid Afrika.*

Tesis: MIng (E&E)

Maart 2019

Daar is 'n wêreldwye strewe om die benuttingsgraad van energieomsetting te verhoog as gevolg van die toenemende aanvraag vir energie, beperkte hulpbronne en die wêreldwye tendens in die rigting van alternatiewe energie. Terwyl die fotovoltaïese industrie deurlopende groei ervaar, is daar nog baie uitdagings in die effektiewe bestuur van fotovoltaïese aanlegte. Verskeie studies het al getoon dat verhoogde vlakke van monitering van fotovoltaïese aanlegte kan lei tot verhoogte energieopbrengs en minder aftyd. Dit verhoog egter terselfdertyd die aanvanklike kapitale koste wat weer 'n nadelige invloed kan hê op koste mededingendheid en lewensvatbaarheid.

'n In situ fotovoltaïese moniteringstelsel wat gebruik maak van sturingstegnieke om fotovoltaïese stelsels effektief te monitor word in hierdie tesis voorgestel. Die moniteringstelsel bestaan uit 'n fotovoltaïese module moniteringstoestel, 'n sturingstoestel (ingesluit in die moniteringstoestel) en 'n data inwinningstoestel. Die fotovoltaïese moniteringstoestel meet die module temperatuur en I-V data gelyktydig tydens die sturings teen 'n voorafgestelde interval. 'n Draadlose sensor netwerk word dan gebruik om die gemete data na die inwinningstoestel te stuur.

Die sturingstoestel gebruik twee tegnieke. Hierdie sturingstegnieke lê verskillende intensiteitsvlakke van ossilasie aan deur twee verskillende inskakel konfigurasies van 'n induktor en 'n kapasitor oor die module. Die ossilasies versteur die fotovoltaïese module se werkpunt tydelik sodat daar op en af beweeg word op die karakteristieke I-V kurwe teen 'n tempo vinnig genoeg om nie die werking van die fotovoltaïese stelsel te beïnvloed nie. As die intensiteit van die ossilasies genoeg is om verby die kniepunt van die I-V kurwe te beweeg, kan die maksimum drywingspunt van die fotovoltaïese module te bepaal.

Die doeltreffendheid van die moniteringstelsel is eerstens gesimuleer en toe eksperimenteel geverifieer terwyl die fotovoltaïese modules teen verskillende bedryfspunte op die I-V kurwe bedryf is. Die gevolgtrekking is dat die sturingstegniek wat groter ossilasies teweeg bring die maksimum drywingspunt van die fotovoltaïese module die beste kan bepaal, insluitend wanneer die fotovoltaïese module vêr van die maksimum drywingspunt bedryf word.

Acknowledgements

"non-ministrari sed-ministrare"

Truly grateful to my Creator, for the beneficial knowledge, courage and strength for completing this thesis.

I would like to express my sincere gratitude to the following people...

Dr Johann M. Strauss, for being a wonderful and exceptional study leader and for allowing me the opportunity to have been part of research I am passionate about. I am forever grateful for the wisdom, experience and knowledge gained on this journey.

My parents, for being exceptional role models, without your guidance, support and so much more I would not be who and where I am today.

The workshop and administrative staff Andre, Murray, Pietro, Howard, Wessel, Gift, Wynand and Jenny for your assistance. I am truly grateful for all your efforts.

My advisor's, support and office colleagues, which includes Armand Du Plesis, Jason Samuels, Carmen Lewis, Cundell Statt, Emile Klien, Tafara Mahachi, Brian De Beer, Tafadzwa Gurupira. It was great sharing a office, ideas, thoughts and the occasional banter with you all.

Shameema Hartley, for supporting me all the way on this journey. Thank you for your understanding and I am forever grateful to you. I love you dearly.

Dedications

This thesis is dedicated to my lovely wife Shameema...

Contents

Declaration	i
Abstract	ii
Uittreksel	iii
Acknowledgements	iv
Dedications	v
Contents	vi
List of Figures	x
List of Tables	xiv
Nomenclature	xv
1 Introduction	1
1.1 Background	1
1.2 Research motivation and problem statement	3
1.2.1 Research questions	4
1.2.2 Research objectives	4
1.2.3 Research tasks	4
1.2.4 Hypotheses	5
1.3 Scope And Limitations	5
1.4 Thesis Overview	6
2 Literature review and background study	8
2.1 Chapter overview	8
2.2 Previous research	8
2.2.1 PV cells	8
2.2.2 Mismatch in PV arrays	10
2.2.3 Monitoring in PV systems	11
2.2.4 PV inverter topologies	14
2.2.5 Monitoring approaches for PV systems	15
2.2.6 PV Module Monitoring	17
2.2.7 Internet of Things (IoT)	18
2.3 Natural and step response of RLC circuit	19
2.3.1 Resonance and natural frequency	20
2.3.2 Damping	21

3	Monitoring device	22
3.1	Overview	22
3.2	Function of the Monitoring Device	22
3.3	Conceptual hardware design	23
3.3.1	General system overview	23
3.3.2	Power supply and voltage sources	23
3.3.3	Micro-controller	24
3.3.4	Printed circuit board design	25
3.3.5	IEEE 802.15.4 connectivity	25
3.3.6	Measurements	27
3.3.6.1	ADCs	27
3.3.6.2	Current measurement	29
3.3.6.3	Voltage measurement	30
3.3.6.4	Temperature measurements	31
3.4	Detailed Software Design	33
3.4.1	Programming the MCU	33
3.4.2	Overview of data retrieval	33
3.4.3	Communications	33
3.4.4	USART communication	33
3.4.5	SPI communication	35
3.4.6	Monitoring device MDC user interface commands	35
3.4.7	Wireless IEEE 802.15.4 communication	37
4	Perturbation devices	42
4.1	Introduction and chapter overview	42
4.2	Perturbation fundamentals	43
4.2.1	Perturbation topology validation	43
4.2.2	PD functionality	44
4.2.3	Theoretical calculations	45
4.3	Perturbation simulation	48
4.3.1	Introduction to Simplorer	48
4.3.2	Simulation set up	48
4.3.3	Simulated results	51
4.3.4	Evaluation of the simulated results	56
4.4	Perturbation hardware	58
4.5	PCB Design	60
5	Data acquisition device	62
5.1	Overview	62
5.2	Data acquisition objective	62
5.3	Hardware overview	63
5.3.1	ESP32 module	63
5.3.2	ESP32 communication	63
5.3.3	ESP32 real time clock (RTC)	64
5.3.4	Programming and flashing	64
5.3.5	SD card	65
5.4	Detailed software design	66
5.4.1	Programming the ESP32	66
5.4.2	Data retrieval overview	66
5.4.3	TCP socket communication	66

5.4.4	ESP32 Master and user interface commands	66
6	Experimental set up and methodology	69
6.1	Overview	69
6.2	Practical implementation	69
6.2.1	Monitoring strategy	70
6.2.2	LC - Perturbation strategy (no stored energy)	71
6.2.3	L-LC Perturbation strategy (stored energy)	72
6.3	Application of perturbation technique	74
6.3.1	Grid-tie inverter	75
6.3.2	Charge controller	76
7	Results and Analysis	77
7.1	Overview	77
7.2	Raw data validation	77
7.2.1	Overview	77
7.2.2	PV module data	77
7.2.3	MD measurements	78
7.3	Data alignment, storage and monitoring	78
7.4	Data related documentation	79
7.5	Problems encountered during the process of data acquisition	80
7.6	Data extraction and filtering process	82
7.6.1	Data extraction	82
7.6.2	Data filtering	82
7.7	Experimental results and discussion	82
7.7.1	Overview	82
7.7.2	PV module monitoring	82
7.7.3	Quantifying the monitoring data	84
7.7.4	Perturbation results	85
7.8	Summary of results	96
7.8.1	Overview	96
7.8.2	Monitoring device	96
7.8.3	Perturbation techniques	97
8	Conclusions and Recommendations	98
8.1	Introduction	98
8.2	Chapter reflections	98
8.2.1	Chapter 1:	98
8.2.2	Chapter 2:	98
8.2.3	Chapter 3:	98
8.2.4	Chapter 4:	99
8.2.5	Chapter 5:	99
8.2.6	Chapter 6:	99
8.2.7	Chapter7:	99
8.3	Thesis evaluation	99
8.3.1	Research tasks evaluation	99
8.3.2	Research objectives and question evaluation	100
8.4	Recommendations	100
	Appendices	102

A	Research test facility	103
A.1	Infrastructure	103
A.1.1	Network configuration	105
A.1.2	SMA grid-tie configuration	105
A.1.3	Micro Care MPPT configuration	106
B	Monitoring device PCB design	107
B.0.1	Relevant data sheet information	107
B.0.2	MD earlier versions	109
B.0.3	Atmel Studio	110
B.0.4	MD PCB design documents	110
B.0.5	IEEE 802.15.4 RX_AACK and TX_ARET state diagrams.	116
C	Perturbation device's PCB designs	118
C.0.1	PD's RLC circuits	118
C.0.2	ANSYS Simplorer	119
C.0.3	PD PCB design documents	121
D	Data acquisition device (DAD)	128
D.0.1	ESP32 firmware	128
D.0.1.1	Environment setup	128
D.0.2	Python client program	128
D.0.3	Web Server and online database	129
D.0.4	ESP32 programmer PCB design documents	129
E	Calibration process for monitoring devices	134
E.0.1	MD measurement verification using an oscilloscope	137
	List of References	139

List of Figures

1.1	Global Cumulative Installed PV Capacity [GW_p] [8]	2
1.2	SA utility scale RE technologies by program for bidding rounds 1-4 [12]	2
2.1	PSC on (a) PV modules or (b) PV array	9
2.2	P - V characteristics for mismatched PV modules [26]	10
2.3	Gartner monitoring solution overview [18]	12
2.4	PV plant topologies: a) central inverters; b) string inverters; c) module inverters; d) multi-string inverters [41]	14
2.5	Parallel and series RLC circuit [74]	19
3.1	Monitoring device conceptual hardware layout	23
3.2	MD PCB circuit design 3D view	25
3.3	IEEE 802.15.4 network topologies	26
3.4	MCU extended operating mode state diagram	27
3.5	MD Current measurement circuit.	30
3.6	MD Voltage measurement circuit	31
3.7	MD temperature sensor design	32
3.8	USART MODBUS adoption, delays between packets	34
3.9	MD USART transmit and receive flow diagram	34
3.10	Data packet format from DAD to MDC	35
3.11	MD USART software flow diagram for received data	36
3.12	IEEE802-15-4-physical-layer [80, p.67]	37
3.13	IEEE 802.15.4 Frame Format - MAC-Layer Frame Structure [80, p.68]	39
3.14	MD IEEE 802.15.4 software flow diagram for received data	40
4.1	Illustration of parasitic capacitance	43
4.2	I-V curve characteristics and under-damped waveform	44
4.3	PD LC implementation in PV array	49
4.4	PD L-LC implementation in PV array	50
4.5	300 W PV module current and voltage waveforms with LC perturbation applied at the MPP operating point	51
4.6	300 W PV module I-V curve with LC perturbation applied at the MPP operating point	51
4.7	300 W PV module P-V curve with LC perturbation applied at the MPP operating point	51
4.8	300 W PV module current and voltage waveforms with LC perturbation applied to the right of MPP operating point	52
4.9	300 W PV module I-V curve with LC perturbation applied to the right of MPP operating point	52
4.10	300 W PV module P-V curve with LC perturbation applied to the right of MPP operating point	52

4.11	300 W PV module current and voltage waveforms with L-LC perturbation applied at the MPP operating point	53
4.12	300 W PV module I-V curve with L-LC perturbation applied at the MPP operating point	53
4.13	300 W PV module P-V curve with L-LC perturbation applied at the MPP operating point	53
4.14	300 W PV module current and voltage waveforms with L-LC perturbation applied to the right of MPP operating point	54
4.15	300 W PV module I-V curve with L-LC perturbation applied to the right of MPP operating point	54
4.16	300 W PV module P-V curve with L-LC perturbation applied to the right of MPP operating point	54
4.17	255 W PV module I-V and P-V curve with LC perturbation applied at the MPP operating point	55
4.18	RLC inductor voltage and current waveforms during LC perturbation approach with 300W PV modules at the MPP operating point	55
4.19	RLC inductor voltage and current waveforms during L-LC perturbation approach with 300W PV modules at the MPP operating point	55
4.20	Perturbation device schematic	59
4.21	Perturbation device LC PCB design	61
4.22	Perturbation device L-LC PCB design	61
5.1	DAD layout	63
5.2	ESP32 programmer PCB design	65
5.3	Data packet format from user to DAD	67
5.4	DAD TCP server software flow diagram for received data	68
6.1	Monitoring strategy overview	70
6.2	No stored perturbation flow diagram	72
6.3	L-LC perturbation flow diagram	73
6.4	Experimental setup, circuit breakers, grid-tie inverter and charge controller	75
7.1	Monitoring website displaying the latest measurement data for all MD's	79
7.2	MD1-4 (Day 1) - Daily monitoring (13:14-19:08) of the four 300 W Renesola PV module's connected to the grid-tie inverter	83
7.3	MD1-4 (Day 2) - Daily monitoring (07:06-19:30) of the four 300 W Renesola PV module's connected to the grid-tie inverter	83
7.4	MD1-2 (Day 3) - Daily monitoring (09:35-15:15) of the two 300 W Renesola PV module's connected to the charge controller	83
7.5	PV array evening shade	84
7.6	PV module 1 PSC	84
7.7	PV module 1 and 2 PSC	84
7.8	MD1 (Day 1) - 300 W PV module with LC perturbation	85
7.9	MD2 (Day 1) - 300 W PV module with L-LC perturbation	85
7.10	MD3 (Day 1) - 300 W PV module with LC perturbation	86
7.11	MD4 (Day 1) - 300 W PV module with L-LC perturbation	86
7.12	MD1 (Day 2) - 300 W PV module with LC perturbation	87
7.13	MD2 (Day 2) - 300 W PV module with L-LC perturbation	87
7.14	MD3 (Day 2) - 300 W PV module with LC perturbation	87
7.15	MD4 (Day 2) - 300 W PV module with L-LC perturbation	88

7.16	MD1 (Day 3) - Daily monitoring (09:37-15:18) of 300 W PV module connected to charge controller with LC perturbation applied	89
7.17	MD2 (Day 3) - Daily monitoring (09:37-15:18) of 300 W PV module connected to charge controller with L-LC perturbation applied	89
7.18	MD1 (Day 3) - Point F, current and voltage waveforms with LC perturbation	90
7.19	MD2 (Day 3) - Point F, current and voltage waveforms with L-LC perturbation	90
7.20	MD1-2 (Day 3) - Point F, I-V curve waveforms	90
7.21	MD1-2 (Day 3) - Point F, P-V curve waveforms	91
7.22	MD1 (Day 1) - Point A, current and voltage waveforms with LC perturbation	91
7.23	MD2 (Day 1) - Point A, current and voltage waveforms with L-LC perturbation	92
7.24	MD1-2 (Day 1) - Point A, I-V curve waveforms	92
7.25	MD1-2 (Day 1) - Point A, P-V curve waveforms	92
7.26	MD1 (Day 2) - Point B, during morning shade applying LC perturbation	93
7.27	MD2 (Day 2) - Point B, during morning shade applying L-LC perturbation	93
7.28	MD1-2 (Day 1) - Point B, P-V curve waveforms	93
7.29	MD3 (Day 2) - Point B, during morning shade applying LC perturbation	93
7.30	MD4 (Day 2) - Point B, during morning shade applying L-LC perturbation	93
7.31	MD3-4 (Day 2) - Point B, P-V curve waveforms	93
7.32	MD1-4 (Day 2) - Point D, P-V curve waveforms	94
7.33	MD1-4 (Day 2) - Point E, P-V curve waveforms for PSC on PV module 1	95
7.34	MD1-4 (Day 2) - Point E, P-V curve waveforms for PSC on PV module 1 and 2	95
7.35	Summary of perturbation technique in tracking MPP for the experimental setup	96
A.1	Research test facility.	104
A.2	Experimental set up, circuit breakers, grid-tie inverter and charge controller	104
A.3	Outdoor WiFi AP for the DAD ESP32	104
A.4	4 x 300 W Renesola PV modules.	104
A.5	MD set up for the experimental results	104
A.6	Morning shade cause by surrounding buildings	104
A.7	Morning shade cause by surrounding objects	104
A.8	Internal network server setup.	106
A.9	MD1-2 - Daily monitoring (07:43-18:11) of the two 300 W Renesola PV module's connected to the charge controller, with inaccurate ADC readings	106
B.1	ATL321 cathode current vs voltage	107
B.2	ADS8866 ADC 4-wire mode timing requirements	108
B.3	ADC voltage and current sample time	108
B.4	Previous version of the MD PCB design 3D view	109
B.5	Atmel Studio	110
B.6	MD power supply schematic	111
B.7	MD MCU, ESP32 and RFM98 schematic	112
B.8	MD measurement circuitry schematic	113
B.9	MD PCB design 3D view	114
B.10	MD PCB design 2D view	115
B.11	MCU RX_AACK (receive) state	116
B.12	MCU TX_ARET (transmit) state	117
C.1	Perturbation device schematic	118
C.2	Single diode model	120
C.3	Simplorer perturbation simulation set up with LC (no stored energy) design	120
C.4	Simplorer perturbation simulation set up with L-LC (stored energy) design	121

C.5	PD LC schematic	122
C.6	PD LC PCB design 3D view	123
C.7	PD LC PCB design 2D view	124
C.8	PD L-LC schematic	125
C.9	PD L-LC PCB design 3D view	126
C.10	PD L-LC PCB design 2D view	127
D.1	Morning shade cause by surrounding buildings	128
D.2	Morning shade cause by surrounding objects	128
D.3	SQL database table structure for MD's.	129
D.4	ESP32 programmer schematic.	131
D.5	MD PCB design 3D view.	132
D.6	MD PCB design 2D view.	133
E.1	Voltage and current calibration process.	135
E.2	Current sensor linearity	136
E.3	Voltage sensor linearity for MDC	137
E.4	Simultaneous sample of 500 Hz sine wave at both ADC inputs	137
E.5	MD and oscilloscope voltage measurements sampled at the same time.	138

List of Tables

2.1	MPP for shaded PV cells [23]	9
2.2	Nature of the characteristic roots	20
3.1	Short summary of the microcontroller specifications [80]	24
3.2	List of the available serial HEX-41 and HEX-42 MDC commands	36
3.3	List of the available HEX-41 and HEX-42 MD commands via IEEE 802.15.4	41
4.1	RLC design specifications	47
4.2	RLC inductance at various damping ratios	47
4.3	Perturbation LC technique states	49
4.4	Perturbation L-LC technique states	50
4.5	RLC inductance at various damping ratios.	60
5.1	List of the available python HEX-41 and HEX-42 MC commands	67
6.1	Perturbation strategy (no stored energy) sampling method	71
6.2	Perturbation strategy (stored energy) sampling method	73
7.1	Instrument measurement accuracy and IEC 61724 standards	78
7.2	Average daily (Day 1) energy for the LC and L-LC perturbation, extracted from Figures 7.8-7.11	86
7.3	Average daily (Day 2) energy for the LC and L-LC perturbation, extracted from Figures 7.12-7.15	88
7.4	Average daily (Day 3) energy for the LC and L-LC perturbation, extracted from Figures 7.16-7.17	90
7.5	MD1-4 (Day 2) - Point B, morning shade overview, extracted from Figure 7.3	93
7.6	MD1-4 (Day 2) - point D, fault condition, extracted from Figure 7.32	94
7.7	MD1-4 (Day 2) - Point E, P-V curve waveforms for both PSC experiments, extracted from Figure 7.33 and 7.34	95
A.1	Research test facility infrastructure.	103
E.1	Current calibration accuracy.	136
E.2	Current calibration accuracy.	136

Nomenclature

Symbols and Variables

T_{cell}	Cell Temperature	[°C]
T_{STC}	temperature at Standard Test Conditions	[°C]
P_{MPP}	Power at Maximum Power Point	[W]
MPP	Maximum Power Point	[W]
I_{SC}	Short Circuit Current	[A]
V_{OC}	Open Circuit Voltage	[V]
V_{MPP}	Voltage at Maximum Power Point	[V]
I_{MPP}	Current at Maximum Power Point	[A]
f_{OSC}	clock source oscillating frequency	[Hz]
θ_{sa}	Sink to ambient thermal resistance	[W/°C]
θ_{cs}	Case to sink thermal resistance	[W/°C]
θ_{dc}	Device to case thermal resistance	[W/°C]
T_{amb}	Ambient temperature	[°C]
T_{dev}	Device temperature	[°C]
T_{case}	Case temperature	[°C]
T_{snk}	Sink temperature	[°C]
P_D	Power dissipated	[W]
I_{SW}	Switching current	[A]
f_S	Switching frequency	[Hz]
P_{cond}	Conduction power losses	[W]
P_{sw}	Switching power losses	[W]
V_{BAT}	Battery supply voltage	[V]
R_S	Series resistance	[Ω]
R_{SH}	Shunt resistance	[Ω]

Abbreviations

PCB	Printed Circuit Board
MCU	Micro Controller Unit
IC	Integrated Circuit
USART	Universal Synchronous and Asynchronous serial Receiver and Transmitter
MISO	Master In Slave Out
MOSI	Master Out Slave In
SPI	Serial Peripheral Interface
I^2C	Two-wire interface
I^2S	Inter-IC Sound Bus
SCK	Serial Clock
SDIO	Secure Digital Input Output
GND	Ground
HEX	Hexadecimal
PV	Photovoltaic
MPPT	Maximum Power Point Tracking
DC	Direct Current
IEA	International Energy Agency
ADC	Analogue To Digital
SD	Secure Digital
I-V	Current Voltage
ESR	Equivalent Series Resistance
TX	Transmit
RX	Receive
SRAM	Static Random Access Memory
PSC	Partial Shading Conditions
IP	International Protection marking
IEEE	Institute of Electrical and Electronics Engineers
API	Application Programming Interface
SDK	Software Development Kit
RTC	Real Time Clock
EEPROM	Electrically Erasable Programming Read-Only Memory

WSN	Wireless Sensor Network
PLC	Power Line Communication
Wi-Fi	Wireless Fidelity
SQL	Structured Query Language
AP	Access Point
RF	Radio Frequency
ROM	Read-Only Memory
MOSFET	Metal Oxide Semiconductor Field Effect Transistor
CMOS	Complementary Metal Oxide Semiconductor
BJT	Bi-polar Junction Transistor
MAC	Medium Access Control
CSMA-CA	Carrier Sense Multiple Access with Collision Avoidance
NTP	Network Time Protocol
CSV	Comma-Separated Values
OSI	Open Systems Interconnection
PHY	Physical Layer
PSDU	PHY Service Data Unit
MPDU	MAC Protocol Data Unit
SFD	Start of Frame Delimiter
SHR	Synchronization Header
PHR	PHY Header
MHR	MAC header
PAN	Personal Area Network
FCF	Frame Control Field
FCS	Frame Check Sequence
IP	Internet Protocol
NAT	Network Address Translation
DHCP	Dynamic Host Configuration Protocol
DNS	Domain Name System

Chapter 1

Introduction

1.1 Background

Fossil fuels (oil, coal or gas) are the key sources and conventional forms of energy generation in the world. These energies are used for transport, electricity or thermal energy used for heating [1]. Fossil fuels emit green house gases into the atmosphere, which is the major factor contributing to climate change and this has resulted in critical pollution limits [1]. The increasing global demand for energy and the depletion of fossil fuel reserves have also resulted in the global fostering of new research efforts in renewable energy, an alternative energy that is unlimited and can be continuously used [2]. These renewable energies include wind, hydro, geothermal, tidal and solar. Photovoltaic (PV) solar power can generate electricity for a wide range of applications, scales, different climates, geographical locations and has been increasingly used worldwide in recent years [3].

The first generation of PV solar cells, discovered by American scientists in the 1950s only had an efficiency of 5%-6% [4, 5]. During this time, PV solar energy generation was not feasible and competitive compared to conventional energy generation. This was due to high cost, low demand and short lifespan of silicon [6]. The continuous Research and Development (R&D) in PV solar energy has resulted in the cost reduction of PV technology, whilst the efficiency of PV cells increased and, as a result, by 2002 the global PV production was increasing by 20 % annually [5, 7]. This is known as the *solar boom* in the PV solar industry, which started in the early 2000s when Germany introduced the Feed-in Tariff (FiT) program that overcame the financial barrier that limited solar PV's market penetration [4]. This program allowed grid-connected PV generation plants in Germany to receive a high and flat tariff for every kWh generated for 20 years [4]. Demand for PV solar significantly increased, which caused a domino effect that resulted in mass production, increased investment, improvement of the technology and competition among suppliers [4]. The ongoing competition in the PV market continues to enable R&D in PV technologies [6]. Therefore, PV manufactures always strive to compete for lower production costs and higher energy output efficiencies [6]. According to research done by the Fraunhofer Institute for Solar Energy Systems (ISE), the global cumulative PV installation up until the end of 2017 is 415 GW_p [8], as illustrated by Figure 1.1. Historically, the ongoing development of PV technology and exponential growth in the global PV industry, as shown in Figure 1.1, is a result of the solar learning rate. The term *solar learning rate* describes how the cost of PV cell technology decreases as the technology becomes cheaper [8, 9]. According to Fraunhofer, in the last 37 years the PV module prices reduced by 24% with the doubling of the cumulated PV module production [8]. South Africa has also set a target to purchase 10% (7 GW) of its electricity from renewable sources by

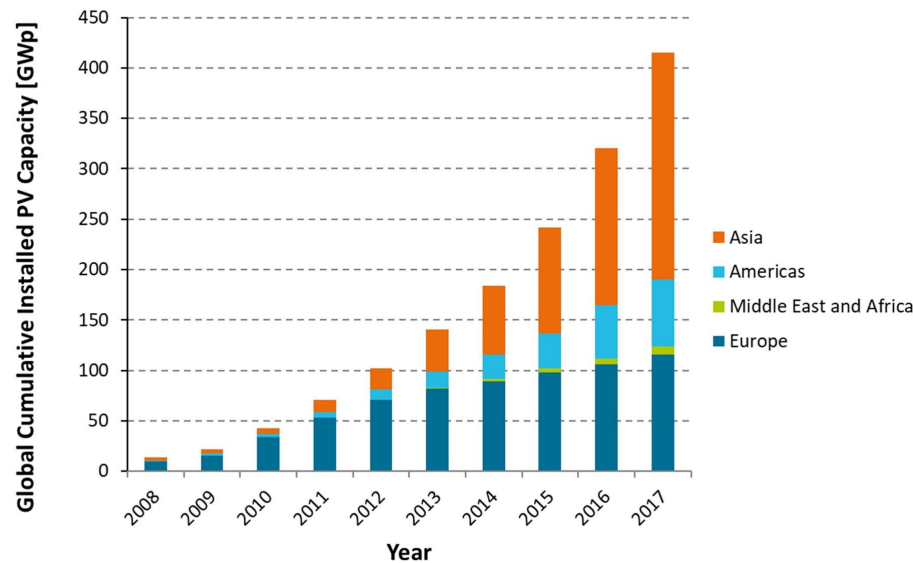


Figure 1.1: Global Cumulative Installed PV Capacity [GW_p] [8]

2020 and 17.8 GW by 2030 [10, 11]. In August 2011, the South African Department of Energy (DoE) introduced the Renewable Energy Independent Power Producer Procurement Program (REIPPPP) that has successfully attracted investment for independent power producers in South Africa to drive investment for renewable energy generation in the country [10]. This incorporated 5 successful bidding rounds and assisted South Africa in reducing its dependence on fossil fuels [10]. South Africa's utility scale renewable energy technologies

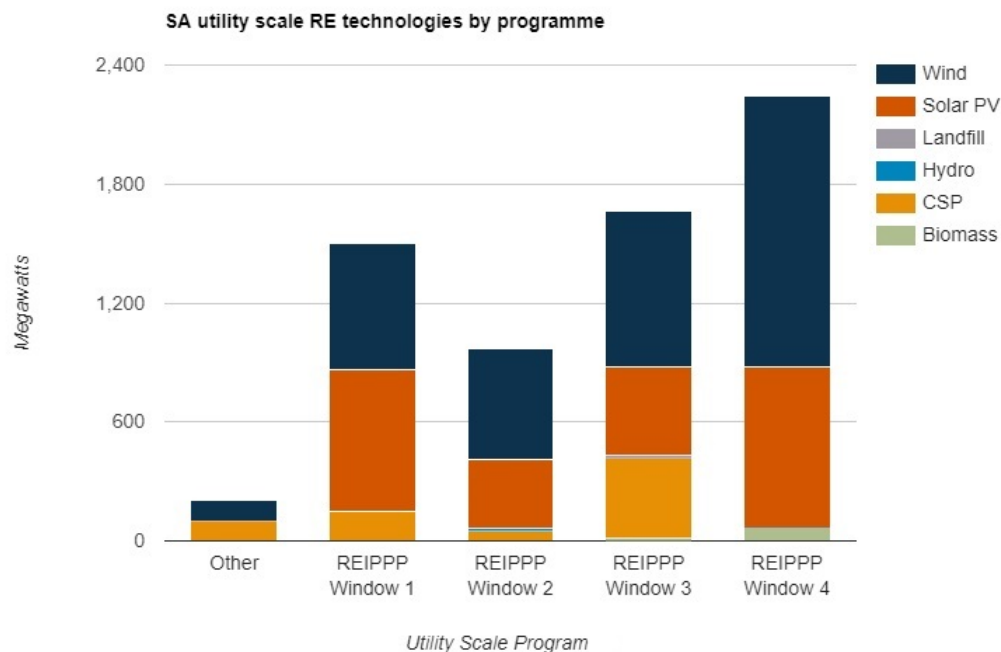


Figure 1.2: SA utility scale RE technologies by program for bidding rounds 1-4 [12]

program overview, shown in Figure 1.2, illustrates the first four bidding windows. Note that other refers to renewable energy plants that existed before the introduction of the REIPPPP.

As of April 2016, 6.4 GW of the 7 GW has been procured from bidding windows 1-4 [10] and by October 2016, 2.8 GW of the procured capacity had already started operations [10]. Solar PV tariffs reduced from 2.76 (ZAR/kWh) in bidding round one to 0.79 (ZAR/kWh) in round four, with a 75 % reduction in the tariff [13, 14]. In financial terms, with these competitive tariffs, any external factors influencing the initial capital costs are of concern to investors and PV operators to remain economically viable. With this in mind, energy generation, particular in the renewable energy sector, are striving for higher levels of efficiency.

1.2 Research motivation and problem statement

The *solar learning rate* and ongoing innovations in the PV solar industry have made PV technology a viable solution for widespread adoption [15]. At the same time, there are several issues that prevent PV installations from functioning as ideal power sources, given that PV modules are exposed to elements for a life span of 20-30 years [15]. During this time, PV modules can be affected by issues such as shading, soiling, silicon ageing, temperature gradients and much more that result in PV module degradation, which causes mismatch between PV modules [15]. This results in PV arrays losing power and has an effect on the amount of energy a PV array can produce [15, 16]. The main concern for investors, PV operators and stakeholders are to ensure that PV systems generate energy as predicted by effectively monitoring PV systems [17]. PV energy generation plants generally require an integrated management system throughout the duration of the PV plant's life cycle [18]. PV operators and designers are always striving to optimise maximum energy yield, while keeping installation costs to a minimum. The more detailed and sophisticated the PV monitoring solutions are, the more costly. Investors and PV plant operators can only select an appropriate monitoring solution mainly based on the feed-in-traffic rate in order to stay economically viable [19]. The unexpected faults lead to downtime and energy loss, which is detrimental for the financial return on investment [16, 17]. Detailed PV monitoring solutions provide more information regarding the PV plant and the overall performance of the PV system is compromised by the contribution of each subsystem [16, 19]. Hence, monitoring PV systems on a higher resolution, such as a module level monitoring system, can better assist in effectively managing PV systems [15] at extra cost.

On the one hand, the advancement of communication mediums with the integration of informatics and continuous advances in micro-controller, CMOS RF-transceivers are enabling technologies for low cost wireless communication [20]. Furthermore, low cost wireless communication is enabling the expansion of the Internet of Things (IoT) to extend internet connectivity to embedded devices [21]. These advancements have allowed authors such as M. Gargiulo et al. [22] to use this technology to successfully investigate and implement real-time PV module monitoring using low cost wireless communication.

This thesis will implement in-situ real-time PV module monitoring and perturbation techniques to a PV module by introducing under-damped oscillations to determine if the current operation point of the PV module is indeed the Maximum Power Point (MPP) without affecting the PV array operation. Data acquisition is performed via wireless communication and the hardware has a technology readiness of level 6. This device prototype aims to assist all PV plant stakeholders with the relevant detailed information regarding the health of PV modules, which can identify defective modules, faults and energy loss in PV systems.

1.2.1 Research questions

The project motivation serves as an incubator for the following questions:

- How can PV module monitoring effectively manage PV systems and assist in improving energy yield?
 - What parameters need to be monitored?
 - How should these parameters be monitored?
 - How is monitored data handled?
 - How accurate should the measurements be?
 - How significant are the mismatches between PV modules, if any?
- Will the proposed perturbation techniques identify if a PV module is operating at maximum power?
 - Can the MPP be located from any operating point of the PV module?
 - Does the applied PV module perturbation techniques have any influence on the PV array operation?
 - How does the perturbation techniques perform under varying irradiance conditions?
 - If the PV modules are not operating at MPP, can the proposed monitoring solution determine how much excess power is available?

1.2.2 Research objectives

The following research objectives are set to execute this research:

- Acquire real-time data from actual field-exposed PV modules with the use of a monitoring device.
- Extract simultaneous voltage, current and back-plate temperature measurements from individual PV modules with and without perturbation.
- Analyse the effects of the perturbation techniques and determine whether a PV module is operating at MPP.
- Analyse whether the proposed monitoring and the perturbation techniques can provide meaningful information to effectively manage the PV systems.

1.2.3 Research tasks

The research objectives can be accomplished by the following tasks:

- Design and build a monitoring device that is capable of measuring a PV module's power output.
- Design and build a perturbation device that is capable of oscillating a PV module's operating point around the current operating point fast enough without disturbing the PV array operation.

- Design and build a data acquisition device to collect data from the monitoring devices to be uploaded to an online data base. If internet connectivity is temporarily unavailable the data acquisition device must be capable of storing the sampled data on non-volatile memory acting as a buffer. When internet connectivity is restored, the sampled data stored in the buffer will be uploaded to the online database.
- Make use of existing PV infrastructure to test the proposed system. Install the required communication infrastructure, which allows the transfer of all data acquired from monitoring devices onto an online database via the internet.
- Configure, program and develop the required communications. This includes server, network and database configuration.
- Develop the required user software to conduct a full data analysis, which can determine any mismatches between PV modules and determine if the current operating point is indeed the MPP.

An existing PV infrastructure was used to execute the tasks with the addition of adding the communication infrastructure. The location of this facility is located on a rooftop at Stellenbosch University's Electrical and Electronic Engineering Department. In turn, the existing infrastructure represents realistic conditions, which allows for the research objectives to be completed. For a detailed description of the research facility refer to Appendix A.

1.2.4 Hypotheses

The following hypotheses are made with regards to in-situ monitoring and the applied perturbation techniques:

- PV module monitoring incorporated with embedded low cost wireless technology can be a key factor for higher resolution monitoring in PV systems.
- PV module level monitoring complements the underdamped RLC perturbation technique because the lower power levels and perturbation speed enables smaller hardware components for the perturbation circuitry.
- The perturbation techniques can locate the MPP of a PV module for any operating point without affecting the PV array operation.

1.3 Scope And Limitations

It is not within the scope of this thesis to provide a detailed financial breakdown of the cost of the monitoring topology. This thesis merely aims at demonstrating the PV monitoring solution along with perturbation techniques. Only a selected number of PV modules are installed and are available, which were sufficient to effectively execute the thesis objectives. The installed researched facility consisted of:

1. 4x stationary pc-Si Renesola 300 W PV modules
2. 2x pc-Si Renesola 255 W PV modules in storage
3. 1x 1.6 KW SMA transformer-less grid-tie inverter

4. 1x Micro Care 40 A charge controller
5. 2 x 12 V deep cycle lead-calcium batteries

Back-plate temperature measurements of individual PV modules are not needed for answering the research questions and is only included as an additional feature of the monitoring device for PV module health monitoring. In terms of the experimental set-up and methodology discussed in Chapter 6, the testing duration is not a determining factor of how effective the system is, but rather a demonstration of the intended application operates.

1.4 Thesis Overview

The thesis format is as follows:

- Chapter 2: The literature review presents studies conducted by researchers, experts and scholars who have contributed to work described in this thesis. The initial focus is on cause of PV yield losses and mitigating these losses, which then introduces the need for PV monitoring systems. This is followed by the current monitoring approaches in literature and industry, with particular focus on PV module level monitoring and link between the IoT. The final section of this chapter is dedicated to the relevant theory regarding the natural and step response of RLC circuits, as it is necessary for a basis for the design of the perturbation device.
- Chapter 3: This chapter focuses on the design of the monitoring device, also known as the MD or MDC for the coordinator monitoring device. This device is responsible for measuring the PV module back-plate temperature, measuring current and voltage simultaneously. Furthermore, this device transmits the sampled data wirelessly to the data acquisition device and controls the perturbation device. A complete hardware and software design is provided for this device.
- Chapter 4: This chapter contains the design of the perturbation device (PD) and builds on the theory presented in chapter 2 on the natural and step response of RLC circuits. All the relevant theory and application of the perturbation device is provided in this chapter, particularly of the hardware design of the two perturbation techniques. Along with a simulation on the two perturbation techniques.
- Chapter 5: This chapter is dedicated to the design of the data acquisition device also known as the DAD. Amongst other things, this device serves as a medium to gathering all sampled data from monitoring devices for an end user to store the data on an online database. Data is stored on the DAD non-volatile memory if internet connectivity is unavailable. A hardware and detailed software design is provided for this device.
- Chapter 6: The experimental analysis is discussed in this chapter with all the necessary infrastructure in place. This chapter presents the experimental setup and methodology implemented to ensure that the research objectives are met.
- Chapter 7: This chapter discusses and presents all the acquired data. Before discussing any results, a detailed validation and filtering process is first provided. This is to ensure confidence in the data extraction process.

- Chapter 8: Conclusions are drawn regarding whether the proposed perturbation and monitoring method can determine if PV modules within an array are operating at MPP, given the results in Chapter 7. Based on the results, suggestions are made on whether this proposed solution is possible to effectively monitor PV systems.

Chapter 2

Literature review and background study

2.1 Chapter overview

This chapter presents studies that have been conducted by researchers, experts and scholars who have contributed significant information to the body of knowledge for this particular field. Factors that cause a mismatch in PV arrays are presented. Monitoring in PV systems overview along with the link between the Internet of Things (IoT) and monitoring solutions are presented. The chapter then progresses towards the fundamentals of the natural and step response of RLC circuits.

2.2 Previous research

2.2.1 PV cells

Modelling PV cells provides a convenient method to model the behaviour of PV modules and arrays. Therefore, PV cell theory is fundamental for the design and monitoring of PV systems. PV cells use semiconductor materials to convert sunlight into electricity that typically generates low voltages of 0.5 to 0.8 Volts (V) depending on the semiconductor material and technology [23]. Given the low voltage levels of the PV cells, multiple PV cells are connected together in series to form a PV module, which are then interconnected in series and/or parallel to form a PV panel¹ [23, 24]. A combination of series connections increase the system voltage, while parallel connection increases the current. The combination of series and parallel connections are used to meet the nominal voltage and power level requirements [24].

By the end of 2017, global annual production was 93% for mono- and multi-crystalline cells, and 4.5% for thin film cells [8]. Thin film PV cells are cheaper and less efficient than multi-crystalline PV cell technology [6, 8]. The most common and simplest implementation of a PV cell model is shown in Figure 2.1a, known as the single diode model. Another PV cell model, known as the double diode model, is used for greater accuracy and forecasting PV system performance [25]. The modelling of PV cells is only an idealised representation that assumes each PV cell contributes equal amounts of power to the PV array [23]. In other words, the PV array output characteristics are represented by the super position of each individual PV module and cell, assuming uniform irradiance [26]. If one or a few cells are shaded (non-uniform irradiance), then modelling of the PV array becomes more complex

¹The rest of the thesis will refer to PV panels as PV modules because it conforms to the terminology used by other researchers discussed in this chapter.

[23]. Figure 2.1a illustrates that the top PV cell is shaded in a series connected PV module, using the single diode model - the PV cell current source I_{SC} and diode current I_d is zero. The current from the lower PV cells are forced to flow through both R_p and R_s , reducing the output voltage by $I(R_p + R_s)$. Table 2.1 illustrates the significant power loss of 77% with just a single cell shaded. The implementation of bypass and blocking diodes, as shown

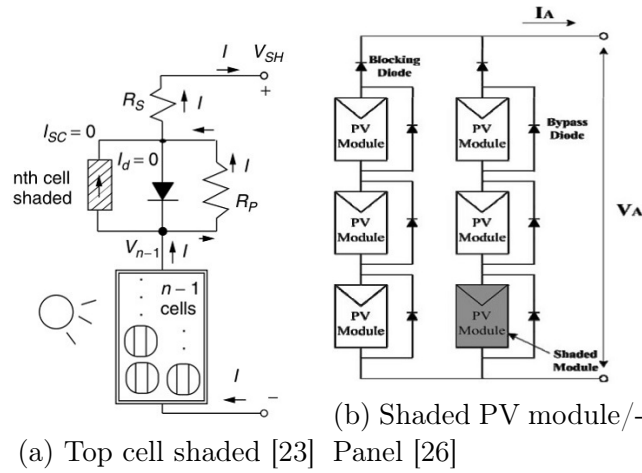


Figure 2.1: PSC on (a) PV modules or (b) PV array

Table 2.1: MPP for shaded PV cells [23]

PV cells shaded	MPP (W) no bypass diodes	MPP (W) with bypass diodes
Full Sun 0%	65	N/A
Dirt 10%	58	N/A
1 cell shaded 50%	40	N/A
1 cell shaded 100%	15	43
2 cells shaded 100%	7	N/A

in Figure 2.1b, is an effective method for solving the voltage drop across the output voltage during shading [23]. Table 2.1 shows the significant amounts of power lost caused by shaded PV cells. By inserting bypass diodes the PV module's power loss for one cell shaded is now reduced to 33% instead of 77% without any bypass diodes. During no shading, there is a voltage rise across the PV cell so the bypass diode is cut off - because no current flows through it. However, during shading current does flow through the bypass diode, turning it on. Thus, the only influence on the output voltage would be the reduction of the bypass diode turn on voltage. Blocking diodes also reduce the output voltage with a purpose of ensuring current always flows out of the PV modules [23]. Typical diodes consume 0.6 V drops during turn on and special diodes can be used that have turn on voltages as low as 0.2 V to further avoid reduction at the output voltage [23]. Placing bypass diodes on each PV cell is feasible although manufacturers provide just a few to cover certain PV cells within the PV module [23, 26]. The use of bypass diodes not only improves the output power and string performance during shading, but it also prevents hot spots from developing on individual shaded PV cells.

2.2.2 Mismatch in PV arrays

Partial Shading Conditions (PSC) is an inevitable phenomenon caused by factors in the environment that significantly reduces power in PV systems [24, 26]. These factors include trees, clouds, humans, buildings, etc. that partially shade PV arrays. During PSC, also known as non-uniform irradiance, the PV system has several local MPP characteristics on the power output [24, 26–28]. Thus, tracking the Maximum Power Point (MPP) becomes challenging and a reliable technique is required to track the local/global maximum power point (GMPP) appropriately for PV systems to produce energy efficiently under these conditions. Maximum power point tracking (MPPT) is an essential method for efficient power generation in PV systems - given the non-linear characteristics of the PV array [26]. Conventional MPPT methods, such as the perturbation and observation (P&O), incremental conductance (IncCond), ripple correlation control (RCC), two-mode, etc. are effective for tracking the MPP [24, 26]. However, Ji and Belhachat [24, 26] criticise conventional MPPT techniques because uniform irradiance is assumed for the PV array, which is not always the case and therefore these methods are inadequate to track the GMPP - particularly under severe PSC. All these factors affect the power-voltage characteristic curve on the PV array, resulting in a dramatic decrease of PV system performance [24, 26]. Likewise, modelling of PV cells, modules and arrays are now more complex under PSC, because the PV array is no longer represented by the superposition of PV cells connected in series and/or parallel combinations. This implies that under PSC, an arbitrary number of PV cells are shaded while others are not. Figure 2.2 illustrates the power voltage characteristic curve of the array under PSC. There exists two local MPP, where only one is the MPP [24, 26]. Therefore, conventional MPP techniques fail to adequately track the real MPP under PSC and more sophisticated methods are required.

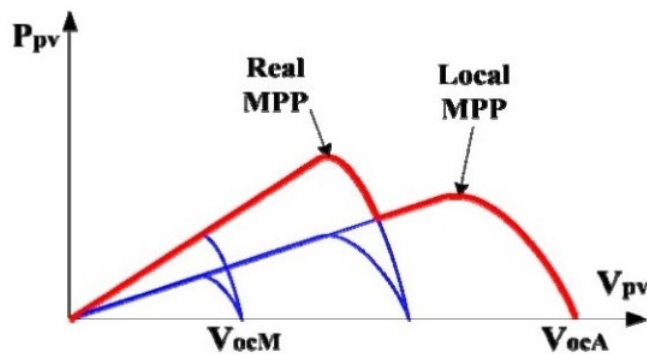


Figure 2.2: P - V characteristics for mismatched PV modules [26]

In literature, there are various MPPT techniques that detect the GMPP under PSC. A recent review (May 2018), compiled by Belhachat et al. [24] - discusses the differences between the current GMPP techniques presented in literature, which are determined by the convergence speed, design complexity, sensor requirements, control parameters and hardware implementation costs and the effectiveness of the operating range. Each GMPPT technique is favourable depending on the intended application. Over 52 different methods for determining GMPP under PSC are discussed in this review, based on recently published scientific literature [24]. GMPPT methods under PSC can be classified into four categories: optimisation based methods, methods based on hybrid approaches, mathematical model based methods and other GMPPT. Optimisation based MPPT methods are algorithms that find the best optimal solution given certain conditions. The hybrid approach combines two or

more approaches by overcoming the drawback of one approach. Mathematical models and other MPPT methods were also introduced in this review to address tracking the GMPP under PSC. PSC is unavoidable and is most certainly going to occur in PV systems whether by living beings or cloud cover. Therefore, a GMPPT algorithm is required to ensure efficient energy harvesting capability [24]. The comparison between methods discussed in this review shows that the GMPPT methods perform better than conventional methods under PSC. Optimisation based methods are effective under PSC in tracking the GMPP. However, the performances differ in efficiency, tracking speed and complexity depending on the algorithm used. Hybrid methods improve tracking under PSC because they implement a combination of different algorithms, combining optimisation algorithms or integration of other methods, which are better than original or single algorithms. Belhachat et al. [24] concludes that, despite all the developed methods and those that are enhanced in performance, it was very difficult to conclude which technique is the most well-rounded. Thus, the selected method is reliant on several parameters such as the application, hardware availability, cost, convergence speed, precision and system reliability. Belhachat et al. [24] findings is based on the fact that 69% of the topologies are stand-alone applications and this is mainly due to a low complexity of 17%, medium tracking speed that varies vastly from a maximum of 4.6 to a minimum of 0.02 seconds [17]. Therefore, reinstated from Belhachat [17], the best developed method depends on the intended application. For this reason, it would be recommended for inverter designs to have a range for various different applications with the appropriate tracking method or allow capability for users to select a predefined GMPPT based on the intended application.

2.2.3 Monitoring in PV systems

The primary objective of any power plant is reliable and continuous operation in order to generate maximum energy yield for maximum economic returns, whereby the exact same applies for PV plants using a dedicated PV monitoring system [29]. Continuous operation is achieved by mitigating and detecting faults, and avoiding energy yield losses. Some of the issues contributing to energy loss in PV systems were discussed in the previous sections and gives the reader a better understanding of why monitoring is required in PV systems. This section will further discuss why PV systems incorporate monitoring solutions and how they are implemented, to better understand what impact they have on the energy yield. Therefore, good questions to ask are what should be measured, how is it measured and how are measurements handled? These questions assist with selecting a monitoring approach depending on how each PV subsystem is grouped - the overall performance of the entire PV system compromises each individual subsystem [16]. Therefore, by monitoring each subsystem, PV monitoring is performed on a higher resolution and at the same time regrettably comes with extra cost. For this reason investors and PV plant operators only select the most cost effective PV monitoring solution based on the feed-in tariff to remain economically viable [19]. Irrespective, monitoring is a vital aspect in PV systems, whether on a large or small scale. A recent review article on monitoring, diagnostics, and power forecasting for PV systems by Daliento et al. mentions that there are fabrication defects and anomalies in PV modules despite the reduction costs of PV modules [16]. These negative consequences still reduce energy yield and the profit for all stakeholders, therefore early fault detection and real-time monitoring is vital for short downtime and time maintenance, but also avoids equipment damage, minimum energy loss and safety concerns [16]. Small scale (households) PV systems have basic monitoring solutions built into the inverter, such as, power output, daily energy production, data logging solutions for online monitoring and tracking [30]. Large scale (solar farm) PV plants' operations and management (O&M) require an inte-

grated management system throughout the life cycle of the PV plant [18]. According to Daliento et al. [16] and Gartner Instruments [18], a PV monitoring system should mitigate risks for investors, provide suitable feedback for O&M, plant performance statistics, have a track record and the ability to control the plant. Detailed (each sub-system) PV monitoring provides more information to better effectively manage the PV system [16, 17]. Furthermore, utility scale PV monitoring systems provide energy yield information that is compared with the predicted yield, which is a major concern for investors, O&M and stakeholders [17]. The installed assets and investment in PV plants globally are as a result of reliable and effective data monitoring solutions [18].

While mainly focusing on literature studies, the current PV monitoring solutions offered in industry should also be of interest, as there is most likely to be a similarity between the two given that the proposed implementation is a development prototype. PV Manufacturers discussed in this chapter are some of many well established companies in the PV industry and are presented with the purpose of illustrating to the reader what currently is available on the market. Manufacturers do face competition with one another and remain competitive by advancing and expanding their product capabilities with new technology and research [31]. One example of this was in 2016, SMA Solar Technology AG acquired a 27% stake in Tigo Energy in order to integrated Tigo Energy's IoT based smart module monitoring technology with their current range of products to remain competitive in the PV market [32].

SMA Solar Technology AG [19] is one of many solar PV companies that specialise in solar inverters for PV systems and monitoring solutions. SMA's PV strings are categorised as zone or string monitoring. String monitoring is more detailed than zone monitoring, because each PV string entering the combiner box is monitored, zone monitoring, on the other hand, only monitors the output of the combiner box that feeds into the inverter input [19]. String monitoring is a more costly option over zone monitoring, because more information about each sub-system in the PV system is being monitored. Figure 2.3 illustrates the overview of Gartner Instruments [33] (company specialising in precision measurements, control instrumentation and systems) PV monitoring solution of a typical large scale PV plant, where monitoring occurs at various different levels. As can be seen in Figure 2.3, each PV string is being measured in the combiner box, hence string monitoring is taking place.

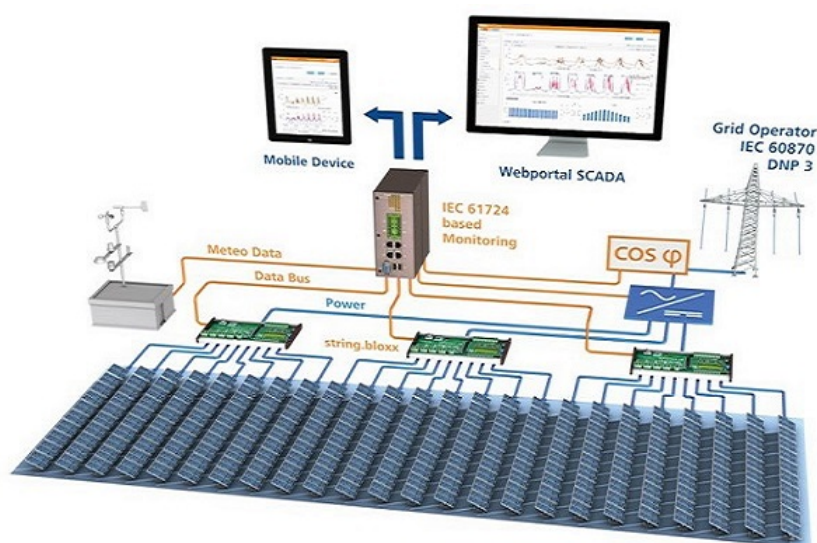


Figure 2.3: Gartner monitoring solution overview [18]

Gartner combiner boxes (termed "string.bloxx") use DC shunts to measure the PV string

current because they are typically 10 times more accurate, not susceptible to temperature variance than hall-effect current sensing, which better detect under performance due to the long term degradation of PV modules [18]. Gartner's string.bloxx (combiner boxes) monitoring hardware consumes low power of less than 1.5 W and can be supplied power via the RS485 communication cable or via a DC/DC converter [18]. Both SMA plant controller [34] and Gartner [18] Q.reader inverters offer grid management solutions to properly connect PV systems to the grid. The inverter is a vital but basic component for converting the PV array's DC power to AC power, to supply energy to the grid. At the same time, inverters can have dual features during night time or on cloudy days, when PV systems are unable to generate active power. Certain PV inverters have the capability to be used for VAR compensation to support and stabilise the grid [35]. Therefore, both SMA and Gartner's inverters grid management allow for export limitations and power analyser control at the grid connection to meet settling times defined by the grid operator [18, 34]. Other features also include fail safe operation, direct marketing, reactive power supply and zero export [18, 34].

Belhachat et al. [24] vaguely concluded that each GMPPT is selected for specific application and installing the wrong inverter topology could result in energy loss while attempting to track the GMPP. PV inverter manufacturers that offer multiple GMPPT (hybrid approaches) along with traditional MPPT solutions have a competitive edge in the market by addressing this shortfall in inverter capabilities during PSC. Inverter manufacturer SMA [36] provides a dual approach, also known as the hybrid approach, by implementation of its "OptiTrac" operation control on PV strings, which is an additional function added to the standard MPP tracking on some of their inverters to track the GMPP under PSC. This feature operates the PV array at great distances from the known operating point in order for the inverter to always find the GMPP. However, using this procedure introduces unavoidable losses during the searching procedure of the GMPP. During no PSC the "OptiTrac" limits searching losses to a maximum of 0.2% when searching for a second MPP. SMA "OptiTrac" is disabled by default and this dual functionality allows the inverter to be used in a variety of different operating conditions.

Tigo Energy Inc and SolarEdge Technologies Inc are both PV manufacturer companies that specialise in PV module monitoring and power optimization. Tigo Energy is known for its TS4 PV module monitoring and power optimization [37] features along with similar products from competitor SolarEdge, with their power optimization using a DC-DC converter and monitoring capabilities [38]. Both products also provide additional features such as fire safety, automatic shut-down protection, warranty tracking, claims to reduce O&M costs and its monitoring platforms are accessed via a portal providing sufficient detailed information to identify defective or faulty PV modules [15, 37, 38].

Furthermore, Tigo Energy provides case studies to further market their products. A particular case study is of interest because it is a large scale PV plant with the capacity of 1.78 MW implemented by Tigo Energy's TS4 technology, situated in Tsungi, Japan [39]. This utility PV plant consists of 6624 PV modules forming 288 PV strings connected to 3 central inverters [39]. After being commissioned it was found that several PV modules were showing open circuit or low voltage levels [39]. Further investigation revealed that these PV modules had fault diodes that had to be replaced [39]. Tigo Energy's TS4 further detected four PV strings that were open circuits, due to a faulty connection [39]. The PV plant also experiences shade in winter and Tigo optimizers improved energy production by 5-10% during these conditions [39]. This case study does not directly state whether or not all the PV modules have the TS4 product installed and therefore, it is speculated that they are installed on all PV modules. Heavy shading is caused by nearby trees and power poles, which could be the main reason

the TS4 power optimiser technology was implemented. On the other hand, it could be due to a favourable feed-in-tariff. The TS4 does have the advantage of immediately detecting a fault the minute they occur, such as the faulty diodes and the PV string fault. However, it could be argued that string monitoring could also detect this and maybe zone monitoring as well. A second case study using the TS4 technology showed a 13% increase in energy yield, on a 2.64 MW PV plant located in central Italy and the TS4 optimiser functionality increased the energy yield during shading caused by nearby power lines [40]. Testing was performed on 8 days without and with the TS4 device, thereafter using numerical methods to determine the difference in performance. It is particularly uncommon to see PV module level monitoring on such a huge scale in both case studies. With the information provided in the case study, it is difficult to speculate the main motive for using the TS4 topology, specifically whether it is a cost effective solution.

2.2.4 PV inverter topologies

The most common inverter topologies are illustrated in Figure 2.4.

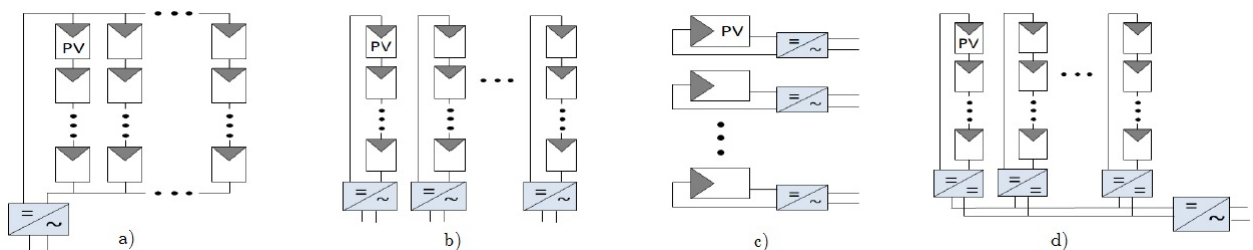


Figure 2.4: PV plant topologies: a) central inverters; b) string inverters; c) module inverters; d) multi-string inverters [41]

The different inverter topologies are discussed by [41–44] are classified by the following:

1. **Central inverters:** One central inverter is fed by several hundred, and even a thousand, PV modules. The majority of utility scale PV plants adapt this topology. Multiple PV strings, consisting of series connected (to boost the voltage) and parallel connections (to boost the current) of PV modules are fed into the inverter.
2. **String inverters:** Each PV string has its own inverter with the advantage of MPPT occurring on the string level. This increases performance by mitigating mismatches of individual strings associated with central inverters. The disadvantage is that it increases overall costs.
3. **Module inverters/converters:** Individual inverters for each PV module optimise MPPT on a module level. This topology significantly increases plant cost and is only practical and economical for small scale PV systems that are often shaded. Module converters are a DC-DC converter that extracts the MPP for each PV module within the string and are much cheaper than PV module inverters.
4. **Multi-string inverters:** These are similar to the string inverter topology, but instead a DC-DC converter is implemented. An adequate number of strings are then connected to an AC-DC inverter. This topology is an active area of research and specific applications.

The economics of the feed-in tariff scheme not only dictates the monitoring system, it may also have a slight influence on the inverter topology selection. At the same time, inverter selection is mainly determined by practicality [41]. According to Pavan et al. [45], central inverters (shown in Figure 2.4a) are the preferred method of choice in large utility PV plants because the cost of distributed inverters can be up to 60% higher. Pavan et al. further mentions that, if the distributed topology is implemented in a large scale PV plant, only a very small difference in efficiency is gained to justify an extra cost [45].

There are several research papers and institutional bodies, such as the IEA (International Energy Agency), that have identified extensive causes for low yields in PV systems, in particular the DC section [24]. To name some, these faults are characterised as PV cell cracks, hot spots, accumulation of dirt, PV module mismatches, short circuiting of modules, combiner box faults caused by corrosion or damaged connections, open circuit, short circuit faults and poor MPPT implementation [46]. These faults coincide with discussions already mentioned in Section 2.2.2, regarding GMPP in tracking the true MPP under partial shading conditions. Furthermore, both Gargiulo et al. [22] and Sadineni et al. [41] agree that using module inverters or converters mitigates the need to implement complex MPPT algorithms and topologies to track the GMPP. Sadineni et al. [41] further mention that module inverters or converters increase costs and are mainly used in small PV systems where shading is known to take place. Similarly, as already mentioned by Pavan et al., any extra cost needs to be justified with extra gain in efficiency. At the same time, feed-in-tariffs differ among regions and countries. When South Africa introduced the REIPPPP, there was a higher feed-in-tariff during the initial bidding rounds than in the later bidding rounds, as mentioned in Section 1.1. Likewise, Germany has a greater feed-in-tariff rate where string monitoring is common [19]. The United States of America on the other hand, has a lower feed-in-tariff rate than Germany and it is more common to find zone monitoring [19].

At this point low PV yield losses at the DC side of the PV array are of concern. Literature studies and products in industry were discussed to illustrate how low energy yields are mitigated in PV systems. These include a variety of GMPPT and solutions under various PSC to improve energy yield, as discussed in Section 2.2.2 and 2.2.3. At the same time GMPPT cannot detect individual sub-system faults that occur within the PV array [24]. PV systems where shading is known to occur, a DC-DC converter or micro-inverters at the PV module assist in reducing energy yield losses. PV manufacturers, such as SolarEdge Technologies Inc and Tigo Energy Inc, implement power optimizers (DC-DC converters) under shading conditions with significant yield improvements. These PV modules technologies also provide monitoring and safety in PV systems, whereby, these features allow PV plant operators to identify faults immediately. However, this topology is not economically feasible and cost effective for larger utility scale PV systems, according to Pavan et al. [45]. In contrast, Tigo Energy implemented the PV module optimizer and monitoring topology for PV plants of 2.64 MW capacity. The feed-in-tariff still dictates the monitoring solution rather than the size of the PV plant. Therefore the majority of large utility PV plants use zone and string monitoring as the highest resolution of monitoring. There are still unanswered questions as to how and whether PV module monitoring is the only effective way to manage PV systems and whether PV module monitoring will ever be a cost-effective solution in the future?

2.2.5 Monitoring approaches for PV systems

Daliento et al. [16] review article presents a wide range of literature on monitoring, diagnosing, power forecasting in PV systems. Daliento et al. are in agreement with PV manufacturers SMA, Tigo Energy, SolarEdge, that higher resolution monitoring is the most

effective way to manage PV systems. Higher resolution monitoring improves the accuracy of the monitoring and diagnosis process and is termed "level of granularity" (LoG) [16]. High resolution also implies higher LoG and the lowest LoG implies monitoring the PV system on a macro level. In lower LoG case, measurements are performed on the instantaneous power (electrical parameters) on both the AC and DC sides, which is then converted to energy [16]. Using a monitoring and diagnostic approach, these electrical parameters acquired from PV systems are compared with predicted models [16]. A Performance Ratio (PR), defined according to the IEC standard [47], is then used to analyse the data. Broadly speaking, the performance ratio is the ratio between the measured instantaneous and nominal power of the solar field, scaled by the ratio between instantaneous and temperature at Standard Test Conditions (STC) ($1kW/m^2$) irradiance [16]. There are various PR methods discussed by Daliento [16] in the review, where their accuracy depends on the level of LoG. The aim of these PR models are to get a percentage of the actual and theoretical yields to determine how efficiently the PV plant is performing [48]. Monitoring methods at the array level (zone monitoring) have a drawback of not locating faulty components. A greater level of LoG is essential for reducing maintenance cost by detecting and addressing faults immediately [16]. This can be performed by PV string monitoring and can also be exploited to neglect weather data by comparing PV strings to one another. This approach is well demonstrated by Baba et al.[49], where the PV string currents are compared and faulty ones are directly identified. This approach does fail to identify faults when multiple strings fail.

Although moving towards a greater LoG, assists PV plant operators by providing information about each subsystem to better manage the PV plants and this assists in reducing O&M costs. At the same time, increasing the LoG results in large amounts of data that require sophisticated algorithms to analyse the data and identify faults, which can be performed using Artificial Intelligence (AI) [16]. AI uses available datasets to develop a knowledge base [16]. Thereafter, learning algorithms learn the characteristics of a PV system in order to make predictions. A number of learning algorithms have been proposed in literature for fault detection and diagnostics in PV systems [16, 50–52]. These include the use of artificial neural networks (ANN) for PV systems under PSC, short-circuit detection and PV health monitoring.

Not all monitoring systems can always detect power loss. One way to ensure the PV yield is correct is by using analytical redundancy, which verifies the actual yield with a reference model [16]. This is a basic model that detects power losses by comparing the monitored data with a reference model that uses the meteorological data and if a certain threshold is reached an alarm condition is triggered [53–56]. A reference model is often derived using the single diode model that uses parameters from the PV module datasheet or derived from extraction methods [57]. Therefore, temperature and irradiance measurements are essential for the reference model approach [55]. According to Mellit et al.[58] and Antonanzas et al.[59], the forecasting of energy yield is a key condition supporting the monitoring of PV fields in order to determine if PV plants are under performing. Therefore, meteorological information, such as the temperature and irradiance shown in Figure 2.3, are gathered precisely for forecasting models, which is also in accordance with the IEC 61724 standard [47, 60].

Satellite based monitoring systems have also been presented as another alternative with cost-effective Unmanned Aerial Vehicles (UAV) performing thermal analysis [16, 22]. Standard monitoring approaches in utility scale PV systems can only identify the faulty string. Thereafter the string requires disassembling to identify faulty components, which is time demanding and halts energy generation [16]. PV plants can also be situated in remote areas where accessibility to the PV plant for O&M teams are not straight forward to access. Similarly, PV modules can also be situated on rooftops, where no accessible or restricted

access may be an issue for physical inspections. As a result, the operational safety implies additional maintenance costs. According to recent literature [16, 61–63], thermal monitoring using UAV are equipped to inspect PV fields using thermal and/or visual cameras, along with image processing technology for fault detection and classification. However, some of the drawbacks reported by Leva et al. [64] is the height above the PV arrays, identifying the PV module, as well as defect detection and classification. Other reports by Aghaei et al. [63] and Dotenco et al. [65] suggest that these limitations can be overcome by using costly high resolution cameras and when doing so, UAV will play a vital role in O&M of PV plants due their effectiveness in detecting and locating faults.

2.2.6 PV Module Monitoring

Di Napoli et al. [66] successfully implemented a Power Line Communication (PLC) on a DC bus with a series connected PV modules. This PLC, unlike the standard PLC, can successfully transmit data to transceivers irrespective of their reference voltages. The PLC communication is intended for PV module monitoring by integrating monitoring systems into smart grids to effectively monitor the contribution of each PV module in the PV system. Current solutions make use of dedicated cables or wireless protocols [66], as also seen with Tigo Energies TS4 monitoring device. However, Di Napoli et al. [66] criticise these methods for being unfavourable when the PV plant dimensions increase. Extra growth in wiring and large distances need to be covered, which leads to a rise in energy consumption [66]. This PLC design avoids extra wiring with each board being powered by the PV module being monitored and using supercapacitor-based harvesting circuit, which have a longer number of discharge cycles than electrochemical batteries [67]. Tests further showed that the PLC communication did not affect the operation of the PV module performance. However, no PV motoring tests were performed and PLC communication was merely demonstrated.

Gargiulo [22] also proposed a monitoring circuit for PV module monitoring to reduce costs for O&M. According to Guerriero et al. [68] individual PV modules have a low fault probability (about 15% [69]) and each issue at module level propagates to the entire PV string. However, 15% statistic can definitely be criticised because it is from tests performed during the 1990's [69]. Guerriero et al. further mentions that in recent years medium/high PV power plants have become a reality and the number of PV modules are in the thousands to hundred thousands [68], which coincides with the solar learning rate along with changes to support policies globally [8, 16].

Gargiulo's monitoring circuit implements a harvesting stage using super capacitors, neglecting the need for external supply or batteries similar to that presented in [66]. Data transmission was performed wirelessly via IEEE 802.15.4 2.4 GHz frequency with 250 kbps data rate at a low power 19 mA receiving data, 23 mA consumed when sending data and the circuit consumes 20 mA during normal operation. The IEEE 802.15.4 star topology network structure was implemented, comprising of one network coordinator that controls network traffic and with end devices situated on PV module monitoring devices. This topology aims at simplifying O&M costs by avoiding in-situ inspections. Measurements were performed to determine the PV module open-circuit voltage V_{OC} and short-circuit current I_{SC} , with the measured data being verified using an oscilloscope. The monitoring device took measurements from 5 AM to 7 PM, taking the average of 50 samples' measurement. The downside to this monitoring approach is that the PV module was disconnected from the PV array during measurements. The procedure was first to bypass and disconnect the PV module to not affect PV string operation. Thereafter, the V_{OC} and I_{SC} were performed individually through the day. Guerriero et al. [68] presented an improved version in later years, that

performs additional tests to detect PSC. The effects of partial shading are easily prevalent with the monitoring device measurements clearly indicating the I_{SC} to be more sensitive to shading than V_{OC} [68]. A further test was performed by monitoring a PV string under PSC to determine MPPT failures. The monitoring devices show a sudden drop in power due to shading and the MPPT algorithm attempts to increase the string voltage by assuming uniform irradiance and undesirably tracks the local MPP instead of the GMPP. Although individual PV module monitoring is proposed, there needs to be justification for higher revenues and improving O&M [16]. Solutions that offer power optimization and monitoring, such as Tigo Energy's TS4, solution are better suited for conditions where shading occurs. Gargiulo's monitoring device, along with Guerriero et al.'s improved version, does show the benefits of module monitoring, detecting PSC and MPPT fails under PSC. At the same time there are inverters and power optimizers that can increase energy yield under these conditions as well. In simple terms, monitoring assists all stakeholders with keeping the PV plant operational and ensuring energy yield is as predicted. Furthermore, depending on the level of granularity, PV monitoring systems can reduce O&M costs.

A common issue in literature associated with PV monitoring systems is the transmission of data. The main options are WiFi, Power Line Communication (PLC) and GSM [16]. The drawback with GSM are the high service provider fees [70]. According to Gargiulo et al. [22], PLC communication reduces system's lifespan given the installed hardware, which can be critiqued on any monitoring system. ZigBee is, however, the proposed protocol [16], which is the same 2.4 GHz frequency used by Tigo Energy's SMA optimization PV module technology [71] and operates on the IEEE 802.15.4 protocol. Remote monitoring on individual PV modules is an important concern for the PV community [66, 68]. As previously mentioned, a higher level of granularity provides more detailed information about the overall PV plant performance. The long life cycle of PV plants requires automatic real-time fault detection for all stakeholders to ensure long term energy yield predictions [68]. Current monitoring methods in large scale PV systems are performed at the inverter or combiner boxes, as discussed in the preceding section [34, 68].

2.2.7 Internet of Things (IoT)

The "Internet of Things" (IoT) has seen a tremendous surge in interest by companies who have used the technology to develop IoT related products [31]. A question one may be thinking is what is IoT and why is there a such great interest? The term IoT has been broadly used, however, there has never been any common definition. In simple terms, IoT has enabled everyday objects to communicate via the internet and in some instances controlled via the internet [31]. IoT is characterised by the combination of digital and physical components to create new products. This is mainly due to improving efficient power management systems, broadband communication platforms, reliable memory storage and improvement in microprocessor technologies [20, 31]. Consequently, this has unfolded many opportunities for businesses and entrepreneurs to introduce innovative IoT solutions with existing products for consumers [72]. Therefore, IoT typically combine IT with physical things usually in the form of hardware and software [31]. The future for IoT is bright and prosperous. Simultaneously there are challenges that still need to be addressed from both a business and technological viewpoints [31]. Such challenges are the threats and opportunities IoT poses to a business. The question arises whether current business models need to be adapted or re-defined based on acquiring IoT based products. Entire businesses may need to be re-assessed as competitors enter newer and smarter IoT based devices on the market [31]. The main concerns and challenges here are security and personal privacy, device level energy supply, device identification and addressing, internet scalability, standardisation and harmonisation

[73].

From the preceding sections in this chapter, it was identified that PV module level monitoring does provide better and effective means to monitor PV systems. Cost is the biggest factor that contribute to the fact that PV module level monitoring only occurs in small-scale PV systems. Furthermore, studies have been done by Guerriero et al. using IoT based technologies for small-scale PV module monitoring and the manufacturer Tigo energy specialises in PV module monitoring solutions. IoT and PV model monitoring in large scale PV systems share very similar concerns and issues. Since IoT strives for not only connecting people to the internet but everyday things, these concerns may be mitigated with the continuous emergence of IoT in everyday devices. Hopefully, at the same time PV module monitoring will turn out to be cost-effective in large scale PV plants using IoT technology.

2.3 Natural and step response of RLC circuit

Characteristics of the natural and step response of RLC circuits the fundamental building blocks for the design of the Perturbation Device (PD). As mentioned in chapter 1, the PD must be capable of determining if a PV module is operating at MPP by perturbing the PV module around its current operating point. The term RLC simply means that the circuit contains a resistor (R), inductor (L) and capacitor (C), which is limited to two types of circuits, parallel and series RLC circuit, as illustrated in Figure 2.5. The series RLC circuit is concerned with the current through the series connected elements due to the applied DC voltage source and the parallel RLC circuit is concerned with the voltage created across the parallel branches due to the DC current source [74]. Equations 2.1 and 2.2 are derived from

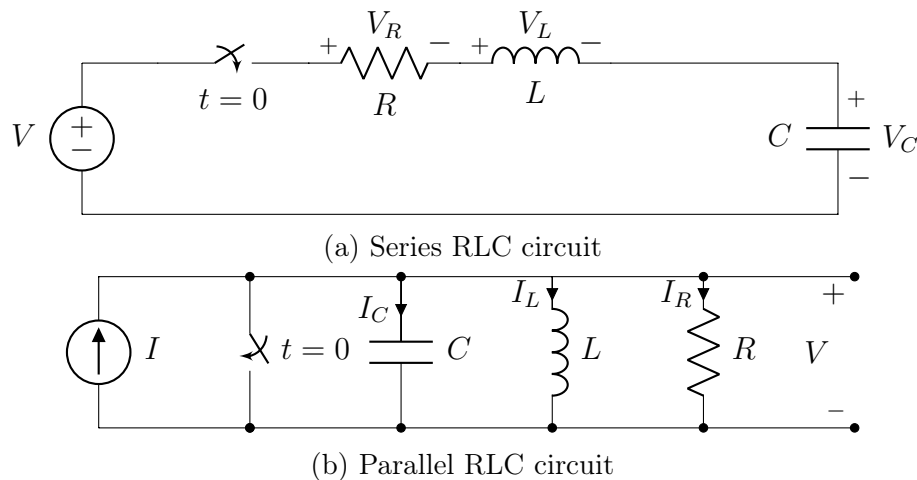


Figure 2.5: Parallel and series RLC circuit [74]

Nilsson [74] by using Kirchhoff's law in order to produce differential equations. Equation 2.1 describes the differential equation for the series RLC circuit shown in Figure 2.5a and Equation 2.2 is the parallel RLC circuit shown in Figure 2.5b.

$$\frac{d^2i}{dt^2} + \frac{R}{L} \frac{di}{dt} + \frac{i}{LC} = 0 \quad (2.1)$$

$$\frac{d^2v}{dt^2} + \frac{1}{RC} \frac{dv}{dt} + \frac{v}{LC} = 0 \quad (2.2)$$

As mentioned by Nilsson et al. [74], both RLC circuits can be modelled by second order differential equations with general solutions shown in equation 2.3.

$$v = A_1 e^{s_1 t} + A_2 e^{s_2 t} \quad (2.3)$$

Equation 2.3 is derived using the *Laplace transform* by assuming that the solution of equations 2.1 and 2.2 are of exponential form [74]. Nilsson et al. verifies [74] this assumption and the general solution, which results in two roots s_1, s_2 shown in equation 2.4.

$$s_1, s_2 = -\alpha \pm \sqrt{\alpha^2 - \omega_0^2} \quad (2.4)$$

The α term differs for the RLC series (Equation 2.5) and parallel (Equation 2.6) circuits with ω_0 remaining the same for both cases.

$$\alpha_s = \frac{R}{2L} \quad (2.5)$$

$$\alpha_p = \frac{1}{2RC} \quad (2.6)$$

$$\omega_0 = \frac{1}{\sqrt{LC}} \quad (2.7)$$

The roots s_1, s_2 can either be real or complex roots and the nature of the roots depend on the values of α and ω . There are three outcomes as shown in Table 2.2.

Table 2.2: Nature of the characteristic roots

Over-damped	Under-damped	Critically damped
$\omega_0^2 < \alpha^2$	$\omega_0^2 > \alpha^2$	$\omega_0^2 = \alpha^2$

The nature of the roots determine the response of the RLC circuit and the roots are determined by neper and resonant radian frequencies, which, in actual fact, are dictated by the resistor, inductor and capacitor values.

2.3.1 Resonance and natural frequency

An inductor stores energy in a magnetic field and a capacitor stores energy in an electric field [75]. Resonant frequency in an RLC circuit occurs when the inductor and capacitor are equal in reactance [75]. This causes the electrical energy to oscillate between the electric field of the capacitor and magnetic field of the inductor. The presence of the resistor causes the oscillations to die out exponentially over a period, known as the damping effect of the resistor. The total impedance for the series RLC circuit shown in Figure 2.5a is given by Equation 2.8 and the parallel RLC circuit shown in Figure 2.5b is given by Equation 2.9.

$$Z = \sqrt{R^2 + (X_L - X_C)^2} \quad (2.8)$$

$$Z = \frac{1}{\sqrt{\frac{1}{R^2} + \left(\frac{1}{X_L} - \frac{1}{X_C}\right)^2}} \quad (2.9)$$

At resonant frequency the reactance of the inductor is equal to the reactance of the capacitor, as illustrated in Equation 2.10.

$$\begin{aligned} X_L &= X_C \\ 2\pi fL &= \frac{1}{2\pi fC} \\ f &= \frac{1}{2\pi\sqrt{LC}} \\ \omega_0 &= \frac{1}{\sqrt{LC}} \end{aligned} \tag{2.10}$$

Equation 2.10 verifies equation 2.7 and the term *natural frequency* refers to the oscillation frequency of the RLC circuit at resonance. At resonant frequency the RLC series circuit has a minimum and the parallel RLC circuit has a maximum impedance, as can be seen from Equations 2.8-2.9.

2.3.2 Damping

Damping is caused by the resistor in the RLC circuit and can be represented by the damping ratio shown in Equation 2.11. The damping ratio determines whether the RLC circuit will be able to resonate (oscillate) naturally. Under-damped circuits resonate, whereas over-damped and critically damped circuits are not capable of doing so.

$$\zeta = \frac{\alpha}{\omega_0} \tag{2.11}$$

The 3 different cases are presented below:

Under-damped

For the under-damped case $\omega_0^2 > \alpha^2$ and to ensure the circuit remains under-damped $0 < \zeta < 1$.

Over-damped

For the under-damped case $\omega_0^2 < \alpha^2$ and to ensure the circuit remains under-damped $\zeta > 1$.

Critically damped

For the under-damped case $\omega_0^2 = \alpha^2$ and to ensure the circuit remains under-damped $\zeta = 1$.

Out of the three different cases, the main focus will be on the under-damped case because it is the only case that can introduce the desired oscillations to perturb a PV module. A further derivation leading to the design of the perturbation device is present in Chapter 4.

Chapter 3

Monitoring device

3.1 Overview

This chapter begins with the conceptual hardware design of the Monitoring Device (MD) and implementation. This is followed by the communication between MD and Monitoring Device Coordinator (MDC) and MDC and Data Acquisition Device (DAD). The DAD is incorporated onto the MDC and is responsible for data acquisition, where the DAD acquires data from the MDs and then sends the sampled data to be sent by an end user to the internet for online database cloud storage. Finally, the software design is presented, with details regarding the interactions that occur within the MDC and MDs also known as MD(C).

3.2 Function of the Monitoring Device

To meet the research requirements set for this thesis, a monitoring device is required to measure the voltage, current and temperature for a PV module within a PV array. This device must be capable of meeting all IEC regulations and standards. Along with the MD is a Perturbation Device (PD), which is incorporated onto the MD and will be discussed in detail in the following chapter. The idea behind the MD is to monitor the PV module with or without the perturbation device enabled. The PD is responsible for introducing oscillations to alter the PV module's operating point around the Maximum Power Point (MPP), while the MD samples the voltage and current during this process. Given the PV characteristic IV curve, a change in voltage causes a change in current, therefore the voltage and current measurements are performed simultaneously. The temperature measurement is an additional feature intended for forecasting purposes and monitoring the PV module's temperature to detect PV module defects such as hotspots. The development in IoT has enabled embedded IEEE 802.15.4 communication technology onto the MD design, which is used to transmit data wirelessly between the MDC and MD. The MDC performs the same task as the MD. However, the IEEE 802.15.4 star network topology is implemented and requires a MD coordinator to govern the network similar to a master and slave topology. Thus, all MDs are slave devices to the MDC and at the same time the MDC is a slave to the DAD. The DAD and MDC communicate via a wired connection and is incorporated onto the same PCB.

In summary, the MDC design must enable the following functionality:

MDC (coordinator) only:

- Serve as a slave for the DAD with communication performed via a wired connection.

- Communicates with MDs (slave) via IEEE 802.15.4 wireless communication and serves as the network coordinator.
- Gets MD's sampled data or its own sampled data to be acquired by the DAD.
- configures MDs or itself via DAD.

MDC (coordinator) & MD (end device):

- IEEE 802.15.4 wireless communication between MDC (master) and MD (slave).
- Measures voltage and current simultaneously.
- Can measure the PV module temperature on 4 different locations.
- Controls perturbation operation.

3.3 Conceptual hardware design

3.3.1 General system overview

An illustration of the MD's hardware layout is illustrated in Figure 3.1. As mentioned, the main purpose of the MD is to monitor the PV module voltage and current simultaneously, as well as provide wireless communication for data acquisition retrieval. The core controlling all of these features is the MD MCU.

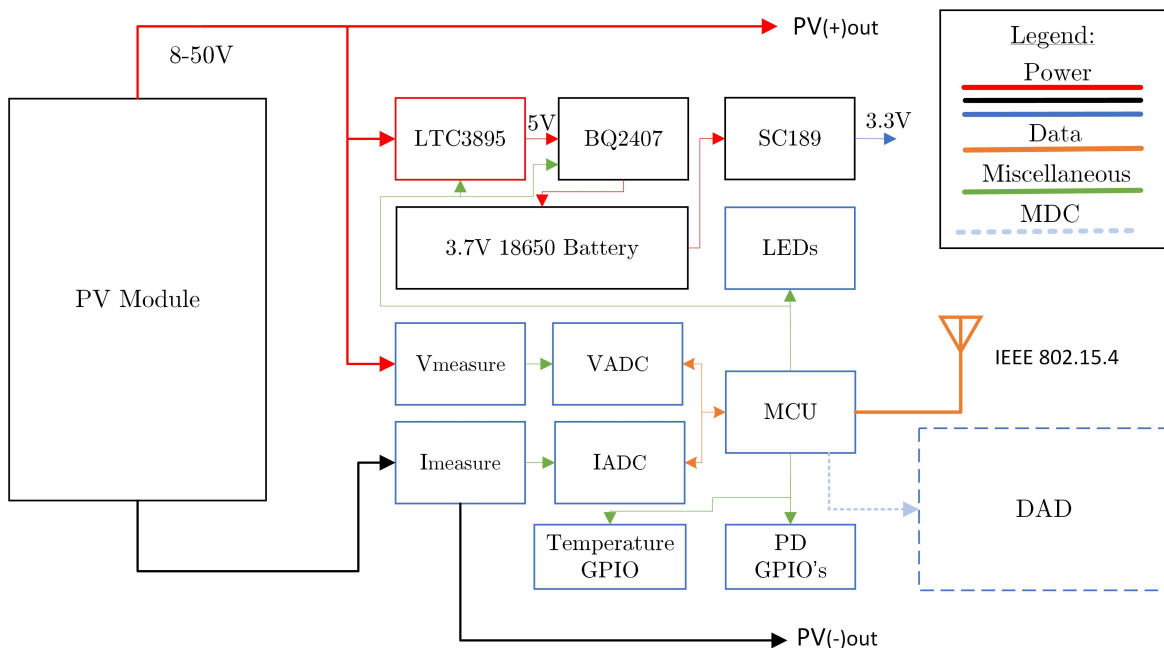


Figure 3.1: Monitoring device conceptual hardware layout

3.3.2 Power supply and voltage sources

The MD incorporates three Power Supply Units (PSU), with the first stage PSU powered from the PV module being monitored. This is performed using Linear technology's LTC3895f step down converter as it was the suitable Integrated Circuit (IC) selection for the first stage

PSU [76] design, given the vast input operating ranges of 8-100 Volts (V) that outputs a constant 5 V. These vast input ranges allow the MD to operate with input voltages for both polycrystalline or thin film PV modules. The second stage PSU is powered from the LTC3895f 5V output that charges a 3.7 V Samsung 18650 lithium ion battery [77]. Charging is done using the Texas Instruments BQ24079 IC [78]. lastly the third stage involves a PSU buck-boost converter that is powered from the 3.7 V Samsung lithium ion battery and outputs 3.3 V, using Semtech's SC189 IC [79]. 3.3 V is the low level voltage required by the core of the MD and DAD, shown in Figure B.7. During a measurement, the first and second PSU are turned off so that the MD is only powered via the Samsung lithium ion battery and the PV module is only being monitored. Thus, the power consumed by the implemented monitoring system does not reduce the PV panel's power during a measurement ensuring greater accuracy in measurements as well as reducing switching noise. All three PSU schematics are illustrated in Figure B.6.

An alternative approach, seen in literature [22, 66, 68], utilises super capacitors instead of batteries. However, for demonstration purposes a lithium ion battery was implemented for this research study. This will be further discussed in the recommendations sections. Furthermore, the first stage power supply is connected in parallel to the PV module and PD. This was an oversight in the design process and this configuration affects the effectiveness of the PD device, due to the first stage PSU input capacitors being more dominant than the perturbation capacitor. One solution to resolve this issue, is to use a relay to completely isolate the MD PSU during a perturbation sample. Refer to Section 7.5 for the solution to overcome this issue.

3.3.3 Micro-controller

The Atmel ATmega1284RFR2 Micro-controller Unit (MCU) used by the MD is an 8-bit AVR RISC-based microcontroller that features on both the MDC and MDs [80]. This MCU has 128 kB of ISP(In System Programmer) flash memory, 4 kB EEPROM, 16 kB SRAM and 32 general purpose I/O pins [80]. The micro-controller (MCU) enables wireless communication via the IEEE 802.15.4 protocol, which is one of the primary reasons this MCU was chosen. Figure 3.1 shows the interaction of the MCU with the other components. Furthermore, the MCU communicates with the Analogue to Digital Converter (ADC) via the Serial Peripheral Interface (SPI) communication line. The MDC uses the USART to communicate with the DAD, while GPIO pins are used to control the PD, LEDs and PSUs. The MCU is programmed via JTAG using an external AVRISP mk2 JTAG programmer [81]. The programmer is connected to a ten pin header on the PCB that is connected to the JTAG pins of the MCU. The MCU is also capable of being programmed via an mk2 in-system programmer [81] using the SPI header pins on the PCB. Details regarding the ATmega 1284P's electrical characteristics are presented in Table 3.1.

Table 3.1: Short summary of the microcontroller specifications [80]

Microcontroller specifications			
16 MHz clock speed (max)	2 x USART channels	3.3 V Supply	$V_{OL} = 0.9 V(max)$
SPI channel	8 bit data bus width	10 bit ADC	$V_{OH} = 2.5 V(min)$
4 kB EEPROM	128 kB Flash memory	16 kB RAM	$V_{IL} = 1.5 V(max)$
JTAG interface	10.1 x 10.1 x 1.05mm	32 x I/O pins	$V_{IH} = 3 V(min)$

3.3.4 Printed circuit board design

The MD(C) PCB was created with the Altium Designer 16.1 software package, illustrated in Figure 3.2, refer to Appendix B.0.4 for the PCB schematics. Figure 3.2 illustrates the power supply circuitry shown on the left, which is kept separate from the rest of the components to avoid unwanted noise that could affect the measurement circuitry and digital signals. Noise reduction is further avoided by using large tracks for power lines and the entire PCB bottom layer is a ground plane to ensure a common ground to all components. The ESP32 and RFM98 footprints are only required by the MDC and are unused when the PCB is being used as an MD.

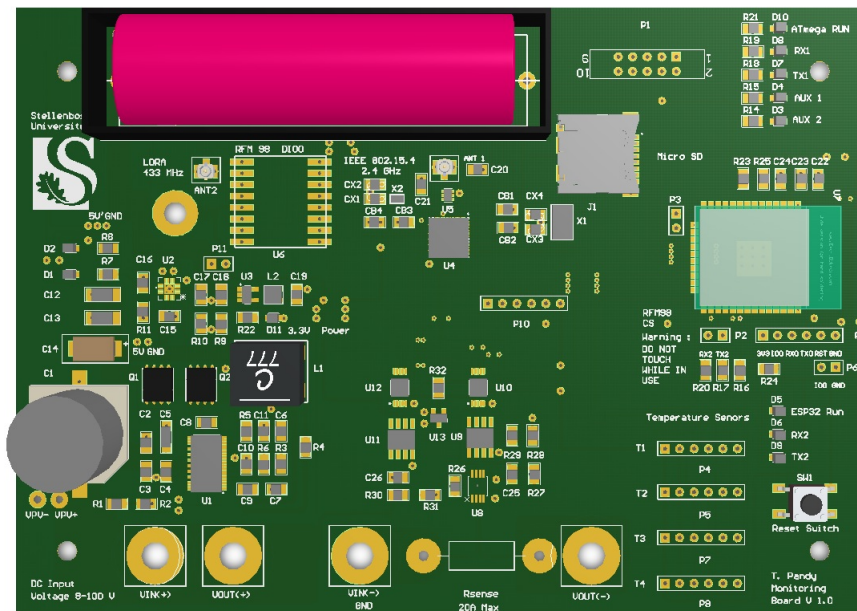


Figure 3.2: MD PCB circuit design 3D view

The 20 A sense resistor uses kelvin connections to reduce stray resistances and inductance, improving the accuracy of the current measurements. The PCB has 5 stand-offs along with a 6 pin header P10, that connect the top PD PCB with the bottom MD(C) PCB. Power from the PV module is supplied from the (top) PB PCB to the MD PCB via the stand-offs, while the 6 pin header sends control signals from the MD/MDC PCB to the top PD PCB in order to control the perturbation circuitry. The MD/MDC core, Atmel ATmega 1284RFR2 is situated at designator U4. Designator ANT1 provides a U.FL male output on the PCB that connects to a U.FL female to SMA connector, whereby an external antenna can be used to improve wireless reception of the IEEE 802.15.4 wireless communication protocol. This PCB is designed to fit in an International Protection marking (IP) 67 outdoor enclosure to be used during operation as displayed in Figure A.5, the external antenna is shown along with the power cables coming out of the enclosure.

3.3.5 IEEE 802.15.4 connectivity

The following information is cited from the Institute of Electrical and Electronics Engineers (IEEE) issue titled, IEEE Standard for Low-Rate Wireless Networks [82]. IEEE 802.15.4 operates in one of two topologies: the star or peer-to-peer topology. Both are shown in Figure 3.3. Before discussing each topology, the characteristics of each node that can occur in IEEE 802.15.4 in both topologies need to be understood. The nodes consist of a PAN (Personal Area Network), router and end device. A PAN is vital in both topologies and each

network should have at least one. Furthermore, a router is essential for another PAN that can serve as a gateway between IEEE topologies and is necessary to improve the range of the network. In other words a router can route its own and other devices' data packets in the network. Lastly, an end device can only route its own data packets to other devices. All devices operating on either topology have their own unique address. There are two address fields that can be used, which is referred to as the short or extended address. The short address is a 16-bit address, while the extended address also known as the IEEE address, is a 64-bit address intended for larger networks. Either address mode can be chosen. In the star topology, communication is established between devices via a single central controller node called the PAN. The peer-to-peer topology also incorporates a PAN. However, it differs from the star topology in that devices can communicate with each other without communication needing to go via the PAN, provided devices are in range of each other. The peer-to-peer topology allows for more complex networks that allow multiple hops to route data packets from any device to any other device on the network. Such functionality is done on higher layers of the OSI (Open Systems Interconnection) model and is not part of the IEEE 802.15.4 standard.

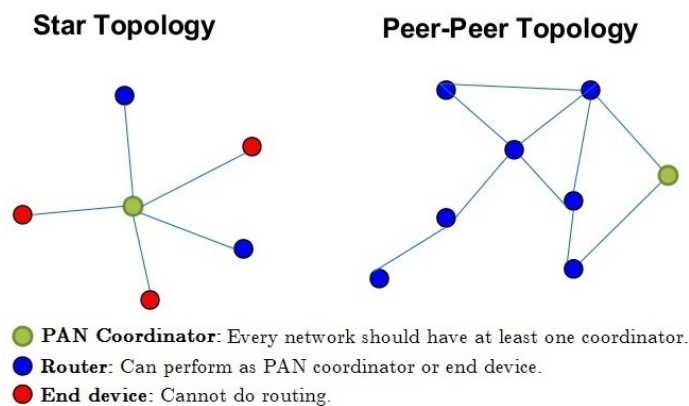


Figure 3.3: IEEE 802.15.4 network topologies
[83]

The MD utilises the star topology with the PAN, representing the MDC, providing a gateway to the end user via the DAD. Likewise, the end devices represent MD. Therefore, one MDC is implemented while the rest of the devices are end devices. In the case of a larger network where the MD is not in range of the MDC, intermediate router nodes can be implemented to improve the network range and size. Given that this thesis intends to demonstrate the technology on a small scale, the star topology is sufficient for this application. The Atmel Atmega 1284RFR2 provides the IEEE 802.15.4 protocol as an on-chip solution with the only external crucial components that is required are antenna, balun, crystal and decoupling capacitors. The transceiver requires a 16 MHz crystal clock for operation and is also the same crystal with which the ATmega1284RFR2 operates. The balun is needed to convert the MCU output impedance from 100 Ω to 50 Ω for the 2.4 GHz operating frequency. The balun 50 Ω output track is connected to a U.FI connector that is soldered onto the PCB. A U.FI to SMA connector cable is used to attach an external 3.2 dB gain dipole antenna to improve the range and quality of connectivity, which is needed at increased data rates. In addition, the MCU has two operating modes - the basic and extended modes as shown in Figure 3.4. The extended operating mode is chosen because the MCU automatically checks for an acknowledgement when sending data packets, therefore reducing coding and handling of events.

(CONVST) input pins at the same time. In the MD case, a single GPIO pin from the MCU (Digital Host) is connected to the conversion input pins of both voltage and current ADCs, as illustrated in Figure B.8.

When a conversion is completed on both ADCs data is retrieved via SPI communication from each ADC individually using the DIN pin as the conventional SPI chip select pin, as shown in figure B.8. Retrieving the data individually per ADC has a slight drawback, which limits the time between samples. The MCU has a second USART port that can be used in SPI mode, however the MCU can only perform tasks sequentially. Hence, the MCU can only use one SPI line at a given time. The verification of the simultaneous voltage and current procedure is demonstrated in Section E by E.4, both inputs are connected together and applied a sinusoidal waveform. There is no way around retrieving the data simultaneously even though the data is sampled simultaneously. One way to retrieve the data simultaneously is to implement programmable logic hardware that is capable of performing tasks simultaneously. The first revision of the MD made use of programmable logic using a Field-Gate Programmable Array (FPGA), which was successful in its implementation, (refer to Section B.0.2). An FPGA not only allows for simultaneous sampling and data retrieval, it also allows for sampling the data at the limits of the ADCs, whereas the MCU SPI peripherals do not allow for this capability. The ADC sampling speed is of importance because the ADC must be able to capture enough samples during a perturbation cycle. However, the final MD design implemented in this thesis has omitted the FPGA to reduce complexity, as it was discovered that the perturbation period could be adjusted to accommodate the MCU SPI peripherals' capabilities. This will be discussed in further detail in the perturbation section.

Furthermore, the ADS8866 is a 16-bit ADC, whereas the MCU's SPI buffer can only store 8-bits. For this reason the sampled 16-bit data is stored on the MCU in two 8-bit parts. Therefore, one sample of current and voltage is 4 bytes and the MCU has 16KB of internal SRAM. However, the internal SRAM is used for other functionalities such as the USART receive and transmit buffers, along with variables used for IEEE 802.15.4 communication. Therefore, the MCU has allocated 4096 KB or 2000 samples for both the voltage and the current. Once the data is requested by the end user, it is merged and scaled appropriately. The number of samples is user-defined However, for the perturbation it is important to capture samples before and after the perturbation is introduced, the amount of samples will be discussed in the perturbation in Section 4.2. The maximum conversion time required by the ADS8866 ADC is $8.8\mu s$ [84]. Thereafter it should take $2\mu s$ for the MCU to retrieve the data via SPI per ADC. Thus, it is a total of $12.8\mu s$ to sample and retrieve data for both current and voltage. However, via practical inspection it was found that the sampling period for both the voltage and current took $22.7\mu s$, as illustrated by Figure B.3. It was further decided the maximum sample period need only be a 1000 samples or 22.7 ms worth of sampling, given that the perturbation period was designed to be around 2 ms (refer to Chapter 4). Reducing the sampling range from 2000 to 1000 samples also reduced the handling and processing of the data.

The ADCs reference voltage is chosen to be 2.5 V, which is within the 2.5-5 V range of the ADC [84]. This implies the maximum analogue input signal to the ADCs for both the current and voltage pre-stage amplifier outputs should be designed not to exceed 2.5 V. The voltage reference was made possible using Texas Instruments ATL431 2.5 V shunt regulator that was powered from the 3.3 V PSU, as illustrated in the schematic in Figure B.8. This shunt regulator was simple to implement, only requiring a resistor to draw sufficient current for the output to remain stable at 2.5 V. Referring to Figure B.1 taken from the ATL431 datasheet - in order for the output voltage to be stable at 2.5 V an input current of $20\mu A$

and above is required. Thus, the resistance is calculated as follows in Equation 3.1.

$$R = \frac{VCC - Vref}{I} \quad (3.1)$$

With $VCC = 3.3$ V, $Vref = 2.5$ V and $I = 20\mu\text{A}$. The resistor is chosen as 1.6 K Ω to ensure sufficient current for the reference voltage to the ADC to remain stable and for sufficient current to be drawn by the ADC V_{ref} inputs. The equation used to calculate the current or voltage is illustrated by Equation 3.2 below:

$$\begin{aligned} ADC_{levels} &= \frac{2^{16} - 1}{2.5} \times V_{Input} \\ &= 26214 \times V_{Input} \end{aligned} \quad (3.2)$$

Where the analogue input to the ADCs is represented by V_{Input} and the digital result of the input voltage is represented by ADC_{levels} . The voltage and current calibration process is performed on each device and discussed in Appendix E. The calibration process is essential to ensure that the MD readings are accurate and non-biased. The IEC60904-1 specifies that voltage and current uncertainties should be no more than $\pm 1\%$ [47, 60].

3.3.6.2 Current measurement

The MD is designed to measure current up to a maximum of 20 A, which is well within the current limits of PV modules used in the experimental setup discussed in Section A. The current is measured using a 5 m Ω shunt resistor connected in series with the PV module, as illustrated in Figure 3.5. The current through the PV module is the same current through the shunt resistor and perturbation device when active. Using Ohm's law, the current through the shunt resistor creates a voltage drop that is fed into a two stage amplifier that is then read by the ADC. Texas Instruments INA156 instrumentation amplifier [85] is the first stage amplifier chosen for its low noise, DC offset and very high common-mode rejection ratio configured for a gain of 10. The second stage is a Microchip MCP601 operational amplifier [86] with a gain of 1.5. The multi-stage was chosen to increase the bandwidth by using lower gains on both amplifiers. The voltage read by the ADC is given in Equation 3.3 below.

$$\begin{aligned} V_{ADC_I} &= V_{5\text{m}\Omega} \times G_1 \times (1 + G_2) \\ &= I_{PV} \times R_{[\text{m}\Omega]} \times G_1 \times (1 + G_2) \\ &= I_{PV} \times 5[\text{m}\Omega] \times 10 \times (1 + 1.5) \\ &= \frac{I_{PV}}{8} [\text{V}] \end{aligned} \quad (3.3)$$

Therefore substituting Equation 3.3 into 3.2, the digital current 16-bit value is calculated as follows:

$$\begin{aligned} ADC_{levels} &= 26214 \times \frac{I_{PV}}{8} \\ I_{PV} &= \frac{ADC_{levels} \times 4}{13107} \end{aligned} \quad (3.4)$$

The earlier revision of the MD, as mentioned in section 3.3.6 performed the current measurement with the aid of a hall-effects current sensor. The hall-effect sensor was replaced by the current shunt method because there was a significant phase shift between current and voltage reading on the perturbation waveforms. This was a result of bandwidth limitations on the hall-effect sensor. Thus, the phase shift meant that plotting the IV curve correctly was no longer possible. For greater accuracy and precision the shunt resistor method is the better alternative and is the method used in the industry by Gartner Instruments for its accuracy, mentioned in Section 2.2.3 [18]. The concern with this method is the voltage drop over the shunt resistor. However, the maximum voltage drop is minimal at 0.1 V at a maximum current of 20A.

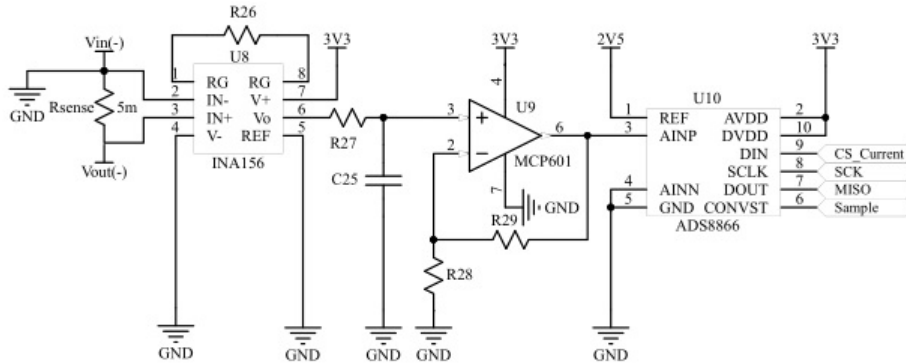


Figure 3.5: MD Current measurement circuit.

The current is chosen to be measured at the negative terminal of the PV module to accommodate for a lower common rejection ratio at the input of the INA156 instrumentation amplifier. The MD ground (GND) occurs at the negative terminal of the PV module to ensure that the MD circuitry current does not flow through the shunt resistor. Hence, the PD device grounding is connected to V_{out-} in order for the perturbation currents to be measured. The current calibration process performed on each device and the calibration process are discussed in Appendix E.

3.3.6.3 Voltage measurement

In the power supply Section 3.3.2, it was mentioned that the first stage PSU is capable of operating for both thin film and polycrystalline PV modules. The same applies for measuring the voltage. However, this large voltage range variation implies that the voltage resolution will be effected. This large voltage range variation reduces the voltage steps read by the ADC, taking this into consideration and given that the testing performed in the thesis was only for polycrystalline PV modules. The MD was chosen to measure up to a maximum of 50 V by selecting suitable resistors for R_{30} and R_{31} , shown in Figure 3.6. The Microchip MCP601 [86] operation amplifier with unity gain is used with voltage divider resistors (R_{30} and R_{31}) to step the input voltage down for a suitable voltage level for the ADC.

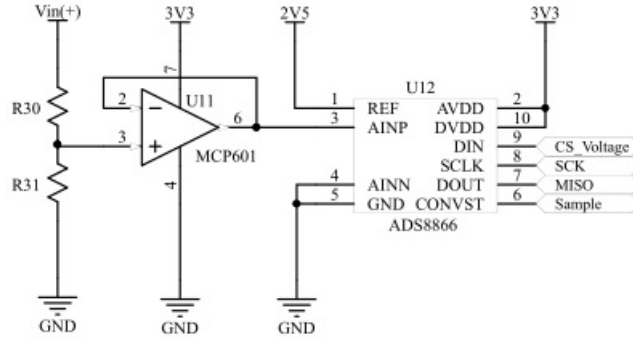


Figure 3.6: MD Voltage measurement circuit

With the maximum input voltage at 50 V, R_1 is chosen as 100k and R_2 chosen as 5.1 K. Equation 3.5 describes the voltage reading to the voltage ADC input.

$$\begin{aligned}
 V_{ADC_V} &= V_{PV} \times \frac{R_2}{R_1 + R_2} \\
 &= V_{PV} \times \frac{5.1K}{100K + 5.1K} \\
 &= V_{PV} \times \frac{51}{1051} [V]
 \end{aligned} \tag{3.5}$$

Therefore substituting Equation 3.5 into 3.2, the digital 16-bit voltage value is calculated as follows:

$$\begin{aligned}
 ADC_{levels} &= 26214 \times V_{PV} \times \frac{51}{1051} \\
 V_{PV} &= \frac{ADC_{levels} \times 1051}{1336914}
 \end{aligned} \tag{3.6}$$

The voltage calibration process is performed on each device and the calibration process is discussed in Appendix E.

3.3.6.4 Temperature measurements

The IEC61724 standard [47] requires a temperature sensor to be fitted with a dedicated back-plate behind the PV module. The MD further enhances this standard by having the capability of mounting four individual temperature sensors in each quadrant of the PV module. These temperature sensors are externally connected with a cable to the MD. Having multiple temperature sensors assists in identifying temperature variations on the PV module, which assists in detecting hotspots. Temperature readings are extracted via SPI communication using a high accuracy ADT7310 13-bit digital temperature sensor with 0.0625 °C resolution [87]. The temperature sensors' outer housing cover was 3D printed and designed using Autodesk Inventor Professional 2016. The MD does not require PV module temperature readings for the data analysis of the perturbation device implementation. However, as mentioned in Section 2.2.5, temperature and irradiance are important parameters required for a reference model to compare actual yield with predicted yield. Generally, as illustrated in Figure 2.3, utility scale PV plants have equipment to measure meteorological information

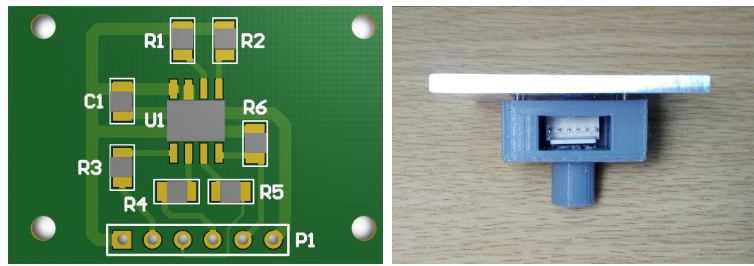


Figure 3.7: MD temperature sensor design

irradiance. The the temperature measurement is merely an additional feature provided by the MD that can assist forecasting models.

3.4 Detailed Software Design

3.4.1 Programming the MCU

Atmel studio 7 is an Integrated Development Environment (IDE) provided by Atmel to write, build and debug code on the ATmega1284RFR2 MCU. The MCU code was in the C programming language and was programmed onto the MCU via JTAG using the AVRISP mk2 in-system [81].

3.4.2 Overview of data retrieval

As mentioned in section 3.2, the Monitoring Device Coordinator (MDC) is a slave device to the Data Acquisition Device (DAD), but serves as master to Monitoring Devices (MDs). All MDs store their own data, while the MDC can contain its own or MDs sampled data. The data retrieval between MDC and MDs is achieved via the wireless IEEE 802.15.4 protocol. DAD acquires the sample data from the MDC via USART (Universal Asynchronous Serial Receiver and Transmitter). All requests are initiated by the DAD as the gateway between the end user and the entire system. Sampled data is either stored to the DAD SD card or uploaded to the online database by the end user. The DAD data acquisition procedure is discussed in Chapter 5.

3.4.3 Communications

To recap, the MD makes use of three communication protocols:

1. USART communication lines between the DAD and MDC.
2. IEEE 802.15.4 protocol for wireless communication between MDC and MDs.
3. MD(C) uses a Serial Peripheral Interface (SPI) to retrieve voltage, current and temperature measurements from external ADCs and temperature sensors.

These communication mediums are used for configuration, reconfiguration and data acquisition between the end user and embedded PV monitoring devices. Furthermore, MD(C) offers built-in AES encryption functionality to encrypt data while using the communication mediums. However, similar to the power saving features, the encryption feature is not utilised as it is not needed to demonstrate the system functionality for this study's objectives. But it is strongly recommended for a commercialised implementation of the proposed device.

3.4.4 USART communication

USART is a built-in functionality of the Atmel MCU and is used to communicate with the DAD, as previously mentioned. The USART requires low level configuration on the MCU, which includes enabling the USART transmitter and receiver mode on dedicated MCU pins, setting the frame format and baud rate. The frame format is set up as: 1 start bit, 8 data bits, no parity, one stop bit and a baud rate of 57600 b.p.s. Data is sent and received asynchronously, with the USART set to operate in the asynchronous-normal mode [80]. The baud rate is set in the UBRRn USART Baud Rate Register and is calculated with equation 3.7 [80].

$$BAUD = \frac{f_{osc}}{16(UBRRn + 1)} \quad (3.7)$$

f_{OSC} is 16 MHz external clock frequency, UBRRn is set as 124 for a 57600 b.p.s. baud rate.

The USART is interrupt driven, using the USART TX and RX interrupt vectors. The USART RX interrupt is triggered when the DAD (master) sends a request to the MDC (slave), whereby the receive buffer is loaded byte by byte from the UDR0 register. A dead time of more or less $3\frac{1}{2}$ characters (28bits) before and after data is sent or received, which is adapted from the MODBUS protocol is displayed in Figure 3.8. The dead time ensures that the MDC can distinguish between two different packets of data received and sufficient time for the MDC to respond to a request. For this reason, the MCU's built-in counter/timer is programmed to keep track of the time elapsed between received bytes. This process is illustrated in Figure 3.9.

Start	Address	Cmdnd	Sub Cmdnd	Data	CRC check	End
≥3.5 char	8 bits	8 bits	8 bits	N x bits	16 bits	≥3.5 char

Figure 3.8: USART MODBUS adoption, delays between packets

Figure 3.8 illustrates the format of data between MDC and DAD. The MDC is configured to have an address byte that can be reconfigured if need be and is stored on the MCU EEPROM non-volatile memory, which is read upon start-up. The purpose of the address byte is to allow multiple devices to communicate with each other on a single USART communication line. Although in this particular topology, communication is only established between two devices and the address byte is not necessary. However, this is still implemented to allow for scalability for future revisions. If the DAD requests data from the MDC, the MDC transmit buffer is loaded in the same format as Figure 3.8, with the same address, command and sub-command bytes. The only difference is the payload data and the two CRC bytes attached to the end on the transmit buffer. The data is sent out byte for byte via register UDR0, using the transmit interrupt vector.

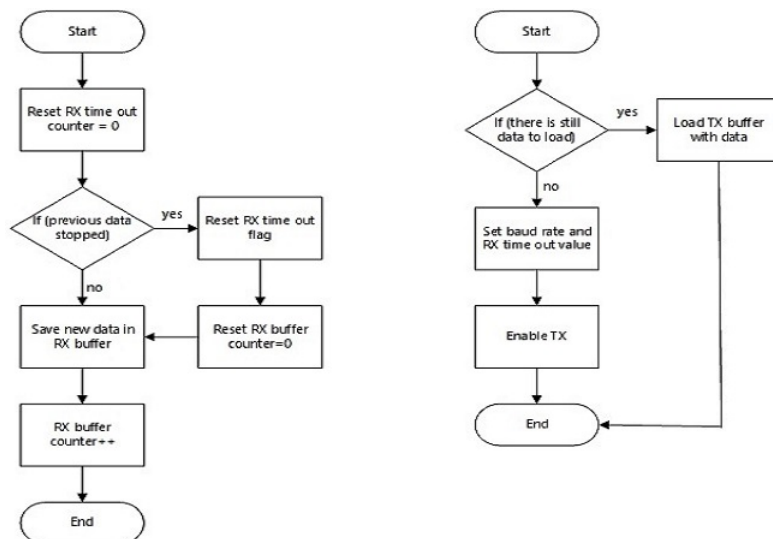


Figure 3.9: MD USART transmit and receive flow diagram

3.4.5 SPI communication

Serial Peripheral Interface (SPI) is another built-in feature of the MCU and allows for high-speed synchronous data transfer. Various functions are implemented to configure the MCU's SPI registers, which include the SPI mode, speed, data order and operation. This is because all devices on the SPI line have speed limitations and alternating between the different configurations is made easy using these functions. On start-up the SPI operates in the master mode and the slave mode is only enabled when the DAD requires communication. However, the SPI line between the MCU and DAD, as illustrated by the MD schematic in Figure B.7, is implemented only when the ESP32 communicates with the RFM98 LORA module. However, the RFM 98 LORA module is not implemented and will be discussed in Section 7.5. The SPI flow diagram for sampling the voltage and currents simultaneously is presented in Section 6.2.

3.4.6 Monitoring device MDC user interface commands

The DAD allows user access to the MDC via predefined commands that are available and enables users to send or retrieve data from MD(C). The predefined user commands are categorised into three groups: HEX-41 (Hexadecimal), HEX-42 and HEX-43 commands. Within each group there are subcommands. Each group command is categorised for a specific purpose and the subcommand within each group contains functions that are associated with the specific group. HEX-41 commands contain configuration and sample request commands. HEX-42 commands are for data retrieval between MDC and MDs or MDC and DAD. The subcommands for each group are listed in Table 3.2 and described. Data sent from the DAD to the MDC conform to the packet format shown in Figure 3.10. For credibility, the MDC returns a reply message with the same packet format shown in Figure 3.10, with the only difference being that, as mentioned in Section 3.4.4, data is sent from the MDC to the DAD along with the CRC bytes.

The MDC software flow diagram for the USART is illustrated in Figure 3.11. When the MDC receives data, the USART RX interrupt is enabled and the software routine is displayed in Figure 3.11. The MDC has internal procedures to verify data validation, address verification and thereafter execute the ServiceComms() function. This function executes the corresponding instructions that was received from the command and sub-command, which conform to the instructions given in Table 3.2.

MD address	MD command	MD sub-command	Data to MD...	CRC1	CRC2
------------	------------	----------------	---------------	------	------

Figure 3.10: Data packet format from DAD to MDC

Users can only interface with the DAD, which is the gateway to the MD(C). The DAD is connected to a WiFi network and has a TCP (Transmission Control Protocol) server that services user commands via the network. This will be further discussed in detail in the DAD section 5.4.4.

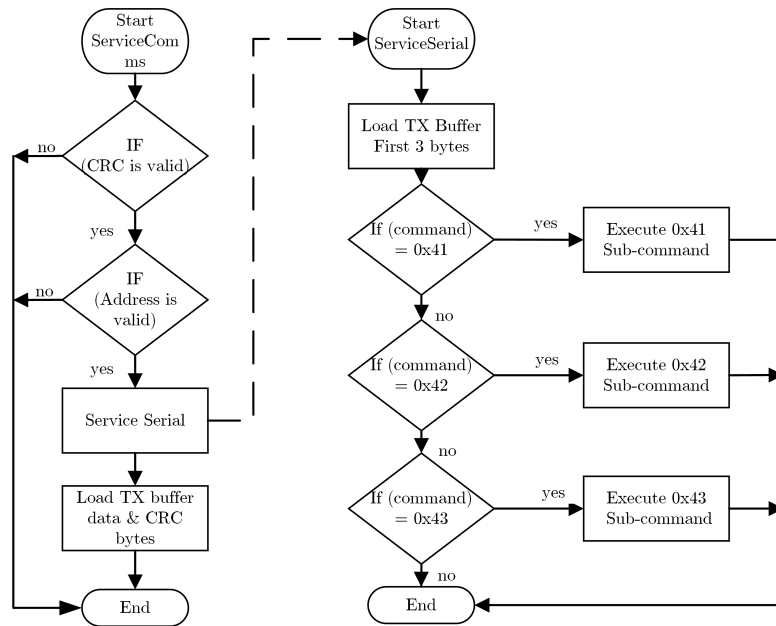


Figure 3.11: MD USART software flow diagram for received data

Table 3.2: List of the available serial HEX-41 and HEX-42 MDC commands

Command 0x41		Command 0x42	
Sub-command	Function()	Sub-command	Function()
0x01	Update-MDC-Channel()	0x01	Get-ED-Current()
0x02	Send-MDC-Channel()	0x02	Get-ED-Voltage()
0x03	Update-MDC-Identification()	0x03	Get-ED-Temperatures()
0x04	Send-MDC-Identification()	0x04	Send-MDC-MD-Stored-Data()
0x05	Update-MDC-IEEEAddress()		
0x06	Send-MDC-IEEEAddress()		
0x07	ClearFrameBuffer()		
0x08	IntialiseFrameBuffer()		
0x09	Sample-MD()		
0x0A	Sample-MD-Current()		
0x0B	Sample-MD-Voltage()		
0x0C	Sample-MD-Temperature()		
0x0D	Sample-MDC()		
0x0E	Sample-MDC-Current()		
0x0F	Sample-MDC-Voltage()		
0x1A	Sample-MDC-Temperature()		
0x0B	Send-MD-CustomCommand()		

HEX-41 commands

Update-MDC-Channel() and **Send-MDC-Channel()**: Update the MDC IEEE 802.15.4 channel from the DAD or send the channel to the DAD.

Update-Coordinator-Identification() and **Send-Coordinator-Identification()**: To conform to the IEEE 802.15.4 protocol, each MD must have a PAN ID and short address. Hence, identification registers are updated via DAD or sent to the DAD from the MD.

Update-MDC-IEEEAddress() and **Send-MDC-IEEEAddress()**: For larger IEEE 802.15.4 networks, the IEEE address 64-bit address register can be used over the 16-bit short address register. This register is updated via the DAD or sent to the DAD from the MD.

ClearFrameBuffer() and **IntialiseFrameBuffer()**: The DAD can clear or initialise the 128 byte FIFO buffer that is used for the IEEE 802.15.4 communication.

Sample-MD(), **Sample-MD-CurrentData()**, **Sample-MD-VoltageData()** and **Sample-MD-TemperatureData()**: The DAD requests the MDC to request a data sample on any MDs. This sample could be the simultaneous voltage and current measurement, followed by the temperature measurement, or each measurement can be requested individually.

Sample-MDC(), **Sample-MDC-CurrentData()**, **Sample-MDC-VoltageData()** and **Sample-MDC-TemperatureData()**: This is similar to the explanation mentioned above with the difference being that the DAD requests samples from the MDC only.

Send-MD-CustomCommand(): The DAD uses the MDC as a gateway to send and customise an MD.

HEX-42 commands

Get-MD-CurrentData(), **Get-MD-VoltageData()** and **Get-MD-Temperatures()**: The DAD requests N to 1000 samples from the MDs to be stored on the MDC. This data includes current, voltage, power and temperature.

Send-MDC-ED-Stored-Data(): The DAD requests N to 1000 amounts of sampled data from the MDC. This data can either be the MDC sampled data or stored sampled data per MD.

The HEX-43 commands are dedicated to special purposes and are only used for testing purposes. The Hex-43 sub-command list is large as it contains functions that can control all GPIO pins on the MCU and reconfigures GPIO registers. These functions were used during debugging and kept in the final code in case of in-field debugging. An example of a Hex-43 function is toggling of a LED on the MD or MDC and for this reason these functions are not listed as their importance is not relevant.

3.4.7 Wireless IEEE 802.15.4 communication

The Atmel ATmega1284RFR2 MCU is fully integrated with a low power transceiver featuring the IEEE 802.15.4 standard for the 2.4 GHz ISM band. The IEEE 802.15.4 standard is defined by the IEEE that only defines the physical layer (PHY) and medium access control MAC as shown in Figure 3.12.

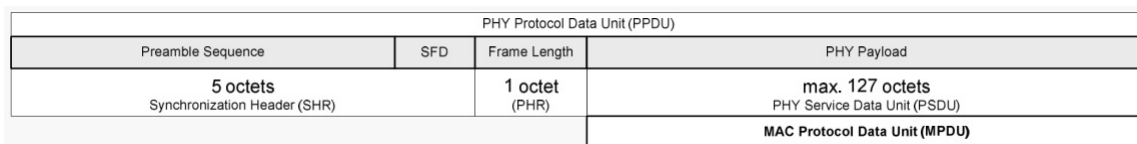


Figure 3.12: IEEE802-15-4-physical-layer [80, p.67]

Communication protocols such as ZigBee, IPv6/6LoWPAN, RF4CE, SP100, WirelessHART and ISM applications are built on the IEEE 802.15.4 standard and occur on higher levels of the OSI model. With this in mind, Atmel does not provide support nor APIs for communication protocols that are built on IEEE 802.15.4, besides the configuration of the IEEE

802.15.4 standard. Given the lack of support for these communication protocols, wireless communication between devices use the IEEE 802.15.4 standard in its most basic form with a custom protocol added. Using a custom protocol avoids additional coding of the developed established protocols mentioned above. The custom protocol is adapted from the MODBUS protocol and very similar to that used for the USART communication in section 3.4.4. The disadvantage of using a custom protocol is that it limits other devices that operate on IEEE 802.15.4 from using this network. The advantage of using a custom protocol is that communication cannot be easily interpreted. The MCU allows for altering of its transceiver hardware, which implies that the MCU settings may differ from the IEEE 802.15.4 standard specifications. This makes it difficult for IEEE 802.15.4 devices operating in promiscuous mode to interpret data packets over the air. The same HEX-41, 42 and 43 command structure is implemented in the IEEE 802.15.4 communication service function with minor differences that will be discussed in this section. The USART implements an address byte, whereas the IEEE 802.15.4 (as mentioned Section 3.3.5) has two addressing modes depending on the size of the network. Given the limited amount of MDs (hardware) used for this thesis (5 MDs), the short addressing mode is sufficient for addressing devices on the network. The short address contains 2 octet/2 bytes with the first byte set 0x00 and the second byte ranges from 0x01 to 0x05 for each of the 5 devices. Device 0x01 represents the coordinator (MDC), while the rest are end devices (MDs).

A functioning IEEE 802.15.4 network requires low level configuration on the MCU. This includes the hardware configuration registers of the MCU transceiver and configuration of the frame buffer that must adhere to the IEEE 802.15.4 standard. To summarise in more detail, the following is configured on each device:

- Unique short or long device address.
- PAN ID address.
- PAN coordinator or end device selection.
- IEEE 802.15.4 Frame Control Field (FCF) configuration.
- IEEE 802.15.4 channel frequency.
- Data transfer rate.
- Transceiver interrupts and operating mode.
- CRC generation on transmitting and receiving data packets.

There are many other configurable registers, however these were left as default. A few of these register are named the start of frame delimiter, transmit power level, frame buffer over write protect, acknowledge waiting period, etc. Furthermore, the 128-byte frame buffer is located within the MCU SRAM address space and is accessible via software (Atmel Studio). The frame buffer contains the PHY service data unit (PSDU) data of one IEEE 802.15.4 transmission or reception of maximum frame length at a time, as illustrated in Figure 3.12 and 3.13.

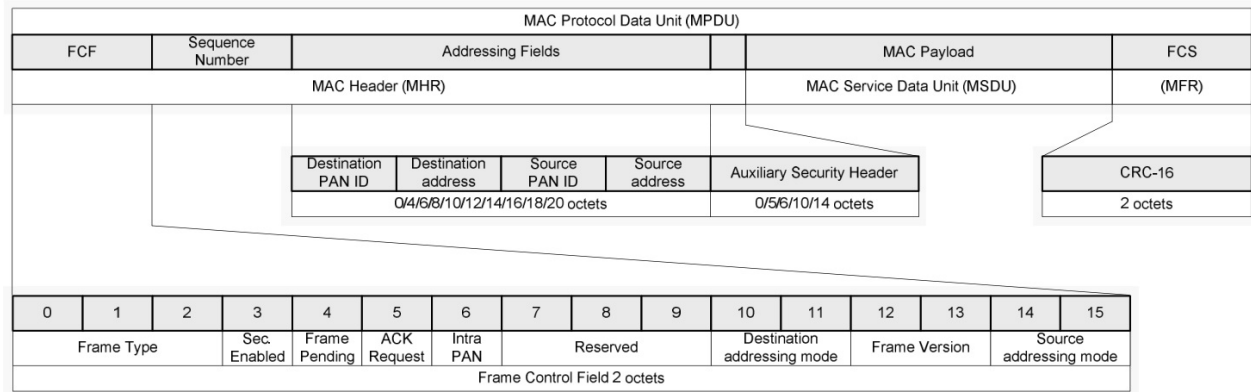


Figure 3.13: IEEE 802.15.4 Frame Format - MAC-Layer Frame Structure [80, p.68]

From Figure 3.12 the synchronization header (SHR) is a 4 byte preamble (all zero), followed by a start of frame (SFD), which by default is predefined in the MCU register with the value 0xA7. During transmission the SHR is automatically generated and the frame buffer contains the PHY header (PHR) and PSDU only. The first byte of the frame buffer is the PHR, which contains the frame length of the PSDU data. The remaining 127 bytes of the frame buffer contain the FCF, sequence number, addressing fields, MAC payload and FCS. The MAC header (MHR) contains the FCF, sequence number and addressing fields. The 2 byte FCF field contains details of the data packet and conforms to the IEEE 802.15.4-2006 specification, which includes the frame type, data encryption status, frame pending data status, acknowledge request, frame version and addressing modes. The sequence number byte is used to detect duplicated frames, in particular when large data packets are being sent. This is followed by the source and destination address (PAN ID and short address), then followed by the MSDU and lastly the last two bytes MAC footer (MFR) containing the Frame Check Sequence (FCS) or also known as CRC. FCS is implemented to detect corrupted frames in the same manner this was done in the USART communication. The last two bytes always contain the FCS bytes and is automatically generated upon transmission. Likewise, on frame reception FCS is checked automatically.

The MCU extended mode states are shown in Figure 3.3 and is particularly chosen for its enhanced hardware features that reduce coding. This includes an automatic retransmit if an acknowledgement was not received. The "RX_AACK", "TX_aret" and "PLL_on" states have 5 interrupts that are enabled during operation. The first interruption, the "TRX24_PLL_LOCK" interrupt, indicates whether the transceiver has locked onto the selected IEEE 802.15.4 frequency channel. In the "RX_AACK" (receive mode) state, three interrupts occur, the first being when the "TRX24_RX_START" is triggered when a valid PHR is signaled. This is followed by the "TRX24_AMI" address match interrupt that indicates an address match. The completion of the frame reception triggers the "TRX24_RX_END" for a valid FCS. Given that the slotted operation is disabled, it implies that the software does not handle automatic acknowledgement and this is done within the MCU hardware. The next interrupt that is triggered is the "TRX24_TX_END" interrupt, which sends an automatic acknowledgement to the sender. During "TX_aret" (transmit mode) state, only the "TRX24_TX_END" interrupt signals the end of transmission. The flow diagram for the "RX_AACK" and "TX_aret" states are displayed in Figures B.11, B.12. A more simplified flow diagram for receiving data via IEEE 802.15.4 is shown in Figure 3.14. This flow diagram (3.14), also illustrates the software routine when receiving data addressed to the end device from the coordinator. The frame buffer content is overwritten by a new trans-

mit/receive and must be reconfigured during each cycle. Additional registers are configured for the IEEE 802.15.4 channel frequency, data rates and other IEEE 802.15.4 parameters that can be altered to suit the desired application. The PAN ID address is a unique address that is associated with the PAN coordinator in the network. The PAN ID address is a 2 byte address that allows PAN coordinators to communicate with each other. The PAN ID address is vital for end devices to associate themselves with the PAN coordinator. Along with the addressing field, the IEEE 802.15.4 accommodates 16 channels (11 - 26) that are available for the 2.4 GHz frequency with 5 MHz channel spacing. Arbitrary choice was chosen for the channel frequency and PAN ID for all devices.

The MDC communicates with the MDs via predefined commands similar to that used between DAD and MDC. These user commands are also categorised into three groups, HEX-41 (Hexadecimal), HEX-42 and HEX-43 commands. Similarly to that discussed in Section 3.4.6, within each command are subcommands. HEX-41 commands contain configuration and a sample request and HEX-42 commands are for data retrieval between MDC and MD. The subcommands are listed in Table 3.3 and described.

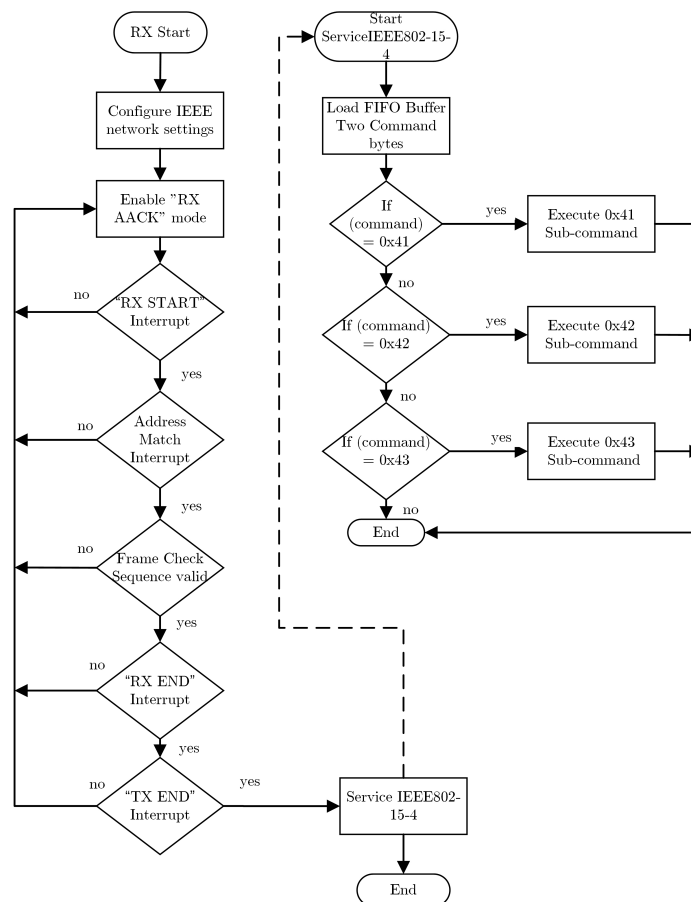


Figure 3.14: MD IEEE 802.15.4 software flow diagram for received data

Users can only interface with the DAD, which is the gateway to the MDC. The DAD is connected to a WiFi network and has a TCP (Transmission Control Protocol) server that services user commands. This will be discussed in further detail in the DAD section 5.4.4.

Table 3.3: List of the available HEX-41 and HEX-42 MD commands via IEEE 802.15.4

Command 0x41		Command 0x42	
Sub-command	Function()	Sub-command	Function()
0x01	Update-MD-Channel()	0x01	Send-MD-CurrentData()
0x02	Send-MD-Channel()	0x02	Send-MD-VoltageData()
0x03	Update-MD-Identification()	0x03	Send-MD-TemperatureData()
0x04	Send-MD-Identification()	0x04	Send-MD-Calibration-Constants()
0x05	Update-MD-IEEEAddress()		
0x06	Send-MD-IEEEAddress()		
0x07	Sample-MD()		
0x08	Sample-MD-Current()		
0x09	Sample-MD-Voltage()		
0x0A	Sample-MD-Temperature()		

HEX-41 commands

Update-MD-Channel() and **Send-MD-Channel()**: Update the end device IEEE 802.15.4 channel from the DAD or send the channel to the DAD via the MDC.

Update-MD-Identification() and **Send-MD-Identification()**: To conform to the IEEE 802.15.4 protocol, each MD must have a PAN ID and short address. Hence, identification registers are updated via DAD or sent to the DAD from the MD.

Update-MD-IEEEAddress() and **Send-MD-IEEEAddress()**: For larger IEEE 802.15.4 networks the IEEE address 64-bit address register can be used over the 16-bit short address register. This register is updated via the DAD or sent to the DAD from the MD.

Sample-MD(), **Sample-MD-Current()**, **Sample-MD-Voltage()** and **Sample-MD-Temperature()**: The MDC requests the MD to sample, which could be the simultaneous voltage and current measurement, followed by the temperature measurement, or each measurement can be requested individually.

HEX-42 commands

Send-MD-CurrentData(), **Send-MD-VoltageData()** and **Send-MD-TemperatureData()**: The DAD requests N to 1000 from the MD end device to be stored on the MDC. This data includes current, voltage, power and temperature.

Send-MD-Calibration-Constants(): The DAD requests N to 1000 amounts of sampled data from the MDC. This data can either be the MDC sampled data or stored sampled data from an MD end device.

Similar to the HEX-43 serial command the IEEE 802.15.4 HEX 43 commands serve the exact same purpose and are therefore not listed below.

Chapter 4

Perturbation devices

4.1 Introduction and chapter overview

One of the thesis goals mentioned in Chapter 1, was to determine whether a PV module within the PV array is operating at the MPP. To accomplish this goal, an in-situ Perturbation Device (PD) was designed to deviate the operating point of a PV module (while still connected in the PV array) to locate the MPP, without affecting the PV array operation. The deviation is caused by implementing an under-damped RLC circuit to introduce oscillations to the PV module. The current operating point of the PV module determines how severe the perturbation must be to locate the MPP.

There are various methods in literature along with products on the market that deal with tracking MPP under PSC. Yet, many scholars have spoken about the need for improving the level of granularity in PV systems. Although there are products on the market, they are not always cost effective for PV plants and products such as Tigo Energy TS4 PV module monitoring, optimizer, fire safety or all-in-one products that are mainly installed in PV systems where shading occurs. As mentioned in literature, Gargiulo [22] has introduced a PV module monitoring topology that can determine open-circuit voltage and short-circuit current of a PV module. Guerriero further developed this topology to successfully detect PSC in PV systems [68]. Although this topology is effective in its operation, the downside is that it requires disconnecting the PV module from the PV string, thus reducing power in the system. Likewise, a PV module power optimizer using a DC/DC converter or micro-inverters has the downside of introducing additional cost to the PV system.

With the fundamental theory of the natural response of RLC circuits presented in Chapter 2.3, this chapter further adds to the theory of the perturbation device designs. Two design topologies are presented to determine which method performs optimally for various conditions that occur in PV systems. These conditions include the PV array operating at and away from the MPP, mismatching conditions due to under-performing PV modules, charge controllers at float voltage and PV inverters during VAR compensation. A simulation was performed to verify the proposed theoretical designs in computer aided design (CAD) software along with presenting and discussing the simulated results. The PD's PCB designs and hardware selection are discussed in Section 4.4. Further detailed explanations regarding the PDs, along with additional diagrams and figures are presented in Appendix C, to give the reader more insight into the content discussed in this chapter.

4.2 Perturbation fundamentals

Perturbation is the deviation of a system by means of external influence [88]. The Perturbation Device (PD) is an external device designed to disturb the current operating point of a PV module by introducing under-damped oscillations by means of an RLC circuitry. The perturbation must occur fast enough to not affect the PV array operation and sufficient enough for the MD hardware to sample the perturbation. Two under-damped RLC circuit topologies are proposed with one introducing oscillations more servilely than the other. The introduction of oscillations to the PV module causes the operating point to move along the IV characteristic curve with the hope of passing the MPP before settling on the equilibrium point due to the exponential decay.

4.2.1 Perturbation topology validation

It is vital to consider whether generic models can be used for the proposed perturbation topology. These models include the RLC circuit model and single diode PV model, which is adopted by the IEC 61724 [47] standards. The RLC circuit model consist of basic components such as an inductor, capacitor and equivalent resistance of the PV module. A combination of these values determine whether the system is under-damped, critically damped or over-damped. Therefore, any external stray inductance and capacitance can affect the dynamics of the system. The impedance of stray inductance and capacitance are influenced by factors such as the perturbation frequency and inverter topologies. A PV module also has parasitic capacitance that may influence the perturbation dynamics. Studies have found that a PV modules exhibit capacitance towards the environment due to the mechanical structure of PV modules when installed [89]. According to a technical report from SMA Solar Technology AG, there exists various capacitance between the PV array and ground as shown in Figure 4.1

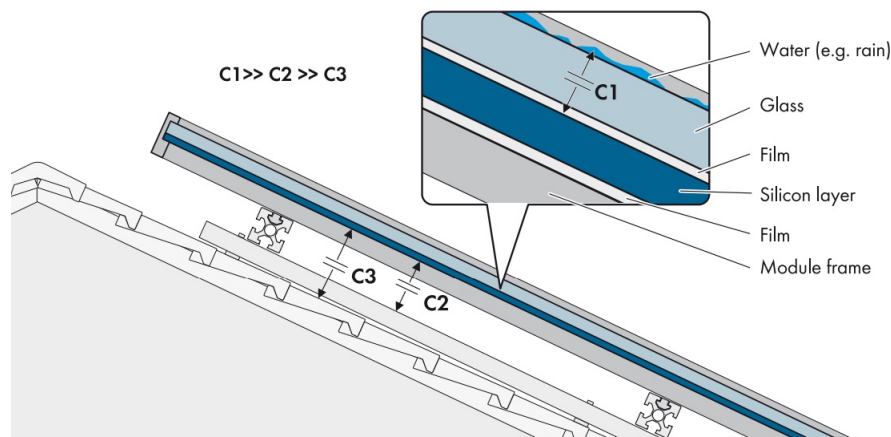


Figure 4.1: Illustration of parasitic capacitance [89]

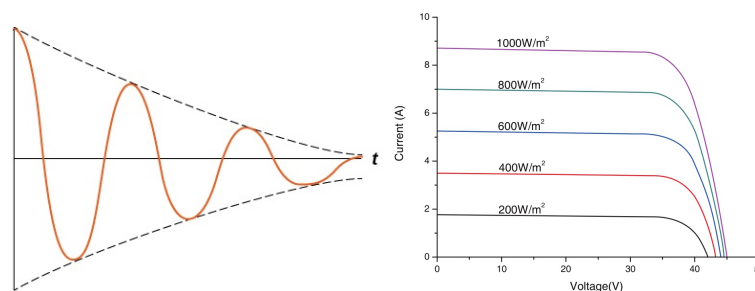
In conditions where the PV array is moist, the relative permittivity of water is much greater than air and glass. Therefore, $C_1 \gg C_2 \gg C_3$, where the capacitance of water is more dominant [89]. Furthermore, the introduction of cheaper and lighter transformer-less inverters have the downside of no isolation between the DC and AC components, thus in a single phase system, half of the grid is passed onto the PV modules [89]. The presence of the grid frequency on the DC side show that stray inductance and leakage capacitance are

present in the model, which need to be identified and then evaluated to determine if there is any significance influence in the model. The question of whether the single diode model is still valid for modelling the perturbation device topologies are still unanswered and requires validation via experiments. Likewise, the experimental setup implements a transformer-less inverter to investigate the influences of the stray inductance and capacitance.

Although the validity of the models are being considered, to avoid implementation of complex PV models and further investigation, the experimental setup would give enough justification if the perturbation topologies perform as expected by comparing it to simulation results. Stray inductance and capacitance can often be unavoidable in PV systems. To combat any influences on the design model, the RLC circuit parameters should always be chosen so that they are more dominant in the RLC circuit. The perturbation frequency can also be reduced to assist in reducing stray inductance and capacitance. The perturbation frequency has an influence on the RLC component size selection. Decreasing the perturbation frequency implies that the RLC hardware components increase in size and therefore, this should be kept in mind when selecting the perturbation frequency.

4.2.2 PD functionality

To understand the operations of PDs, assume the following scenario: the operating point of a PV module is very close to the MPP. By introducing under-damped oscillations (perturbation) to the PV module, the operating point is disturbed. The characteristics of the RLC under-damped implementation causes the PV module's operating point to shift back and forth on the characteristic I-V curve until eventually settling on the original operating point, if we assume environmental factors have remained the same. This is performed with the hope that the oscillations cause the operating point to at least reach the MPP on the I-V curve before settling back on the original operating point. The MD samples the current and voltage during the oscillation to determine if the MPP has been reached. The PD aims to determine whether a PV module is operating at optimal power. If the PV module is not operating at optimal power, the PD will display the extra power available. Therefore, the PD can detect under performing PV modules under PSC. As well as compare the energy yields with other PV modules in the PV systems to effectively detect and identify faulty PV modules.



(a) Under-damped oscillation waveform (b) Renesola 300W I-V curve characteristics [90]

Figure 4.2: I-V curve characteristics and under-damped waveform

Figure 4.2a illustrates the oscillating waveform of an underdamped RLC circuit. The exponential decay is caused by the RLC resistance, which in the proposed perturbation topologies is the equivalent load resistance of the PV module. The PV module equivalent load resistance can be determined from the PV module I-V curve shown in Figure 4.2b. Using Ohm's

law the resistance is the ratio of the PV module's operating voltage divided by the current. The exponential decay shown in Figure 4.2a, will die out faster with increased resistance. In summary, the PV modules operating point has an equivalent resistance that determines the exponential decay of the introduced oscillations. These oscillations alter the PV module's operating point, to shift along the PV characteristic I-V curve with the hope of reaching the knee point, i.e. the MPP. If a PV module operates at a lower equivalent load resistance, then a lower level of perturbation intensity is required to reach the maximum power point. This thesis proposes the investigation of two perturbation topologies that apply different levels of perturbation severity to the PV module to determine which topology is optimal for find the MPP. Furthermore, as seen in Figure 4.2b, different levels of irradiance can affect the current and therefore a decrease in current implies an increase in the PV module's equivalent resistance. A question that may arise is, wouldn't the higher perturbation intensity always find the MPP and the best solution to implement? This question will need to be investigated as it is not known how the PV load will react with high levels of perturbation intensity.

4.2.3 Theoretical calculations

The equations presented below describe the natural step response of under-damped oscillations of an RLC series circuit required for the design of the PD. Equations that were presented in Chapter 2.3 are repeated here:

$$\zeta = \frac{\alpha}{\omega_0} \quad (4.1)$$

$$\omega_0 = \frac{1}{\sqrt{LC}} \quad (4.2)$$

$$\alpha = \frac{R}{2L} \quad (4.3)$$

$$\omega_d = 2\pi f_d = \frac{2\pi}{\tau_d} = \sqrt{\omega_0^2 - \alpha^2} \quad (4.4)$$

$$V_{PD} = V_{PV} + e^{-\alpha t}(B_1 + B_2)(\cos\omega_d t + \sin\omega_d t) \quad (4.5)$$

Where the variables in Equations (4.1) - (4.5) are defined as:

ζ	= Damping ratio, $\zeta < 1$ for under-damped case
α	= Neper frequency
ω_0	= Resonant frequency
R	= Resistor
L	= Inductor
C	= Capacitor
ω_d	= Damped radiant frequency
τ_d, f_d	= Damped period and frequency
V_{PD}	= Perturbation voltage
V_{PV}	= PV module voltage
B_1, B_2	= Constants, determined by initial conditions

As discussed in chapter 2, the series RLC circuit has a lower impedance than the parallel RLC circuit. Referring to Equation 4.5, the lower impedance implies that the under-damped

response will result in greater voltage and current oscillation amplitudes before settling at equilibrium, due to the exponential decay. Reaching a greater amplitude during oscillations implies a better chance of reaching the MPP. The damping ratio describes the intensity of the oscillations, discussed in Section 2.3.2, as the system's natural ability to oscillate. Hence, a smaller damping ratio results in more oscillations and vice versa. To clarify this mathematically, Equation 4.2 can be rearranged and substituted with 4.4:

$$\begin{aligned}
 \omega_d &= \sqrt{\omega_0^2 - \alpha^2} \\
 &= \sqrt{\left(\frac{\alpha}{\zeta}\right)^2 - \alpha} \\
 &= \sqrt{\alpha^2\left(\frac{1}{\zeta^2} - 1\right)} \\
 &= \alpha\sqrt{\frac{1 - \zeta^2}{\zeta^2}} \\
 &= \frac{\alpha\sqrt{1 - \zeta^2}}{\zeta}
 \end{aligned} \tag{4.6}$$

Equation 4.6 illustrates that the damped radian frequency increases as the damping ratio approaches 0. Hence, the damping period becomes smaller, resulting in more oscillations occurring within the resistive exponential decay period. The more oscillations within the exponential decay period, the greater the peak amplitude. Furthermore, the RLC circuit inductance (L) can be calculated by substituting Equation 4.3 with 4.6:

$$\begin{aligned}
 2\pi f_d &= \frac{R\sqrt{1 - \zeta^2}}{2L\zeta} \\
 L &= \frac{R\tau_d\sqrt{1 - \zeta^2}}{4\pi\zeta}
 \end{aligned} \tag{4.7}$$

The remaining unknown variables are vital for the PD design. These are the RLC resistor, oscillation period and the damping ratio. The damping ratio and oscillation period may alter depending on the inductor and capacitor selections that are available. The RLC resistive value will be the resistive load of the PV array, which means this value may also alter depending on the PV module voltage and current operating point. If each PV module in the PV array have the same characteristics and are operating at the same operating point, it is assumed to be the MPP. Then it can be safe to say, using Ohm's law, that the resistive load of the PV array is the MPP voltage divided by the MPP current. Scaling down to a PV module, the same applies assuming uniform irradiance to the PV array. Renesola's Virtus II 255 W and 300 W PV module was used in the experimental setup. From the datasheet under Standard Test Conditions (STC) [91], the MPP voltage and current of the 255 W module were used to determine the RLC resistance (refer to Table 4.1). The RLC resistor value is calculated with the MPP parameters of the PV module to ensure that proposed methods oscillate around MPP. The MD is capable of performing 1000 samples over more or less a 22.7-25 millisecond (ms) period (as mentioned in 3.3.6.1). In addition, the PD perturbation must be designed to be within 25 ms, fast enough to not influence the PV array or module operation and slow enough for a single diode PV cell model to still be applicable. During the

initial development phase of the MD and PD designs, it was discovered that when trying to perturb too quickly, the PV cell single diode model was no longer valid as there were large spikes on the voltage and current measurements. Appendix B.0.2 provides a more detailed explanation. Thus, the damping radiant period is chosen as 2 ms, which is sufficient time for the ADC to collect samples before and after perturbation occurs. The last unknown required for calculating the inductance is the damping ratio, which for the under-damped case is between $0 < \zeta < 1$. ζ is chosen at 0.1 for practicality, as can be seen from Table 4.2. A very small damping ratio will result in large oscillations. The downside of a larger inductor and capacitor value not only becomes large in physical size, but is also not cost-effective. A summary of the damping ratio, resistance and oscillation period values are shown in Table 4.1 below:

Table 4.1: RLC design specifications

RLC design specifications	
R	= 3.6234
τ_d	= 2 ms
ζ	= 0.1

The RLC capacitor value can be calculated by substituting Equation 4.3 and 4.2 into Equation 4.4:

$$\begin{aligned} \frac{2\pi}{\tau_d} &= \sqrt{\omega_0^2 - \alpha^2} \\ \omega_0^2 &= \left(\frac{2\pi}{\tau_d}\right)^2 + \left(\frac{R}{2L}\right)^2 \\ \left(\frac{1}{\sqrt{LC}}\right)^2 &= \left(\frac{2\pi}{\tau_d}\right)^2 + \left(\frac{R}{2L}\right)^2 \\ C &= \frac{1}{L\left(\left(\frac{\tau_d}{2\pi}\right)^2 + \left(\frac{R}{2L}\right)^2\right)} \end{aligned} \quad (4.8)$$

Using the values for the inductor in Table 4.2, various values for the capacitor can be calculated and are displayed in Table 4.2 below:

Table 4.2: RLC inductance at various damping ratios

ζ	L(mH)	C(uF)
0.3	1.83	50.37
0.2	2.83	34.78
0.1	5.74	17.57
0.05	11.52	8.71
0.01	57.66	1.76

One advantage about designing the RLC circuit for a PV module is that the voltage and current components are much more readily available and cost effective in terms of the required RLC hardware components, as opposed to the RLC circuit being designed for an entire PV array.

4.3 Perturbation simulation

The aim of the perturbation is to verify the effectiveness of the two proposed perturbation designs that are implemented. These two designs are very similar, but differ in the oscillation severity applied to the PV module. The first perturbation method is known as the "LC" (no stored energy in the inductor) method and the second perturbation method is known as the "L-LC" (stored energy in the inductor) method. Both methods will be further discussed in the following chapters. Furthermore, the simulation model is demonstrated using Simplorer, thereafter the simulated results are discussed. The practical components that are available for the actual design as discussed in Section 4.4 are used in the simulation for better verification between the simulation and actual results.

4.3.1 Introduction to Simplorer

The theory behind the perturbation design was verified via simulation using ANSYS Simplorer, which is an efficient and accurate way to design and simulate electronic components. Simplorer is advanced simulation software that contains standard, manufacturer-based and custom electrical elements that enhances the accuracy and specifics of the simulation. From Chapter 2, Section 2.2.1, assuming uniform irradiance, superposition can be used to scale PV cells to PV modules using the single diode model. As mentioned before, this PV cell model also conforms to the IEC 61724 standard [47] and therefore, Simplorer was used to simulate the implementation of the PD topologies on a PV module within a PV array.

4.3.2 Simulation set up

As discussed in Chapter 1, the entire monitoring system along with the PD is intended for PV module monitoring in PV systems. Most PV systems mentioned in Chapter 2 have PV modules connected in series to form a PV string and multiple PV strings are connected at the input side of the inverter or charge control. MPPT techniques are then implemented at the inverter or charge controller side to get maximum energy yield out of the PV array. Furthermore, there are situations when PV strings are not operating at MPP, as discussed in the literature review in Section 2.2.2. For this reason the PD is designed to find the MPP of an individual PV module under various operating conditions.

The simulation was performed to:

- Firstly, verify the perturbation implementation designs via simulation.
- Simulate and perturb a PV module with different power ratings to determine any limitations with designs.
- Simulate the perturbation techniques under different operating points to determine if the MPP is reached.

The simulation simulates the perturbation techniques on a PV module within a PV array to demonstrate conditions of a realistic PV system. These conditions are simulated under uniform-irradiance. However the operating point can be altered by changing the PV array equivalent load resistance. A PV cell is represented using the single diode model and is scaled up to meet the PV module specifications of the 255 W and 300 W Renesola PV modules. These same PV modules will be used during the experimental setup and are further discussed in Chapter 6. The single diode model representation of the Renesola PV modules

can be verified by the simulated results and it should also be noted that the PV module parameters were taken from the data sheet [90, 91] under Standard Test Conditions (STC). The derivation for the PV cell and circuit diagram is presented in Appendix C.0.2. The simulation circuit configurations are shown in Figures C.3 and C.4. The RLC components' values for inductor (L_{PDn}) and the capacitor (C_{PDn}) are calculated in section 4.2.3. The available component parameters used for the hardware design is chosen in the simulation and provided in Table 4.5. The resistive load in the RLC circuit is represented by the PV array load, which is calculated using Ohm's law and is the accumulated resistances of each PV module's operating voltage divided by the current in the PV array. The two proposed perturbation techniques are very much alike with the only difference being that the one technique stores energy (L-LC) and the other stores no energy (LC) in the inductor before applying the perturbation to the PV module. These two techniques are displayed in Figures 4.3 and 4.4. Both Figures represent a scenario of two PV modules in a PV array and illustrates how the two different techniques will be implemented. The voltage measurements are taken over the PV module presented by V_{Mn} and the current is measured by measuring the voltage over R_{SENSEn} . Since the PD is intended for PV module monitoring, PV modules are perturbed individually in a sequential order.

The LC approach is illustrated in Figure 4.3 with all switches open (off state). When the switch S_{1a} (perturb PV module 1) is closed the RLC circuit is connected to the first PV module and oscillations are introduced to the PV module (refer to Table 4.3 for the different states).

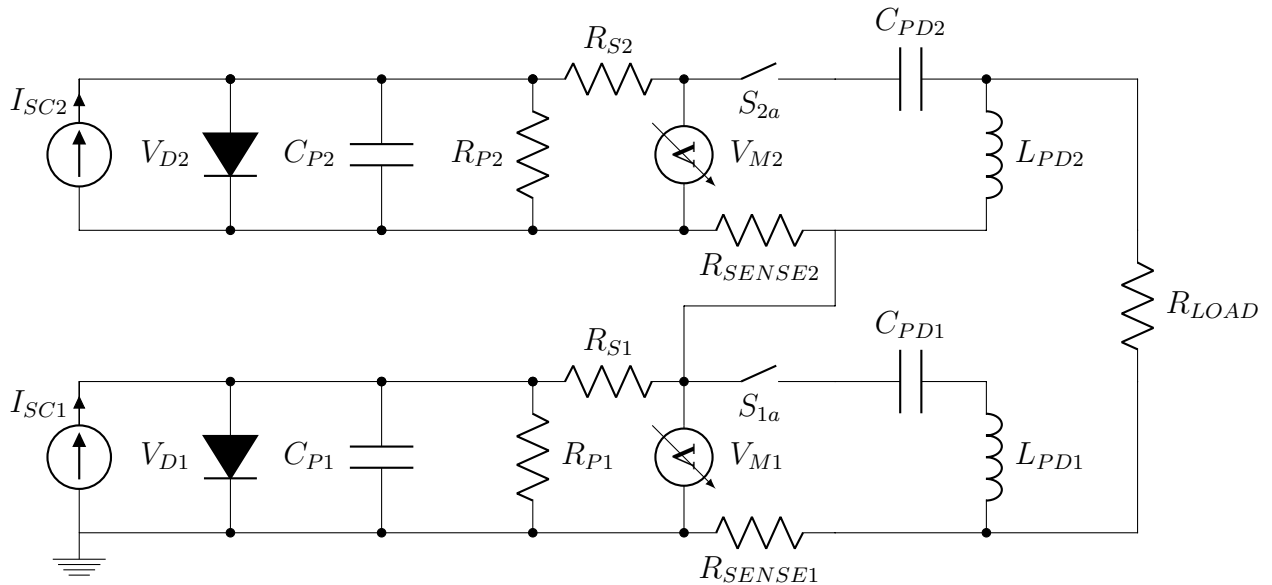


Figure 4.3: PD LC implementation in PV array

Table 4.3: Perturbation LC technique states

State	S_{1a}	S_{2a}
1 (off state)	0	0
2 (perturb state: PV module 1)	1	0
3 (perturb state: PV module 2)	0	1

The L-LC approach illustrated in Figure 4.4, with all switches open (off state), switch S_{1a} (store state: PV module 1) momentarily closes to store energy in the inductor L_{PD1} . At the same time after a set period, switch S_{2a} closes and immediately thereafter switch S_{1a} opens to apply the L-LC approach perturbation to the first PV module (refer to Table 4.4 for the different states for this topology).

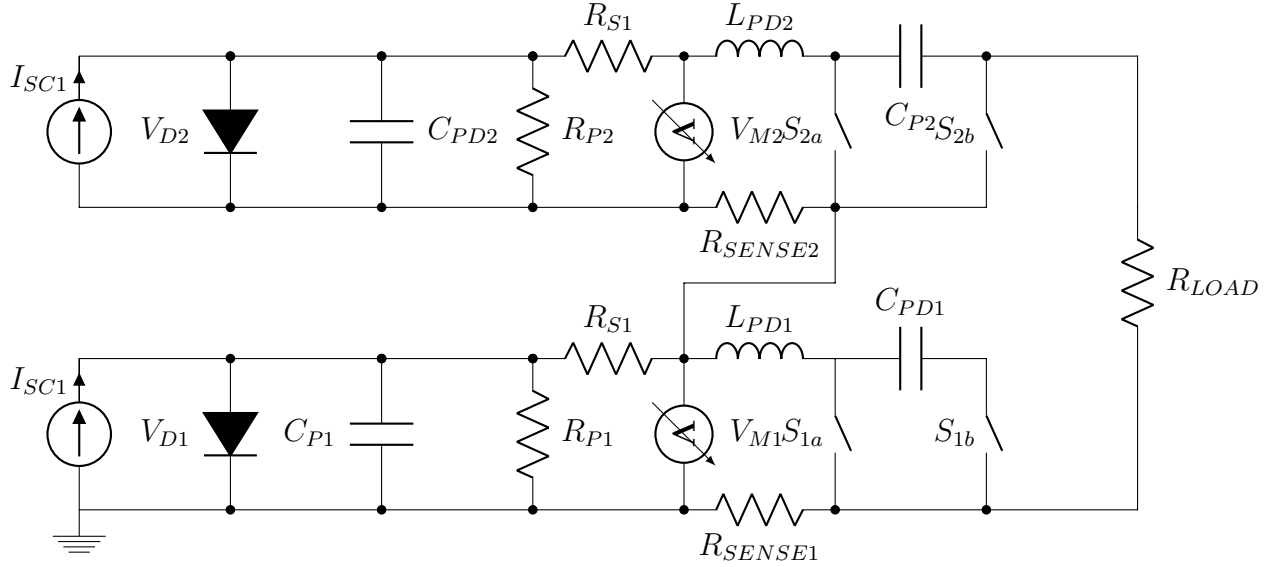


Figure 4.4: PD L-LC implementation in PV array

Table 4.4: Perturbation L-LC technique states

State	S_{1a}	S_{1b}	S_{2a}	S_{2b}
1 (off state)	0	0	0	0
2 (store state: PV module 1)	1	0	0	0
2 (perturb state: PV module 1)	0	1	0	0
4 (store state: PV module 2)	0	0	1	0
5 (perturb state: PV module 2)	0	0	0	1

The simulated results demonstrating both techniques are displayed in the Section 4.3.3. The simulation attempts to verify the PD design and accuracy of the single diode and RLC circuit model. The simulation further attempts to determine the limitations of each perturbation approach.

4.3.3 Simulated results

Figures 4.5, 4.6 and 4.7 illustrate the simulated waveforms of the LC perturbation with the PV array operating at MPP. Figure 4.5 is an illustration of the voltage and current waveforms of the PV module just before and after the LC perturbation is implemented. The corresponding characteristic I-V curve is plotted in Figure 4.6, along with the power voltage plot shown in Figure 4.7.

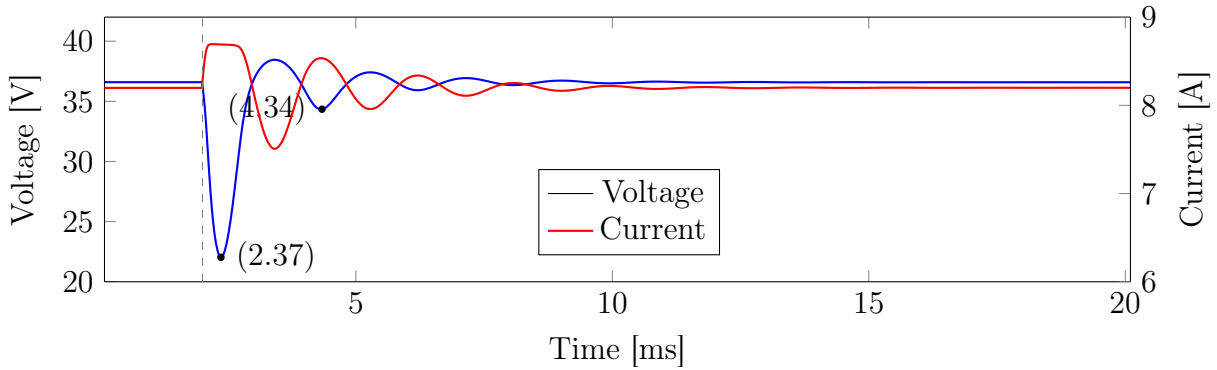


Figure 4.5: 300 W PV module current and voltage waveforms with LC perturbation applied at the MPP operating point

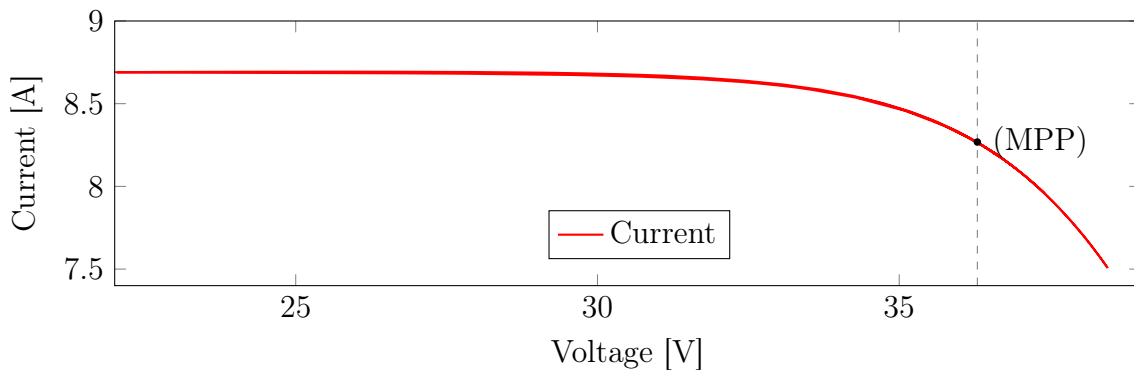


Figure 4.6: 300 W PV module I-V curve with LC perturbation applied at the MPP operating point

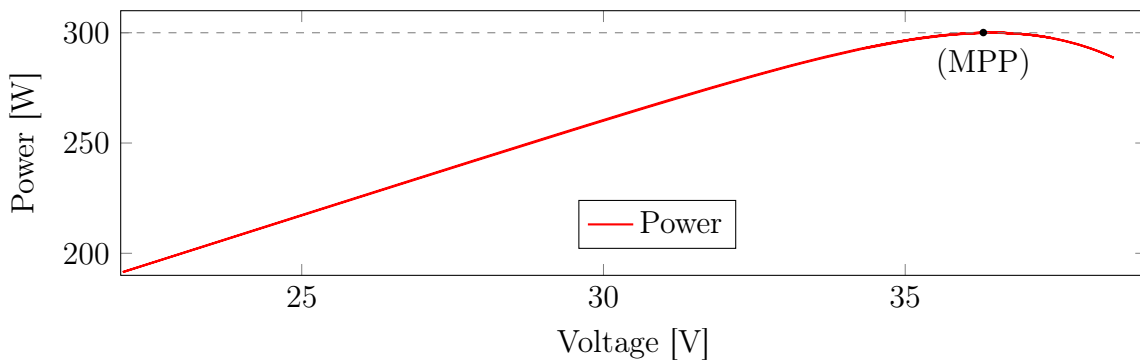


Figure 4.7: 300 W PV module P-V curve with LC perturbation applied at the MPP operating point

Figures 4.8, 4.9 and 4.10 illustrate the simulated waveforms of the LC perturbation with the PV array operating to the right of the MPP. Figure 4.8 is an illustration of the voltage and current waveforms of the PV module just before and after the LC perturbation is implemented. The corresponding characteristic I-V curve is plotted in Figure 4.9, along with the power voltage plot shown in Figure 4.10.

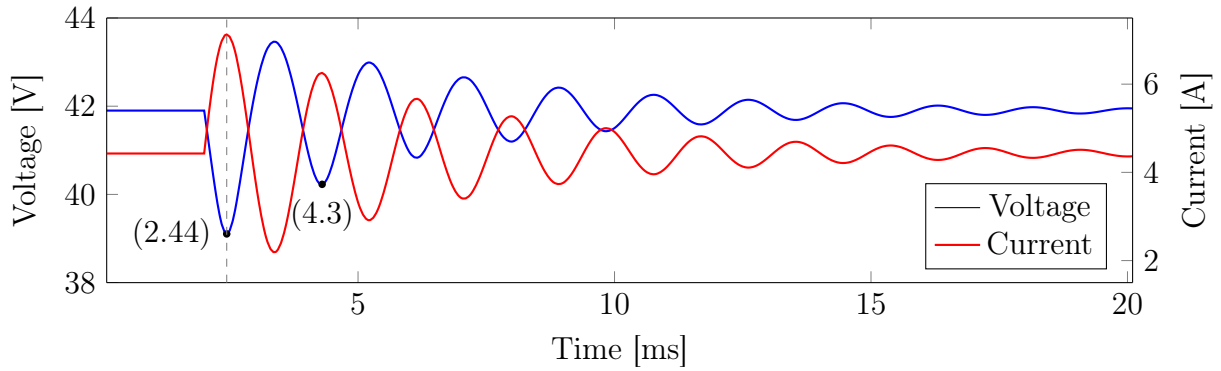


Figure 4.8: 300 W PV module current and voltage waveforms with LC perturbation applied to the right of MPP operating point

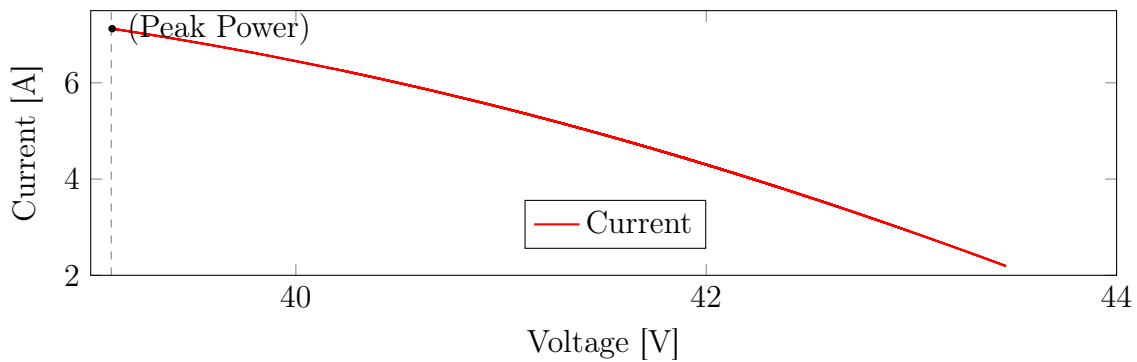


Figure 4.9: 300 W PV module I-V curve with LC perturbation applied to the right of MPP operating point

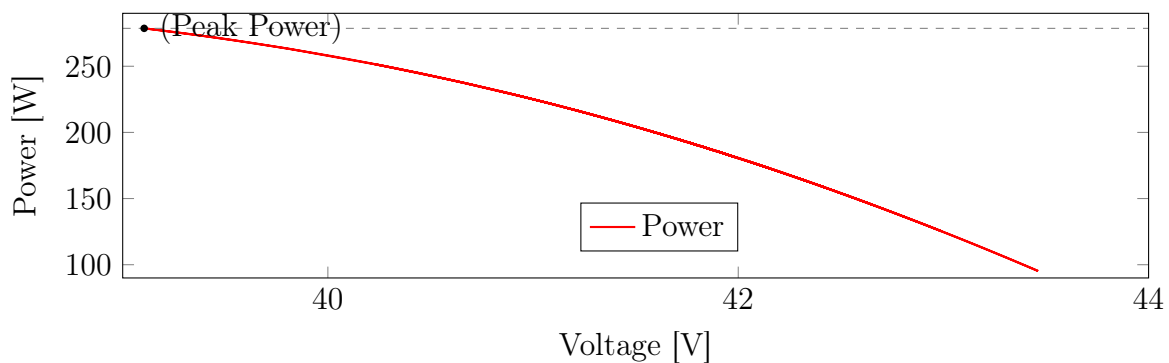


Figure 4.10: 300 W PV module P-V curve with LC perturbation applied to the right of MPP operating point

Figures 4.11, 4.12 and 4.13 illustrate the simulated waveforms of the L-LC perturbation with the PV array operating at MPP. Figure 4.11 is an illustration of the voltage and current waveforms of the PV module just before and after the L-LC perturbation is implemented. The corresponding characteristic I-V curve is plotted in Figure 4.12, along with the power voltage plot shown in Figure 4.13.

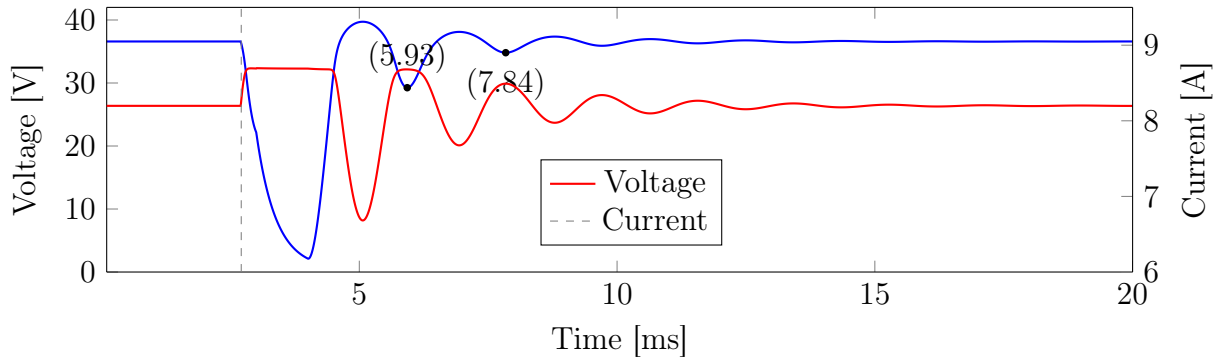


Figure 4.11: 300 W PV module current and voltage waveforms with L-LC perturbation applied at the MPP operating point

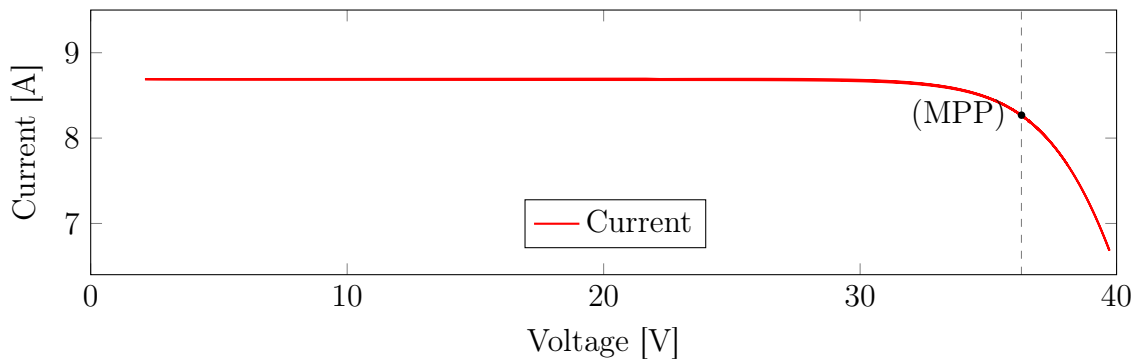


Figure 4.12: 300 W PV module I-V curve with L-LC perturbation applied at the MPP operating point

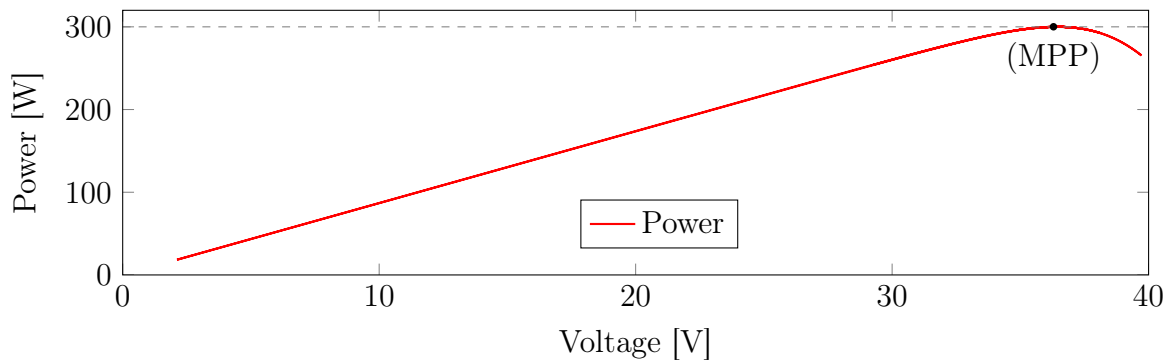


Figure 4.13: 300 W PV module P-V curve with L-LC perturbation applied at the MPP operating point

Figures 4.14, 4.15 and 4.16 illustrate the simulated waveforms of the L-LC perturbation with the PV array operating to the right of the MPP. Figure 4.14 is an illustration of the voltage and current waveforms of the PV module just before and after the L-LC perturbation is implemented. The corresponding characteristic I-V curve is plotted in Figure 4.9, along with the power voltage plot shown in Figure 4.16.

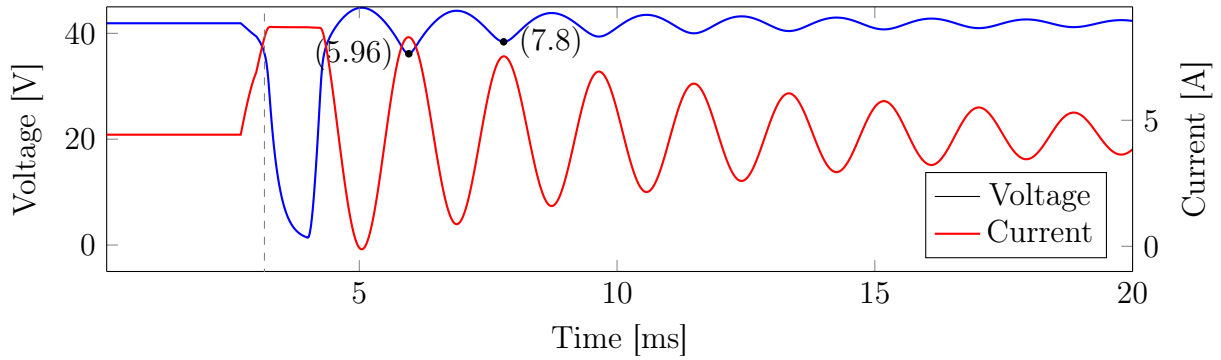


Figure 4.14: 300 W PV module current and voltage waveforms with L-LC perturbation applied to the right of MPP operating point

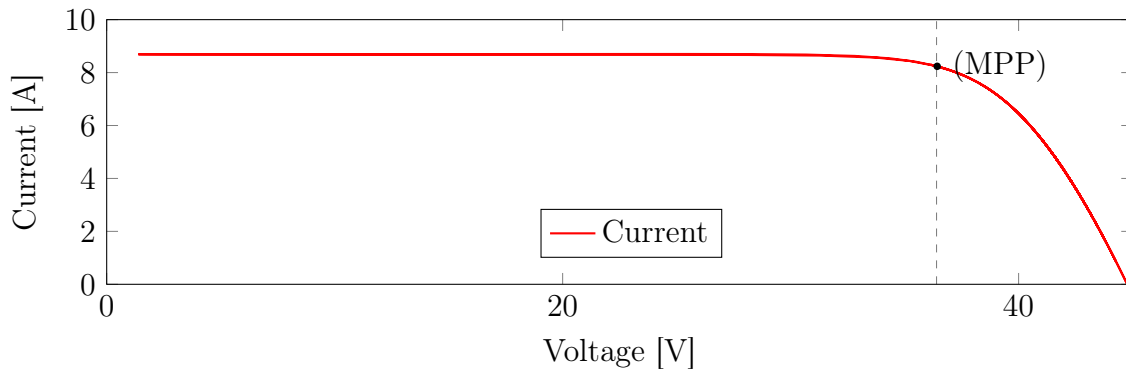


Figure 4.15: 300 W PV module I-V curve with L-LC perturbation applied to the right of MPP operating point

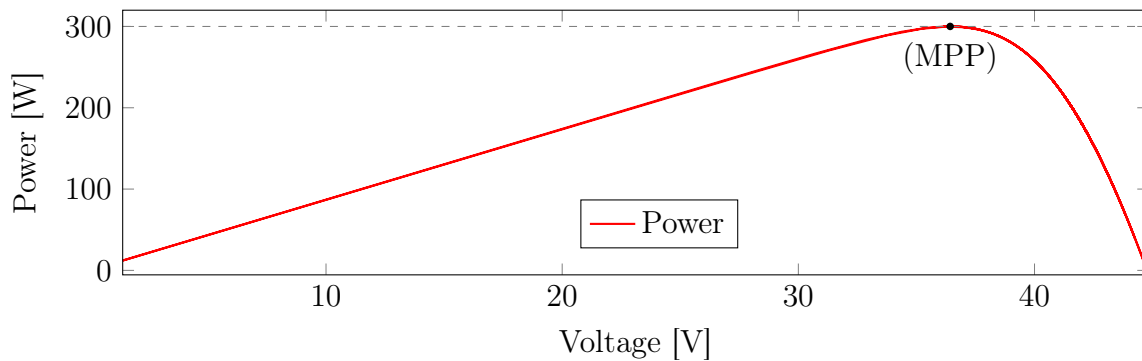


Figure 4.16: 300 W PV module P-V curve with L-LC perturbation applied to the right of MPP operating point

Figures 4.17 illustrate the simulated waveforms of the LC perturbation with the PV array operating at MPP for the 255W PV modules. The inductor voltage and current waveforms for the LC and L-LC perturbation techniques with the 300 W PV module is displayed in Figures 4.18 and 4.19.

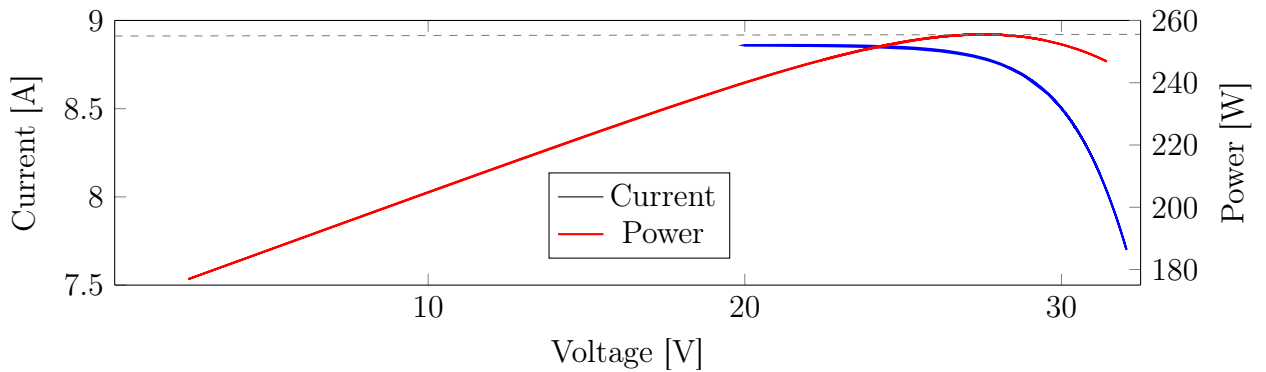


Figure 4.17: 255 W PV module I-V and P-V curve with LC perturbation applied at the MPP operating point

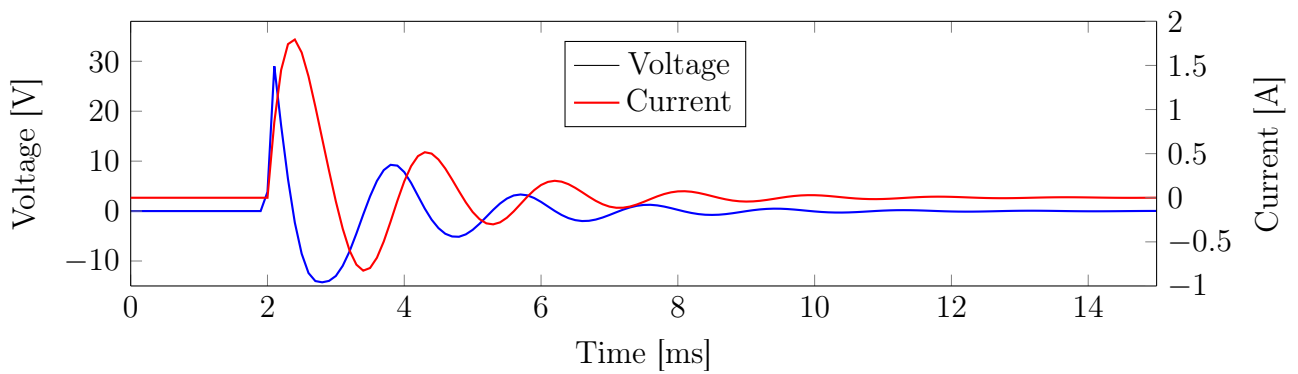


Figure 4.18: RLC inductor voltage and current waveforms during LC perturbation approach with 300W PV modules at the MPP operating point

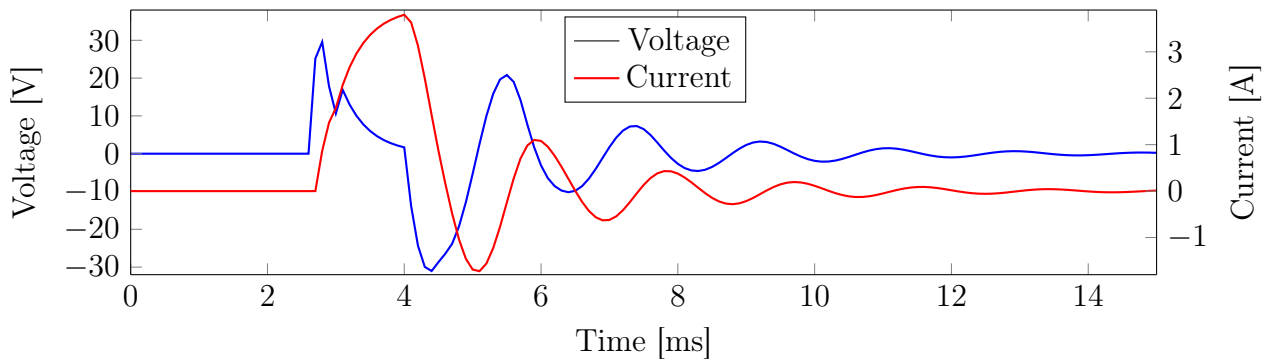


Figure 4.19: RLC inductor voltage and current waveforms during L-LC perturbation approach with 300W PV modules at the MPP operating point

Analysis of these wave forms gives an indication as to the typical power ratings that are expected by the RLC inductor.

4.3.4 Evaluation of the simulated results

To recap, the simulation was performed to verify the theoretical designs, as well as the validation of the single diode and RLC circuit models. The simulation also assists in attempting to answer the research question, by investigating the effectiveness of the perturbation techniques. This is performed by trying to locate the MPP of a PV module from different operating points on the I-V curve. Although the RLC circuit was designed for the 255 W PV module, the only varying factor in the RLC circuit is the PV module's equivalent resistance. Since the equivalent resistance is dependent on the PV modules operating point, RLC circuit can be simulated with the 255 W and 300 W PV modules. The following is taken into account when calculating the perturbation period:

- Switching resistance of the MOSFET topology
- RLC inductor DC resistance
- PV module equivalent load resistance

By referring to Figures 4.5, 4.6 and 4.7, the LC perturbation applied to the PV module in the Simplorer simulation causes an oscillation, which can be observed in Figure 4.5. This oscillation causes a deviation of a minimum PV module voltage of 22.04 V and peak voltage of 38.45 V. At the same time the PV module's characteristics are as expected and illustrated when the perturbation is applied, as the voltage decreases the current increases and vice versa. The PV module current reaches the short circuit current of 8.69 A and when the voltage increases the current decreases to a minimum of 7.5 A, which is not enough to allow the voltage to reach open circuit voltage. The dashed line indicates where the MPP point occurs during the oscillation and it can be seen that the oscillations swing above and below the MPP. Therefore, this deviation is sufficient enough to plot part of the I-V curve shown in Figure 4.6. The perturbation only manages to display part of the I-V curve because the open circuit voltage is not reached. Furthermore, another verification of reaching the MPP is illustrated in Figure 4.7, as the power reaches the 300 W maximum rated power of the PV module. The perturbation period can also be calculated from Figure 4.5 by subtracting the time difference between the two dots, which is 1.97 ms.

As discussed later in the next section, the switching resistances differ in both topologies as n and p channel MOSFETs are used. Whereas, the DC resistance of the inductor remains the same and the RLC capacitor's resistance is ignored because of the capacitor's low Equivalent Series Resistance (ESR). The PV module equivalent load resistance is either the MPP voltage divided by current, i.e the MPP equivalent resistance, or the MPP equivalent resistance added with 10 Ω to the PV array. 10 Ω is chosen arbitrary to determine the effectiveness of the perturbation techniques with the PV module not operating at MPP. In summary, the desired perturbation period can be anything from 1.8 ms to 2 ms as designed. Figure 4.5 displays a time difference of 1.97 ms and not 2 ms as calculated theoretically because, the simulation takes into account the DCR resistance of the actual inductor to be used in the experiment, the discharge resistor required for the RLC capacitor and MOSFET turn on resistance.

The LC perturbation technique is further investigated by shifting the PV array operating point to the right of the MPP by 10 Ω in the Simplorer simulation. The corresponding waveforms are displayed in Figures 4.8, 4.9 and 4.10. Although the LC perturbation illustrates the occurrence of oscillation in Figure 4.8, the peak to peak deviation is smaller compared to when the PV array was at MPP. This is expected as the PV module equivalent load resistance has increased, reducing the intensity of the oscillation. A maximum PV module

voltage of 43.46 V and current of 7.125 A is achieved, just below the short circuit current and not near open circuit voltage. Along with a minimum PV module voltage of 39.10 V and current of 2.19 A. The oscillations are sufficient to display part of the I-V curve in Figure 4.9. However, the I-V curve plot does not provide sufficient information as to whether the knee point can be identified, nor has short circuit current or open circuit voltage been reached in Figure 4.8. The P-V plot in Figure 4.10, firstly shows that the 300 W peak power has not been reached and secondly, the P-V curve does not reach a global maximum peak point. Thus, it can be concluded that the MPP of the PV module has not been reached. The perturbation period is calculated in Figure 4.8, using the time difference between the dots, which is 1.86 ms and is within the desired range.

The L-LC approach is applied to the PV array operating at MPP as displayed in Figure 4.11, 4.12 and 4.13. This approach first stores energy in the inductor for a period of 4 ms before applying the perturbation. As seen in Figure 4.11 the deviation causes the PV module voltage to reach a minimum of 2.1 V when the current is at the short circuit current of 8.69 A and the voltage reaches a maximum of 39.72 V with a minimum current of 6.68 A. The minimum PV module voltage is caused by Equation 4.9 below:

$$V_L = L \frac{d_i}{d_t} \quad (4.9)$$

According to Equation 4.9, the longer the inductor is short circuited to the PV module, the more energy is being stored in the inductor, and with the inductor voltage rising, the PV module voltage decreases. Thereafter, the capacitor and the inductor are switched in series and oscillations are introduced which cause the PV module's operating point to move along the I-V curve shown in Figure 4.12. Therefore, the knee-point of the I-V curve can be identified. Figure 4.13 illustrates that the 300 W peak power of the PV module is reached. Therefore, the MPP (MPP operating point is the dashed line in Figure 4.11) using the L-LC topology with the PV array operating at MPP. The perturbation period is calculated as 1.91 ms using the dots in Figure 4.11, which is within the desired range.

The L-LC perturbation approach is observed through the PV module voltage and current deviations shown in the Simplorer simulation results in Figure 4.14. However, the PV module operating point has been shifted to the right of the MPP. The I-V curve knee point is easily observed in Figure 4.15 and the simulated P-V curve shown in Figure 4.16, verifies that the L-LC perturbation approach does indeed find the MPP although the PV module is well away from the MPP. The PV module short circuit current of 8.69 A and open circuit voltage of 44.8 V was successfully reached and therefore the complete I-V curve and P-V curve is observed. Furthermore, the perturbation period is calculated as 1.84 ms, which is within the desired range.

The LC perturbation is simulated in Simplorer with the 255 W PV module operating at MPP as displayed in Figure 4.17. Since the theoretical design for the perturbation components was implemented for the 255 W PV module, the same simulation outcomes for the 300 W PV module would apply to the 255 W PV module. Therefore, the flexibility of the perturbation technique can be used for varying PV module power ratings. This is because a small damping ratio was chosen for the design and the PV module equivalence resistance between the 300 W and 255 W PV module at MPP used in the design are very close to one another.

It can be concluded based on the Simplorer simulation observations that the single diode model successfully represented the Renesola 255 W and 300 W PV modules. Verification of

the single diode model can be seen by the I-V and P-V waveforms shown in the simulation results. The simulated PV module nominal peak power values correspond with the Renesola datasheet, along with the I-V curve waveforms [90, 91], for the 255 W and 300 W PV modules. The similarity between the simulated I-V curve and Renesola datasheet I-V curve can be observed by comparing Figures 4.12 and 4.2b. The Simplorer simulation also assisted in demonstrating how the L-LC perturbation method outperforms the LC approach in locating the MPP from operating points well away from the MPP. The success behind the L-LC approach is the ability to short-circuit the PV module with an inductor and at the same time, storing energy in the inductor. After a set period (storing energy in the inductor), the inductor is switched in series with the RLC capacitor completing the RLC circuit. As previously mentioned, at the resonance frequency oscillations are introduced due to the interchanging of energy between the magnetic field of the inductor and electric field of the capacitor. These oscillations decay exponentially caused by the PV module equivalent load resistance (RLC resistance). This temporarily deviation causes the PV module operating point to reach short circuit current and the resonance caused by the capacitor, along with the initial energy stored in the inductor, increases the oscillation intensity. By increasing the oscillation intensity there is a greater chance of the PV module operating point reaching the open circuit voltage on the I-V curve. The L-LC perturbation can temporarily deviate the PV module operating point between short circuit current and open circuit voltage. This along with sufficient sampling allows for extracting the PV modules I-V curve, which the knee-point can be identified and therefore the MPP. The LC perturbation fails to track the MPP when the PV module operating point is not near the MPP, simply because there is not sufficient energy in the RLC circuit to cause a serve enough oscillation to swing in-between short circuit current and open circuit voltage. Each methods perturbation period was within the desired range, which was chosen on the assumption that selecting a slow perturbation frequency would reduce the influence of stray impedances. This assumption would allow better comparison between the simulated and experimental models, as well as better validation for using the single diode model and demonstration of the perturbation techniques.

4.4 Perturbation hardware

Two separate PCBs were designed to implement the two perturbation techniques. Figure C.5 illustrates the schematic for the LC approach, which uses high-side PMOS topology for switching and provision was made on the PCB for the L-LC approach by the additional circuitry seen in the schematic. However, high-side PMOS topology only works for the parallel RLC configuration and, hence, an additional PCB had to be designed to demonstrate the L-LC approach. The PMOS topology does not allow the storing of energy in the inductor in the L-LC approach. Therefore, the L-LC approached implements an NMOS topology used for switching which also required a DC-DC boost converter to properly turn on the MOSFETs. The hardware components for the LC PD include an inductor, capacitor and semi-conductor components used for switching and circuit protection (shown in Figure 4.20).

Table 4.5: RLC inductance at various damping ratios.

	ζ	L(mH)	C(uF)
Theoretical design specifications	0.1	5.74	17.57
Actual design specifications	0.136	3.9	22

is below the saturation current. This will ensure that the perturbation occurs as intended, because the inductor is within the saturation region. Similarly, Figure 4.19 illustrates that the inductor current is well past the saturation current. During the energy storing period the inductor is connected across the PV module, which short circuits the PV module. During this process the inductor may saturate if the PV module short circuit current is greater inductor saturation current. Care must be taken to ensure the inductor can handle the PV module short circuit current during the energy storing period. The main objective during the energy storing is for the PV module to reach short circuit current. Thereafter, the inductor is connected in series with the capacitor, which are both in parallel with the PV module, resulting in oscillations. The oscillations that are introduced to the PV module are as a result of the inductor and capacitor combination, which is needed for the PV module to reach open circuit voltage. The intensity of the oscillations is determined by the amount of stored energy in the inductor. The greater the oscillation intensity implies that the PV module has a greater chance of achieving open circuit voltage. The altering between short-circuit current and open-circuit voltage assists in tracking the PV module's MPP.

4.5 PCB Design

There are two perturbation topologies to be implemented and therefore two PDs are designed on two separate PCBs. Choosing to use separate PCBs for the PDs instead of incorporating the topologies on the MD PCB allows the option of implementing various different perturbation topologies while the monitoring device remains the same. This flexibility was shown when the additional circuitry, shown in Figure C.5, was intended to be the L-LC method, but a design oversight prevented this and a separate PCB needed to be designed. Thereby, costs were saved during development and broken or faulty PD components could be replaced more easily. Furthermore, both PDs PCBs are designed to be situated on top of the MD within the enclosure. The MD and PD's are interconnected via five 20mm aluminium stand-offs and a 6 pin header, which also supports the PD PCB above the MD PCB. The 6 pin head provides 3.3 V power and GPIO pins from the MD MCU control the PDs. The input and output power cables from the PV modules are connected to the stand-offs situated on the PD's PCB, which means power is transferred via the stand-offs to the bottom MD PCB. Aluminium is chosen to be the material for the stand-offs, because it has very good electrical conductive properties compared to brass and stainless steel alternatives. The only downside is that pure aluminium is a reactive metal that is prone to corrosion due to oxidation. In an attempt to reduce the oxidation process, stand-offs with an iridite protective coating was chosen. To reduce power losses in the circuit, large PCB tracks and polygon pours are used in both the PDs and the MD circuitry. Only one PD can be used at a given time, although the design allows the two PDs to be cascaded on top of one another. Both PDs are identical in their PCB specifications (size, header location, etc.), as shown in Figures 4.21(a) and 4.22(a), with the only difference being the circuit configuration. The L-LC approach has additional components because it requires a boost converter to properly switch the N-channel MOSFETs on. The LC approach, on the other hand, uses a high side P-channel MOSFET topology switching, which singles out the need for an additional boost converter or other

components for that matter. Figures 4.21 and 4.22 show the two PD's PCB.

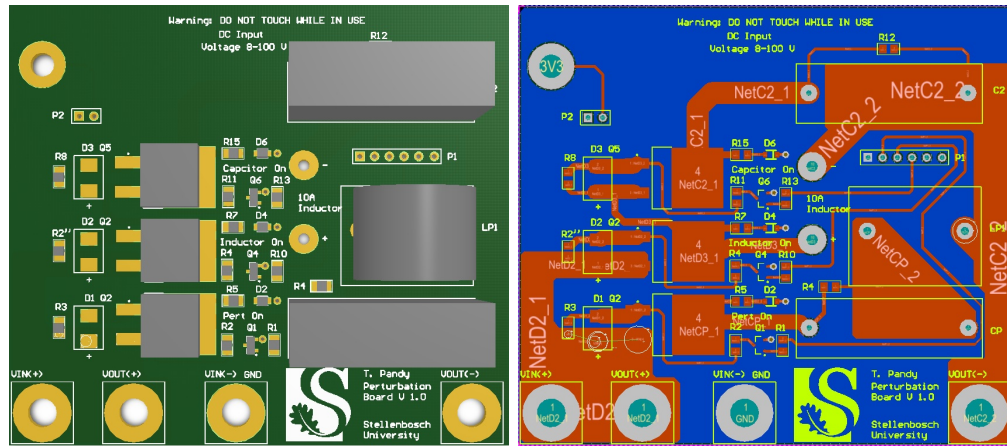


Figure 4.21: Perturbation device LC PCB design

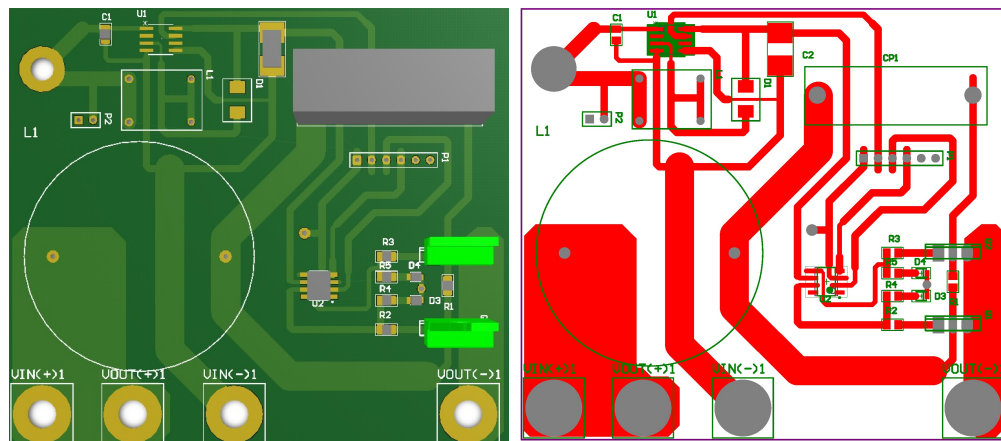


Figure 4.22: Perturbation device L-LC PCB design

The bottom four pads of the PD's PCBs, shown in Figures 4.21 and 4.22, are placement holes for the stand-offs as well as the input and output connection points. Given the operating limits, the MD and PD can operate at a maximum DC voltage of 100 V (using thin-film modules) and current of 20 A, which poses an electrical hazard to living beings. Irrespective of the PCB warning signs, 3D printed cylindrical covers are situated around the stand-off's as a safety measure to prevent electrical shock. The PDs are also situated in an IP67 enclosure for additional safety and circuit protection.

Chapter 5

Data acquisition device

5.1 Overview

This chapter discusses the ESP32-Wroom capabilities, detailed software design, basic operation and infrastructure needed for the data acquisition device.

5.2 Data acquisition objective

Data acquisition is a vital component required for this thesis. As mentioned in chapter 1, a data acquisition device is needed to acquire data from the MDs. Therefore, the DAD also serves as a gateway between the end user (client) and MDs, whereby the end user stores the acquired data onto an online database. To accomplish this goal, the core of the data acquisition device features the ESP32-wroom module from Espressif. This powerful module allows for communication on various platforms, ideal for data gathering and built with different communication protocols. This device is a gateway between the end user and the entire system. Commands are sent from the end user to the MD end devices via the DAD and MDC to fulfil end users' requests. Furthermore, the DAD offers synchronisation as an independent operation or can perform asynchronous tasks by the end user. Figure 5.1 illustrates the layout of the DAD in the overall system.

In summary, the DAD's design must allow the following functionalities

- Provide data acquisition and routinely request a measurement to all or individual measuring devices.
- Provide on-board storage to avoid data loss during periods with no WiFi connectivity.
- Serve as intermediate device for communication between the MD/MDC and user.
- Send collected and processed MD sampled data for the end user to store on the online database.

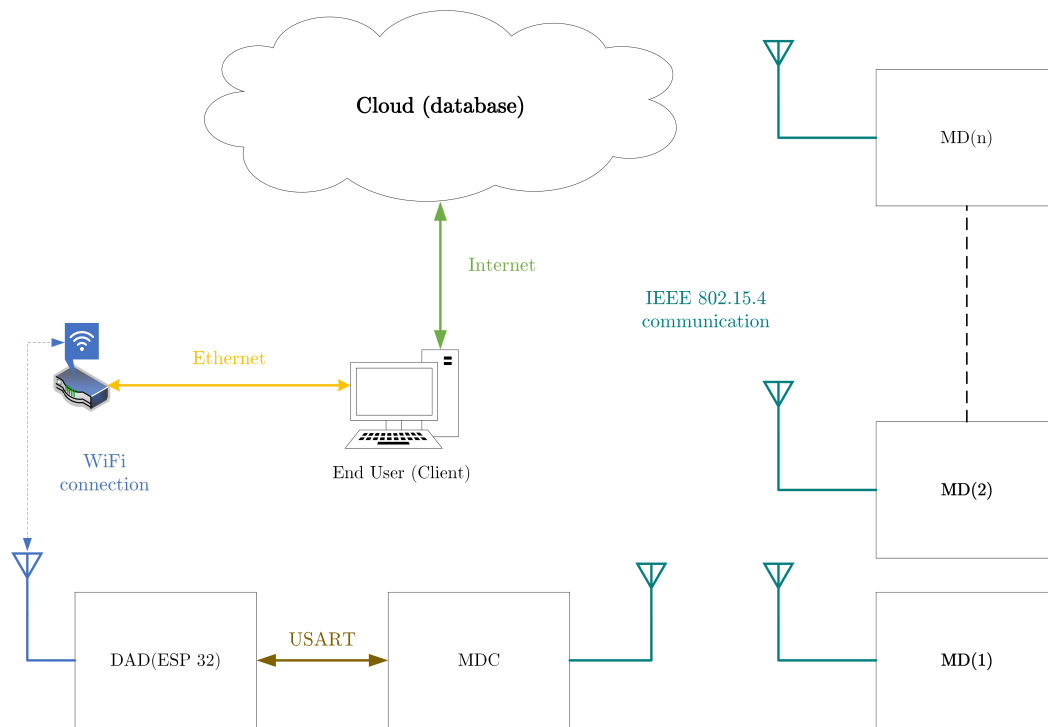


Figure 5.1: DAD layout

5.3 Hardware overview

5.3.1 ESP32 module

The ESP32 module is incorporated onto the Monitoring Device Coordinator (MDC) PCB as shown in Figure 5.1. Only one DAD is needed along with one MDC. The DAD is powered via the MD 3.3 V power supply that is supplied power from the lithium ion battery. One may ask why the ESP32 module was used instead of using the ESP32 IC (Integrated Circuit) on the PCB. This is a possibility for a future design that requires mass produced quantities. However, the main reason the ESP32 module was used is because it has strict design guidelines that require a 4 layer PCB, which is not implemented due to costs, complexity and time constraints. The earlier versions of the DAD made use of a Raspberry Pi, however the ESP32 module is much more versatile in terms of its commercial readiness and its small form factor also allows easy incorporation onto a PCB.

The following paragraph is cited from the ESP32 datasheet [97]. At the core of the ESP32-WROOM module is the ESP32-D0WDQ6 IC. This IC has two CPU cores that can be individually controlled or powered, and the clock frequency can be adjusted from 80 MHz to 240MHz. The CPU may be powered off to reduce power consumption and the coprocessor is used to constantly monitor peripheral changes or crossing thresholds. The ESP32 provides a variety of set peripherals ranging from capacitive touch sensors, hall sensors, low-noise sense amplifiers, SD card interface, ethernet, high speed SDIO/SPI, UART, I2S and I2C. The integration of Bluetooth, Bluetooth LE and Wi-Fi ensures a wide range of applications. The ESP32-WROOM has 448 KB of ROM for booting and core functions. It has 520 KB of on-chip SRAM for data and instruction and 8 KB of SRAM in RTC.

5.3.2 ESP32 communication

The ESP32 and MDC are incorporated on the same PCB and both ICs operate on the same voltage levels. Therefore, the built-in UART functionality of both devices are used for

communication with each other, with the advantage that no additional circuitry is required. The ESP32 has three UART ports, where UART0 is configured as the default port to be used to program the ESP32, with UART1 and UART2 available for general use. The PCB is routed to UART1, however the PCB design allowed for flexibility by having via's with tracks to UART2 pins on the ESP32 if needed. UART2 was needed when restarting issues was experienced with UART1 and was altered to UART2, using a pair of copper wires.

The ESP32 is a large and growing community with various platforms that discuss issues that arise on a daily basis on forums. Espressif provides a developing framework that is constantly changing. Many of the issues experienced by ESP32 users have disappeared when new versions of the framework were made available. Unfortunately there was no solution that addressed the restarting issue experienced on UART1 and it is assumed that the issue could be software related in the Espressif development framework. The ESP32 operates as master to the MDC and gateway between end users and MDC. The MDC UART communication functionality is discussed in 3.4.6. This includes the BAUD rate, UART setup and frame format, which are all software configurable. The ESP32 UART functions are presented in Section 5.4.4.

Furthermore, the ESP32 supports WiFi communication with its own built-in PCB antenna. The WiFi provides the communication between the DAD and end user via TCP socket. The ESP32 has a TCP socket server that listens for requests from end users. When WiFi connectivity is no longer available the DAD is programmed to sample data on a predefined set period and store that sample data on the SD card. Upon re-establishment of the WiFi network the end user then reads the sampled data from the SD card to store on the online database. An additional communication line between the MDC and DAD is established using SPI. The functionality was mainly added to communicate with the RFM 98 LORA module that is situated on the PCB. LORA is a long range, low power wireless platform that forms part of the Internet of Things (IoT). LORA was, however, not used in this thesis due to time constraints and the main aim was the demonstration of the perturbation techniques.

5.3.3 ESP32 real time clock (RTC)

The ESP32's built-in RTC can operate with an internal 150 kHz oscillator or using an external 32 kHz crystal for greater accuracy. The current time is set using an NTP (Network Time Protocol) server when the WiFi connection is established. For this reason the internal oscillator is used for the RTC with the time is updated via the NTP server on a regular 5 minute basis to improve the inaccuracy for the internal RTC. The RTC accuracy is only of concern when the internet is not available as the sampled data is stored on the SD card by time stamp.

5.3.4 Programming and flashing

The ESP32 can compile programs that were written in the C programming language and the code can be compiled on various different platforms and IDEs. The Windows operating system does not have an environment to build code and for that reason the GNU-compatible MYSYS2 environment [98] or the Eclipse IDE is sufficient . There are existing functions that are provided by the ESP32 SDK API and a framework has been developed by Espressif called the IoT Development Framework, also known as the "ESP-IDF", that can be found on GitHub [99]. The ESP-IDF is an evolving platform that is actively being worked on by Espressif and the community. The ESP32 development configuration can also be altered using the MYSYS2 environment to enable security features, partition tables, do peripheral configurations and much more.

The ESP32 is programmed via the UART0, as mentioned in 5.3.2. Additional hardware is required to communicate between a computer's USB and the UART0 of the ESP32. An external USB to UART programmer, also known as a USB to serial adapter, was designed for this purpose, as shown in Figure 5.2 below.

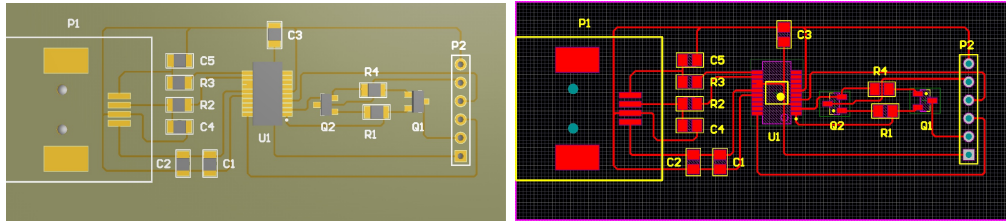


Figure 5.2: ESP32 programmer PCB design

An FTDI FT231 USB to serial IC was used, which converts the USB 5 V power and communication lines to a suitable 3.3 V power and serial communication for the ESP32 UART0. As seen in Figure D.4, an additional two lines are used during flashing to toggle the ESP32 into boot mode and reset the ESP32 after flashing to transition to the normal operating mode. This functionality allows for auto-reset during flashing, which is done using the FT231 RTS and DTR pins with an external NPN BJT transistor. The full schematic and PCB layout is shown in Appendix D.0.4. The ESP32 module has strapping pins that need to be configured during programming and normal operating modes. Before any flashing of the ESP32 is initiated, GPIO_0 must be pulled low and this is achieved by pulling the DTR pin low. The DTR pin is pulled low when there is communication between the USB and serial interface and, at the same time (DTR is low), the ESP32 reset pin is high. The moment flashing is completed, the DTR pin is pulled high along with GPIO_0 and the ESP32 requires the reset pin3 (EN-enable pin) to be pulled low and released to execute the newly flashed program, which is achieved after flashing when RTS is pulled high temporarily (toggled) and DTR pulled low.

5.3.5 SD card

During the absence of WiFi connectivity, the end user is not able to acquire sample data. The ESP32 and MDC MCU on-board memory is not sufficient to store all the sampled data in its memory and is only capable of storing enough data for one device at a time in volatile memory, which could result in data being over-written or corrupted. The addition of an SD card solves all these issues and the ESP32 community provides ample support for fast integration. A micro SD card is chosen because of its form factor. Communication to the SD card is done via its own dedicated SPI line from the ESP32, as shown in Figure B.7. A Hirose manufactured DM3 series surface mount micro SD card connector is used, along with a class 10 SanDisk 16GB memory card. The ESP32 and SD card operate on the same voltage levels and, given that the ESP32 uses a dedicated SPI line to the SD card connector, no additional circuitry is required. The PCB layout between the SD card connector and the ESP32 are illustrated in Figure B.9. The ESP32, as mentioned in Section 5.3.3, uses the internal oscillator to drive the RTC and the initial time is set via the NTP server when there is WiFi connectivity. The sampled data that is written onto the SD card in CSV (Comma-separated values) format with the device name, date and time stamp linked to the file name. Thereafter, once the WiFi connectivity is restored, the sampled data is read from the SD card by the end user and uploaded to the online database with the correct corresponding time stamp associated with the CSV file.

5.4 Detailed software design

5.4.1 Programming the ESP32

The ESP32 code was written in the C programming language and deployed to the device via flashing [100]. The ESP32 environment setup and IDE configuration is discussed in Appendix D.0.1.1.

5.4.2 Data retrieval overview

Section 3.4.2 discusses the data retrieval between MDC and MD as well as the DAD and MDC. The data retrieval between the DAD, end user data and SD card is discussed in this section. The DAD is the master to the MDC and MDs and the DAD is controlled via the TCP socket by end users using the ESP32 WiFi functionality. However, when the WiFi connectivity is unavailable, the DAD initiates a process to sample data from MDs at a fixed interval, gathers all the sampled data from MDs and stores the sampled data on the ESP32 SD card. This process is automatically configured by default and can be disabled by the end user. When WiFi connectivity is restored, the sampled data on the SD card is acquired by the end user, which is then uploaded onto the online database using the Python SQL libraries. Upon startup, if a valid WiFi connection is available, the ESP32 sets the date and time using the network as previously mentioned. The ESP32 keeps track of the date and time using the onboard RTC. During no internet connectivity, the RTC keeps track of the sampling interval and stores the sampled data on the SD by date and time stamp. Figure 5.1 illustrates the entire system communication layout of the data retrieval with database, end user, DAD, MDC, and MD.

Figure 5.1 also illustrates that the system was designed to be easily expanded. The IEEE 802.15.4 is the only communication platform that needs expanding and can be accomplished by introducing additional MDC (coordinator). Furthermore, the ESP32 can be incorporated with web development applications [100] given its WiFi capabilities, eliminating the need for the end user. This was a consideration and is the ideal method of communication for a fully functioning system. However, the end user method reduced additional coding and was sufficient for the experimental data acquisition process.

5.4.3 TCP socket communication

A socket is a two-way communication link between programs running on a network [101]. A socket is bound to a specified port in order for the TCP layer to identify which application the data packets are destined for [101]. The server listens for a client to make a connection request and upon a successful connection the client can use the socket to communicate with the server. The network setup is configured for IP version 4 and clients use the ESP32 IP address and TCP server listening port to access the TCP socket server program running on the ESP32. The TCP server only listens for incoming client connections when there is a valid internet connection. The TCP server and client flow diagram is presented in Figure 5.4.

5.4.4 ESP32 Master and user interface commands

A similar communication structure used by the DAD and MDC is implemented in the TCP communication structure. The TCP socket is not interruption driven like the Atmel ATmega 1284 RFR2 utilized for IEEE 802.15.4 and USART communication, but rather this

communication is software based. The ESP32 allows multi-threading with its dual-core CPU abilities, which was utilised with the TCP socket server. The ESP32 program was listening for clients on the TCP socket server, while also being preoccupied with tasks on the second CPU. Since the TCP socket communication is application (software) based, it allows the ability to be used on different applications and programming languages, provided there is a network between the two programs. The DAD TCP server socket is programmed in the C programming language, while the TCP client (end user) is programmed in python. The versatility of the TCP socket allows for the client to use any programming language, hence giving a platform to communicate with the DAD. This functionality enables user access to the DAD, MDC and MDs. Various commands are readily available for interaction to send or receive data. The TCP socket commands only has a single group user command, the HEX-41 (Hexadecimal), within the HEX-41 are sub-commands with specific functionalities.

These functionalities include sending or receiving data to and from the MDC via the DAD UART and sending or receiving data from the DAD. The sub-command functions are listed and described in Table 5.1.

Data sent to and from the end user to the DAD conform to the packet format shown in Figure 5.3. Similarly, in the USART communication, for credibility the DAD returns a reply message with the same packet format shown in Figure 5.3. The DAD software flow diagram for the data retrieval process is illustrated in Figure 5.4. When the MDC receives USART data the RX interruption is enabled and the software routine is displayed in Figure 3.11. The MDCs have internal procedures to verify if the received data is destined for the MDC via the ServiceComms() function. The function performs a CRC check to verify data validation, address verification and then proceeds with the received data, executing the corresponding instructions that was received.

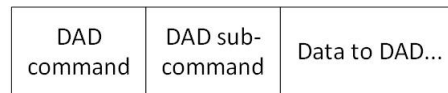


Figure 5.3: Data packet format from user to DAD

Table 5.1: List of the available python HEX-41 and HEX-42 MC commands

Command 0x41	
Sub-command	Function()
0x01	Send-MDC-Custom-Command()
0x02	Send-MDC-Custom-Data()
0x03	Get-MDC-Custom-Data()
0x04	Get-MDC-Sampled-Data()
0x05	Set-DAD-Time()

HEX-41 commands

Send-MDC-Custom-Command(): End user sends MDC a custom command and sub-command with the DAD via TCP socket server.

Send-MDC-Custom-Data(): End user sends MDC a custom data on length N with the DAD via TCP socket server, where N any number less than MDC RX buffer.

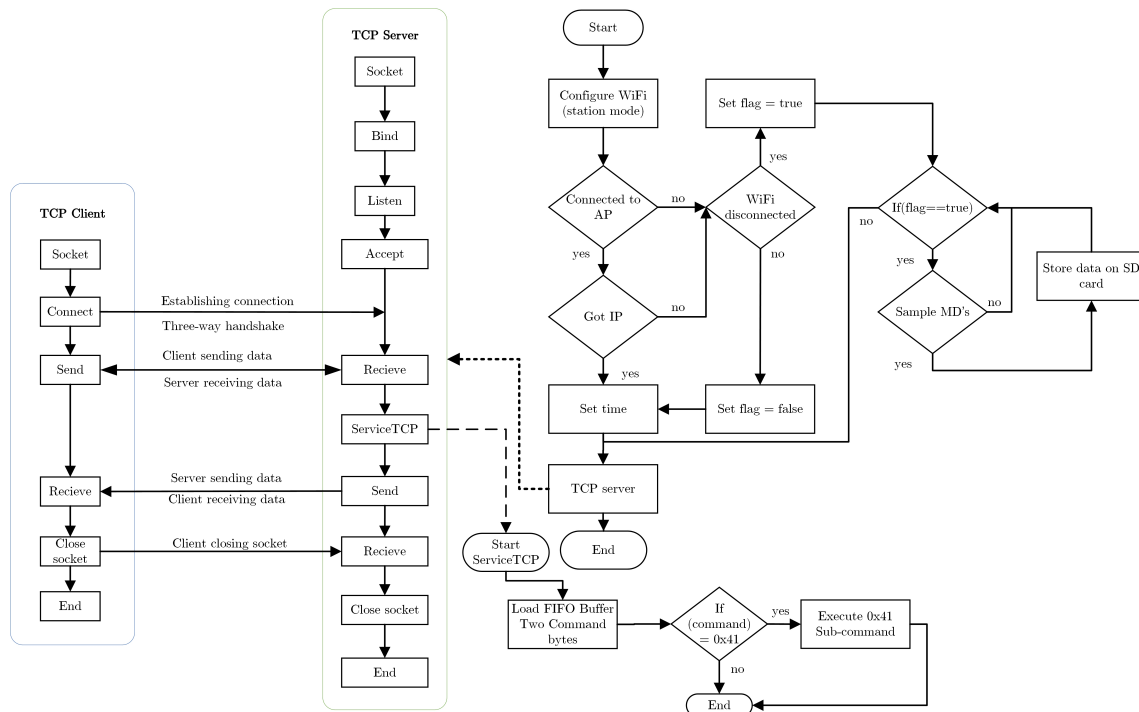


Figure 5.4: DAD TCP server software flow diagram for received data

Get-MDC-Custom-Data(): End user gets N amount data from MDC with the DAD via TCP socket server, where N any number less than MDC TX buffer.

Get-MDC-Sampled-Data(): End user gets N amount of sampled data from MDC with the DAD via TCP socket server, where N any number less than or equal to 1000.

Set-DAD-Time(): End user sets DAD local time using the network via TCP socket server.

The DAD is only intended to pass information between the end user and MDC. To avoid rewriting all the same functions used on the MD(C), only two main functions are used. The Get-MDC-Custom-Data() and Send-MDC-Custom-Data() are flexible functions, which are interpreted by the service TCP function, shown in Figure 5.4, based on the expected variable length that is specified by the user. These two functions simplify the code and allow for flexibility without needing to reprogram the ESP32 to add new functions. In essence, the DAD simply acts as a buffer between the end user and MDC, where data is passed through the DAD bidirectionally.

Chapter 6

Experimental set up and methodology

6.1 Overview

As previously mentioned, this research aims to investigate real-time in-situ PV module monitoring and introduce Perturbation Techniques (PT) to determine if the PV module's operating point is indeed the MPP without affecting PV array operation. The in-situ monitoring and perturbation implementation strategies are presented in this chapter. A complete description and breakdown of each perturbation method is provided along with the monitoring strategy. All the experimental setups and testing were performed at the research test facility, which is discussed in Appendix A.

6.2 Practical implementation

The aim of this section is to verify the simulated results in Section 4.3.3, by setting up a realistic scenario. This will then conclude as to whether or not the proposed PV motoring solution is indeed effective for the intended application. The monitoring strategy is presented in this section along with the perturbation technique strategies. The thought process behind the monitoring strategy is based on the following questions:

1. How often should each PV module be monitored?
2. At what operating points can the MPP be found?
3. What is considered an acceptable error?
4. When do PV arrays not operate at MPP?

In the literature review, it was discovered that there are various factors that prevent PV arrays from performing as ideal power sources, resulting in energy loss. These include factors from the environment or manufacturing defects that both introduce PSC on the PV array. It was further discovered that PV module monitoring is considered monitoring on a higher level of granularity as it provides more detailed information about each PV module's contribution to the PV array. As demonstrated by Guerriero [68], detailed monitoring was used to detect mismatches between PV modules within a PV array. The full design of the Perturbation Device (PD) and two proposed strategies are presented in Chapter 4. The intention behind the PD is to deviate the operating point of a PV module hoping to pass the MPP and determine if the PV module was indeed at MPP or not. This process is performed while the PV module is in operation and the deviation of the PV module operating point is intended to

occur fast enough for the PV array load not to be influenced. Both proposed perturbation strategies implement an under-damped (oscillate) RLC circuit designed with the only difference being that the first method has no stored energy (known as "LC-perturbation") in the inductor and the second method (known as "L-LC-perturbation") stores energy in the inductor, thereafter applying the perturbation. In section 4.3, the simulated results illustrate that the L-LC method has the advantage of finding the MPP of a PV module operating point well away from the MPP. The literature review further discusses that PV plants can be required to assist the grid with VAR compensation, which entails that the PV array will not be operating at MPP during this condition, because the inverters are receiving reactive power. For this reason, one of the this thesis research questions is to know how much excess power is available.

6.2.1 Monitoring strategy

Guerriero [68] successfully implemented a PV module monitoring solution using IEEE 802.15.4 (ZigBee) wireless communication. The monitoring was performed over a two-day period with a power measurement taken every 5 minutes. Each power measurement included an average of 50 samples taken from 5 am to 7 pm. The findings of Guerriero's [68] PV monitoring implementation indicate that the amount of samples and sampling interval were sufficient for the 14 hour sampling period. Furthermore, the IEC 61724 standard [47, 60] specify parameters directly related to irradiance and should be sampled every one minute or less. However, parameters with large time constants should be sampled at every 1 - 10 minute intervals, such I-V curve measurements [47]. Firstly, this information assists in selecting an appropriate sampling period for the monitoring strategy. Secondly, the perturbation period for both perturbation strategies have been designed to be 2 ms in the theoretical design, but given the available hardware selection of the RLC circuit, this was reduced to 1.89 ms because the damping ratio was altered. The simulation also incorporates the hardware selection that was used in the design and therefore also has a perturbation period of 1.89 ms. Lastly, the MD can gather up to 2000 samples, but was limited to a maximum of 1000 simultaneous voltage and current samples that occur in a time of roughly 22.7 ms (refer to Section 3.3.6.1). A sufficient number of samples are required to be allocated for the operating point before and after the perturbation, including the perturbation itself. Figure 6.1 illustrates the monitoring strategy overview, where the input parameters are user defined. After the samples are collected, the sampled data is stored on the online SQL database for data analysis purposes.

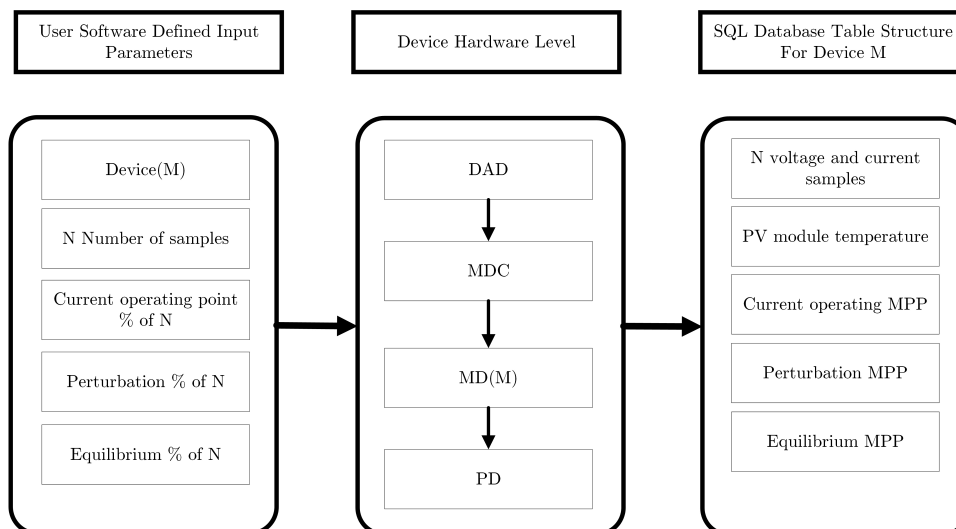


Figure 6.1: Monitoring strategy overview

By referring to Guerriero's [68] monitoring parameters and the IEC 61724 [47] specification as well as taking MD hardware limitations into account, a sampling period of 5 minutes was chosen, along with monitoring the voltage and current for the maximum of a 1000 samples. The amount of samples allocated before (current operating point), during and after (equilibrium) perturbation will be discussed in the perturbation strategy. The MD is in fact a stand-alone device, capable of PV module level monitoring and fault detection similar to the device presented by Guerriero et al. [68] and Gargiulo et al.[22]. Given the common energy yield loss that occur in PV systems, discussed in Chapter 2, the monitoring device is capable of determining mismatch and temperature variance between PV modules. As mentioned, each MD device logs current, voltage and temperature to an online SQL database for further data analysis presented in the following chapter.

6.2.2 LC - Perturbation strategy (no stored energy)

A sampling method is required to sample the LC perturbation method effectively. This approach applies the under-damped RLC circuit, causing oscillations to the PV module operating point with the hope of reaching the MPP. In keeping with the monitoring strategy illustrated in Figure 6.1, it is vital to know how many samples to allocate for each category. The determining factor is certainly the perturbation period. Too little sampling allocation of the perturbation waveform may fail to capture the MPP during a perturbation. On the other hand, too many samples may not provide meaningful information before and after the perturbation occurs. The simulation waveforms come in handy and, at the same time, it should not be forgotten that the perturbation was designed to occur fast enough for the MD to sample, which is not of concern. As shown in Figure 4.5, the current and voltage waveforms both show the exponential decay over time caused by the RLC resistor as expected and previously mentioned. Furthermore, the MPP is reached during the initial first period of the perturbation when the amplitudes are at their peak, as illustrated in Figures 4.6 and 4.7. The question still arises as to how many samples the perturbation period should be allocated, provided that the simulations show that the MPP was achieved in the first period of the LC perturbation. The sampling allocation for the LC perturbation topology is shown in Table 6.1.

Table 6.1: Perturbation strategy (no stored energy) sampling method

Sample % breakdown	Sampling
20 %	Current operating point
60 %	Perturbation MPP point
20 %	Equilibrium MPP

One of the main aims of this thesis was to demonstrate the perturbation techniques and therefore it was decided to sample the perturbation period much longer than what is required. This was also done to compare the simulated with the field results, for an indication of the effectiveness and accuracy of the theoretical model. Thus, each sample will utilise the maximum amount of samples on the MD of a 1000. To improve on Guerriero et al.'s [68] sampling size of 50 samples, it was increased to 200, which is 20% of the MD allocation used for sampling the initial and equilibrium operating point of the PV module after the perturbation. The 60% (13.2 ms) allocation for the perturbation ensures that approximately 7 periods of the perturbation oscillations are captured, which is more than sufficient information to plot significant parts of the IV curve. It should also be noted that only during the

perturbation sampling period the perturbation device is applied (active) to the PV module. It is therefore of importance to know if the perturbation had any effect on the initial and equilibrium operating points. In other words, does the perturbation device implementation affect the MPPT techniques of the PV array? If the results continuously show a consistent initial and equilibrium operating point power deviation, then further investigations are needed to identify if the PV string operation is being affected. Figure 6.2 illustrates the MD flow diagram when sampling with the LC perturbation topology.

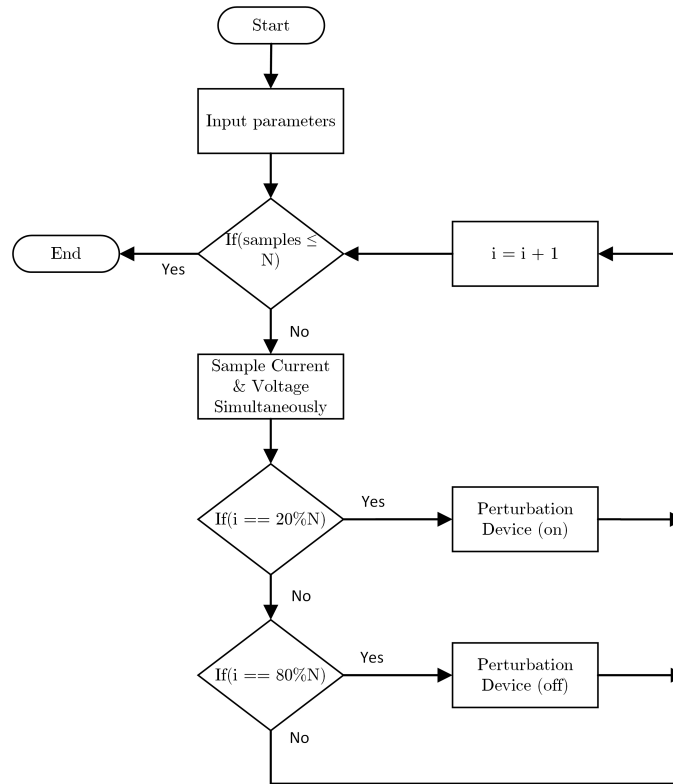


Figure 6.2: No stored perturbation flow diagram

The input parameters shown in Figure 6.2 include the sample size amount, specified as 1000 and whether a perturbation should occur or not. This flow diagram is also used during the calibration process of the MD, discussed in Section E, with the only difference being that the perturbation device is not active. Likewise, if the user would like to monitor the PV module without a perturbation performed, the same process applies.

6.2.3 L-LC Perturbation strategy (stored energy)

Similar to the LC perturbation topology, the L-LC method also requires verification with the theoretical model. At the same time, more information needs to be captured within the 1000 sample capability of the MD. The additional samples are needed for the storing of energy in the inductor, although this is a fairly quick process. Care should be taken as to exactly how quick this process should be. The inductor depicted in Figure 4.4 as L_{PD} , is connected in parallel with the PV module and when switched on, short-circuits the PV module while storing energy. This is illustrated by the voltage and current simulation waveforms in Figure 4.11. The hardware selection in Section 4.4 clearly indicates that the 3.9 mH inductor saturates at 3.3 A [95]. Table 6.2 illustrates the sampling allocation for the stored energy approach. The 20% initial and equilibrium sample allocation is kept to remain consistent with the LC perturbation approach and 20% of the sampling allocation has been taken off

Table 6.2: Perturbation strategy (stored energy) sampling method

Sample % breakdown	Sampling
20 %	Current operating point
20 %	Store energy in RLC circuit
40 %	Perturbation MPP point
20 %	Equilibrium MPP

the perturbation allocation to sample the storing of energy in the inductor. As mentioned in Section 4.4, the inductor is rated at 1.8 A with a saturation current of 3.3 A. The simulations further show that the saturation current is not exceeded during the perturbation; the current is exceeded when energy is stored in the inductor and when shorted to the PV module. Each percentage allocation represents the amount of time each subsection is active.

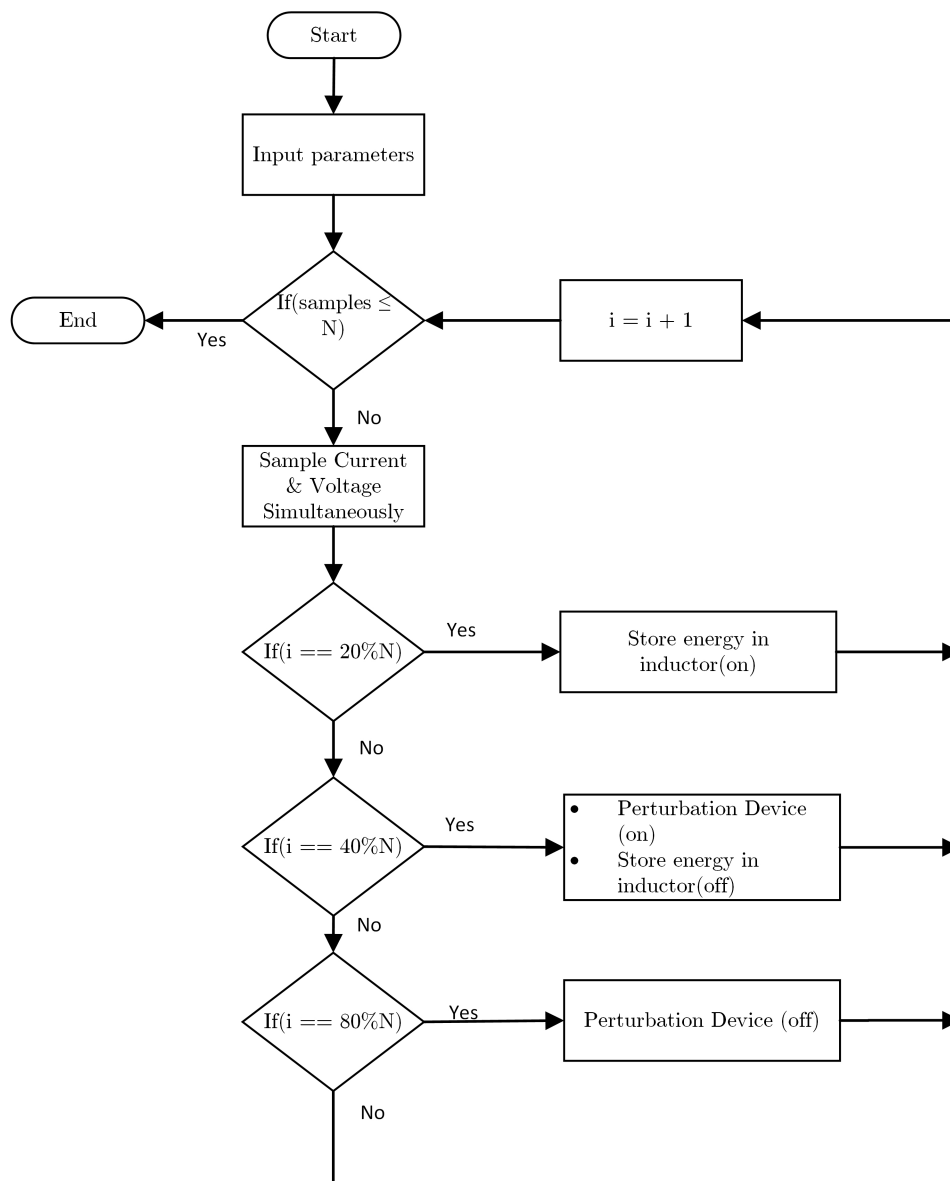


Figure 6.3: L-LC perturbation flow diagram

6.3 Application of perturbation technique

The aim of the PTs are to determine the amount of power loss if any, in a PV module. It is assumed that if the PV array is operating at MPP then each PV module is also at MPP. However, as previously mentioned in Section 2.2.2, PV module mismatch can reduce performance and alter the operating point from the true MPP. If this is the case and PSC does exist, then by monitoring and applying PTs on a module level, significant power loss can be identified if the proposed implementation operates as intended. Comparing the individual PV module's operating points before, during and after perturbation with all other PV modules in the PV array can lead to the following questions:

1. Will the PTs show significant power loss?
2. What effect do the PTs have on the PV array under various operating points?
3. What effect will the PTs have on the PV array load?
4. How effective is the PT on different size PV modules?

Three (before, during and after) significant points during the perturbation are compared to determine if there is any significant power loss in the PV array. If the before and after readings are similar while the perturbation reading is the greatest then it can be concluded that the PV array is not at MPP, provided that the perturbation wave forms conform to that illustrated in the simulated results in Section 4.3.3. It will be of interest to know if the PTs can find the MPP at various different operating points and, in particular, not near the MPP. The perturbation frequency is designed to be fast enough in order for the PV load (inverter, charge controller, etc.) not to notice any variation in the PV array due to the perturbation on an individual PV module. Similarly, by perturbing a PV module in a large PV array the perturbation of one PV module will not have a major variation on the PV array. The last question is concerned with how effective the PTs are when implemented on different PV module sizes. The majority of all PV systems operate with the PV array at MPP to generate maximum energy yield. As mentioned in the literature review, a grid-tie inverter supplies energy to the grid by extracting the maximum power from the PV array. However, it was also discovered that PV plants are used for VAR compensation when needed for grid stability. Hence, the PV array will not operate at MPP during these conditions, because the inverter is not operating at unity power factor. In an attempt to determine the amount of excess power available, it will be of interest to determine if the perturbation techniques are capable of determining the MPP from various operating points for greater flexibility. Thus, during the experimental setup, a grid-tie inverter was implemented to extract the maximum amount of power from the PV array. At the same time, the experiment attempts to determine how effectively the MPPT performed by the inverter and monitor PV modules to detect any mismatch. A charge controller will also be used to recharge deep cycle lead acid batteries. The idea here is to charge the batteries until fully charged until a float voltage is reached. During the float voltage the PV array is no longer operating at MPP and the perturbation device will be applied to determine if the MPP of the PV modules can be achieved. This scenario is also prevalent during PSC in PV arrays when PSC causes the PV array's operating point to deviate from the MPP. Therefore being able to detect under-performance will be of great importance. Figure 6.4 below shows the setup used to perform experiment(s) with the grid-tie and charge controller.

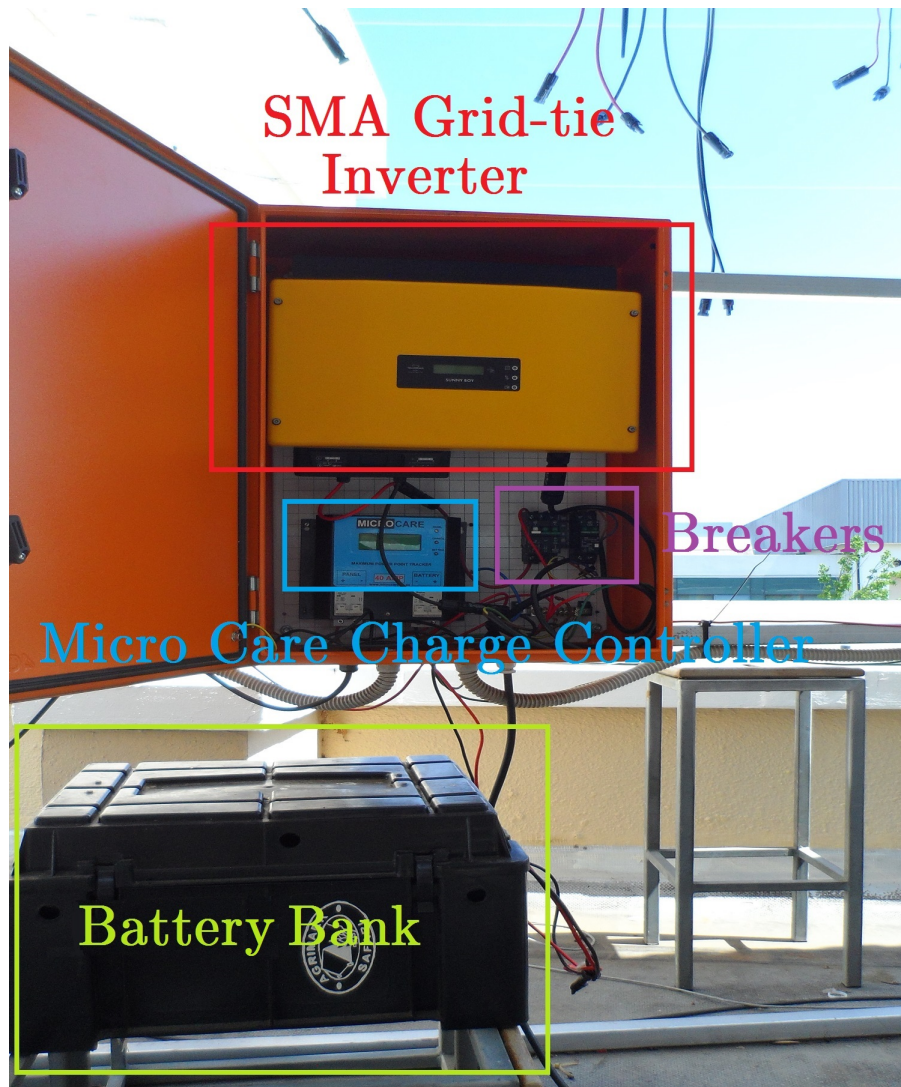


Figure 6.4: Experimental setup, circuit breakers, grid-tie inverter and charge controller

The research test facility infrastructure is discussed in Section A and contains all the specifications of the equipment used during the experimental testing phase.

6.3.1 Grid-tie inverter

A 1.6 KW SMA grid-tie inverter was supplied power from four 300 W Renesola PV modules connected in series. The energy harvested was fed into the electricity grid, ensuring the inverter was operating at MPP with the idea of verifying this information. At the same time, each PV module was monitored with the PTs evenly distributed on the PV array. PV modules 1 and 2 implemented the LC perturbation approach, while PV modules 3 and 4 implemented the L-LC perturbation approach. The testing was performed from early morning until late afternoon to acquire the daily energy generation. The testing time purely depended on when the inverters could switch on in the mornings, all depending on the PV array voltage, which needed to be anything above 120 V [102]. Likewise, the same applies in the evening; the PV array voltage will determine how long into late afternoon testing will occur. The thinking behind this is to show how the PTs performed in all periods of the day for the different levels of irradiance.

6.3.2 Charge controller

A Micro Care charge controller was supplied power from two 300 W Renesola PV modules connected in series. The charge controller then charged two 12 V lead calcium batteries connected in series. Before charge, the batteries were discharged using a load resistor to ensure that the charge controller drew the maximum power from the PV array to recharge the batteries. During this charging period each of the two PV modules performed monitoring using the two different PTs. PV module 1 implemented the LC perturbation approach, while PV module 2 implemented the L-LC perturbation approach. The thought process behind this was to identify if the MPP of the PV modules with the different PTs will reach float voltage from the charger controller after recharging the batteries.

Chapter 7

Results and Analysis

7.1 Overview

This chapter presents the results of the proposed in-situ real-time monitoring device and the implementation of the two perturbation device techniques at the research test facility. This chapter starts off with first addressing the accuracy of the raw data extraction and validation. The final sections present the results of the two perturbation techniques and in-situ real-time monitoring in PV systems, along with discussions on the results thereafter.

7.2 Raw data validation

7.2.1 Overview

The data analysis process is important to draw the necessary conclusions for the proposed implementations in this thesis. Therefore, the necessary procedures are taken to ensure that data uncertainty is minimised for the raw data readings. Reducing uncertainties reduces biased results and improves the overall accuracy of the measured data, which is governed by the IEC60904-1 and IEC61724 standards [47, 60]. Therefore, all data readings are calibrated, along with the data exchange and analysis, to the prescribed IEC standards mentioned above.

7.2.2 PV module data

The 4 PV modules (300 W Renesola Virtus II series) installed at the research test facility are 4.0 years old and were used at another testing location for the majority of the time. Only recently (April 2018) the PV modules were installed at the research test facility to be used for testing the proposed implementation in this thesis. These PV modules are all the same and purchased at the same time. During operation at the other test site, some of these PV modules may have been subjected to lightning and transportation damage. This is mentioned because this situation may be ideal to detect a mismatch in the PV array. Two smaller modules (255 W Renesola Virtus II series) have always been installed at the research test facility since being purchased and are the same age as the 300 W modules. Furthermore, each PV module's voltage and current is recorded, along with the back-plate temperature, as specified by the IEC 61724 standard [47]. Testing was initially performed on the 255 W modules connected in series to a variable load resistor during the development of the monitoring and perturbation devices. The four 300 W PV modules were installed to demonstrate the proposed implementation in a working PV system, as the charge controller and grid-tie inverter required sufficient PV array input voltage to operate. Furthermore, by

using PV modules with different power ratings gives further insight into the effectiveness of the perturbation device capabilities in tracking the MPP. It should also be stated that PV modules are installed on a rooftop to avoid as much shading as possible, (Appendix A). In literature, the performance ratio is a method to measure the performance of a PV module. For the outcome of this research, the performance ratio will not be used although it is used in industry for PV monitoring applications, because this research merely aims to demonstrate a PV module monitoring system with a particular focus on determining whether the current operating point is indeed the MPP. If there are differences in the MPP and operating point among PV modules within the PV array, then the underperforming module can be identified.

7.2.3 MD measurements

As previously mentioned, the MD measurement's accuracy is vital for providing meaningful data in PV monitoring systems. To avoid biased measurements and uncertainty, the MD was designed and calibrated to meet the IEC 61724 standard [47, 60]. The measurement accuracy of the MD is within the minimum requirements of the IEC 61724 standard, as displayed in Table 7.1.

Table 7.1: Instrument measurement accuracy and IEC 61724 standards

Measurement	Unit	MD Accuracy	IEC61724 accuracy
Ambient Temperature	[°C]	$\pm 0.4^{\circ}C$	$\pm 1^{\circ}C$
PV module temp	[°C]	$\pm 0.5^{\circ}C$	$\pm 1^{\circ}C$
I-V curve	[A],[V]	0.13 %, 0.509 %	1 %

The MD temperature sensor is capable of monitoring both ambient or PV module temperature and within the IEC 61724 standards, as shown in Table 7.1. The ADT7310 temperature sensor was only calibrated and tested in the office to measure room temperature before being used, due to its $\pm 0.4^{\circ}C$ from $-40^{\circ}C$ to $+105^{\circ}C$ temperature accuracy [87]. Along with verifying the accuracy of the calibration, another aspect to consider is the occurrence of phase-shifts in the measurements, particularly when sampling the perturbation waveforms. Therefore, to ensure that the MD hardware is not influenced by any phase-shifts in the measurements, a verification process needs to be implemented for this reassurance. This process is done in two parts, first by verifying that the ADCs indeed perform simultaneous sampling and, second, by comparing the exact same measurement performed by MD with an oscilloscope measurement. The first part is verified in Section E, when a 500 Hz sine wave from a signal generator is applied to both ADCs. As illustrated by Figure E.4, the ADCs indeed sample the voltage and current simultaneously. Part two is verified by Section E.0.1, the setup is a PV module connected to a variable load resistor that is adjust to the PV module MPP. Thereafter, a perturbation is sampled on the MD and at the same time the same voltage and current signals are captured via the oscilloscope. Figure E.5, clearly illustrates that there is no phase shift in the PV module voltage. That issue, was caused by the first stage PSU. Therefore, it can be concluded that there is no phase-shift between the voltage and current measurements.

7.3 Data alignment, storage and monitoring

Although the monitoring system in this thesis is relatively small with only 4 MDs and 1 MDC, data alignment, storage and monitoring are still vital. The DAD keeps track of time

using the ESP32 onboard RTC, whereby the time is initially set upon connecting to the WiFi network. The ESP32 only uses the date and time to log sampled data to the SD card when WiFi connectivity is down. The uncertainty around accuracy of the onboard ESP32 RTC are easily mitigated by updating the RTC on a regular 5 minute basis (during every sample) via the network. Furthermore, the client (python script) acquiring the data from MD and MDC via the DAD, processes that data to then be sent to the online SQL database¹ using the time stamp of the user client PC. Afterwards, the PC date and time is synced and verified via the network (internet) before sampling data. Having the time stamp recorded along with the sampled data conforms to the IEC61724 standard [47, 60].

An online SQL database was chosen over configuring a local SQL database on a lab PC, because of data reliability. Online hosting providers ensure greater data reliability by incorporating cloud based data storage systems over a single hard drive in a lab PC. Although, this downfall can be mitigated by a RAID storage configuration, the online SQL database approach has further reliability with systems in place in case of power failures and allows global access via the internet. The device status of each MD's or MDC's latest activities are displayed via a website². This website is designed to display the latest entries into the SQL database providing end users with live real-time monitoring of the entire PV array. This greatly avoids the tedious process of analysing each MD table individually. During testing, this website was displayed in the lab on a dedicated LCD screen to ensure that the data logging activities went smoothly, no problems are encountered without knowing about it, and to affirm of the data acquisition process. This ironically, is a monitoring system for the PV monitoring system and is a great method to respond to system failures and address them immediately. Figure 7.1 illustrates the monitoring website page that was developed.

Research Test Facility With Perturbation

Device	Time	Temperature	Current OP	Perurbation PP	Equilibrium OP
MD1	13:00:07	48.69 °C	261.81 W	265.9 W	261.03 W
MD2	13:00:12	47.69 °C	259.77 W	267.2 W	259.41 W
MD3	13:00:17	47.88 °C	255.7 W	261.15 W	255.14 W
MD4	13:00:22	47.19 °C	256.58 W	259.61 W	256.76 W

Date: Wednesday, 28 November 2018

Time: 17:07:57

Figure 7.1: Monitoring website displaying the latest measurement data for all MD's

7.4 Data related documentation

Irregular activities that might affect the data collection process were accounted for by using a log document, which is also in according to the IEC 61724 standard [47]. Any issues, problems encountered, faults, downtime and usual external influences that may influence the data were recorded. The research test facility is also used by other colleagues but very rarely. During testing it was noted when anyone needed to be at the research test facility and

¹The online infrastructure regarding the SQL database was created by the thesis author. The database forms part of the registered domain name of www.pvsoiling.co.za.

²This website was also created by the thesis author and can be viewed via the URL www.pvsoiling.co.za/monitoring.

before testing was performed the PV modules were scanned for bird droppings and removed if any were found. All this information was logged and is kept in mind for any irregular findings in the results, as well as a record to track back if there are any other uncertainties.

7.5 Problems encountered during the process of data acquisition

As expected, there were some challenges during the development of the MD, data collection and experimental setup.

MD current measurement

The MD measurement showed a significant phase shift between the voltage and current during a perturbation, which made it nearly impossible to plot the IV curve and track the MPP accurately. To verify the accuracy of the MD measurement, an oscilloscope was used and the outcome was that there was no phase shift seen by the oscilloscope. This implies that the phase shift was being caused by something on the MD that affect the reading. This could be hardware limitations of the current sensing method or some other influence caused by other hardware devices or even the PCB layout. After further investigations the cause was discovered. An obvious oversight that was not taken into consideration can be identified by referring to the MD power supply schematic in Figure B.6. The first stage PSU is the only PSU connected directly to the PV module and its presence changes the parameters of the perturbation device. The first stage input capacitance of 100 μ F plays a dominant role in the phase shift and alteration to the perturbation circuit. This issue was resolved by cutting the tracks between the PV module and the first stage PSU on all MD PCB's, which further meant that the lithium ion batteries were no longer able to charge. Before testing, the lithium ion batteries were charged using an external charger. A future PCB design can correct this oversight by using a relay to isolate the first stage PSU and the entire MD circuitry during a perturbation.

ADC measurements

The ADC was not sampling measurements correctly due to a digitising jump seen on the sampled output. Figure A.9 is an example of a sampled waveform with digitation error. The error was corrected by altering the software and hardware. The software was adjusted to accommodate for a long conversion period as shown in Figure B.2, from 8.8 μ s to 9 μ s. The ADC hardware required a 10-22 μ F capacitor on the ADC voltage reference input, which was not adhered to. This was corrected by using a 22 μ F capacitor on the ATL 431 voltage reference output, which corrected the issue by ensuring more stable reference voltage output.

MD power supplies

To reduce noise during measurements, the first and second stage PSU was turned off. The LTC3895f first stage PSU IC malfunctioned on more than one occasion when the IC was turned off and on too quickly. The solution was to turn the IC off and on at a slower rate. Another issues was experienced on the SC289 third PSU when the lithium ion battery was accidentally inserted in the reverse order, which caused the IC to malfunction and needed to be replaced. Thus, the MD lacks proper circuit protection from user error. The recommendation section provides suggestions for further versions of the MD.

IEEE 802.15.4 communication

To improve the data acquisition process between devices the IEEE 802.15.4, the data rate was increased from the default of 250 kbps to the maximum of 2000 kbps. During testing in the lab, this significantly improved unnecessary time delays when waiting for IEEE 802.15.4 data transfer over the air to be completed. The increase in the data rate did result in a shorter distance needed between the MDC and MD for reliable IEEE 802.15.4 communication that was experienced during testing. This was easily solved by placing the MDC in the centre of the PV array during the experimental setup. Furthermore, during a calibration of MD3, the IEEE 802.15.4 2.4 GHz antenna was not properly tightened and intermittent communication was experienced with that device.

Temperature sensors

Initially during the development phase, temperature readings were consistent and the sensor was working correctly. When longer power and communication cabling were used for the temperature sensor to reach the PV module from the MD, inconsistent readings of zero degrees were read. After tediously trying another sensor and using an oscilloscope to monitor the SPI lines, it was determined that communication lines were not transmitting the data correctly. The solution was to add terminating resistors (47Ω) in series with the SCLK and MOSI lines at the MD side as well as the MISO line on the sensor side of the SPI cable connection.

SQL database remote access

Another issue occurred when trying to connect to the pvsoiling.co.za SQL database remotely. The domain control panel allows remote connection from a list of IPs. If a remote device is not specified in that list and there are too many attempts to access the SQL database, that IP address gets blacklisted and is beyond the user's control to remove it, even if it is added to the list at a later stage. This occurred with the lab PC running the Python 2.7 script used for the data acquisition process. The IP was removed from the blacklist by calling the domain service provider.

ESP32

The ESP32 had two major issues: the first was USART 1 communication and second was trying to communicate (TCP socket) with the ESP32 connected to a WiFi AP in station mode. The USART issue is briefly discussed in Section 5.3.2. The ESP32 continuously restarted when trying to send large chunks of data. The MDC PCB layout was designed to be versatile for such situations and it was very easy to solder to wires onto the PCB to use UART 2 instead and the issue was resolved. As discussed in 5.3.2, this may have been a firmware or memory issue that requires further investigation. The ESP32 prints panic commands via serial on USART 0 and those commands can be researched to determine the possible cause. However, once the issue was resolved by changing USARTs this issue was never revisited.

The second issue arose when the ESP32 successfully connected to a WiFi AP, but did not obtain an IP address, as the server was configured to assign IPs automatically. Assigning a static IP on the ESP32 also did not work. However, when the ESP32 was configured in AP mode, other devices could communicate with it via WiFi and the TCP socket server worked correctly. The issue was resolved by changing the WiFi AP security settings to that which

the ESP32 had in AP mode. These security settings were WPA2 (WiFi Protected Access version 2) with AES (Advanced Encryption Standard) encryption.

7.6 Data extraction and filtering process

7.6.1 Data extraction

The data extraction process between the DAD and online SQL database is performed with a Python 2.7 script running on a lab PC. Python's MySQLdb library functionality was used to execute the data transfer. The lab PC has Windows 10 64-bit operating systems, with 16 GB of RAM and a 3.6 Ghz i7 4th generation processor. The python script running on the laboratory PC processes the data in the correct format before sending it to the SQL database.

7.6.2 Data filtering

The data analysis aims to demonstrate the PV monitoring capabilities of the MD and furthermore, illustrate the effectiveness of the PTs. The raw data validation is defined in Section 7.2 and, to proceed, a dataset is required for the data analysis process. A data set is required that is a true and accurate representation of the PV module characteristics. Any influences that may alter the data credibility is neglected. This process is known as filtering of the data. A series of questions must be asked to define the makeup of the dataset and data validity. Before testing, any oppings on the PV module were removed. All MD's start and stop sampling at the same time for each sampling day. All faults as previously mentioned are logged in a log book. Any part of the day is sufficient for testing as long as the inverter minimum input voltage of the PV array was met. Natural or deliberate PSC are performed to identify the effectiveness of the PT's under PSC.

7.7 Experimental results and discussion

7.7.1 Overview

All the results and discussions are presented in this section. The analysis of the PV module monitoring is presented, which is then followed by the analysis of the PTs. Thereafter, the effectiveness of the PTs are compared.

7.7.2 PV module monitoring

Before presenting the data analysis on the effectiveness of the PTs, it is important to get a holistic perspective of the data captured from the MDs at the test research facility. This is to familiarise the reader with the dataset before diverging into in depth discussions on the findings. The daily energy production during the experimental setup with the charge controller and grid-tie inverter are displayed in Figures 7.2, 7.3 and 7.4. Figure 7.2 illustrates the first day's energy production of all four PV modules powering the grid-tie inverter from 1 PM till just after 7 PM in the evening. The second day's energy production is illustrated in Figure 7.3 with the same configuration as mentioned before, monitors from 7 AM in the morning till just after 7 PM in the evening. The third day of testing was performed with two PV modules supplying power to the charge controller from 9:36 AM till just after 3 PM and the daily energy production is illustrated in Figure 7.4.

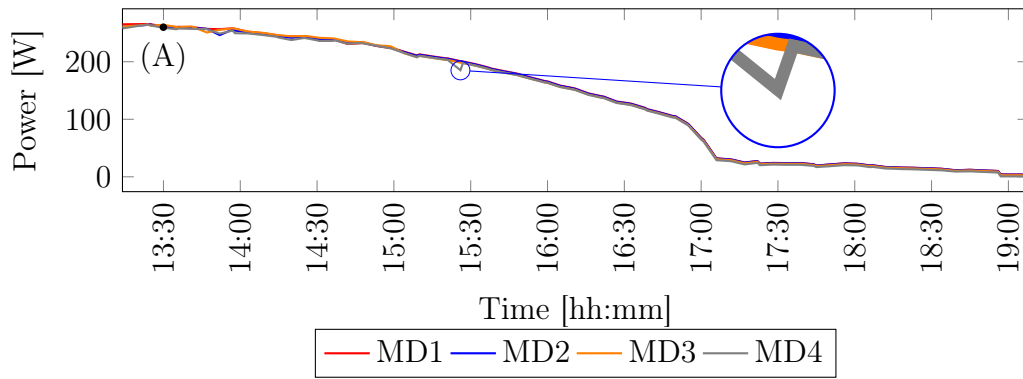


Figure 7.2: MD1-4 (Day 1) - Daily monitoring (13:14-19:08) of the four 300 W Renesola PV module's connected to the grid-tie inverter

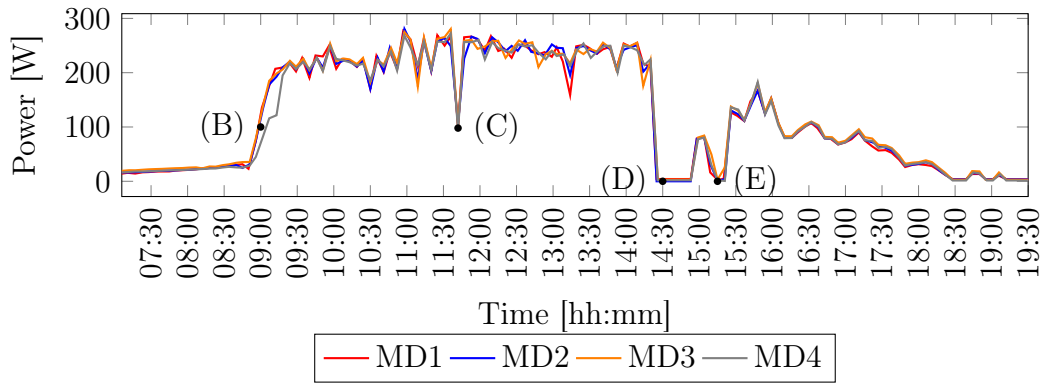


Figure 7.3: MD1-4 (Day 2) - Daily monitoring (07:06-19:30) of the four 300 W Renesola PV module's connected to the grid-tie inverter

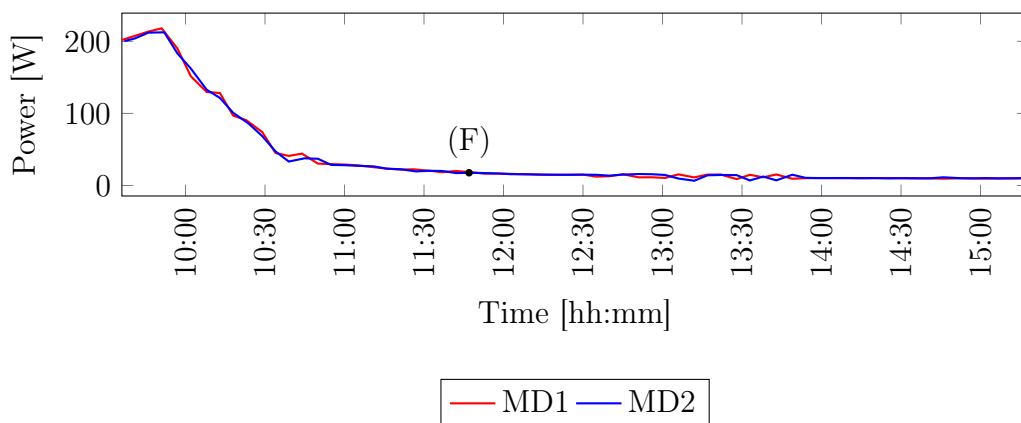


Figure 7.4: MD1-2 (Day 3) - Daily monitoring (09:35-15:15) of the two 300 W Renesola PV module's connected to the charge controller

7.7.3 Quantifying the monitoring data

The first day measurements was performed on a clear day, which can be seen from Figure 7.2 where each of the four PV modules have consistent power readings and are almost on top of each other. This further illustrates the accuracy of the MD as discussed in Section E. On a few occasions device MD4 would return 0 or values that are slightly off, as can be seen by the enlarged area in Figure 7.2. The uncertainty in the values is due to a digitising jump on the ADC. A zero data return was experienced on all the devices when the external antenna was not connected and MD4 is situated the furthest from MD1 (MD Coordinator) in the PV array, which may be the cause of the data uncertainty at odd occasions. The IEEE 802.15.4 data rate is set to maximum, which resulted in the range between end devices and coordinator needing to be closer for reliable communication. Furthermore, the steep drop in the power wave forms near 17:00 is caused by evening shade as shown in Figure 7.5.



Figure 7.5: PV array evening shade

The second day of testing was performed on a cloudy day with varying irradiance levels as seen by Figure 7.3 by the fluctuating power levels. The steep climb in the power around 09:00 is caused by morning shade as shown in Figures A.6 and A.7. Point C, was caused by low irradiance levels due to cloud cover. A fault occurred between 14:20-14:25 and was only detected via the www.pvsoiling.co.za monitoring website at 14:55, thereafter corrected. MD2 had a faulty cable connection and the entire PV array was disconnected from the grid-tie inverter and hence the energy was zero. Two deliberate shading tests were performed on PV modules 1 and 2, these tests included vertically shading a portion of PV module 1 at 15:15 as illustrated in Figure 7.6. Thereafter, shading both a portion of PV module 1 and 2 at 15:20 as shown in Figure 7.7. Partial shading conditions were deliberately introduced to determine whether the perturbation techniques could identify a mismatch. Figure 7.3 illustrates the significant power loss due to the effects of PSC on the PV array.



Figure 7.6: PV module 1 PSC



Figure 7.7: PV module 1 and 2 PSC

The results of the test performed on day 3 is presented in Figure 7.4 and the daily power displayed two PV modules in series connected to a charge controller that charged two lead-calcium deep cycle batteries. The batteries were semi-charged already and discharged using a load resistor. However, just before 10:00 in Figure 7.4, the charge controller recharged the batteries within a couple of minutes. Thereafter, the power slowly reduced until just before

11:00, when a float voltage was applied to the deep cycle batteries to keep the charge. Day 3 was performed on a clear day with sufficient irradiance and the perturbation results is able to indicate how much power is available once at the float voltage.

7.7.4 Perturbation results

The entire Chapter 6 is dedicated to the experimental set up and methodology implemented to assist in answering the thesis research questions. In summary, the monitoring device, first monitors the PV module, applies the perturbation while monitoring and then monitors after a perturbation is completed. This entire process is described in detail in Chapter 6. The aim of the perturbation techniques are to determine whether the PV module is operating at optimal power and there are various tests that are performed to determine how effective the two perturbation techniques are.

Figures 7.8, 7.9, 7.10 and 7.11 display the daily energy, along with the applied perturbation techniques for each monitoring device for day 1. Day 1 was a clear and sunny day with four 300 W Renesola PV modules connected in series to supply power to the grid-tie inverter from 13:14 to 19:00. Each graph illustrates the daily energy Current Operating Point (C-OP), Perturbation Peak Power (P-PP) and Equilibrium Operating Point (E-OP). MD1 and MD3 apply the LC perturbation, while MD2 and MD4 apply the L-LC perturbation.

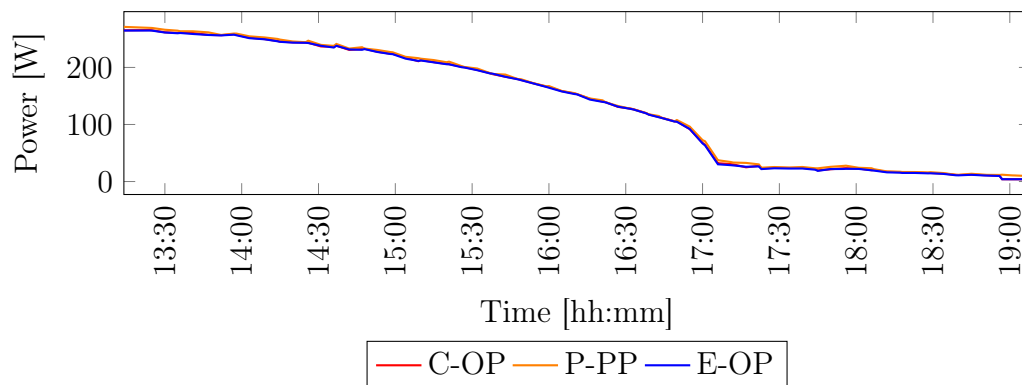


Figure 7.8: MD1 (Day 1) - 300 W PV module with LC perturbation

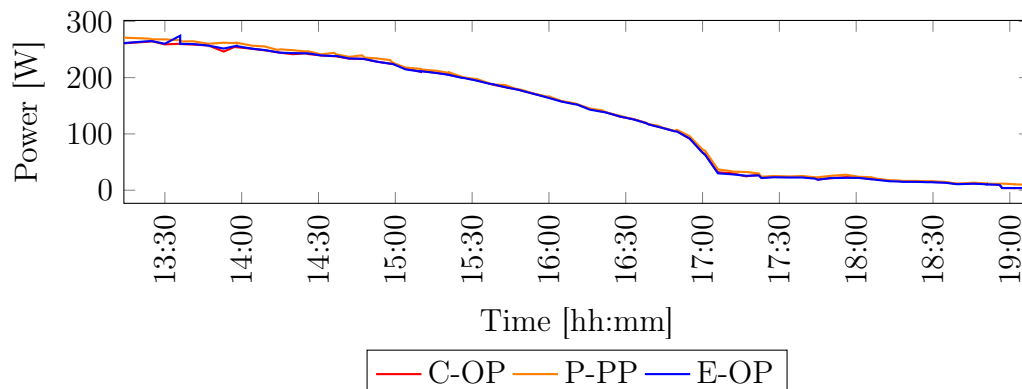


Figure 7.9: MD2 (Day 1) - 300 W PV module with L-LC perturbation

Figures 7.8, 7.9, 7.10 and 7.11 illustrates that the current operating point, perturbation peak power and equilibrium operating point waveforms (for all monitoring devices) are all very close to one another, which indicates that the PV array is operating fairly close to the MPP throughout the monitoring duration. By closer inspection the perturbation peak power

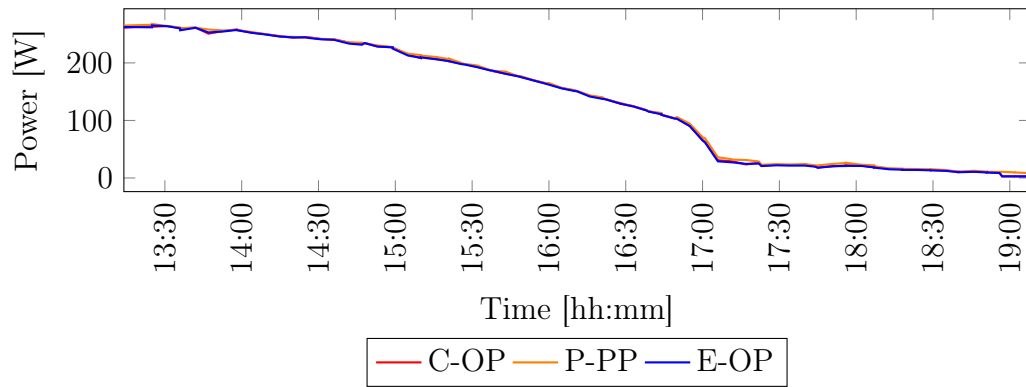


Figure 7.10: MD3 (Day 1) - 300 W PV module with LC perturbation

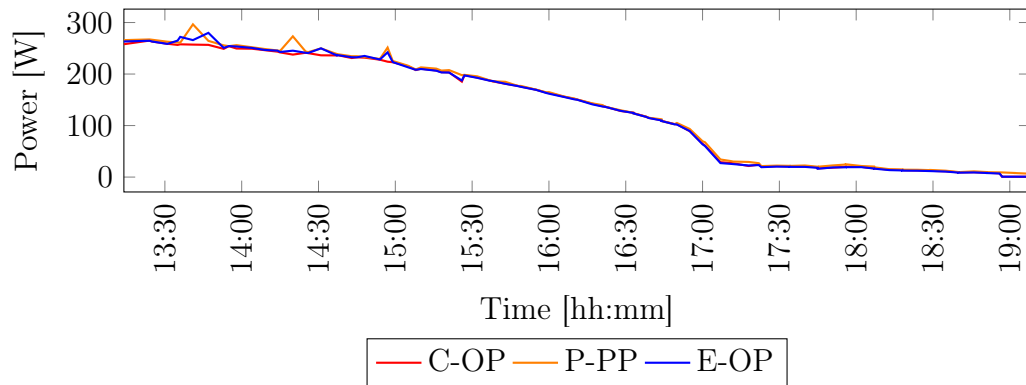


Figure 7.11: MD4 (Day 1) - 300 W PV module with L-LC perturbation

waveforms are slightly above the rest, majority of the time. Table 7.2, shows the average energy between the current, perturbation and equilibrium points.

Table 7.2: Average daily (Day 1) energy for the LC and L-LC perturbation, extracted from Figures 7.8-7.11

PV module average power	C-OP [W]	P-PP [W]	E-OP [W]
MD1	130.23	132.55	129.68
MD2	129.73	132.79	129.60
MD3	129.20	130.98	128.62
MD4	127.39	131.03	128.19

The results in Table 7.2 indicated that MD4 has the maximum deviation from the MPP of 3.64 W and MD3 indicated a minimum of 1.78 W from the MPP. Table 7.2 indicated that the PV array is very near the MPP. However, there was a slight mismatch between PV modules that caused the slight deviation. This mismatch could be due to many factors, such as dirt modules, degradation of the PV modules, etc. Furthermore, it could be seen that the perturbation technique did not affect the MPPT operation of the grid-tie inverter because the current and equilibrium operating points were fairly similar. It can be concluded that both the LC and L-LC perturbation techniques tracked the MPP appropriately, while the PV array was operating at the MPP.

Figures 7.12, 7.13, 7.14 and 7.15 display the daily energy, along with the applied perturbation techniques for each monitoring device for day 2. Day 2 was overcast with four 300 W Renesola

PV modules connected in series that supplied power to the grid-tie inverter from 07:06 to 19:30. Each graph illustrates the daily energy Current Operating Point (C-OP), Perturbation Peak Power (P-PP) and Equilibrium Operating Point (E-OP). MD1 and MD3 applied the LC perturbation, while MD2 and MD4 applied the L-LC perturbation.

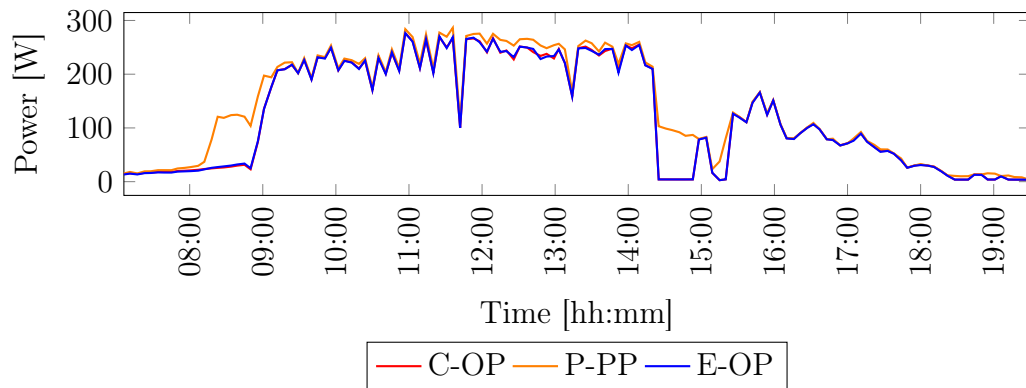


Figure 7.12: MD1 (Day 2) - 300 W PV module with LC perturbation

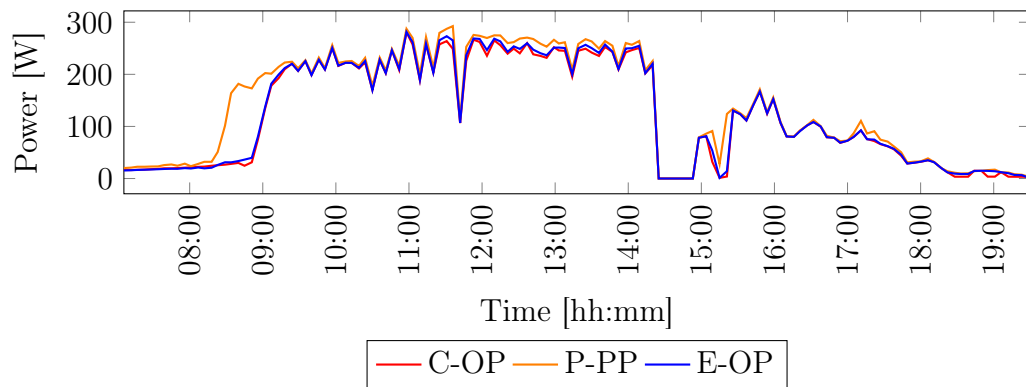


Figure 7.13: MD2 (Day 2) - 300 W PV module with L-LC perturbation

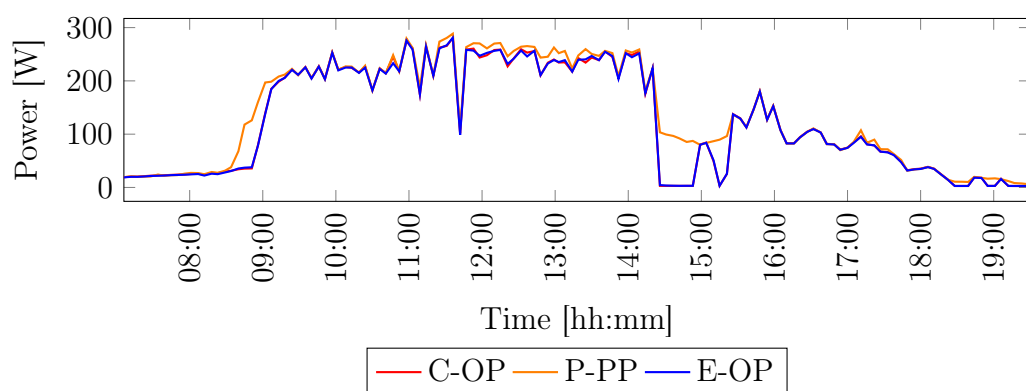


Figure 7.14: MD3 (Day 2) - 300 W PV module with LC perturbation

Figures 7.12, 7.13, 7.14 and 7.15 illustrated the current operating point, perturbation peak power and equilibrium operating point waveforms (all monitoring devices) that differ during morning shade (point B), fault condition (point D) and the PSC (point E). Each point B, D and E will be discussed in further detail in the following paragraphs. On all other points during the day, each of the MD's track the MPP quite closely. Upon further inspection

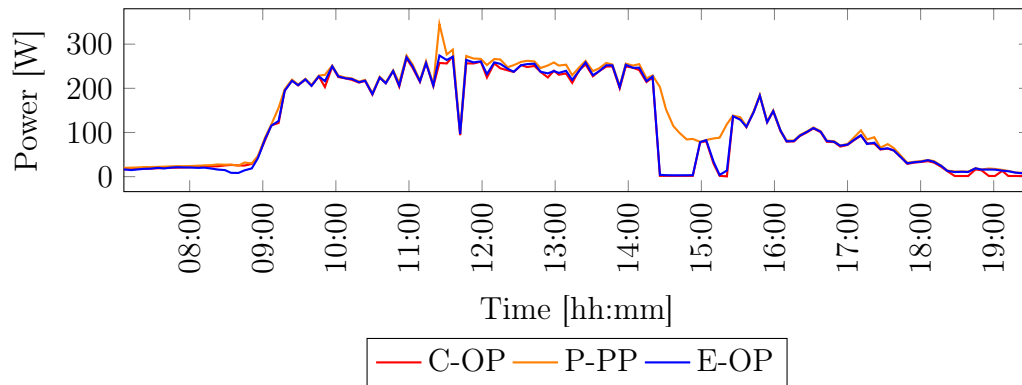


Figure 7.15: MD4 (Day 2) - 300 W PV module with L-LC perturbation

of MD4 illustrated in Figure 7.15, an example of MD4 digitising jump can be visualised between 11:00-12:00. Justification of the digitising jump is concluded by comparing the reading of MD4 to the other three PV modules and a reading greater than the rated 300 W is highly unlikely. Upon further inspection, the perturbation peak power waveform is above the other two waveforms majority of the time. Table 7.3, shows the average energy between the current, perturbation and equilibrium points.

Table 7.3: Average daily (Day 2) energy for the LC and L-LC perturbation, extracted from Figures 7.12-7.15

PV module average power	C-OP [W]	P-PP [W]	E-OP [W]
MD1	122.96	138.42	122.75
MD2	123.29	138.70	125.59
MD3	125.88	137.77	125.50
MD4	121.49	135.32	123.13

Table 7.3 shows the daily average energy. The results show that there is a significant difference between the current operating point and perturbation operating point. A maximum difference of 15.46 W and minimum of 11.89 W. This significant difference is due to partial shading conditions on the PV array, where both perturbation techniques show that there is extra power available. Therefore, the PV array is not at the global maximum power point but rather the local maximum power point due to the tracking capabilities of the SMA grid-tie inverter. It should also be noted that the PV array output voltage was close to the minimum inverter input voltage. Further experiments will be required before making a final remark on the inverters ability to fully track the GMPP, as the inverter may have adjusted the PV array voltage to be within its operating limits to remain operational. It may be that the actual GMPP voltage during morning shade may have been below the inverter operating limits.

Figure 7.16 and 7.17 display the daily energy, along with the applied perturbation techniques for each monitoring device for day 3. Day 3 was a clear day with two 300 W Renesola PV modules connected in series to supply power to the charge controller from 09:37 to 15:18. Each graph illustrates the daily energy Current Operating Point (C-OP), Perturbation Peak Power (P-PP) and Equilibrium Operating Point (E-OP). MD1 applied the LC perturbation and MD2 applied the L-LC perturbation.

As previously mentioned, there are conditions when the PV array do not always operate at MPP. These include VAR compensation, PSC when failing to track the GMPP, when a

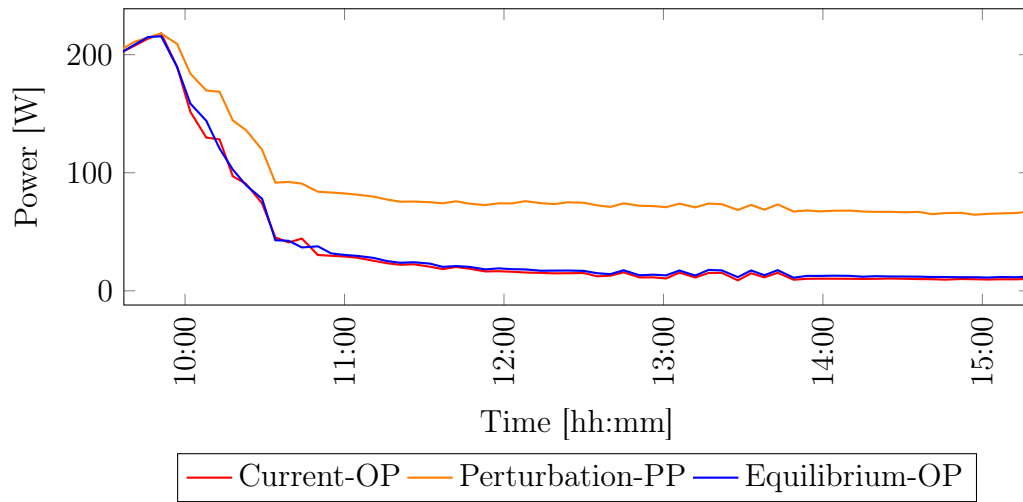


Figure 7.16: MD1 (Day 3) - Daily monitoring (09:37-15:18) of 300 W PV module connected to charge controller with LC perturbation applied

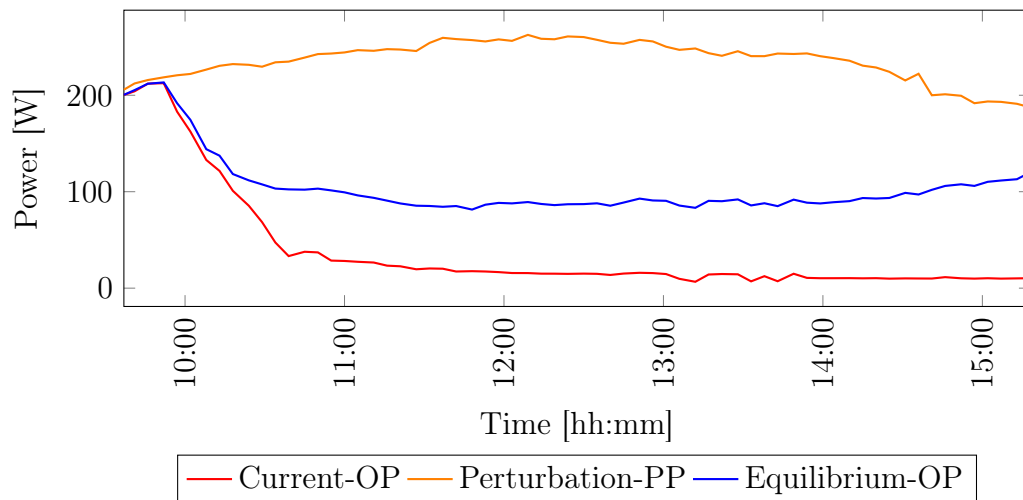


Figure 7.17: MD2 (Day 3) - Daily monitoring (09:37-15:18) of 300 W PV module connected to charge controller with L-LC perturbation applied

charge controller has full charge batteries as the load. This thesis also aims at determining how effective the two perturbation techniques are in tracking the MPP of a PV module from various operating points on the I-V curve. A Micro-Care 40 A charge controller was used to charge two 12 V lead-calcium batteries from two 300 W Renesola PV modules connected in series. The experimental setup is discussed in detail in Chapter 6. Figures 7.16 and 7.17 display the battery charging cycle from 09:37 to just before 10 am and thereafter the the PV array power decreases until a battery float voltage is reached to keep the batteries charged. It should also be noted that the batteries were nearly fully charged and hence the small period needed to fully charge them. A longer battery charging cycle is shown in Figure A.9. However, this was captured when there was uncertainty in the ADC readings and only the shape of the waveforms will be referred to. Irrespective, Figures A.9 and 7.4 both illustrate how the PV array power decreases as the batteries reaches its maximum charge capacity. This implies that the PV array is at MPP during the charging cycle and thereafter the PV array shifts away from MPP towards the required power to keep the batteries at float voltage.

Figures 7.16 and 7.17 illustrate the two perturbation techniques. It can clearly be illustrated that the L-LC perturbation out performs the LC perturbation, simply because the L-LC

perturbation has the ability display much more of the PV module I-V curve than the LC perturbation technique. This is shown in Figures 7.20a and 7.20b.

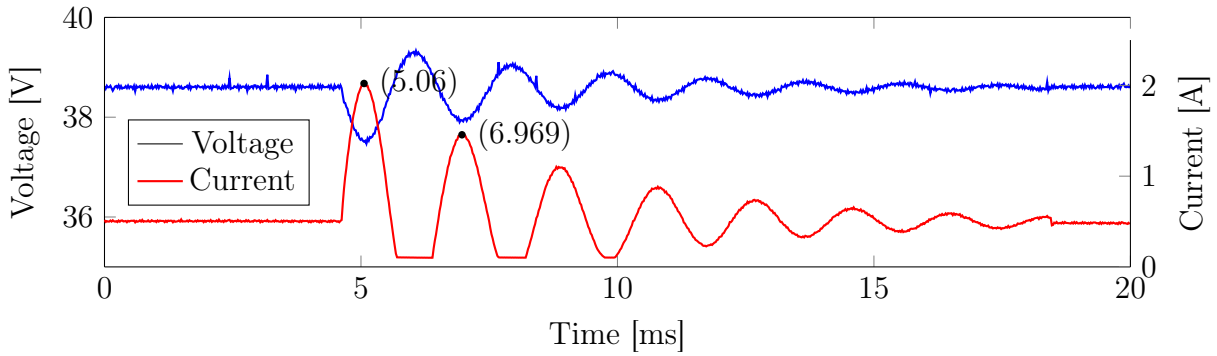


Figure 7.18: MD1 (Day 3) - Point F, current and voltage waveforms with LC perturbation

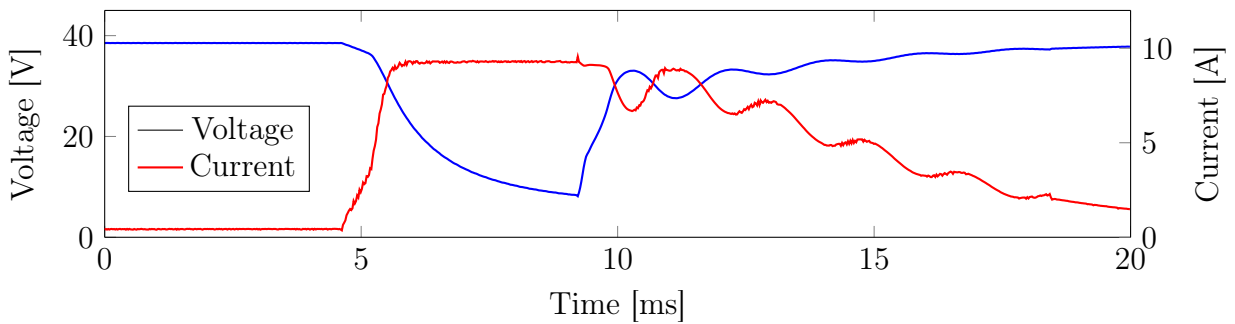
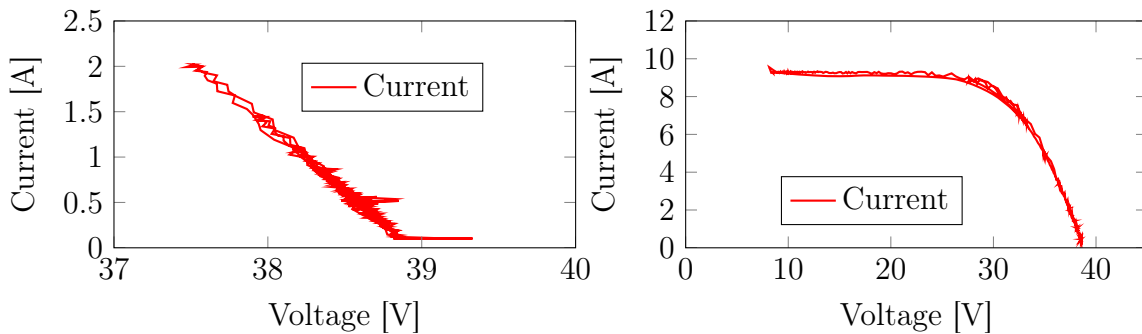


Figure 7.19: MD2 (Day 3) - Point F, current and voltage waveforms with L-LC perturbation

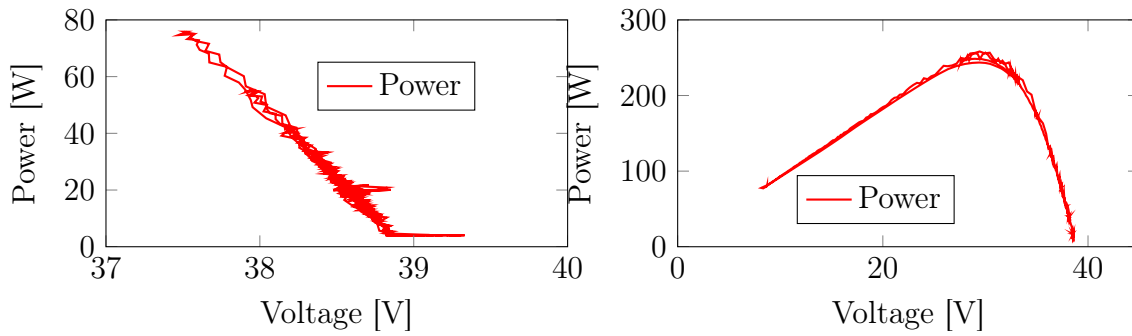


(a) MD1 (Day 3) - Point F, I-V curve with LC perturbation (b) MD2 (Day 3) - Point F, I-V curve with L-LC perturbation

Figure 7.20: MD1-2 (Day 3) - Point F, I-V curve waveforms

Table 7.4: Average daily (Day 3) energy for the LC and L-LC perturbation, extracted from Figures 7.16-7.17

PV module average power	C-OP [W]	P-PP [W]	E-OP [W]
MD1	39.49	90.77	41.35
MD2	39.11	236.01	105.37



(a) MD3 (Day 3) - Point F, P-V curve with LC perturbation (b) MD2 (Day 3) - Point F, P-V curve with L-LC perturbation

Figure 7.21: MD1-2 (Day 3) - Point F, P-V curve waveforms

Table 7.4 further illustrates how the L-LC perturbation technique outperforms the LC perturbation technique. Since the charging cycle was performed for a short period over the total monitoring period, the average current operating point power is mainly the batteries float power. Therefore, Table 7.4 displays the L-LC perturbation technique peak power average, with the LC perturbation technique peak power average. The equilibrium operating point does follow the current operating point when applying the LC perturbation technique as shown in Figure 7.16 and Table 7.4. However, by referring to Figure 7.17 and Table 7.4, it can be seen that the equilibrium operating point does not return to the current operating point immediately. It is assumed that the L-LC perturbation technique causing a fast surge of energy into the system and after the perturbation this energy has no where to dissipate fast enough. Further experiments need to be performed to determine how the charge controller handles this energy dissipation process. It can be concluded that the L-LC perturbation technique is much more effective in tracking the MPP of a PV module not operating at optimal power. Figures 7.22 and 7.23 display the voltage and current waveforms for MD1-2 at point A shown in Figure 7.2. This followed by MD1-2 I-V and P-V curves waveforms displayed in Figures 7.24a, 7.24b, 7.25a and 7.25b for point A shown in Figure 7.2.

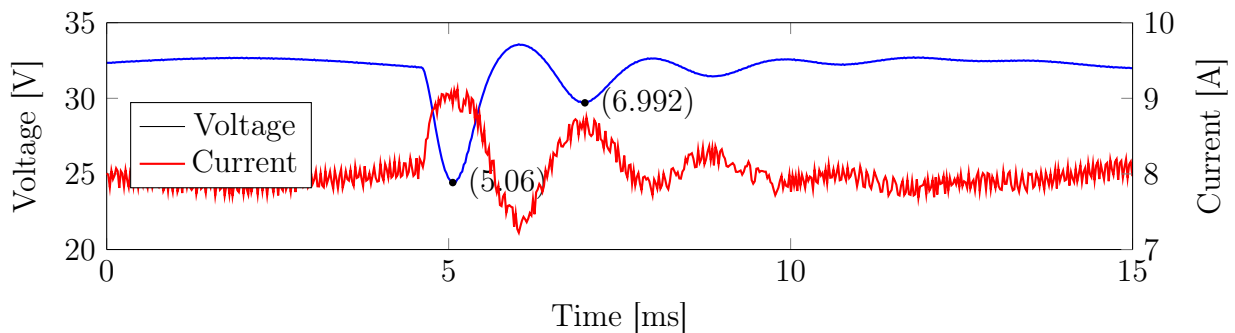


Figure 7.22: MD1 (Day 1) - Point A, current and voltage waveforms with LC perturbation

The voltage and current waveforms shown in Figures 7.22 and 7.23 are similar to those seen in the simulation results in Section 4.3.3. The SMA grid-tie inverter is a transformer-less inverter and therefore an alternating frequency of twice the grid frequency (100 Hz) was seen on the DC input.

Figure 7.24a and 7.24b show the two perturbation techniques track the I-V curve. It can be seen that the L-LC perturbation displays more of the I-V curve than the LC approach,

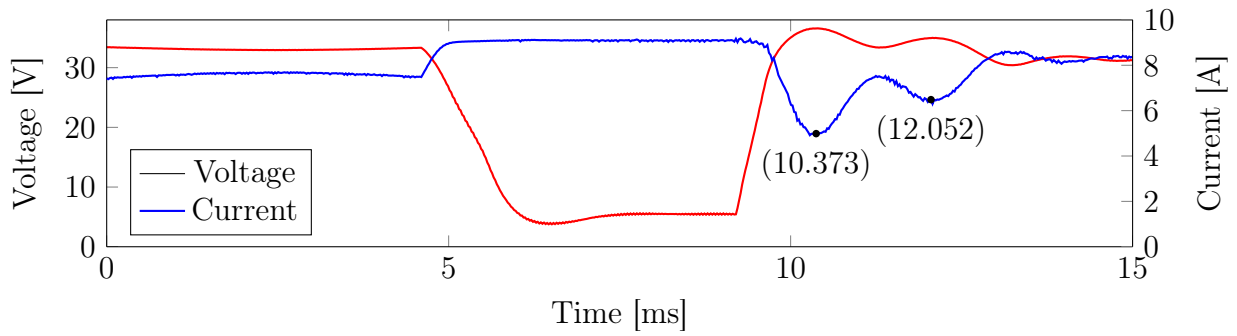
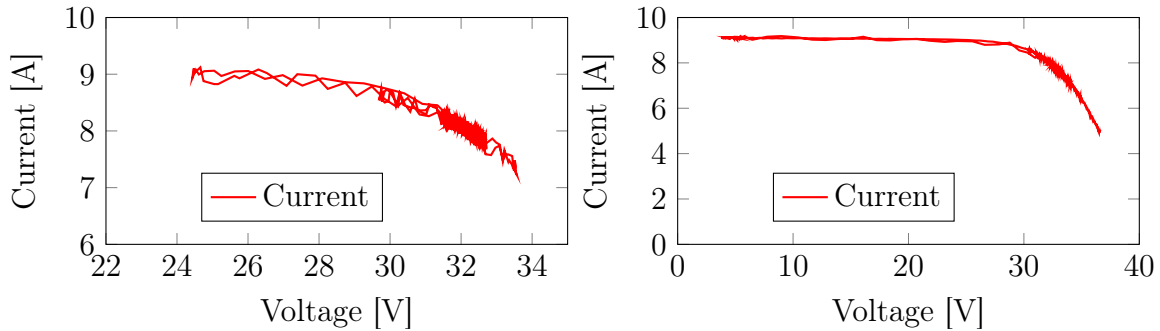
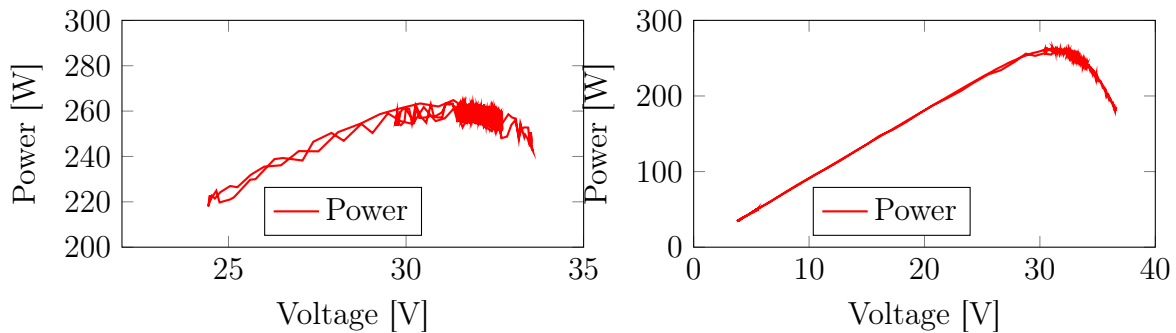


Figure 7.23: MD2 (Day 1) - Point A, current and voltage waveforms with L-LC perturbation



(a) MD1 (Day 1) - Point A, I-V curve with LC perturbation (b) MD2 (Day 1) - Point A, I-V curve with L-LC perturbation

Figure 7.24: MD1-2 (Day 1) - Point A, I-V curve waveforms



(a) MD1 (Day 1) - Point A, P-V curve with LC perturbation (b) MD2 (Day 1) - Point A, P-V curve with L-LC perturbation

Figure 7.25: MD1-2 (Day 1) - Point A, P-V curve waveforms

because the L-LC approach has greater oscillation intensity. Both these I-V curve waveforms conform to what was discovered in the simulation results shown in Section 4.3.3.

Figures 7.26, 7.27, 7.29 and 7.30 illustrate the P-V curves for each monitoring device during morning shade at point B shown in Figure 7.3.

Previously it was mentioned that the SMA inverter may have not been capable of tracking the GMPP during morning shade because the PV array output voltage is close to the limits of the inverter input and further experiments may be needed before making any remarks on the inverter capabilities. It should also be noted that MD1 receives sunlight first and thereafter MD2 and so forth. Figure 7.26 shows how the LC perturbation fails to track the MPP and reaches a peak power value of 124 W. Figure 7.27 shows how the L-LC perturbation

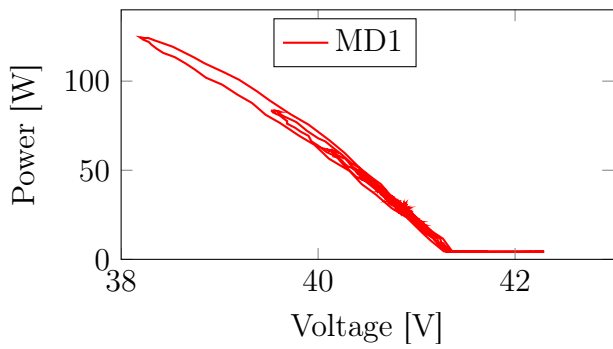


Figure 7.26: MD1 (Day 2) - Point B, during morning shade applying LC perturbation

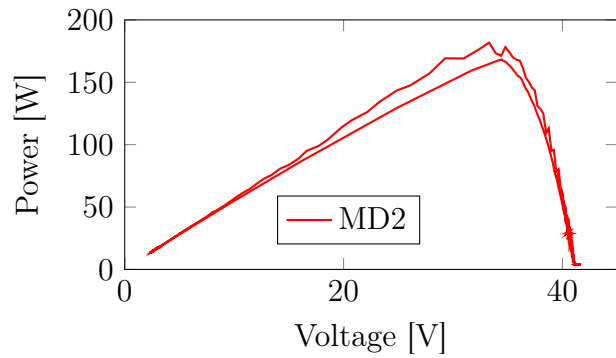


Figure 7.27: MD2 (Day 2) - Point B, during morning shade applying L-LC perturbation

Figure 7.28: MD1-2 (Day 1) - Point B, P-V curve waveforms

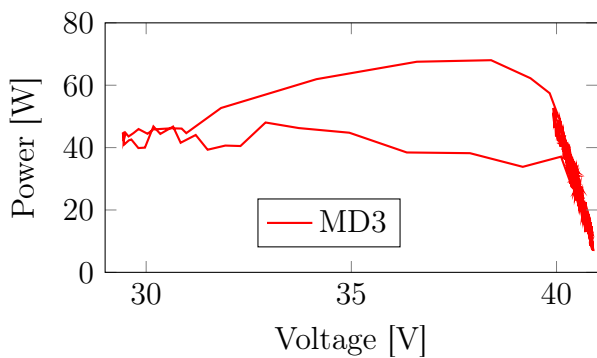


Figure 7.29: MD3 (Day 2) - Point B, during morning shade applying LC perturbation

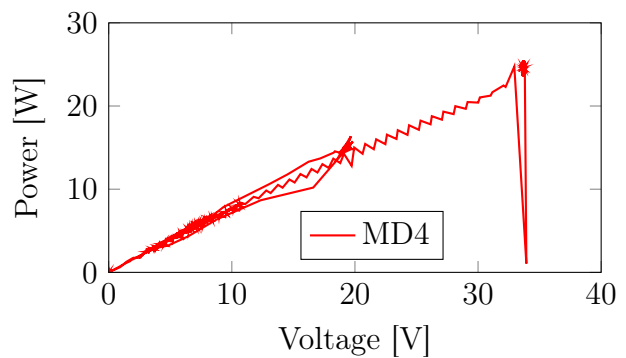


Figure 7.30: MD4 (Day 2) - Point B, during morning shade applying L-LC perturbation

Figure 7.31: MD3-4 (Day 2) - Point B, P-V curve waveforms

tracks the MPP with a value of around 181 W. Similarly MD3 (LC perturbation technique) in Figure 7.29, tracks the MPP with a value of 68 W. MD4 (L-LC perturbation technique) shown in Figure 7.30, is inconclusive as to whether the MPP has been reached and peak power value of 25 W. Figures A.6 and A.7 illustrate the morning shade and the MDs show that PV modules 1,2 and 3 are all pulled by PV module 4, which is completely shaded. The perturbation techniques also show that PV module 4 is shaded while PV modules 1,2 and 3 are partially shaded. Table 7.5 shows the amount of excess power available during morning shade conditions.

Table 7.5: MD1-4 (Day 2) - Point B, morning shade overview, extracted from Figure 7.3

PV module average power	C-OP [W]	P-PP [W]	E-OP [W]
MD1	29.87	124.57	31.99
MD2	29.94	181.79	33.52
MD3	34.10	68.02	35.54
MD4	25.51	24.74	28.40

From Table 7.5, a significant amount of excess power is available during morning shading conditions. MD2 (L-LC perturbation technique) shows a 150 W of power available and the same can be assumed for MD1 since the LC perturbation failed to track the MPP. Therefore,

the MD's provided sufficient information to assist in identify a PSC, how much extra power is available and which PV modules are shaded.

As previously mentioned a fault occurred during the monitoring duration, where MD2 had a faulty cable connection and the entire PV array was disconnected from the grid-tie inverter. The P-V curves for all four PV modules are shown in Figure 7.32.

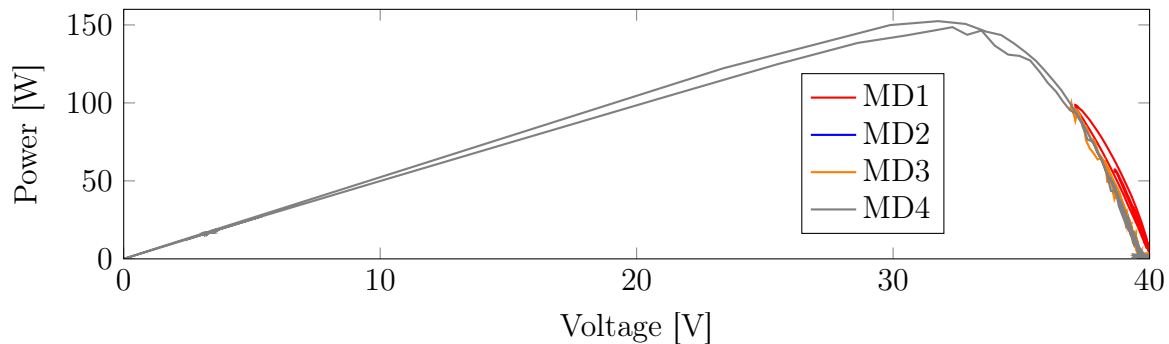


Figure 7.32: MD1-4 (Day 2) - Point D, P-V curve waveforms

From Figure 7.32 it can be seen that there is no P-V curve present for MD2. MD1 and 3 show part of the P-V curve because the LC perturbation technique is used. MD4 uses the L-LC perturbation technique and therefore the full P-V curve is present. This information identified the fault PV module and with zero readings it can further be concluded that the fault occurred between the PV module 2 and the MD2 because, the perturbation reading is also zero, as shown in Table 7.6.

Table 7.6: MD1-4 (Day 2) - point D, fault condition, extracted from Figure 7.32

PV module average power	C-OP [W]	P-PP [W]	E-OP [W]
MD1	4.17	103.15	4.16
MD2	0.00	0.01	0.00
MD3	2.98	103.493	4.43
MD4	1.81	202.86	4.17

As previously mentioned, point E in Figure 7.3, two deliberate partial shading tests were performed on PV modules 1 and 2. These tests included vertically shading (PSC1) half of PV module 1 at 15:15 as illustrated in Figure 7.6. Thereafter, shading (PSC2) half of PV module 1 and 2 at 15:20 as shown in Figure 7.7. These partial shading conditions were deliberately introduced to determine whether the perturbation techniques could identify a mismatch. Figure 7.3 illustrates the significant power loss due to the effects of PSC on the PV array, when only two PV module are shaded. Although, the unshaded PV module are not operating at MPP, the shaded PV modules alter the operating point of the PV array, effecting the overall contribution of power from each PV module. Figure 7.33 illustrates the P-V curve of first PSC condition by covering nearly half of PV module 1 and Figure 7.34 illustrates the P-V curve of the second PSC condition by covering half of PV modules 1 and 2. Table 7.7 shows the current operating point (C-OP), perturbation peak power (P-PP) and equilibrium operating point (E-OP).

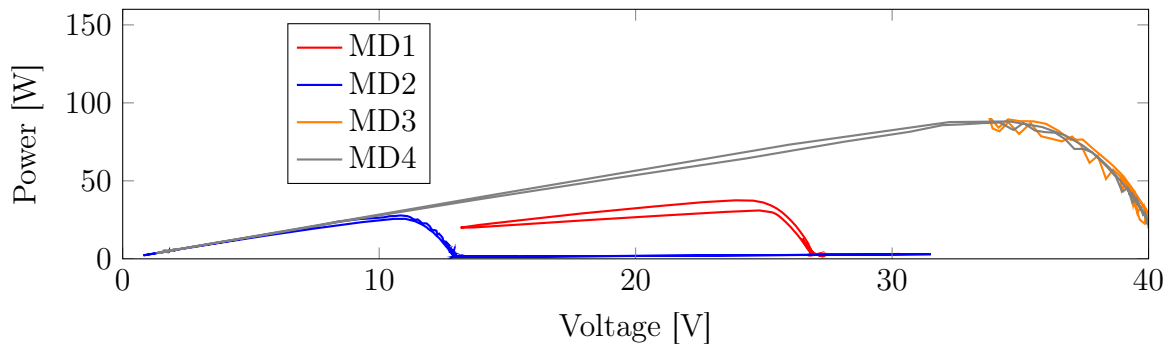


Figure 7.33: MD1-4 (Day 2) - Point E, P-V curve waveforms for PSC on PV module 1

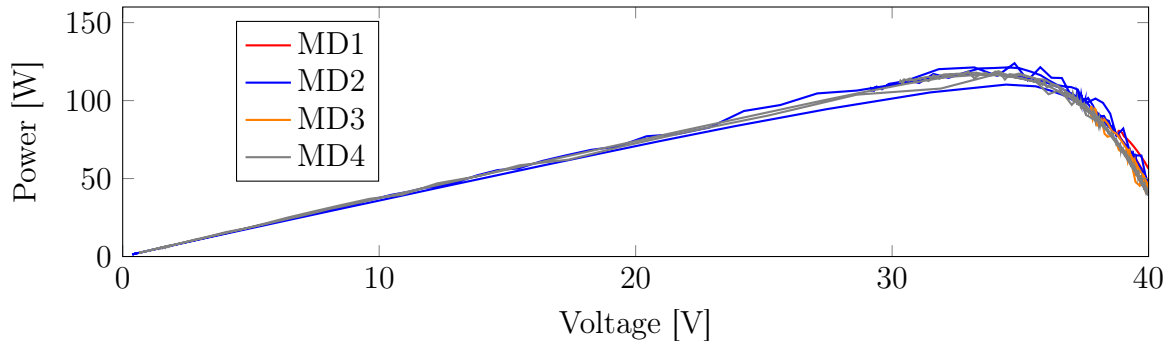


Figure 7.34: MD1-4 (Day 2) - Point E, P-V curve waveforms for PSC on PV module 1 and 2

Table 7.7: MD1-4 (Day 2) - Point E, P-V curve waveforms for both PSC experiments, extracted from Figure 7.33 and 7.34

PV module power (PSC 1)	C-OP [W]	P-PP [W]	E-OP [W]
MD1	2.79	37.52	2.80
MD2	1.24	27.81	1.28
MD3	3.04	89.63	3.11
MD4	1.83	88.11	3.87
PV module power (PSC 2)	C-OP [W]	P-PP [W]	E-OP [W]
MD1	4.28	80.63	4.28
MD2	3.89	123.95	14.08
MD3	25.45	96.43	25.63
MD4	0.62	118.85	13.83

From Table 7.7 both PSC reduced the PV array power significantly and the perturbation peak power shows how much extra is available. In particular, PV modules 3 and 4 which are not shaded. The PSC conditions was performed on a cloudy day and the 4 PV modules just meet the inverter input power. It may be that during the PSC test the inverter may have not had sufficient power to operate. Nevertheless, by referring to the perturbation peak power for the first PSC, it can easily be identified that PV modules 1 and 2 are shaded. PSC condition 2, is difficult to conclude because the LC perturbation lacks in finding the MPP. MD2 shows more power than MD4, which was not shaded. Therefore, no further remarks will be made on this test besides the fact that the PV array is not operating at the MPP, due to the shading.

7.8 Summary of results

7.8.1 Overview

The summary of the PV monitoring and perturbation results are presented in this section. Figure 7.35 displays a summary of the experiments and the effectiveness of the perturbation technique in tracking the MPP.

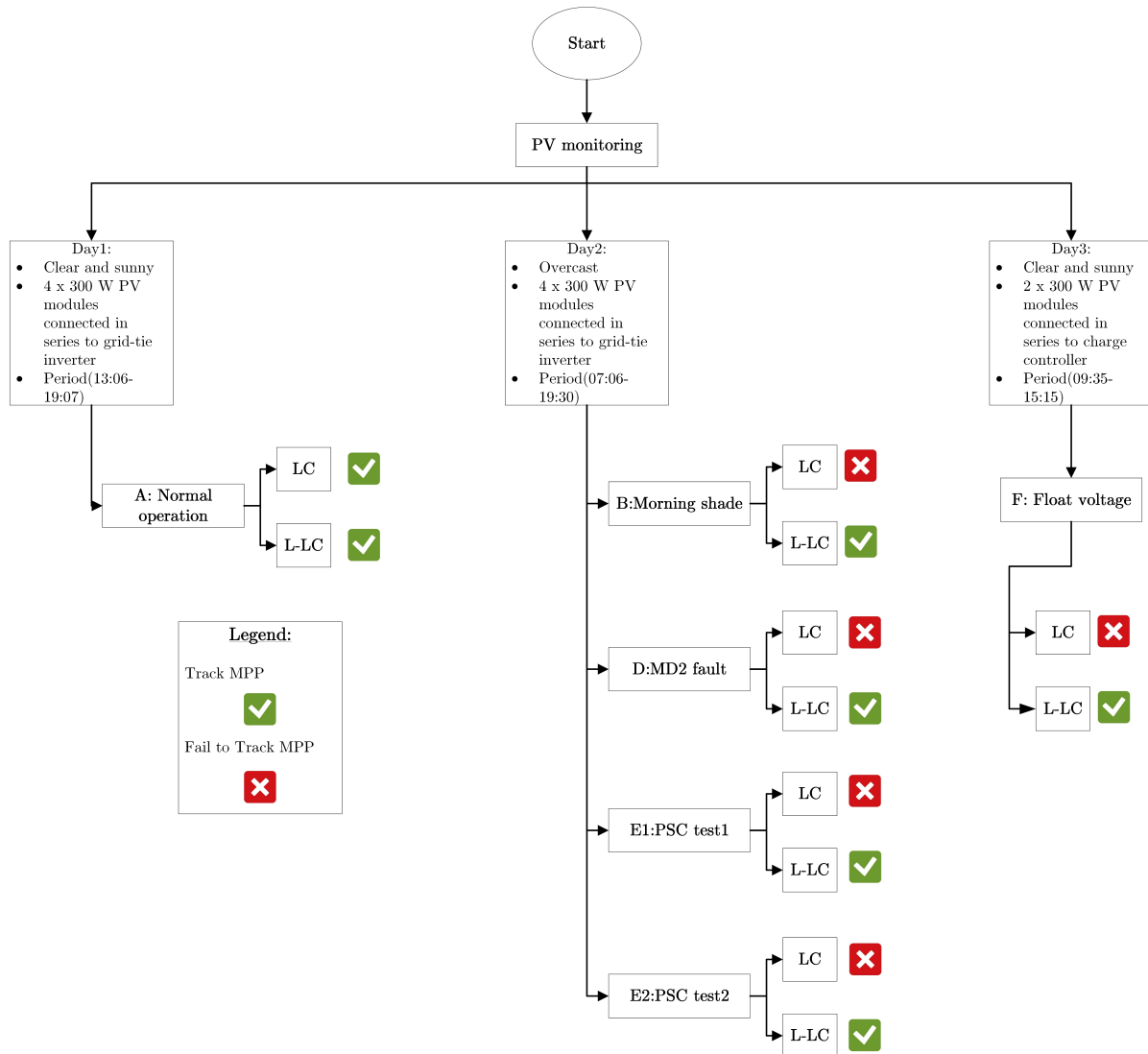


Figure 7.35: Summary of perturbation technique in tracking MPP for the experimental setup

Figure 7.35 illustrates how dominant the L-LC perturbation technique is in tracking the MPP for various operating points on the I-V curve of the PV module. The LC perturbation technique is only successful when the PV module operating point is near the MPP.

7.8.2 Monitoring device

The monitoring device captured the PV module back-plate temperature readings successfully, along simultaneous voltage and current readings, with accuracy well below the IEC 61724 [47] standards of 1 %. The monitoring device was also successful in capturing sufficient samples for the two perturbation techniques and transferring of the data wirelessly via IEEE 802.15.4 to the DAD. The DAD TCP socket was successfully used for communication with end users

and then storing the sampled data on an online database. Figure 7.18 current illustrates that the MD hardware cannot measure currents below 0 A caused by the perturbation. As mentioned in Section 2.2.1, the PV module uses bypass diodes to ensure that current always flows out of the PV module. Thus, the perturbation techniques does not affect the PV module by negative currents.

7.8.3 Perturbation techniques

The two perturbation techniques was introduced in Chapter 4, along with the simulation results. Chapter 7 displays the experimental results of the perturbation techniques. The outcome of both results are discussed in this section to verify which perturbation techniques track the PV module MPP effectively. The simulated results concluded that the L-LC outperforms the LC perturbation technique. Similarly as displayed in Figure 7.35, the L-LC perturbation technique also outperformance the LC perturbation technique. A comparison between the simulated and experimental waveforms of the perturbation techniques are of interest.

The first perturbation waveforms for both the LC and L-LC approach is shown in Figures 7.18 and 7.19, which is represented by point F in Figure 7.4. At this point the PV array is at float voltage and therefore the PV array is not operating at MPP. From Figure 7.18, the perturbation period is calculates as 1.909 ms by subtracting the two dots, which is within the 1.8 -2 ms desired period. The transformer-less inverter as mentioned in Section 4.2.1, provides no isolation between the DC and AC components. The lack of isolation causes half of the grid voltage to occur on the PV array, at times making it difficult to determine the period of the L-LC perturbation, as shown in Figure 7.19. However, Figure 7.23 applies the L-LC perturbation at point A shown in Figure 7.4. The perturbation period is calculated as 1.679 ms by subtracting the time between the two dots, which is below the 1.8-2 ms designed period. The LC perturbation period shown in Figure 7.22 is calculated as 1.932 ms, by subtracting the two dots. The perturbation period for the LC perturbation is within desired range. By comparing the LC perturbation period of charge controller with the grid-tie inverter, gives an indication if the transformer-less inverter increases the occurrence of stray inductors and capacitors. A difference of 23 μ s is identified, which is one sampling point difference. Therefore, by comparing the charge controller and grid-tie inverter LC perturbation periods the influence of parasitic impedances cause by the transformer-less inverter is negligible.

Chapter 8

Conclusions and Recommendations

8.1 Introduction

This chapter discusses a summary of the research presented in this thesis. Reflections are made on each chapters findings. Thereafter, an evaluation of the thesis and recommendations are presented.

8.2 Chapter reflections

8.2.1 Chapter 1:

This chapter discusses the global efforts and the strive towards sustainable alternative energy solutions through government incentives and policies, which lead to the motivation behind the research presented in this thesis. This is then followed by the research questions, objectives, tasks, hypotheses, scope and limitations.

8.2.2 Chapter 2:

This chapter presented a background study for the content presented in the thesis, initially discussing the characteristic of PV cells and causes of energy loss. Then moving towards investigating current methods and products in the industry that reduce low energy yields associated with the DC side of PV systems. This then proceeds to the need for monitoring in PV systems and the current PV monitoring approaches. A focus on PV module level monitoring approaches in literature was of interest and it was discovered that improving the level of granularity in PV monitoring is required to effectively manage PV systems. It was further discovered, that the PV monitoring system selection is generally dependent on the feed-in tariff. A discussion on the Internet of Things (IoT) are presented to discuss embedded devices being able to access the internet and allowing the low cost development of monitoring solutions. Lastly, the natural and step response of RLC circuits are discussed for introducing the theory behind the perturbation device.

8.2.3 Chapter 3:

In this chapter the hardware and software design of the monitoring device is presented in detail, along with additional information provided in Appendix B. The hardware design involves temperature and simultaneous voltage and current measurements, along with PCB design layout and hardware selection. The software setup includes the programming of all communications, mediums and protocols used. These include the wireless IEEE 802.15.4,

wired USART and SPI communication. Programming is further required for the sampling of measurements. The monitoring device conformed to guidelines of the IEC 61724 standard [47] and the calibration process is presented in Section E.

8.2.4 Chapter 4:

The theory and design of the perturbation techniques are presented in this chapter. Followed by the perturbation simulation setup, results and evaluation of the results. This chapter then ends off with the hardware design of the perturbation devices and topology.

8.2.5 Chapter 5:

This chapter is dedicated to the data Acquisition Device (DAD) starting with an overview of the DAD and its objective. A description of the ESP32 hardware capabilities and features are discussed. Followed by a detailed software design and the data retrieval overview.

8.2.6 Chapter 6:

The research methodology implemented at the test research facility is discussed in this section. The experimental setup is formulated to assist in answering the research questions.

8.2.7 Chapter 7:

Chapter 7 presents the results and analysis. The chapter begins with raw data validation process that takes the necessary procedures to ensure data uncertainty is minimised. This is followed by the data acquisition process and discussions on data synchronization. A discussion on problems encountered during the data acquisition process are presented. The data filtering is presented to formulate a dataset for data analysis to commence. This is presented by the results and discussion thereof.

8.3 Thesis evaluation

The thesis evaluation presents discussions on the final summary on whether the research objectives were met, tasks completed and questions were answered.

8.3.1 Research tasks evaluation

The research tasks were successfully implemented by designing and building a monitoring device for PV module level monitoring with a technology readiness of level 6. Along with the monitoring device, a perturbation device was also successfully designed and built to deviate a PV module's current operating point without affecting the PV array operation. At the same time the perturbation device can determine whether a PV module is operating at MPP and if not how much excess power is available. This is performed using two different perturbation techniques that was investigated. The simulation and experimental results show that the L-LC perturbation approach is the preferred approach in tracking the PV module MPP from various operating points on the I-V curve. A data acquisition device was designed and incorporated onto one monitoring device to acquire the sampled data from the rest of the monitoring devices. This data was acquired by an end user which was successfully uploaded onto an online database, to be used for data analyses. Temporary storage is available on the data acquisition device should internet connectivity be unavailable. An existing PV

structure was utilised for the experimental testing, along with installing a WiFi network to communicate with the data acquisition device, which was configured correctly for its intended purpose.

8.3.2 Research objectives and question evaluation

The monitoring device successfully monitored field-exposed PV modules by simultaneously measuring the voltage and current, along with back-plate temperature measurements. The back-plate temperature measurements were not needed in answering the research questions. However, PV module temperature measurements can assist in energy yield forecasting in PV systems and the detection of PV module hotspots as mentioned in Chapter 2. During the experimental setup the temperature measurements were recorded and an illustration is shown in Figure 7.1. Real-time voltage and current measurements were successfully captured from exposed PV modules using the designed monitoring device, over an experimental period of 3 days. The testing duration provided sufficient information to analyse the effects of the perturbation techniques and determine whether a PV module is operating at MPP. The simulation and experimental results show that the L-LC perturbation technique is the most effective in tracking the PV module MPP from different operating points of the PV module on the I-V curve. The LC perturbation at times fails to track the MPP because the LC technique only reaches a peak-power value, implying that there could still be additional energy available.

In summary, the L-LC perturbation technique can identify if a PV module is operating at MPP and if not, showing the amount of extra power available. Partial shading conditions on the PV array, defective and faulty PV modules can also be identified by the L-LC perturbation technique. The real-time PV monitoring interval of the MD can be altered to a shorter or longer interval. This flexibility immediately allows the PV plant operators to identify underperforming or defective PV modules at a set period, which assists in better PV plant management and reduction of O&M costs.

8.4 Recommendations

Recommendations are made by the author for future development research with the work discussed in this thesis.

- A super capacitive power supply topology implementation as presented by Guerrio [68] should be implemented to reduce the PCB layout area taken up by the lithium-ion battery and PSU. This implementation also mitigates the need for the 3.3 V switching power supply, reducing noise in the circuit which improves conditions for the measurement circuitry. In essence, reducing three power supplies with the current configuration to one.
- Investigation using LORA will mitigate the need for a coordinator or multiple coordinators/routers for a large PV plant
- Investigate how much faster the perturbation can be in order to use even smaller RLC components and also taking into account the influences of stray inductances and capacitance.
- Cheaper and lower resolution ADC should be investigated.

- A proposed isolation relay between MD circuitry and PB while measuring to ensure isolation of external influences during a perturbation.
- Program the ESP32 to send sample data directly to online SQL database.
- Smart monitoring suggestion, the MD's provide sufficient feedback for the inverter to track the MPP optimally.

Appendices

Appendix A

Research test facility

The research test facility is situated at Stellenbosch University Electrical and Electronic (EE) Engineering Department, Coordinates: -33.928219,18.867139. A structure simulating a pitched roof top is situated on the roof top of the EE department building. This structure contains the PV modules used during the testing, the roof is pitched at 30° that is north facing. Electrical boxes to store the MPPT charge controller, grid-tie inverter hardware, network switch and connectivity, power outlets, and much more multi-purpose uses.

A.1 Infrastructure

The research test facility was developed by the researcher in a previous project and modified slightly to meet the requirements for this dissertation, the required items used are listed in Table A.1 below.

Item	Item
2 x Orange metal enclosures	4 x 300W PV modules
rooftop structure	PVC piping
2 x 12 V Batteries	1 x MPPT charge controllers
network server	1x outdoor wi-fi router
SMA 1.6 KW grid-tie inverter	network switch

Table A.1: Research test facility infrastructure.

The orange boxes was used for multiple purposes, the majority serving as a power point, network point, hardware storage space for both the grid-tie inverter and charge controller. The 12 V batteries were stored in a secure plastic box elevated from the floor to prevent water damage. The outdoor WiFi AP was mounted to the structure - consisted of an TP-Link 2.4GHz antenna and powered by a Mikrotik Groove 52 HPn 2.4/5.8GHz radio, running RouterOS. All power cabling were protected using sufficient PV piping.



Figure A.1: Research test facility.



Figure A.2: Experimental set up, circuit breakers, grid-tie inverter and charge controller



Figure A.3: Outdoor WiFi AP for the DAD ESP32



Figure A.4: 4 x 300 W Renesola PV modules.



Figure A.5: MD set up for the experimental results



Figure A.6: Morning shade cause by surrounding buildings



Figure A.7: Morning shade cause by surrounding objects

A.1.1 Network configuration

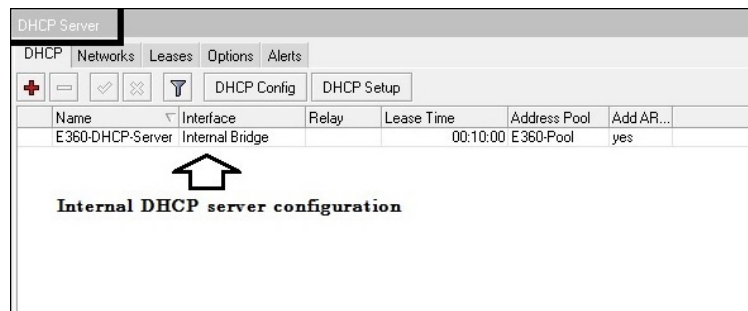
A network is vital for the TCP socket communication to operate. Therefore, this network requires a WiFi access point (AP) to communicate with the ESP32 module. A separate internal network was created for this purpose using a spare lab computer with two network cards. The first card was used for the internal network and a Ethernet cable was connected between the internal network and the outdoor WiFi AP. The second network card was used to connect to the university network and provides the communication link to the internet (external network). The lab computer utilised the Windows operating system running Mikrotik RouterOS in a virtual machine. RouterOS is an advanced routing software with the necessary features required to configure the internal network, the configuration includes the following setting:

- DHCP (Dynamic Host Configuration Protocol) server
- DNS (Domain Name System)
- Firewall
- NAT (Network Address Translation)
- Port Forwarding
- Routing

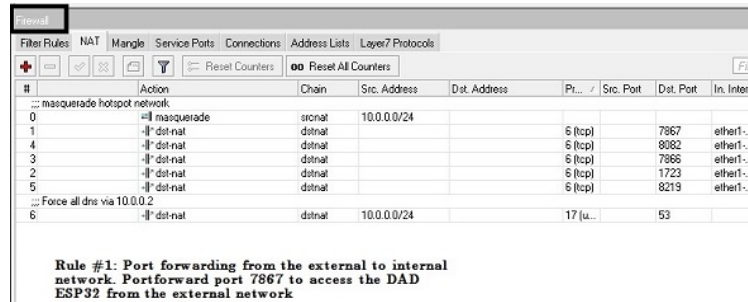
Port forwarding was used and configured on the network server to communicate from the external to internal networks. A lab PC on the external network communicated with the DAD via the server as a gateway. The DHCP server automatically assigned IP address to new clients joining the network, however IP binding was configured in order for the port forwarding to work correctly. IP binding assigns a fixed IP address to a clients based on their MAC address and the IP protocol version 4 was implemented. The DNS was configured to the external network settings, which allows all clients on the internal network to access websites or clients based on IP's. Furthermore, A firewall was configured on the internal network as an extra security measure that blocks network access to all clients with MAC address that are not registered on the server. The internal network card is connected with Ethernet cable to a unmanaged network switch, which is then also connected via Ethernet cable to the outdoor wireless AP via ethernet. Figure A.8 illustrates the internal network server configurations.

A.1.2 SMA grid-tie configuration

The minimum required input voltage to the 1.6 KW SMA grid-tie inverter is 125V and the rated voltage is 400V [102, p.48]. The PV array open circuit voltage is $4 \times 41.9 = 167.6V$ and MPP voltage should be $4 \times 33.4 = 133.6V$, which means that four 300W PV modules that are available have sufficient power for the grid-tie inverter to operate, however this may only work during non cloudy days. The orange boxes were large enough for the inverter to fit inside and also contained the PV module DC output and grid AC input cables. Appropriate circuit breakers were used in the orange boxes for both the DC and AC power cables, which provided safety, easy isolation and protection.



(a) Mikrotik Router OS DHCP server configuration



(b) Mikrotik Router OS firewall and port-forwarding configuration

Figure A.8: Internal network server setup.

A.1.3 Micro Care MPPT configuration

The Micro Care MPPT [103] was supplied power by two 300W Renesola PV modules connected in series, which the charge controller, charged two 12V deep cycle lead calcium batteries connected in series. The batteries had no load to power, however a 10A rated dump resistors was used to discharge the batteries before testing. The idea of discharging the batteries would allow the charge controller to draw the maximum power from the PV array until the batteries were fully charged and then draw sufficient power from the PV array (i.e. not the MPP) to keep the batteries charged at a floating voltage. Figure A.9, illustrates the charge cycle of the two 12 V deep cycle batteries. It should be noted that Figure A.9 was performed when there was uncertainty in the ADC readings and the graph is shown here to display the format of the charging cycle.

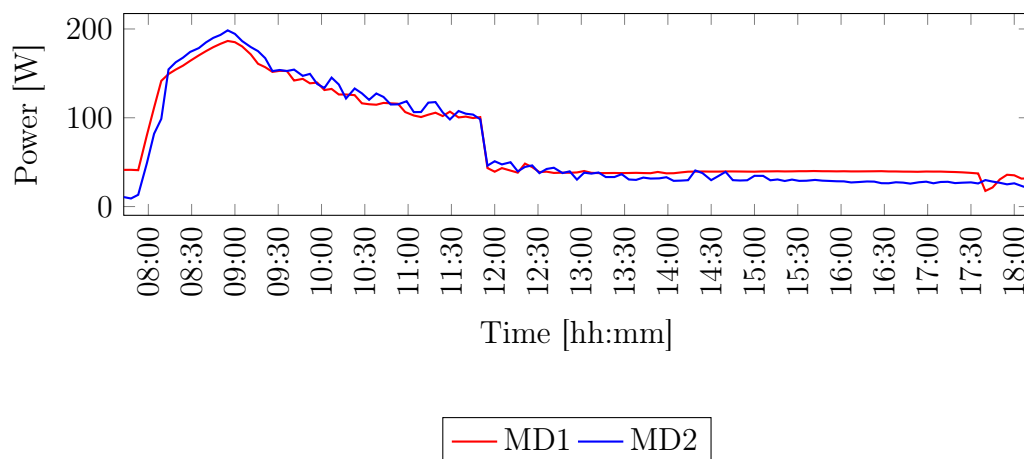


Figure A.9: MD1-2 - Daily monitoring (07:43-18:11) of the two 300 W Renesola PV module's connected to the charge controller, with inaccurate ADC readings

Appendix B

Monitoring device PCB design

B.0.1 Relevant data sheet information

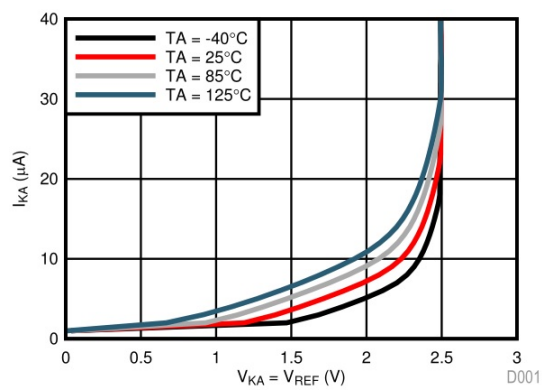


Figure B.1: ATL321 cathode current vs voltage [105]

4-WIRE OPERATION

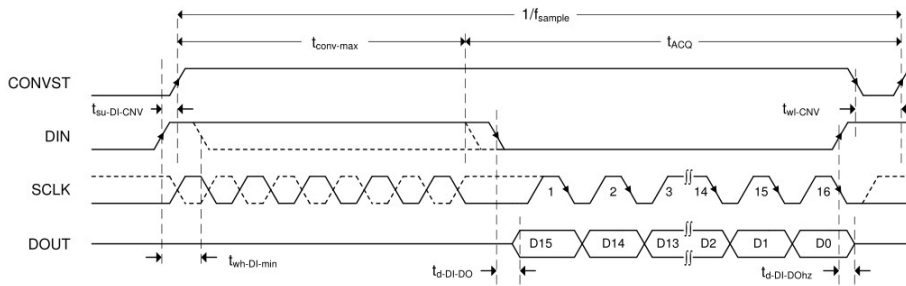


Figure 2. 4-Wire Operation: DIN Functions as Chip Select

Table 2. TIMING REQUIREMENTS: 4-Wire Operation⁽¹⁾

PARAMETER	MIN	TYP	MAX	UNIT
t_{ACQ} Acquisition time	1200			ns
t_{conv} Conversion time	500		8800	ns
$1/f_{sample}$ Time between conversions	10000			ns
t_{wh-DI} Pulse duration: DIN high	10			ns
$t_{wh-DI-CNV}$ Pulse width: CONVST low	20			ns
$t_{d-DI-DO}$ Delay time: DIN low to MSB valid			12.3	ns
$t_{d-DI-DOhz}$ Delay time: DIN high or last SCLK falling edge to DOUT 3-state			13.2	ns
$t_{su-DI-CNV}$ Setup time: DIN high to CONVST rising edge	7.5			ns
$t_{h-DI-CNV}$ Hold time: DIN high from CONVST rising edge	0			ns

Figure B.2: ADS8866 ADC 4-wire mode timing requirements [84]

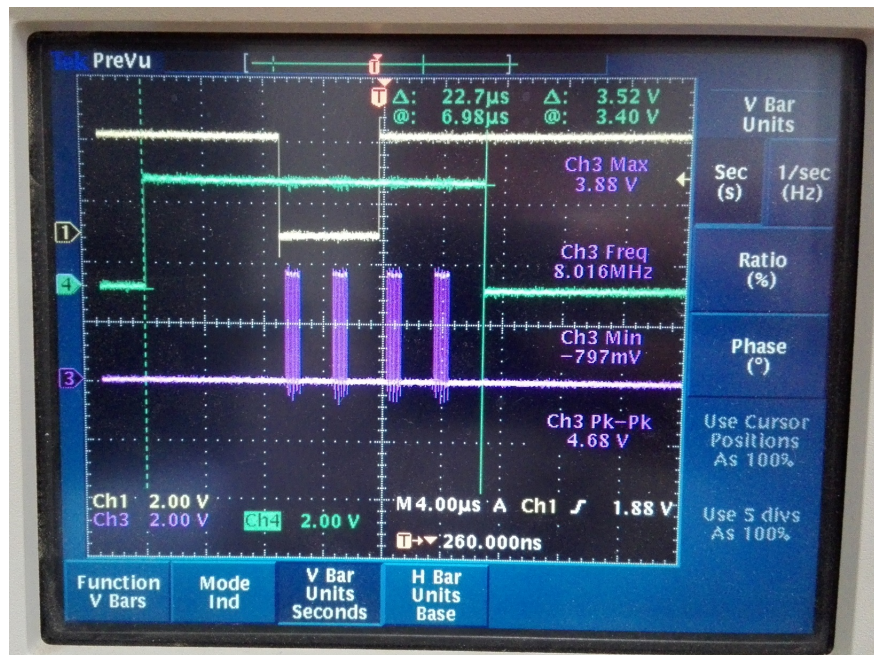


Figure B.3: ADC voltage and current sample time

Figure B.3 illustrates one sample period for both voltage and current. Channel 4 on the oscilloscope measures the CONVST (start of conversion) input to both ADC's. The time cursor is then used to measure the pulse of this signal to determine the time take per sample, which is 22.7 us per sample.

B.0.2 MD earlier versions

Figure B.4 below, shows the earlier version of the MD, which incorporated a Field-Gate Programmable Array (FPGA) and was successful in it's application.

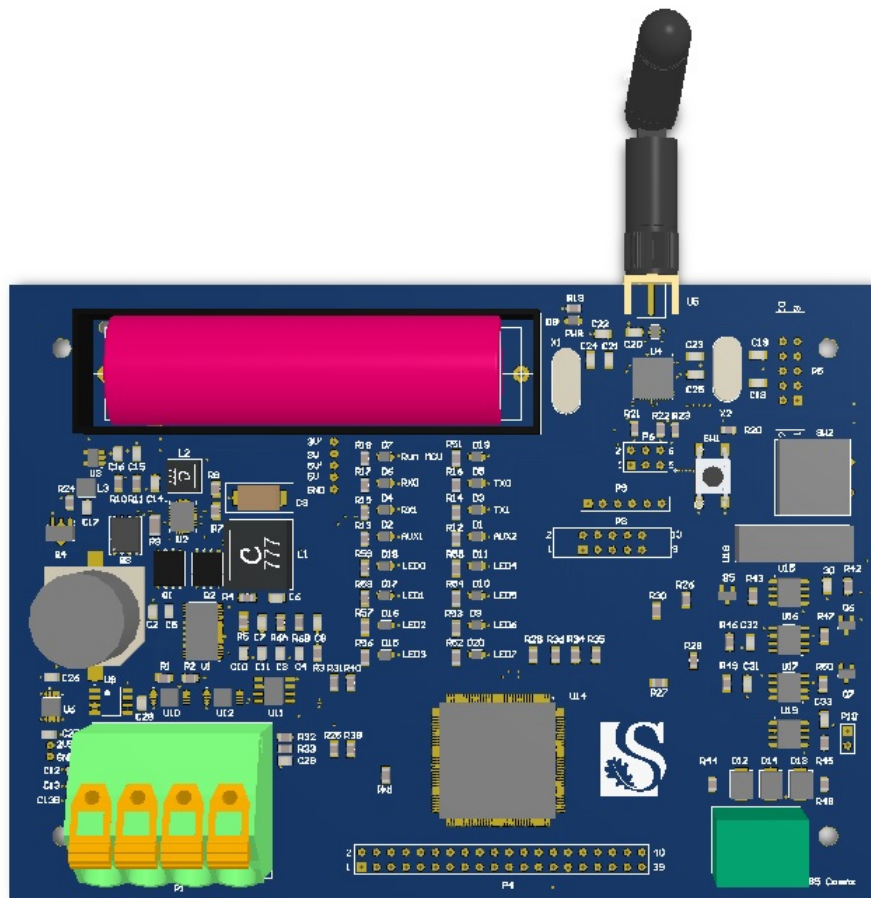


Figure B.4: Previous version of the MD PCB design 3D view

The idea behind the FPGA was to sample at the limits of the ADC, which the MCU cannot do due to the 16 MHz clock it uses. The reason for sample the ADC so quickly was to reduce the RLC circuit components size and therefore cost. At the time, the current was measured using a hall-effect current sensor with limited bandwidth and this caused a phase-shift and current spike peaks during perturbation. The current peaks may have been caused by inductance when perturbing at such high frequencies. Therefore, the simulated model may have differed from the practical implementation. For this reason it was decided to measure and perturb at a lower frequency to nearly demonstrate the proposed solution for this dissertation. At the same time, there is no ruling out that going the FPGA route and perturbing at a higher frequency could work given that the cause of the phase-shift was identified by a design oversight caused by the first stage PSU and that the current shunt method is implemented. The cost of an FPGA implementation verses larger RLC circuit component size and cost should also be kept in mind.

B.0.3 Atmel Studio

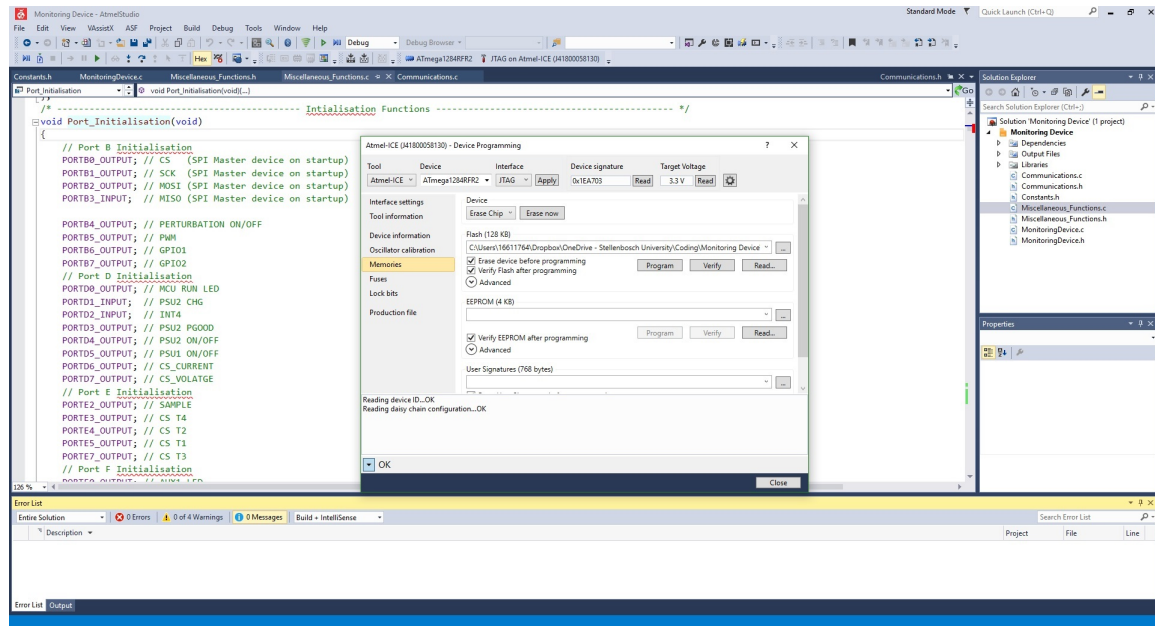
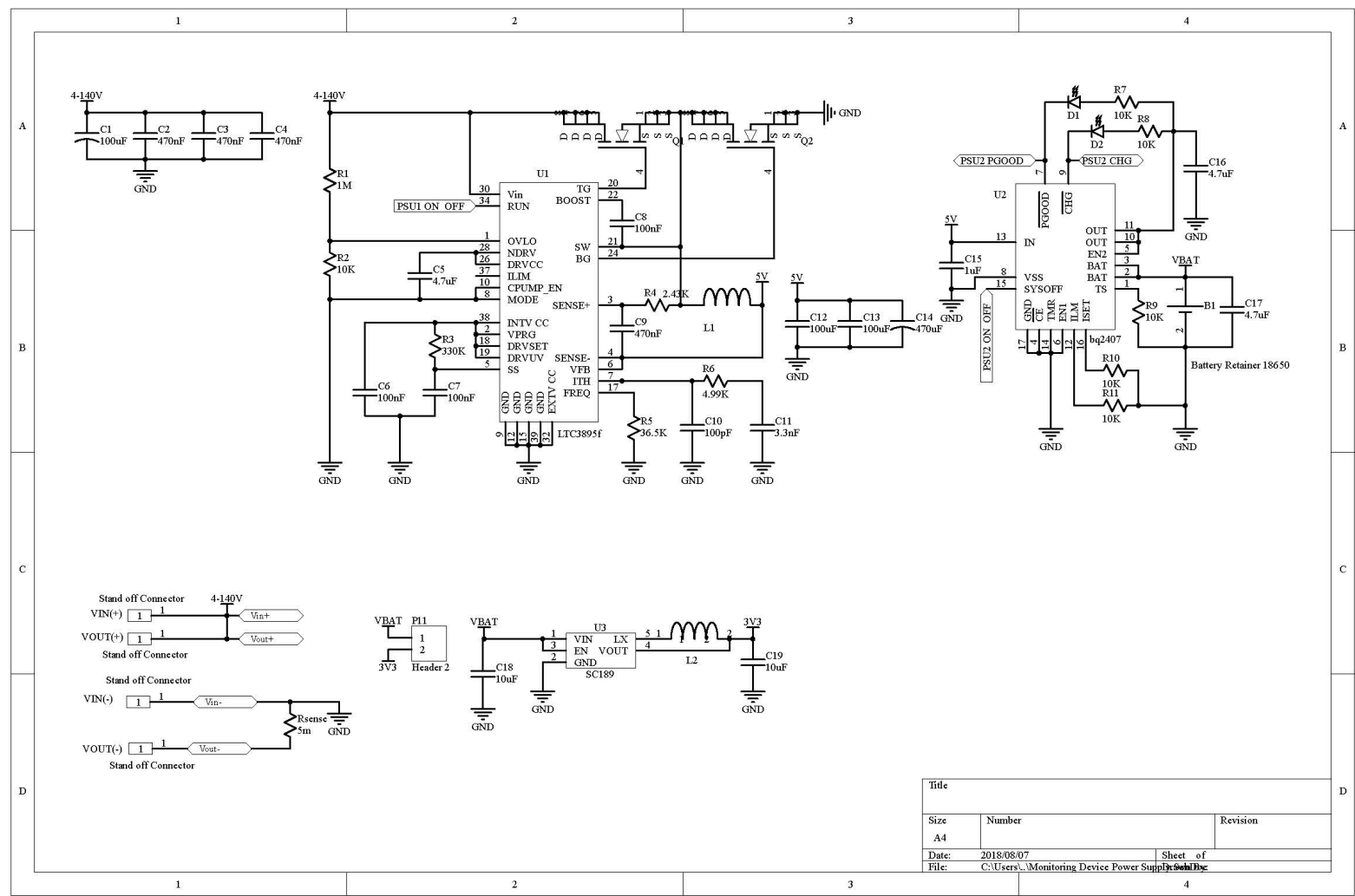


Figure B.5: Atmel Studio

Atmel studio was used to program the MD(C) in the C programming language, Figure B.5 is an illustration of the of the IDE and programming wizard.

B.0.4 MD PCB design documents



Title		
Size	Number	Revision
A4		
Date:	2018/08/07	Sheet of
File:	C:\Users\... \Monitoring Device Power Supply	Sheet Dsc

Figure B.6: MD power supply schematic

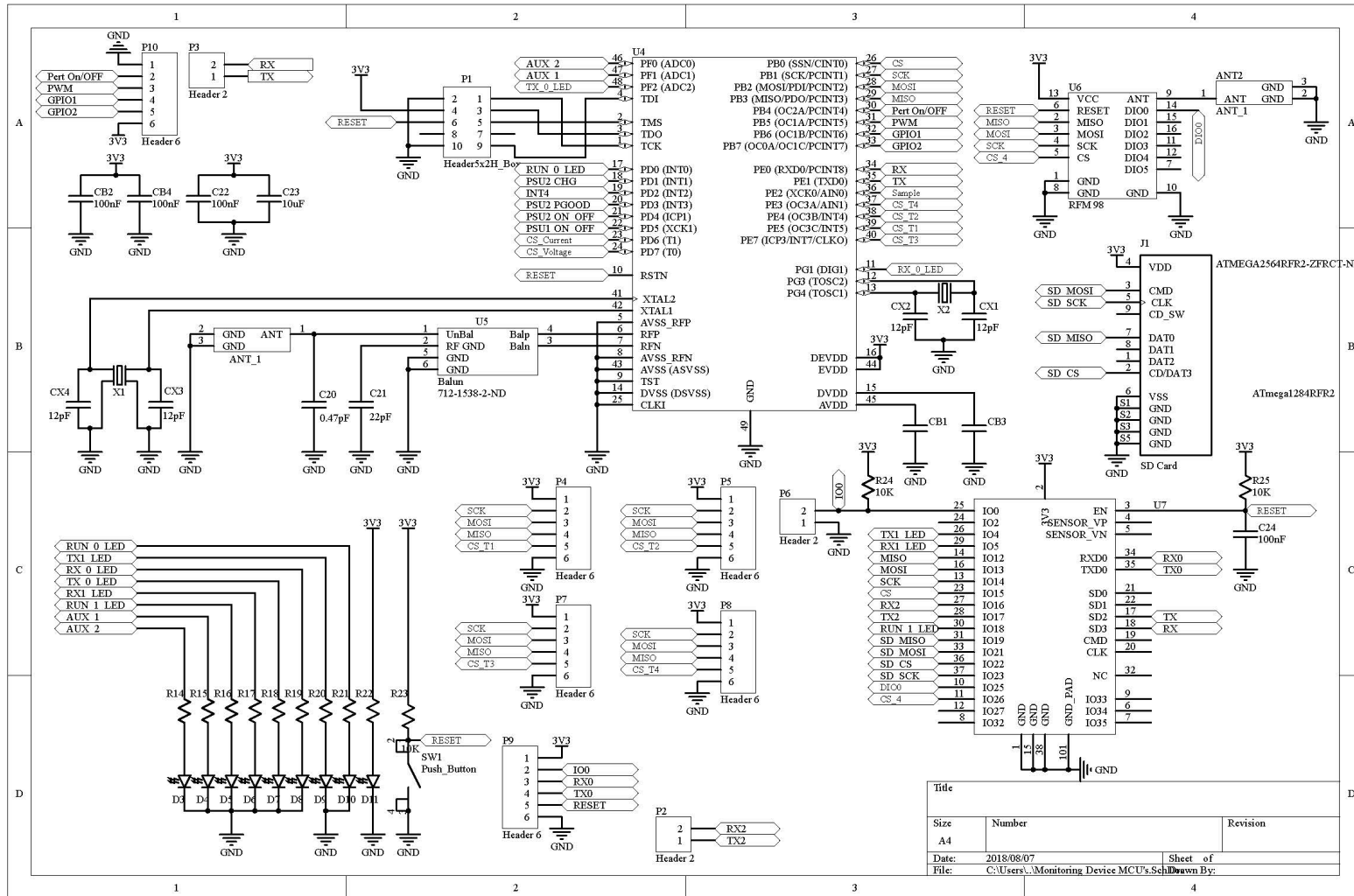


Figure B.7: MD MCU, ESP32 and RFM98 schematic

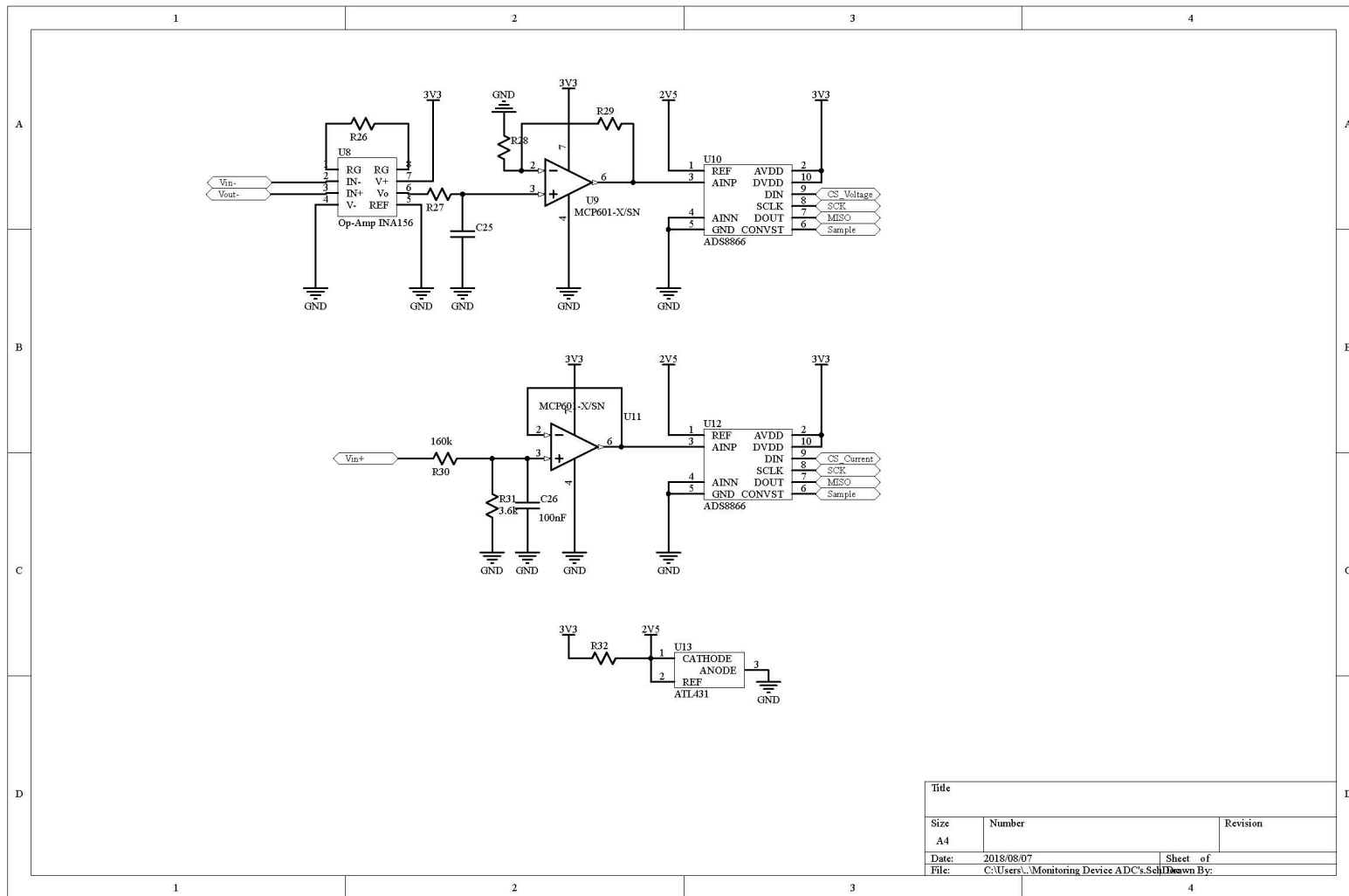


Figure B.8: MD measurement circuitry schematic

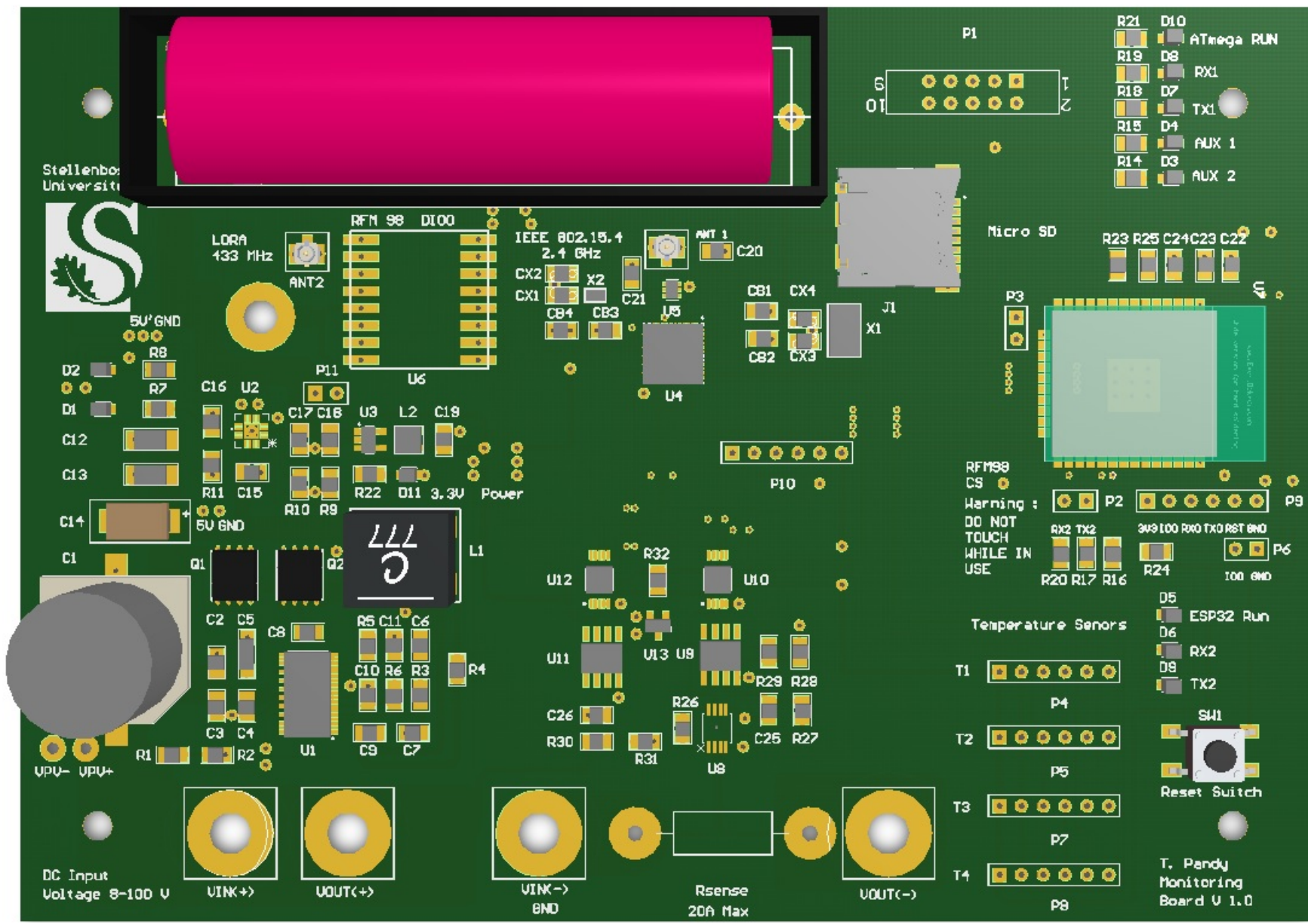


Figure B.9: MD PCB design 3D view

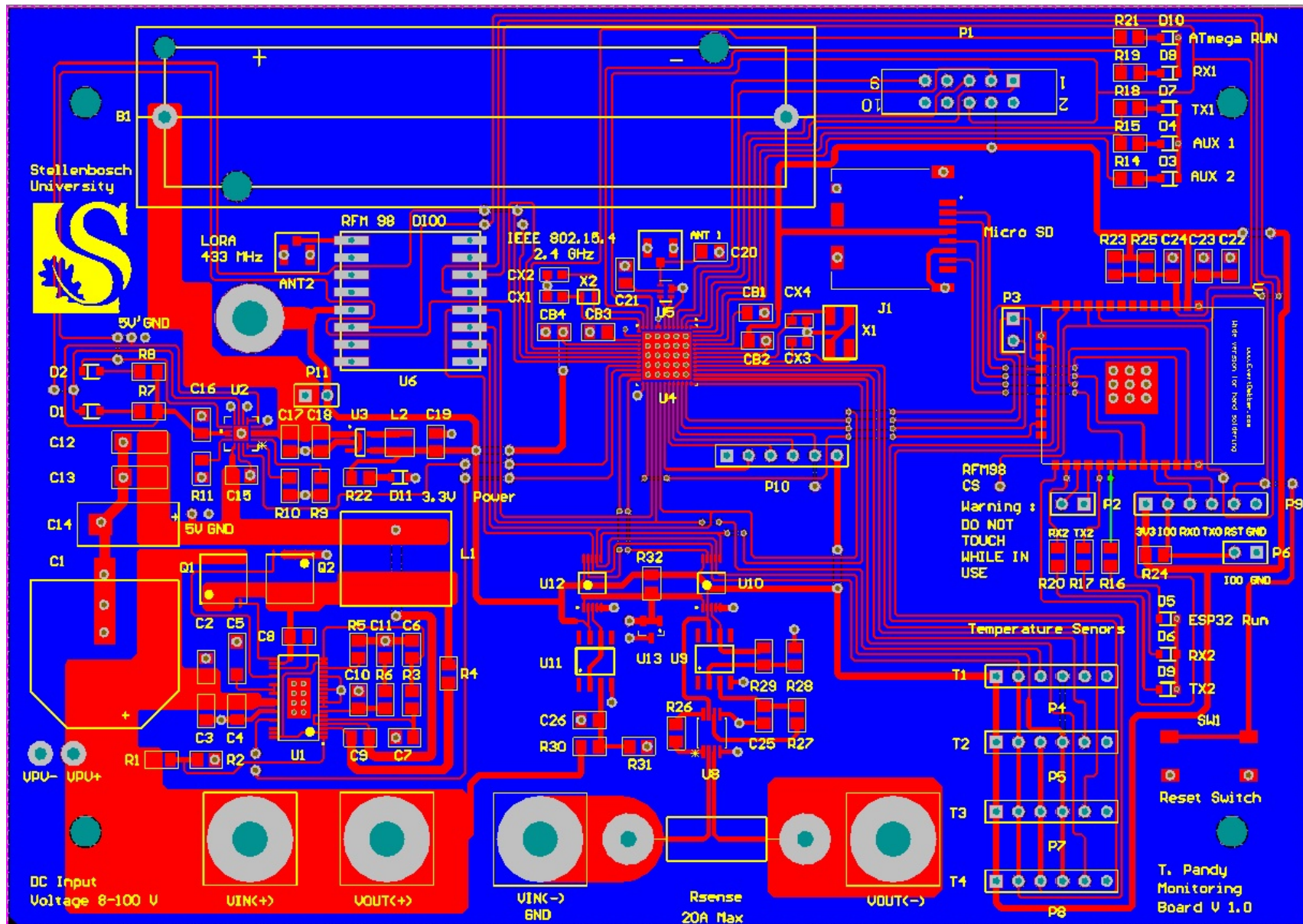


Figure B.10: MD PCB design 2D view

B.0.5 IEEE 802.15.4 RX_AACK and TX_ARET state diagrams.

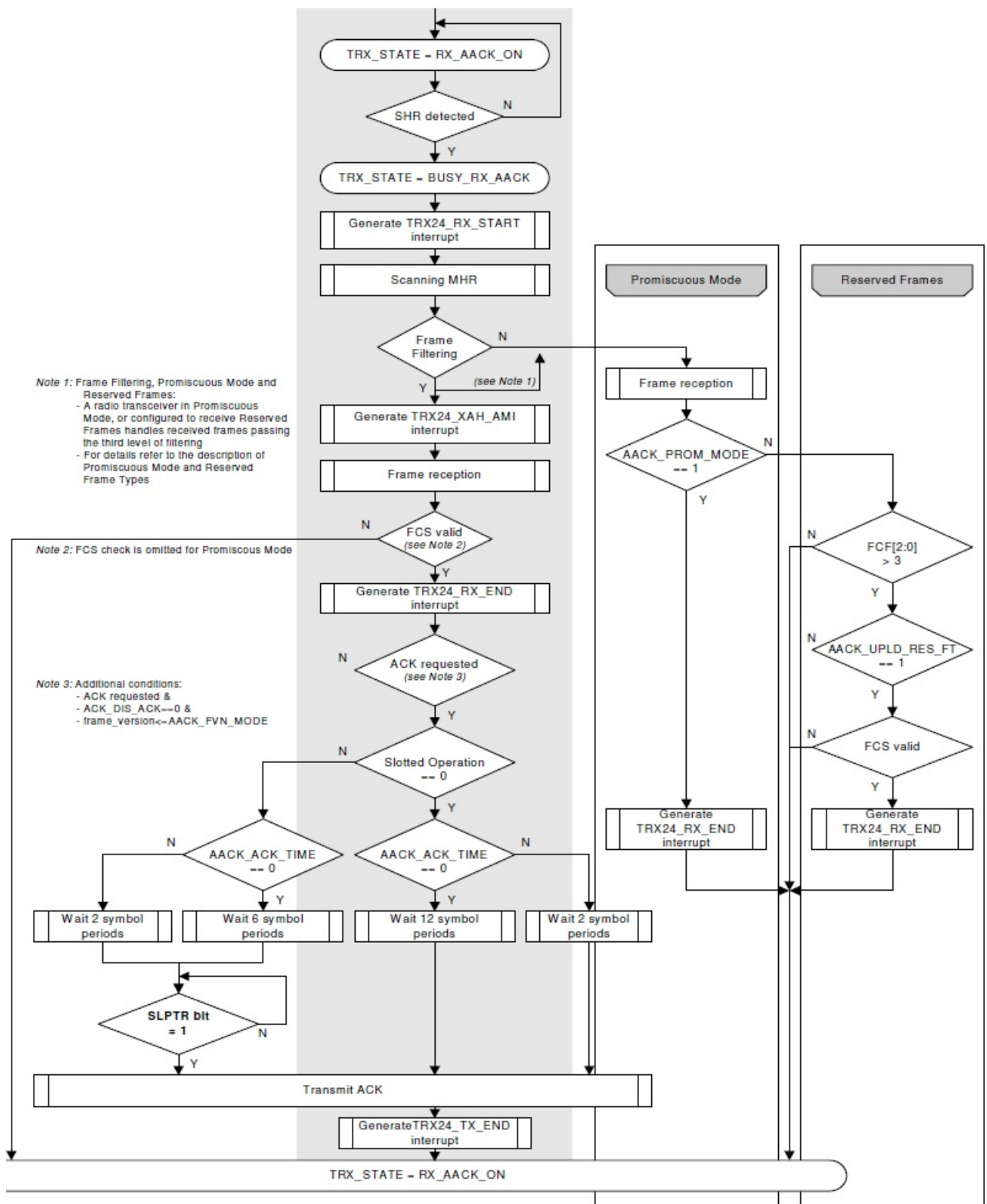


Figure B.11: MCU RX_AACK (receive) state

Appendix C

Perturbation device's PCB designs

C.0.1 PD's RLC circuits

The high side P-channel MOSFET topology used in the no storage perturbation topology allows for the NPN BJT Q_1 gate driver to be supplied power from the input voltage of the PV module. Figure 4.20 is re-shown from Section 4.4 for the readers convenience.

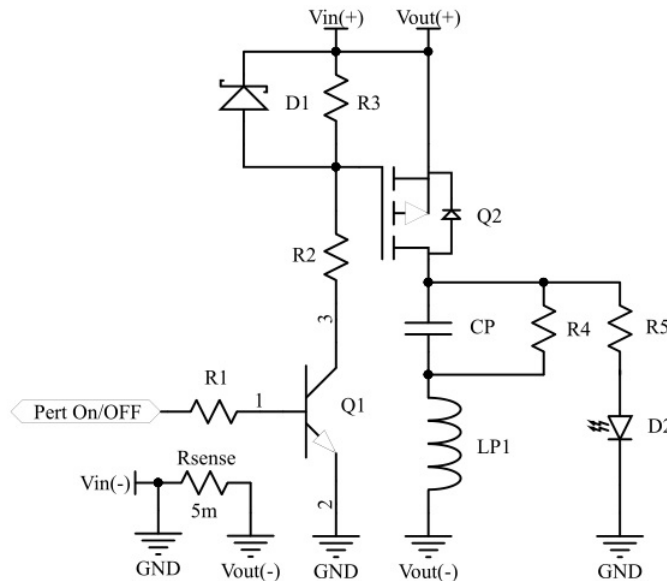


Figure C.1: Perturbation device schematic

The 1SMB5925BT3G 10 V zener diode D_1 from ON Semiconductor [106] is sufficient for protecting the source to gate voltage of Q_2 when the switching circuitry is active. The switching circuitry is active when the gate pin of Q_2 is pulled low by turning Q_1 on. During the switching on state, resistor R_3 only draws sufficient current to turn D_1 on while the rest of the current required by Q_1 flows via D_1 . At the same time D_1 protects Q_2 by clamping the source to gate voltage by 10 V. Resistor R_3 is selected at 10 K, which means that 1mA flows through R_3 in order to turn D_1 on at 10 V. Furthermore, care must be taken to ensure the current drawn by Q_1 is limited to not draw too much current from the zener diode. Thus, to reduce power consumption and heat dissipation in D_1 , Q_1 is designed to saturate (switch on) at low currents that is within the current limits of D_1 . The node voltage at the gate pin of Q_2 is given by Equation C.1.

$$V_g = V_{in} - V_{D1} \quad (\text{C.1})$$

Equations C.2 and C.3 can assist with calculating resistors R_2 and R_1 .

$$V_{GPIO} = I_B \cdot R_1 + V_{BE(on)} \quad (C.2)$$

$$V_g = I_C R_2 + V_{CE(sat)} \quad (C.3)$$

The $V_{CE(sat)}$ voltage for the BC846ALT1G NPN transistor is 0.25 V for a collector current of 10mA and $V_{BE(on)}$ of 0.7 V as given in the datasheet [107]. The collector current is chosen as 5mA which well within the limits of zener diode D_1 . The zener diode D_1 power consumption is $P_{D1} = 10V \times 5mA = 50mW$, where D_1 datasheet describes the thermal resistance from junction-to-ambient as $R_{\theta JA} = 226 [C^\circ/W]$ above ambient 25 C°. Thus, the operating temperature of D_1 is $T_{D1} = 45 C^\circ + 226 \times 50mW = 56.3 C^\circ$, which is well within the maximum operating temperature of 150 C°. It should be noted that 45 C° was chosen over 25 C° to compensate for the PCB board temperature as the PCB is designed to handle a maximum of 20 A that can cause the PCB board temperature to rise above ambient.

Thus, assuming an input voltage range of 8-50 V and $R_2 = 5.1KW$, from Equation C.2 R_1 is calculated as:

$$1 = \frac{I_C R_1}{\beta}$$

With $\beta = 50$, R_1 is calculated as 10 K Ω , however R_1 is chosen to be 1 k Ω to ensure saturation and that the transistor turns on.

C.0.2 ANSYS Simplorer

The single diode model is shown in Figure C.2. The shunt and series resistors were determined via trial and error. The parasitic capacitance is chosen as 110 nF based diode voltage and temperature discussed by [108]. The simulation electrical parameters was choose for STC conditions given in the datasheet for both Renesola PV modules. The short circuit current are given as $I_{SC(255W)} = 8.86A$ and $I_{SC(300W)} = 8.69A$ [90, 91]. Furthermore, the Renesola 255 W PV module contains 60 PV cells connected in series and the 300 W PV module contains 72 PV cells connected in series [90, 91]. The following equations below assist in determine the thermal voltage, PV cell voltage and saturation current required for the diode parameters.

$$V_{Thermal} = \frac{KT}{Q} = 0.0257 \frac{K}{C}$$

- K - is Boltzmann's constant.
- Temperature in Kelvin at 25 C°.
- Electron charge constant.

$$V_{PV(percell)} = \frac{V_{OC}}{n_{numberofPVcells}}$$

For the 255 W PV module the PV cell voltage is 0.625 V and the 300 W PV module the PV cell voltage is 0.6222 V. The scaled up thermal voltage is the thermal voltage at STC

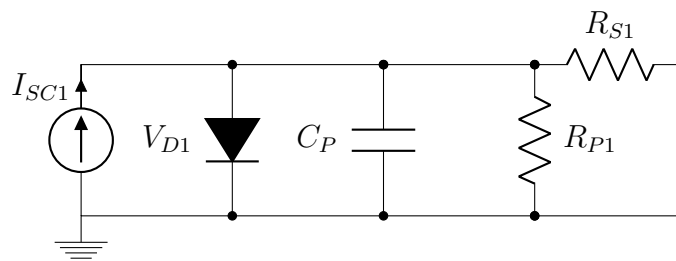


Figure C.2: Single diode model

multiplied by the number of PV cells. Therefore, the scaled diode thermal voltage for the 255 W PV module is calculated as 1.542 V and the 300 W PV module as 1.8504 V.

From Figure C.2, the PV module is at at open circuit voltage (no load), if the series and parallel resistor are ignored, then using Kirchoff's current law the following is valid:

$$0 = I_{SC} - I_0 \left(e^{\frac{qV_{PV}}{KT}} - 1 \right)$$

$$I_0 = \frac{I_{SC}}{\frac{qV_{PV}}{eKT} - 1} \tag{C.4}$$

Using Equation C.4, the 255 W PV module saturation current is 243.107 pA and the 300 W PV module saturation current is 270.856 pA.

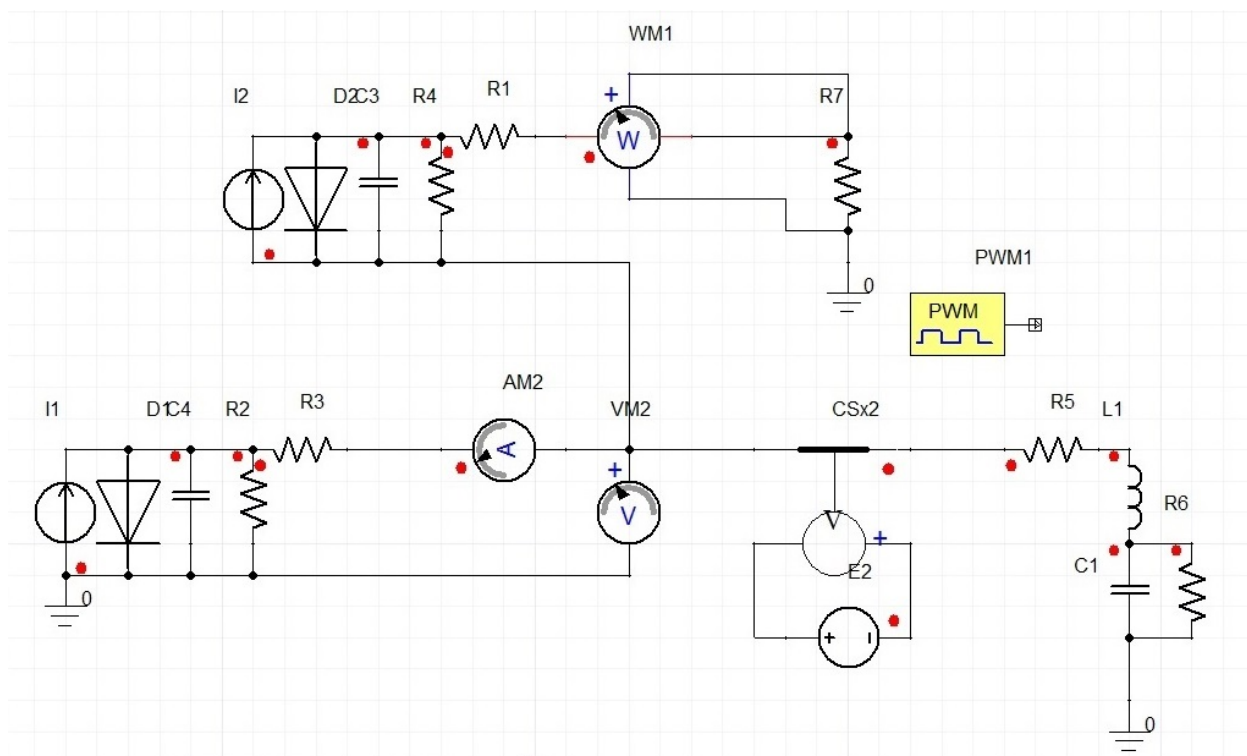


Figure C.3: Simpler perturbation simulation set up with LC (no stored energy) design

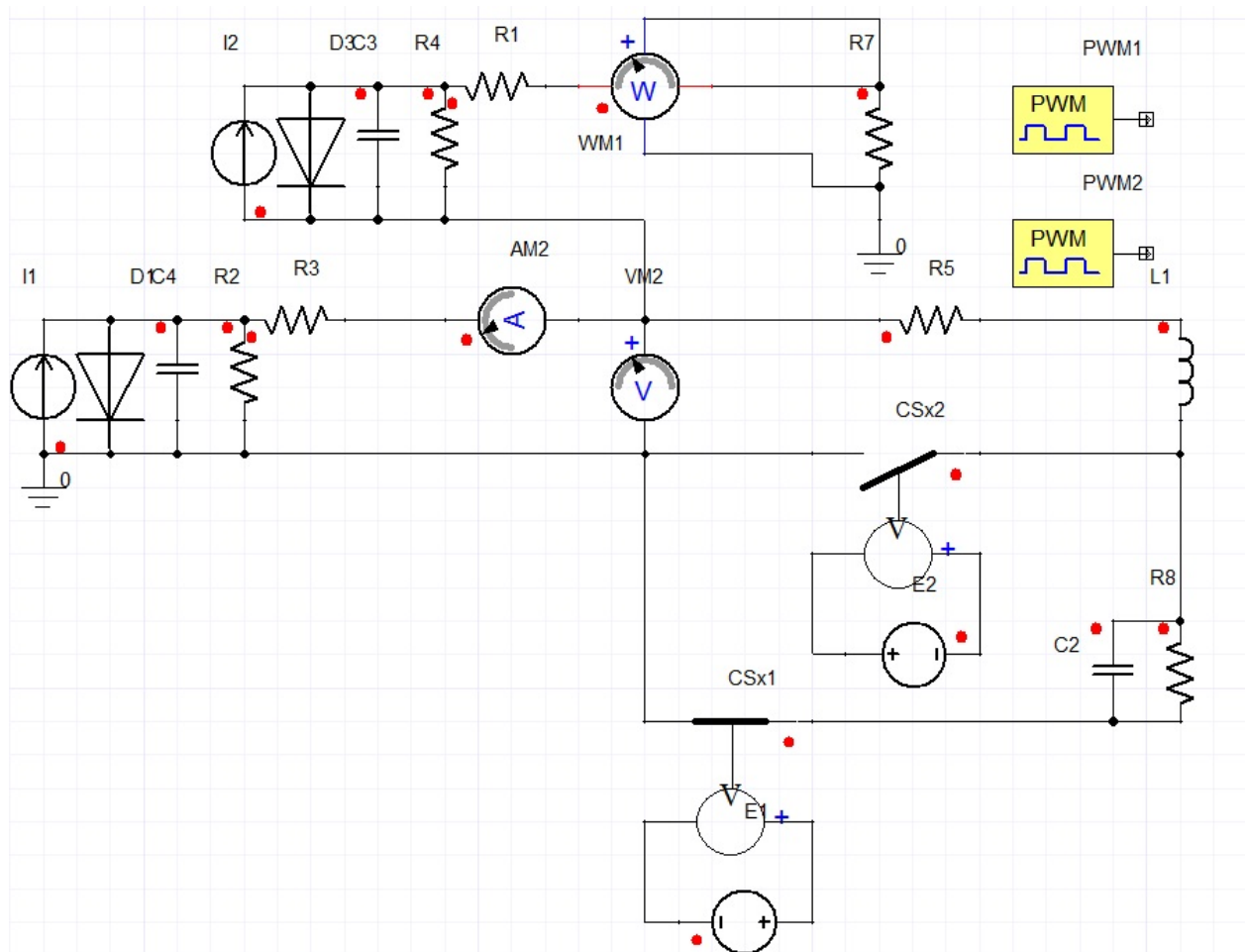


Figure C.4: Simplorer perturbation simulation set up with L-LC (stored energy) design

C.0.3 PD PCB design documents

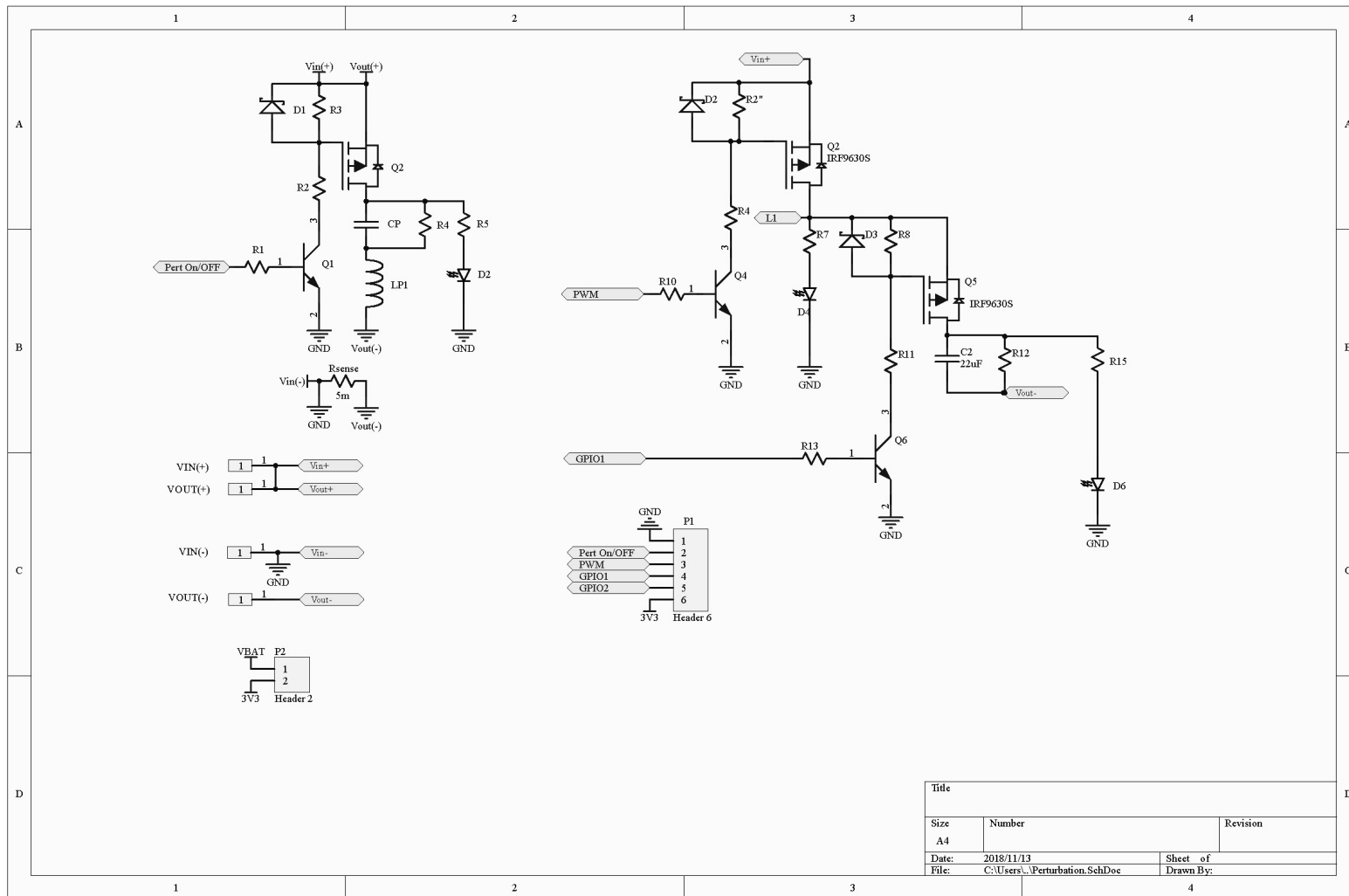


Figure C.5: PD LC schematic

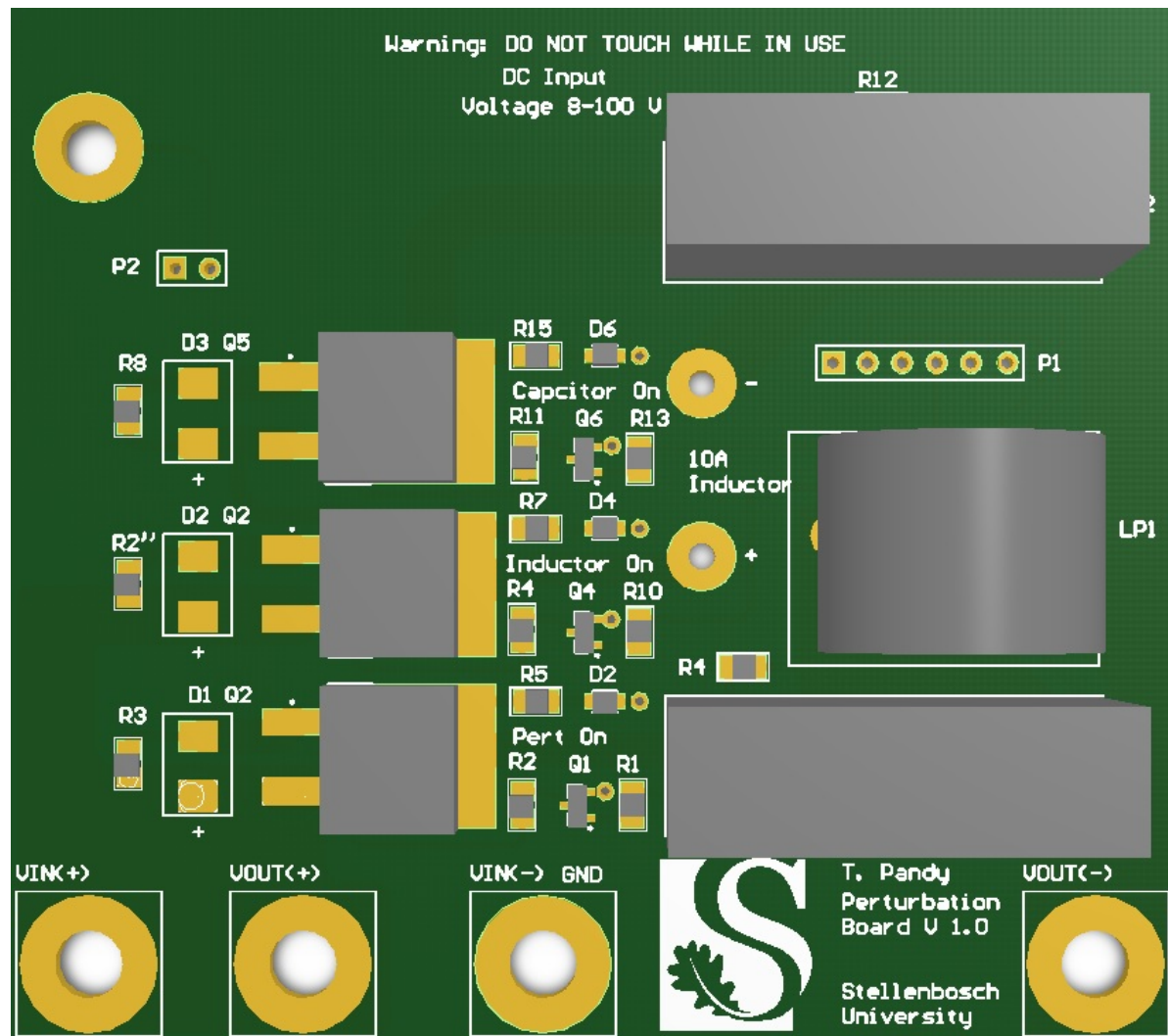


Figure C.6: PD LC PCB design 3D view

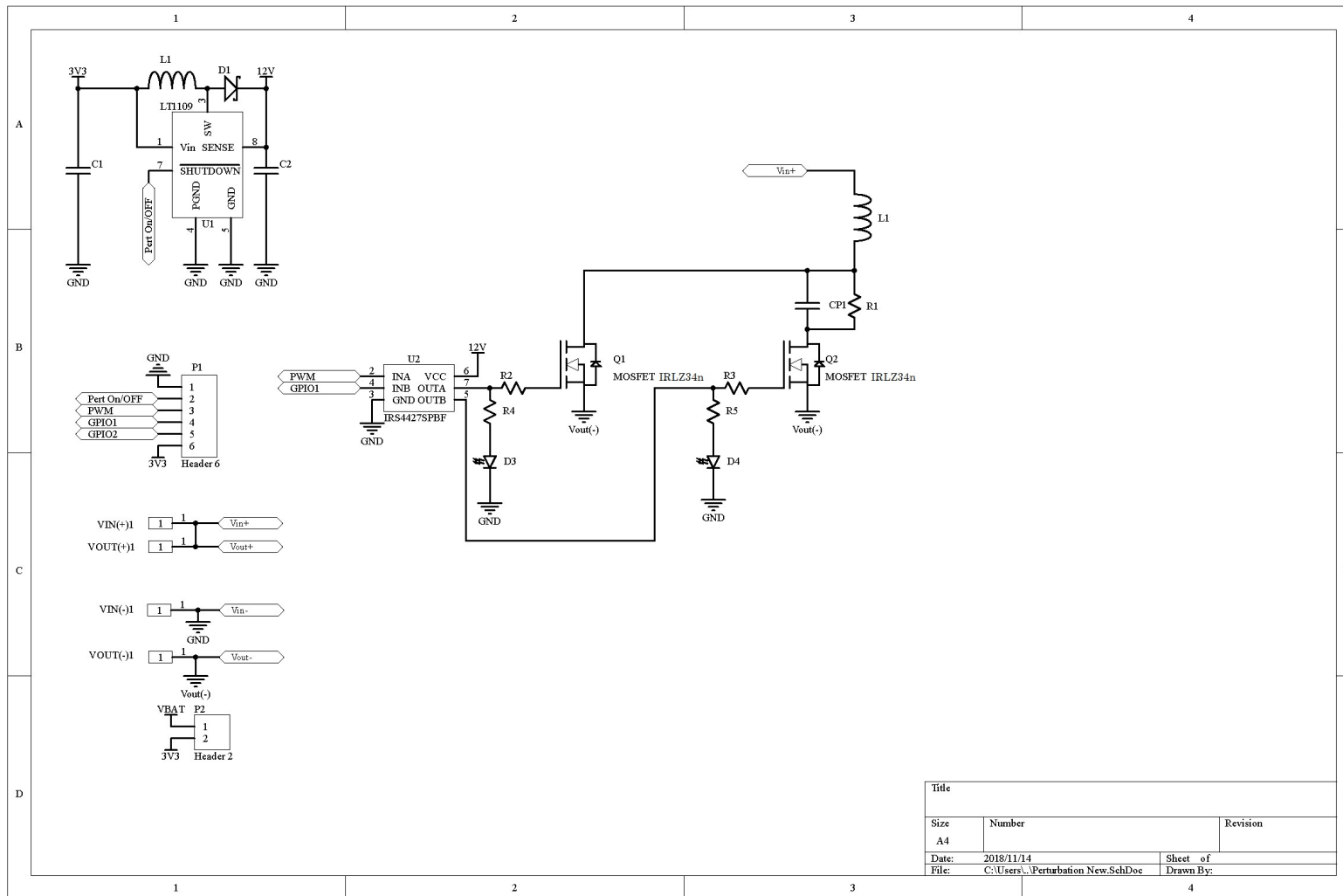


Figure C.8: PD L-LC schematic

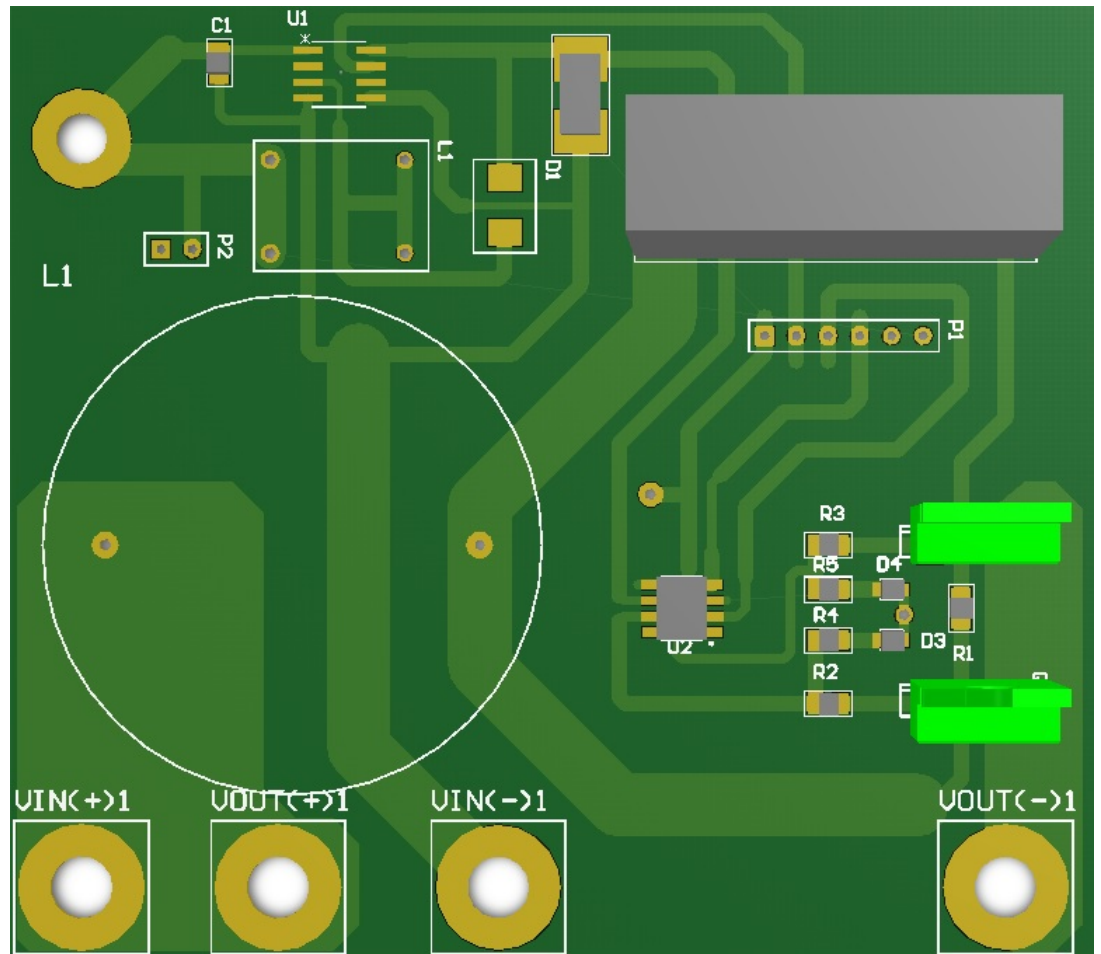


Figure C.9: PD L-LC PCB design 3D view

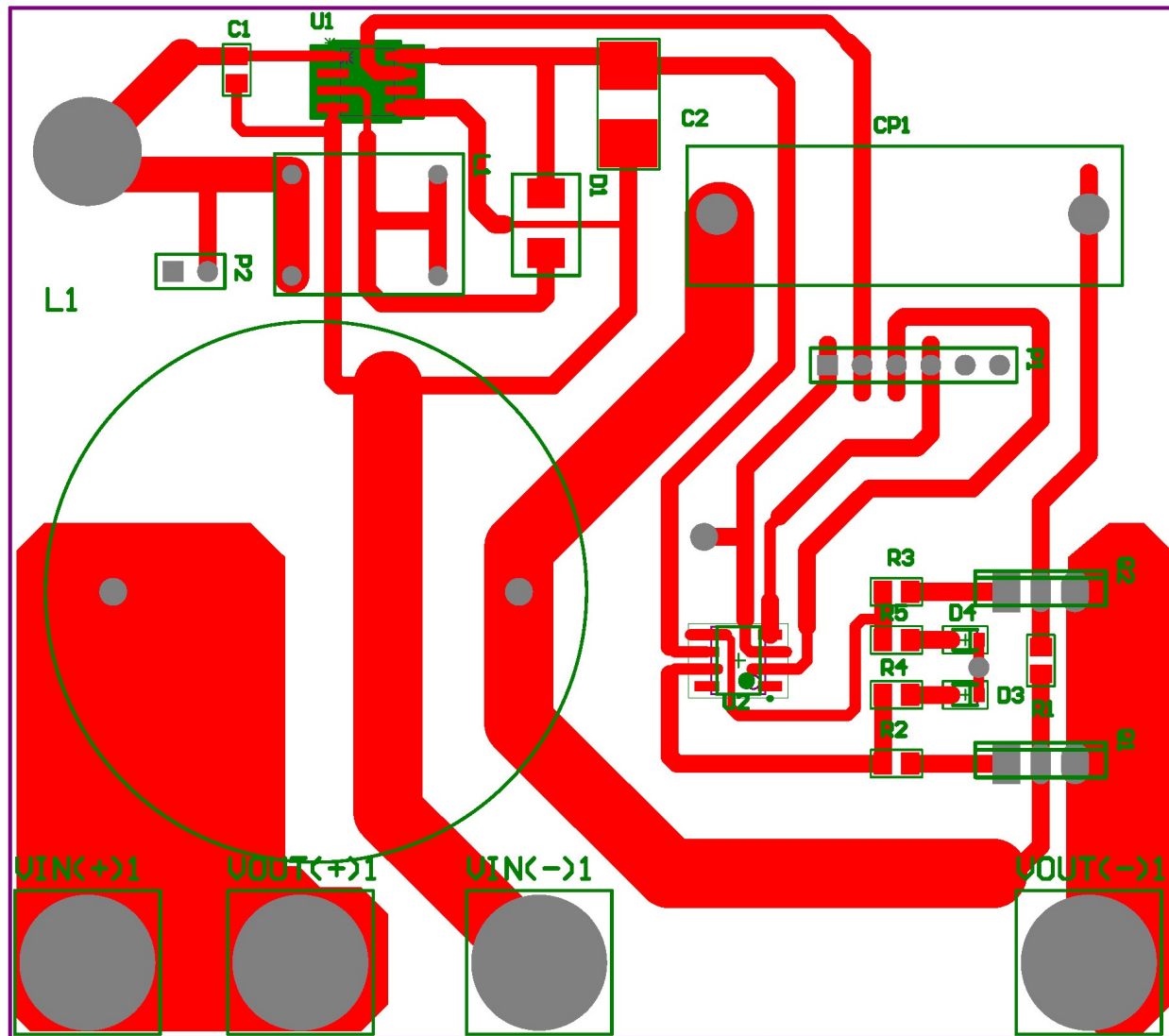


Figure C.10: PD L-LC PCB design 2D view

Appendix D

Data acquisition device (DAD)

D.0.1 ESP32 firmware

All the firmware development was completed using Eclipse IDE and programmed in the C programming language.

D.0.1.1 Environment setup

Espressif provides the official development framework for the ESP32 online via www.github.com [99], also known as the "ESP-IDF". The "ESP-IDF" and firmware needs to be correctly setup before use in Eclipse. A step-by-step programming guide for is Eclipse IDE is provided by Espressif [109]. Figure D.1 and D.2 is an illustration of the MSYS32 environment where the ESP32 default configuration settings can be altered.



Figure D.1: Morning shade cause by surrounding buildings

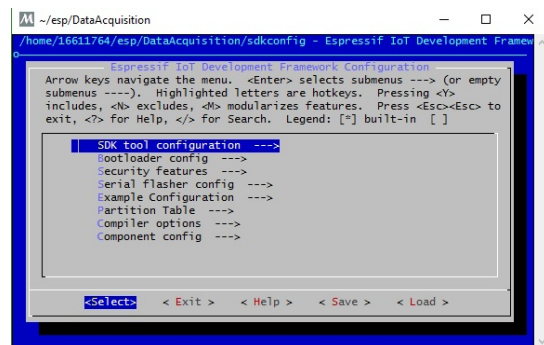


Figure D.2: Morning shade cause by surrounding objects

These include the default USART frequency, security setting, implementing the example configuration, boot loader and much more.

D.0.2 Python client program

A python client program was created to communicate between the DAD TCP server, which was done via the Python socket libraries. Python is a extremely well-rounded language and assisted with converting sampled data to CSV format and using the SQL library to send sampled data to the online SQL online database.

D.0.3 Web Server and online database

Figure D.3 is an illustration of data storage structure on the online database. This functionality allows the data to be accessed anywhere in the world.

The screenshot displays the phpMyAdmin interface for the 'xpiosbkm_Tashriq' database, specifically the 'MD1' table. The table structure is as follows:

ID	DATE	TIME	Temperature	Data	DataV	CurrentMPP	PertMPP	ChangeMPP
82	07-11-2018	10:18:15	41.6719	[BLOB - 18.6 KiB]	[BLOB - 18.7 KiB]	259.041	262.336	257.825
83	07-11-2018	10:23:24	41.6719	[BLOB - 18.6 KiB]	[BLOB - 18.8 KiB]	256.441	263.821	254.445
84	07-11-2018	10:28:32	41.6719	[BLOB - 18.5 KiB]	[BLOB - 18.8 KiB]	264.154	267.721	262.311
85	07-11-2018	10:33:41	41.6719	[BLOB - 18.5 KiB]	[BLOB - 18.8 KiB]	263.075	268.833	264.431
86	07-11-2018	10:38:49	41.6719	[BLOB - 18.5 KiB]	[BLOB - 18.7 KiB]	266.965	270.759	267.336
87	07-11-2018	10:43:58	41.6719	[BLOB - 18.5 KiB]	[BLOB - 18.7 KiB]	267.06	274.079	268.275
88	07-11-2018	10:49:07	41.6719	[BLOB - 18.5 KiB]	[BLOB - 18.7 KiB]	269.55	274.198	268.943
89	07-11-2018	10:54:15	41.6719	[BLOB - 18.4 KiB]	[BLOB - 18.9 KiB]	276.607	278.724	276.535
90	07-11-2018	10:59:24	41.6719	[BLOB - 18.4 KiB]	[BLOB - 18.9 KiB]	277.225	280.674	277.353
91	07-11-2018	11:04:33	41.6719	[BLOB - 18.4 KiB]	[BLOB - 19 KiB]	275.67	277.791	275.563
92	07-11-2018	11:09:41	41.6719	[BLOB - 18.4 KiB]	[BLOB - 18.7 KiB]	268.793	275.758	266.59
93	07-11-2018	11:14:50	41.6719	[BLOB - 18.5 KiB]	[BLOB - 18.7 KiB]	268.484	279.402	265.675
94	07-11-2018	11:20:05	41.6719	[BLOB - 18.5 KiB]	[BLOB - 18.7 KiB]	267.896	280.904	265.628
95	07-11-2018	11:25:14	41.6719	[BLOB - 18.6 KiB]	[BLOB - 18.8 KiB]	258.169	277.753	255.674
96	07-11-2018	11:30:23	41.6719	[BLOB - 18.5 KiB]	[BLOB - 18.8 KiB]	254.181	278.582	248.912
97	07-11-2018	11:35:31	41.6719	[BLOB - 18.6 KiB]	[BLOB - 18.8 KiB]	251.041	275.153	248.892
98	07-11-2018	11:40:40	41.6719	[BLOB - 18.5 KiB]	[BLOB - 18.8 KiB]	261.31	281.924	257.409
99	07-11-2018	11:45:48	41.6719	[BLOB - 18.5 KiB]	[BLOB - 18.8 KiB]	259.259	277.429	262.284

Figure D.3: SQL database table structure for MD's.

D.0.4 ESP32 programmer PCB design documents

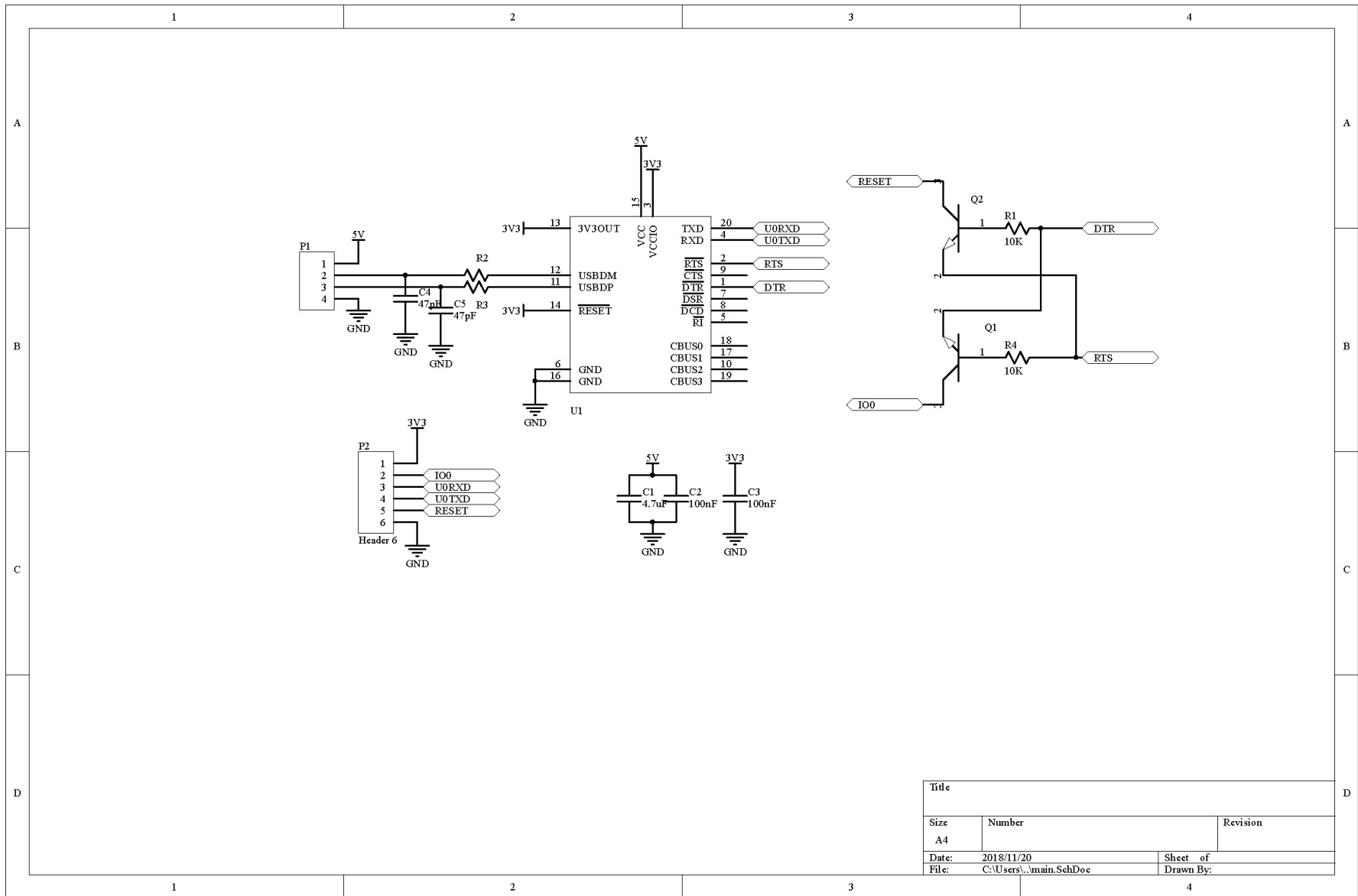


Figure D.4: ESP32 programmer schematic.

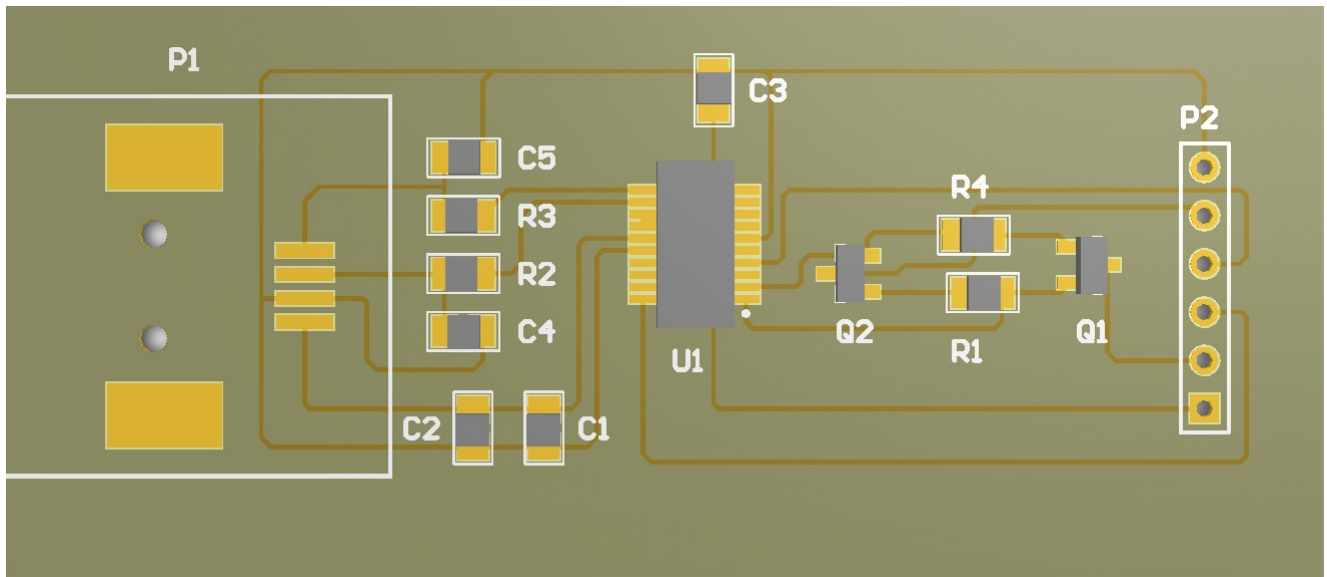


Figure D.5: MD PCB design 3D view.

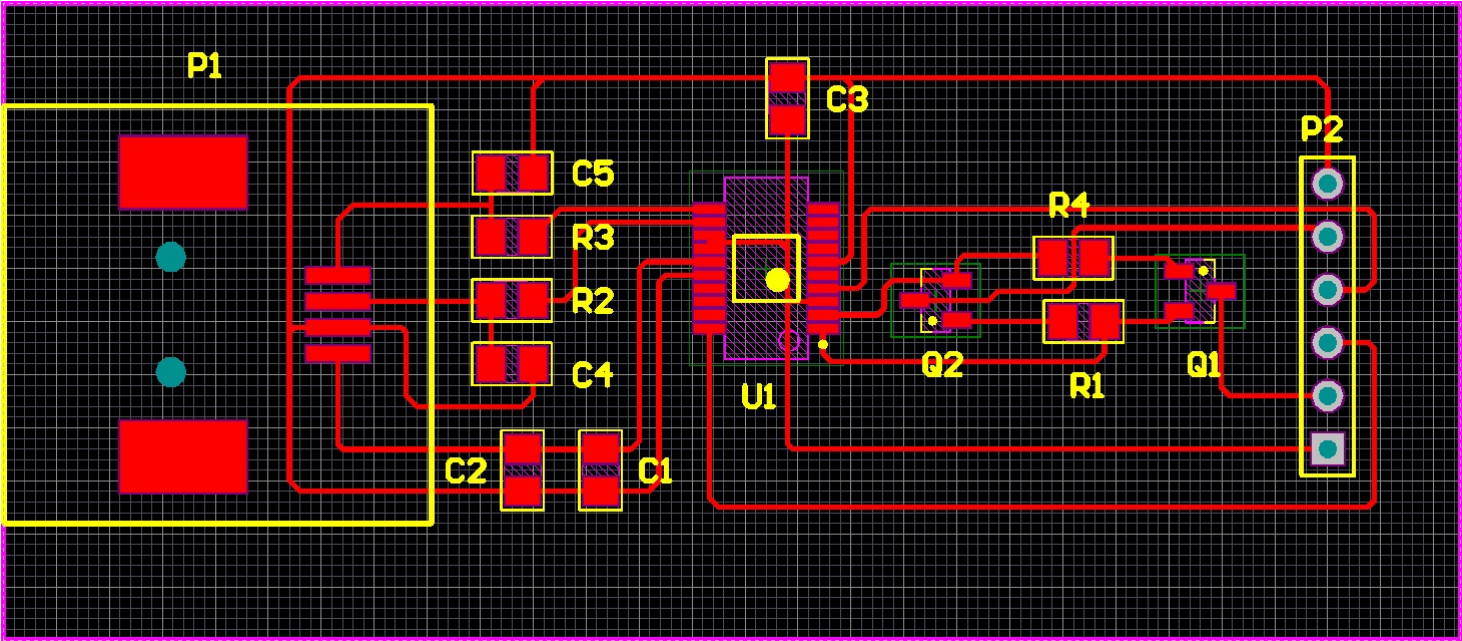


Figure D.6: MD PCB design 2D view.

Appendix E

Calibration process for monitoring devices

The monitoring device was calibrated using a two point calibration process, which re-scales the output by correcting slope and offset errors. This form of calibration is used in the case when the sensor output is known to be reasonably linear. This process was implemented to calibrate the current and voltage readings of the ADC's. The two point calibration process is performed in the following manner:

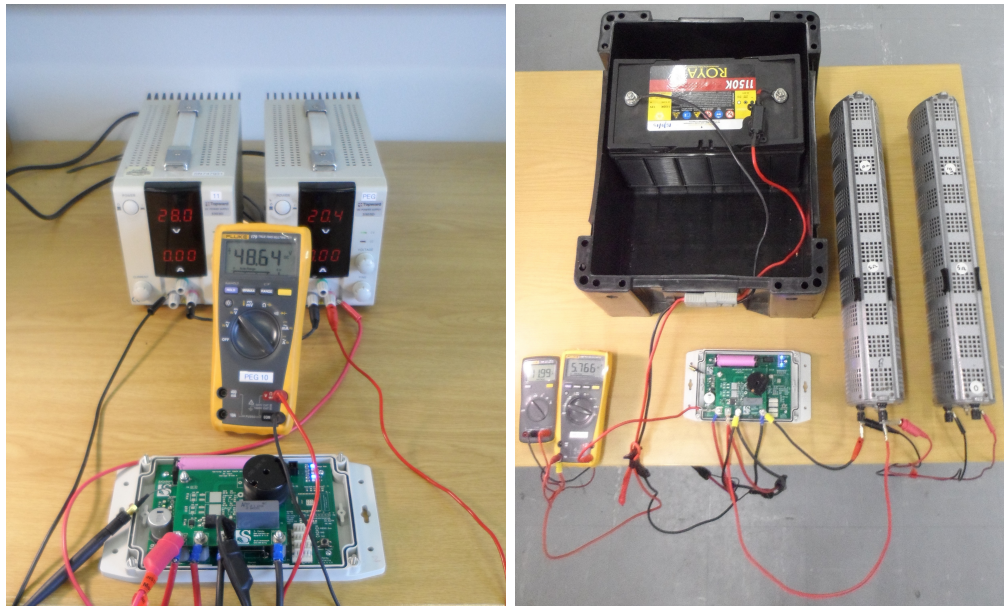
1. Taking two measurement readings for both the voltage and current ADC: One reading near the low end of the measuring range and another near the high end of the measuring range. These values are recorded as RawLow and RawHigh.
2. The same is repeated for the reference instrumentation. These values are recorded as ReferenceLow and ReferenceHigh.
3. Next is to calculate the RawRange, which is the difference between RawHigh - RawLow.
4. Followed by calculate the ReferenceRange, which is the difference between ReferenceHigh - ReferenceLow.

The corrected value is then given by Equation E.1 given below:

$$CorrectedValue = \frac{(RawValue - RawLow) \times ReferenceRange}{RawRange} + ReferenceLow \quad (E.1)$$

The RawValue is the digital value of the ADC analogue input. The voltage and current calibration process was performed individually, the following equipment was utilised and also illustrated in Figure E.1:

1. 2 x 10 ohm 10A resistor.
2. 1 x 12 V deep cycle batteries.
3. 2 x Fluke multimeter, accurate up to 3 decimal places.
4. Bench power supply.



(a) Voltage calibration process.

(b) Current calibration process.

Figure E.1: Voltage and current calibration process.

As illustrated in Figure E.1b, the two 10 A rated load resistors was connected in parallel to draw the sufficient current for the two point calibration process using the 12 V battery, which is more than capable of drawing sufficient current during for this process. The two Fluke multimeter's measured the voltage over the input voltage and the current on the negative terminals on the input side of the MD - exactly how voltage and current is measured on the MD. First, the raw low values are determined for the voltage and current by sampling a measurement with no load and power supplied. Thereafter, the same is performed with the load resistors drawing 9. A as the maximum current. The voltmeter multimeter was used to ensure that the 12 V lead acid battery did not drop below 11 V to protect the battery from internal damage, while drawing current from the load resistor. Two bench power supplies connected in series was used to calibrate the voltage measurement because, the input voltage could be varied to that maximum input of the MD input voltage range of 50 V, refer to Figure E.1a for an illustration of this process. Each sample on both voltage and current was an average of the MD maximum amount of sample, which is a 1000 as mentioned in Section 3. A Python script is used to extract the 1000 voltage and current samples, where the averaging is performed in the python code. This process was performed for raw low, raw high, which was tabulated for the MDC and each of the four MD. The reference values were read of the Fluke multimeter's. The calibration constants are stored on the MCU's non-volatile memory of the MD(c), which were read upon device start up for the the device to scale the sampled data correctly. Thereafter, the accuracy of the calibration process was tested. The calibration accuracy is tabulated in Table E.1 and E.2 of all the devices, accuracy is calculated a percentage between the reference and ADC readings. The reference current is plotted against the ADC current reading for the MDC (device 1) as illustrated in Figure E.2 with a gradient of 0.995, nearly close to 1. The voltage ADC reading is also plotted against the reference reading for MDC (device 1) shown in Figure E.3 with a gradient of 1.007434.

Table E.1 also shows MD2-4 current accuracy taken at similar reference current intervals.

Table E.2 also shows MD2-4 voltage accuracy taken at similar reference voltage intervals.

Figure E.4 illustrates the simultaneous sampled waveform of a 500 Hz sine wave applied at the input of both ADCs, in fact the 500 Hz sine wave was applied to the scaling amplifiers

Table E.1: Current calibration accuracy.

Accuracy[%] MDC	Accuracy[%] MD2	Accuracy[%] MD3	Accuracy[%] MD4
N/A	N/A	N/A	N/A
0.016	0.051	0.029	0.067
0.038	-0.651	-0.011	0.065
0.027	0.025	0.026	0.039
0.045	-0.047	-0.02	0.014
0.022	0.001	0.037	0.053
-0.193	0.021	0.078	-0.09
0.001	N/A	-0.020	0.042
-0.01	N/A	N/A	N/A

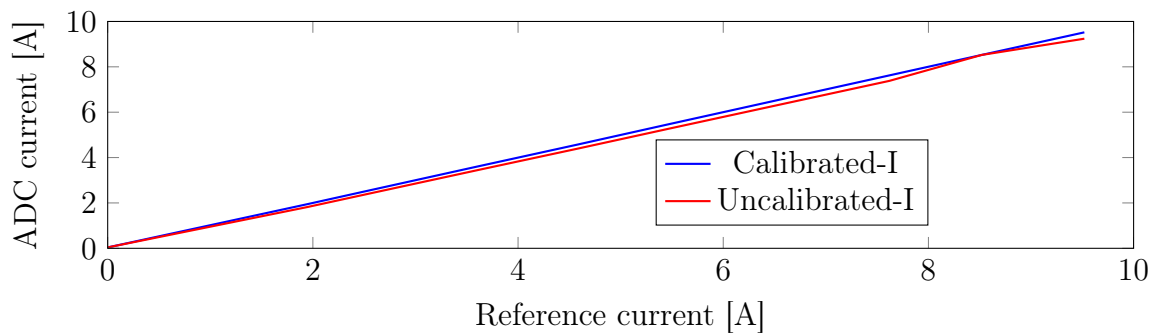


Figure E.2: Current sensor linearity

Table E.2: Current calibration accuracy.

Accuracy [%] MDC	Accuracy [%] MD2	Accuracy [%] MD3	Accuracy [%] MD4
N/A	N/A	0.028	-0.030
0.059	0.029	0.001	0.009
0.098	-0.04	0.002	0.031
-0.013	0.028	0.018	0.014
0.044	0.019	0.001	0.014
-0.056	-0.004	-0.003	-0.016
-0.013	0.013	-0.0086	-0.097
-0.028	0.036	-0.0372	0.042
-0.015	0.017	0.0091	0.001

(MCP601 and INA156) before the ADCs. Hence, the need for scaling the outputs, as shown in Figure E.4. An average scaling was implemented deliberately, so that both graphs are not necessary on top on each other all the time in order to distinguish both wave forms. It is clearly seen that the two ADC sample simultaneously although the each ADC has a minimum and maximum conversion time of 500-8800 ns, shown in Figure B.2. The sine wave was generated with a signal generator and 500Hz frequency was chosen since it is fairly close to the perturbation frequency.

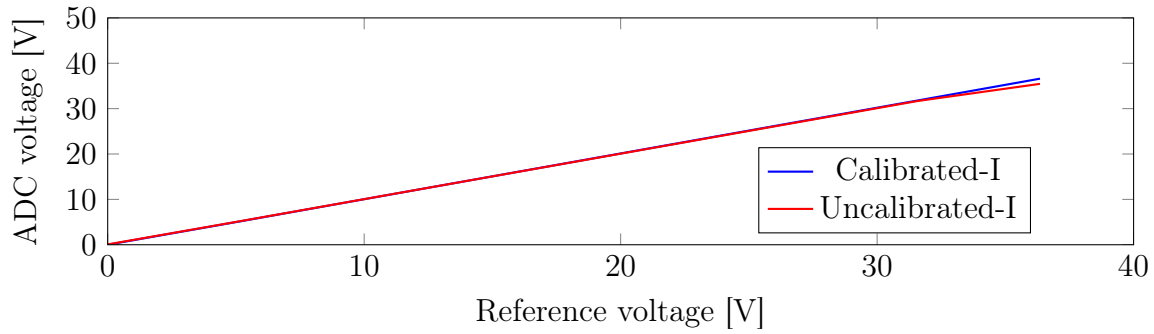


Figure E.3: Voltage sensor linearity for MDC

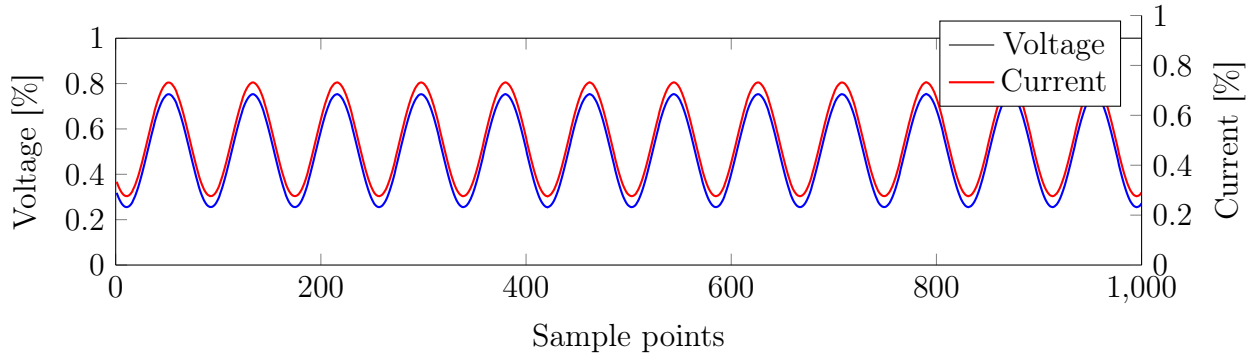


Figure E.4: Simultaneous sample of 500 Hz sine wave at both ADC inputs

E.0.1 MD measurement verification using an oscilloscope

Figure E.5 illustrates the MD(C) voltage waveform plotted against the oscilloscope waveform for further verification of the monitoring device accuracy. This process compares the waveforms of the MD to that of an oscilloscope by capturing the exact same reading with both devices. To ensure that the oscilloscope is adequate for this verification process the main contributor to sample the perturbation waveforms correctly is to ensure sufficient bandwidth capability. The perturbation waveform frequency is determined by the perturbation period, which is roughly around 500 Hz. Thus, the bandwidth capabilities of the oscilloscope measuring equipment for the voltage is 60 MHz and current is 15 MHz [110, 111]. The oscilloscope is well more than two decades above the perturbation frequency and therefore adequate enough to verify the MD(C) voltage reading. Likewise for the current although there is no waveform to illustrate this, the fact that the voltage and current measure simultaneously as shown in Figure E.4 ensure that the MD(C) ADC reading is also sufficiently. Further verification of this will be seen in the experimental results. Any phase shift errors will show on the I-V plot and look like an ellipse, which is not sufficient to determine the MPP.

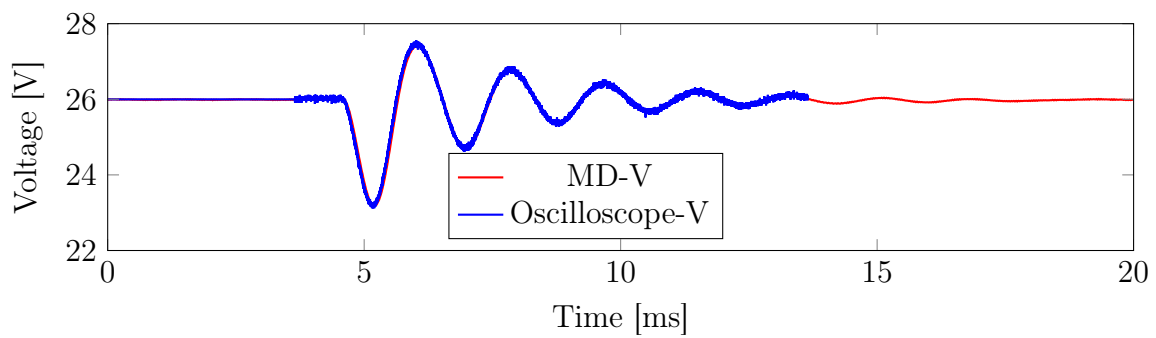


Figure E.5: MD and oscilloscope voltage measurements sampled at the same time.

List of References

- [1] N. Chimres and S. Wongwises, "Critical review of the current status of solar energy in thailand," *Renewable and Sustainable Energy Reviews*, vol. 58, pp. 198–207, 2016.
- [2] F. Grimaccia, M. Aghaei, M. Mussetta, S. Leva, and P. B. Quater, "Planning for pv plant performance monitoring by means of unmanned aerial systems (uas)," *International Journal of Energy and Environmental Engineering*, vol. 6, no. 1, pp. 47–54, 2015.
- [3] S. S. Hegedus and A. Luque, "Status, trends, challenges and the bright future of solar electricity from photovoltaics," *Handbook of photovoltaic science and engineering*, pp. 1–43, 2003.
- [4] F. Meneguzzo, R. Ciriminna, L. Albanese, and M. Pagliaro, "The great solar boom: a global perspective into the far reaching impact of an unexpected energy revolution," *Energy Science & Engineering*, vol. 3, no. 6, pp. 499–509, 2015.
- [5] U. D. of Energy. (2017) The history of solar. [Online]. Available: https://www1.eere.energy.gov/solar/pdfs/solar_timeline.pdf
- [6] M. S. Cengiz and M. S. Mamiş, "Price-efficiency relationship for photovoltaic systems on a global basis," *International Journal of Photoenergy*, vol. 2015, 2015.
- [7] Y. Aldali, D. Henderson, and T. Muneer, "A 50 mw very large-scale photovoltaic power plant for al-kufra, libya: energetic, economic and environmental impact analysis," *International Journal of Low-Carbon Technologies*, vol. 6, no. 4, pp. 277–293, 2011.
- [8] F. Ise, "Photovoltaics report," *Fraunhofer Institute for Solar Energy Systems ISE*, 2018.
- [9] T. Randall. (2016, June) The world nears peak fossil fuels for electricity. [Accessed: 27-June-2016]. [Online]. Available: <http://www.bloomberg.com/news/articles/2016-06-13/we-ve-almost-reached-peak-fossil-fuels-for-electricity>
- [10] D. of Energy, "Integrated resource plan for electricity (irp) 2010-2030," 2011.
- [11] M. Chidi, M. Nthontho, S. Chowdhury, and S. Chowdhury, "Viability of grid-connected domestic solar photovoltaic systems in south africa," in *Power and Energy Society General Meeting, 2012 IEEE*. IEEE, 2012, pp. 1–6.
- [12] energy.org.za. (2018) Sa utility scale re technologies by programme. [Online]. Available: <https://www.energy.org.za/data-and-tools/data-viz/south-africa-utility-scale-technologies-per-programme>
- [13] M. G. Tshehla, "Renewable Energy - 2015 - Market Intelligence Report," Tech. Rep., November 2015. [Online]. Available: <http://greencape.co.za/assets/Uploads/GreenCape-Market-Intelligence-Report-2015-Renewable-Energy.pdf>
- [14] P. Papapetrou, "Enabling Renewable Energy in South Africa : Assessing the Renewable Energy Independent Power Producer Programme," Tech. Rep., 2014. [Online]. Available: http://awsassets.wwf.org.za/downloads/enabling_re_in_sa.pdf

- [15] Tigo Energy. (2011) About Tigo Energy - YouTube. [Online]. Available: <https://www.youtube.com/watch?v=yJl1uch9Yjo>
- [16] S. Daliento, A. Chouder, P. Guerriero, A. M. Pavan, A. Mellit, R. Moeini, and P. Tricoli, "Monitoring, diagnosis, and power forecasting for photovoltaic fields: a review," *International Journal of Photoenergy*, vol. 2017, 2017.
- [17] S. Baschel, E. Koubli, J. Roy, and R. Gottschalg, "Impact of component reliability on large scale photovoltaic systems' performance," *Energies*, vol. 11, no. 6, p. 1579, 2018.
- [18] Gantner Instruments Germany, "Complete monitoring solution "Made in Germany" for utility-scale PV plants worldwide | PV Tech," 2018. [Online]. Available: <https://www.pv-tech.org/guest-blog/complete-monitoring-solution-made-in-germany-for-utility-scale-pv-plants-wo>
- [19] SMA Germany, "SMA STRING MONITOR." [Online]. Available: https://www.sma-france.com/fileadmin/content/www.sma-france.com/Service/Documents/Livre_Blanc_zone_monitoring.pdf
- [20] P. Papageorgas, D. Piromalis, K. Antonakoglou, G. Vokas, D. Tseles, and K. Arvanitis, "Smart solar panels: In-situ monitoring of photovoltaic panels based on wired and wireless sensor networks," *Energy Procedia*, vol. 36, pp. 535–545, 2013.
- [21] U. Z. A. Hamid, H. Zamzuri, and D. K. Limbu, "Internet of vehicle (ioV) applications in expediting the implementation of smart highway of autonomous vehicle: A survey," in *Performativity in Internet of Things*. Springer, 2019, pp. 137–157.
- [22] M. Gargiulo, P. Guerriero, S. Daliento, A. Irace, V. d'Alessandro, M. Crisci, A. Smarrelli, and M. Smarrelli, "A novel wireless self-powered microcontroller-based monitoring circuit for photovoltaic panels in grid-connected systems," in *Power Electronics Electrical Drives Automation and Motion (SPEEDAM), 2010 International Symposium on*. IEEE, 2010, pp. 164–168.
- [23] G. M. Masters, *Renewable And Efficient Electric Power Systems*, 2nd ed. Hoboken, New Jersey: John Wiley & Sons, Inc., 2013.
- [24] F. Belhachat and C. Larbes, "A review of global maximum power point tracking techniques of photovoltaic system under partial shading conditions," *Renewable and Sustainable Energy Reviews*, vol. 92, pp. 513–553, 2018.
- [25] T. Ahmad, S. Sobhan, and M. F. Nayan, "Comparative analysis between single diode and double diode model of pv cell: concentrate different parameters effect on its efficiency," *Journal of Power and Energy Engineering*, vol. 4, no. 03, p. 31, 2016.
- [26] Y.-H. Ji, D.-Y. Jung, J.-G. Kim, J.-H. Kim, T.-W. Lee, and C.-Y. Won, "A real maximum power point tracking method for mismatching compensation in pv array under partially shaded conditions," *IEEE Transactions on power electronics*, vol. 26, no. 4, pp. 1001–1009, 2011.
- [27] H. Patel and V. Agarwal, "Maximum power point tracking scheme for pv systems operating under partially shaded conditions," *IEEE transactions on industrial electronics*, vol. 55, no. 4, pp. 1689–1698, 2008.
- [28] K. Kobayashi, I. Takano, and Y. Sawada, "A study on a two stage maximum power point tracking control of a photovoltaic system under partially shaded insolation conditions," in *Power Engineering Society General Meeting, 2003, IEEE*, vol. 4. IEEE, 2003, pp. 2612–2617.

- [29] F. Belfiore, T. Taylor, B. Moisan, M. Zappia, and E. Cinarelli, "Risks and opportunities in the operation of large solar plants," in *Solar Power Gen 2013*, 2013.
- [30] R. Hren. Monitoring Batteryless PV Systems | Home Power Magazine. [Online]. Available: <https://www.homepower.com/articles/solar-electricity/equipment-products/monitoring-grid-tied-pv-systems>
- [31] F. Wortmann and K. Flüchter, "Internet of things," *Business & Information Systems Engineering*, vol. 57, no. 3, pp. 221–224, 2015.
- [32] SMA Solar Technology AG. (2016) SMA Solar Technology AG Acquires Stake in Tigo Energy, Inc. to Tap into the Market for Smart Module Technology. [Online]. Available: <https://www.sma.de/en/newsroom/current-news/news-details/news/2000-sma-solar-technology-ag-acquires-stake-in-tigo-energy-inc-to-tap-into-the-market-for-smart-module-technology>
- [33] electrical4u. (unknown) Rlc circuit. [Online]. Available: <https://www.gantner-instruments.com/us/about-us-company/>
- [34] SMA Germany, "POWER PLANT CONTROLLER | SMA Solar." [Online]. Available: <https://www.sma.de/en/products/monitoring-control/power-plant-controller.html>
- [35] N. Solanki and J. Patel, "Photovoltaic solar farms operating in var mode: A review," *Journal of Power Electronics and Power Systems*, vol. 6, no. 1, 2016.
- [36] SMA Germany, "Shade Management - Efficient Operation of Partially Shaded PV Systems with OptiTrac Global Peak." [Online]. Available: <http://files.sma.de/dl/7418/GlobalPeak-TI-en-12.pdf>
- [37] T. Energy. (unknown) TS4 Platform. [Online]. Available: <https://support.tigoenergy.com/hc/en-us/articles/205846878-TS4-Platform>
- [38] S. T. Inc. (unknown) Power Optimizer Module Add-on. [Online]. Available: <https://www.solaredge.com/products/power-optimizer#/>
- [39] T. Energy. (unknown) Case Study: Tsunagi, Japan - First Full Mega Solar PV system in Japan . [Online]. Available: <https://www.tigoenergy.com/library/view/Revealing+Open+Circuit+Issues+through+Tigo%27s+online+monitoring+system.pdf/>
- [40] ——. Case Study: 13Ground Mount PV . [Online]. Available: <https://www.tigoenergy.com/library/view/Testing+a+Utility-scale+PV+system%27s+13%25+Energy+Increase+with+Tigo%27s+optimizers.pdf/>,urldate={2013-08-04},year={unknown}
- [41] S. B. Sadineni, J. D. Realmuto, and R. F. Boehm, "An integrated performance monitoring and solar tracking system for utility scale pv plants," in *ASME 2011 Power Conference collocated with JSME ICOPE 2011*. American Society of Mechanical Engineers, 2011, pp. 517–522.
- [42] G. Cramer, M. Ibrahim, and W. Kleinkauf, "Pv system technologies: State-of-the-art and trends in decentralised electrification," *Refocus*, vol. 5, no. 1, pp. 38–42, 2004.
- [43] W. Rohouma, I. Molokhia, and A. Esuri, "Comparative study of different pv modules configuration reliability," *Desalination*, vol. 209, no. 1-3, pp. 122–128, 2007.
- [44] M. Meinhardt, G. Cramer, B. Burger, and P. Zacharias, "Multi-string-converter with reduced specific costs and enhanced functionality," *Solar Energy*, vol. 69, pp. 217–227, 2001.
- [45] A. M. Pavan, S. Castellan, S. Quaia, S. Roitti, and G. Sulligoi, "Power electronic conditioning systems for industrial photovoltaic fields: Centralized or string inverters?" in *Clean Electrical Power, 2007. ICCEP'07. International Conference on*. IEEE, 2007, pp. 208–214.

- [46] M. Munoz, M. C. Alonso-García, N. Vela, and F. Chenlo, “Early degradation of silicon pv modules and guaranty conditions,” *Solar energy*, vol. 85, no. 9, pp. 2264–2274, 2011.
- [47] I. E. Commission *et al.*, “Photovoltaic system performance monitoring-guidelines for measurement, data exchange and analysis,” *IEC 61724*, 1998.
- [48] SMA Germany, “Performance ratio - quality factor for the pv plant.” [Online]. Available: <http://files.sma.de/dl/7680/Perfratio-TI-en-11.pdf>
- [49] M. Baba, T. Shimakage, and N. Takeuchi, “Examination of fault detection technique in pv systems,” in *Telecommunications Energy Conference ‘Smart Power and Efficiency’ (INTELEC), Proceedings of 2013 35th International*. VDE, 2013, pp. 1–4.
- [50] D. D. Nguyen, B. Lehman, and S. Kamarthi, “Performance evaluation of solar photovoltaic arrays including shadow effects using neural network,” in *Energy Conversion Congress and Exposition, 2009. ECCE 2009. IEEE*. IEEE, 2009, pp. 3357–3362.
- [51] E. Karatepe, T. Hiyama *et al.*, “Controlling of artificial neural network for fault diagnosis of photovoltaic array,” in *Intelligent System Application to Power Systems (ISAP), 2011 16th International Conference on*. IEEE, 2011, pp. 1–6.
- [52] D. Riley and J. Johnson, “Photovoltaic prognostics and health management using learning algorithms,” in *Photovoltaic Specialists Conference (PVSC), 2012 38th IEEE*. IEEE, 2012, pp. 001 535–001 539.
- [53] D. Stellbogen, “Use of pv circuit simulation for fault detection in pv array fields,” in *Photovoltaic Specialists Conference, 1993., Conference Record of the Twenty Third IEEE*. IEEE, 1993, pp. 1302–1307.
- [54] H. Haeberlin and C. Beutler, “Normalized representation of energy and power for analysis of performance and on-line error detection in pv-systems,” in *Proc. 13th EU PV Conf., Nice, 1995*, p. 934.
- [55] A. Drews, A. De Keizer, H. G. Beyer, E. Lorenz, J. Betcke, W. Van Sark, W. Heydenreich, E. Wiemken, S. Stettler, P. Toggweiler *et al.*, “Monitoring and remote failure detection of grid-connected pv systems based on satellite observations,” *Solar energy*, vol. 81, no. 4, pp. 548–564, 2007.
- [56] S. Silvestre, M. A. da Silva, A. Chouder, D. Guasch, and E. Karatepe, “New procedure for fault detection in grid connected pv systems based on the evaluation of current and voltage indicators,” *Energy Conversion and Management*, vol. 86, pp. 241–249, 2014.
- [57] G. T. Klise and J. S. Stein, “Models used to assess the performance of photovoltaic systems,” *Sandia National Laboratories*, 2009.
- [58] A. Mellit, A. M. Pavan, and V. Lughi, “Short-term forecasting of power production in a large-scale photovoltaic plant,” *Solar Energy*, vol. 105, pp. 401–413, 2014.
- [59] J. Antonanzas, N. Osorio, R. Escobar, R. Urraca, F. Martinez-de Pison, and F. Antonanzas-Torres, “Review of photovoltaic power forecasting,” *Solar Energy*, vol. 136, pp. 78–111, 2016.
- [60] R. Smith, “Monitoring system performance,” 2011.
- [61] P. Guerriero, F. Di Napoli, and S. Daliento, “Real time monitoring of solar fields with cost/revenue analysis of fault fixing,” in *Environment and Electrical Engineering (EEEIC), 2016 IEEE 16th International Conference on*. IEEE, 2016, pp. 1–6.

- [62] P. B. Quater, F. Grimaccia, S. Leva, M. Mussetta, and M. Aghaei, "Light unmanned aerial vehicles (uavs) for cooperative inspection of pv plants," *IEEE Journal of Photovoltaics*, vol. 4, no. 4, pp. 1107–1113, 2014.
- [63] M. Aghaei, A. Gandelli, F. Grimaccia, S. Leva, and R. Zich, "Ir real-time analyses for pv system monitoring by digital image processing techniques," in *Event-based Control, Communication, and Signal Processing (EBCSP), 2015 International Conference on*. IEEE, 2015, pp. 1–6.
- [64] S. Leva, M. Aghaei, and F. Grimaccia, "Pv power plant inspection by uas: Correlation between altitude and detection of defects on pv modules," in *Environment and Electrical Engineering (EEEIC), 2015 IEEE 15th International Conference on*. IEEE, 2015, pp. 1921–1926.
- [65] S. Dotenco, M. Dalsass, L. Winkler, T. Würzner, C. Brabec, A. Maier, and F. Gallwitz, "Automatic detection and analysis of photovoltaic modules in aerial infrared imagery," in *Applications of Computer Vision (WACV), 2016 IEEE Winter Conference on*. IEEE, 2016, pp. 1–9.
- [66] F. Di Napoli, P. Guerriero, V. d'Alessandro, and S. Daliento, "A power line communication on dc bus with photovoltaic strings," 2014.
- [67] V. Raghunathan and P. H. Chou, "Design and power management of energy harvesting embedded systems," in *Proceedings of the 2006 international symposium on Low power electronics and design*. ACM, 2006, pp. 369–374.
- [68] P. Guerriero, V. d'Alessandro, L. Petrazzuoli, G. Vallone, and S. Daliento, "Effective real-time performance monitoring and diagnostics of individual panels in pv plants," in *Clean Electrical Power (ICCEP), 2013 International Conference on*. IEEE, 2013, pp. 14–19.
- [69] U. Jahn and W. Nasse, "Operational performance of grid-connected pv systems on buildings in germany," *Progress in Photovoltaics: Research and applications*, vol. 12, no. 6, pp. 441–448, 2004.
- [70] M. Gagliarducci, D. Lampasi, and L. Podesta, "Gsm-based monitoring and control of photovoltaic power generation," *Measurement*, vol. 40, no. 3, pp. 314–321, 2007.
- [71] SMA Germany, "Ts4-r module technology." [Online]. Available: <https://files.sma.de/dl/29010/TS4-R-DEN1725-V32web.pdf>
- [72] Y. Yoo, O. Henfridsson, and K. Lyytinen, "Research commentary-the new organizing logic of digital innovation: an agenda for information systems research," *Information systems research*, vol. 21, no. 4, pp. 724–735, 2010.
- [73] L. Atzori, A. Iera, and G. Morabito, "The internet of things: A survey," *Computer networks*, vol. 54, no. 15, pp. 2787–2805, 2010.
- [74] R. S. Nillson James, *Electric Circuits 9th Edition*, 9th ed. Prentice Hall, 2011.
- [75] electrical4u. (2017) Rlc circuit. [Online]. Available: <https://www.electrical4u.com/rlc-circuit/>
- [76] L. Technologies, "LTC3895 - 150V Low IQ, Synchronous Step-Down DC/DC Controller," Datasheet.
- [77] Samsung, "Samsung Lithium-Ion ICR18650-26F," 2009.
- [78] Texas Instruments, "bq24074 1.5 A USB Friendly Li-Ion Battery Charger and Power-Path Management IC," 2015.
- [79] Semtech, "2.5MHz, 1.5A Synchronous Step Down Regulator," 2010.

- [80] Atmel, “Microcontroller with Low Power Transceiver for ZigBee and ATmega2564RFR2 ATmega1284RFR2 ATmega644RFR2 1 Pin Configurations,” 2011.
- [81] —, “Programmers and debuggers avrisp mkii,” User guide, Jan 2016. [Online]. Available: http://www.atmel.com/Images/Atmel-42093-AVR-ISP-mkII_UserGuide.pdf
- [82] IEEE Standards Association, *IEEE 802.15.4-2015 Standard*, I. The Institute of Electrical and Electronics Engineers, Ed. The Institute of Electrical and Electronics Engineers, Inc, 2015, vol. 2015. [Online]. Available: <http://standards.ieee.org/about/get/802/802.html>
- [83] S. Amean, “Ieee 802.15.4 and cc2420,” Lecture Notes, 2015. [Online]. Available: https://www.slideshare.net/salahcom/wsn-protocol-802154-together-with-cc2420-seminars?from_action=save
- [84] T. Instruments, “Single-ended input , sar analog-to-digital converter,” Datasheet, Apr 2013. [Online]. Available: <http://www.ti.com/lit/ds/symlink/ads8866.pdf>
- [85] —, “Single-supply, rail-to-rail output, cmos instrumentation amplifier,” Datasheet, Dec 1999. [Online]. Available: <http://www.ti.com/lit/ds/symlink/ina156.pdf>
- [86] Microchip, “Mcp601/1r/2/3/4,” Datasheet, May 2007. [Online]. Available: <http://ww1.microchip.com/downloads/en/DeviceDoc/21314g.pdf>
- [87] A. D. Inc, “Digital spi temperature sensor adt7310,” Datasheet, year:unknown. [Online]. Available: <http://www.analog.com/en/products/analog-to-digital-converters/integrated-special-purpose-converters/integrated-temperature-sensors/adt7310.html>
- [88] The American Heritage® Science Dictionary, “Perturbation | Define Perturbation at Dictionary.com,” 2011. [Online]. Available: <http://www.dictionary.com/browse/perturbation?s=t>
- [89] SMA Germany, “Technical Information - Capacitive Leakage Currents - Information on the design of transformerless inverters of type Sunny Boy, Sunny Mini Central, Sunny Tripower.” [Online]. Available: <http://files.sma.de/dl/7418/Ableitstrom-TI-en-25.pdf>
- [90] Renesola, “Renesola Virtus II Module 300W,305W,310W,” Renesola Datasheet, May 2014. [Online]. Available: www.ReneSola.com
- [91] —, “Renesola Virtus II Module 240W, 245W, 250W, 255W, 260W,” Renesola Datasheet, February 2013. [Online]. Available: www.ReneSola.com
- [92] L. Technologies, “Micropower low cost dc/dc converter, adjustable and fixed 5v, 12v,” Datasheet. [Online]. Available: <https://www.analog.com/media/en/technical-documentation/data-sheets/lt1109.pdf>
- [93] I. Rectifier, “Hexfet power mosfet,” Datasheet. [Online]. Available: <http://www.irf.com/product-info/datasheets/data/irlz34n.pdf>
- [94] —, “Dual low side driver,” Datasheet. [Online]. Available: https://www.infineon.com/dgdl/Infineon-IRS4426-DS-v02_01-EN.pdf?fileId=5546d462533600a40153567ba2532856
- [95] B. Inc, “High current chokes,” Datasheet, year:2011. [Online]. Available: https://www.bourns.com/docs/Product-Datasheets/1140_series.pdf
- [96] KEMET, “General purpose metallized polyester film capacitors,” Datasheet, year:2018. [Online]. Available: https://content.kemet.com/datasheets/KEM_F3103_R60.pdf
- [97] Espressif, “ESP32-WROOM-32 Datasheet - Espressif Systems,” 2017.
- [98] MSYS2. (2018) Msys2 installer. [Online]. Available: <http://www.msys2.org>

- [99] Github. (2018) Github. [Online]. Available: <https://github.com/espressif/esp-idf>
- [100] N. Kolban, “Kolban’s book on esp32,” 2017.
- [101] What is a socket? [Online]. Available: <https://docs.oracle.com/javase/tutorial/networking/sockets/definition.html>
- [102] S. S. T. AG, “Sunny boy 1300tl / 1600tl / 2100tl - operating manual,” Datasheet, 2014. [Online]. Available: <http://files.sma.de/dl/5684/SB13-21TL-BE-en-11.pdf>
- [103] M. Care, “Microcare 20-100 amp lcd mppt solar regulator,” Datasheet. [Online]. Available: <http://microcare.co.za/wp-content/uploads/2014/10/MC-20-100A-LCD-MPPT-SpecSheet-2016v2.0.pdf>
- [104] Royal, “Lead calcium semi-sealed maintenance free battery,” Datasheet. [Online]. Available: <http://www.sinetech.co.za/assets/img/royal/Royal%20Battery%20July%202014.pdf>
- [105] T. Instruments, “2.5-v low iq adjustable precision shunt regulator,” Datasheet, Mar 2015. [Online]. Available: <http://www.ti.com/lit/gpn/at1432a>
- [106] O. Semiconductor, “Plastic SMD Zener Voltage Regulator Diodes,” 2016.
- [107] —, “General Purpose Transistors NPN Silicon,” 2017.
- [108] L. Jolly and R. R. Panchal, “Implementation of one diode model solar cell capacitance to measure temperature.”
- [109] Espressif. (2018) ESP-IDF Programming Guide. [Online]. Available: <https://docs.espressif.com/projects/esp-idf/en/latest/get-started/>
- [110] Tektronix, “Digital storage oscilloscopes - tds1000b series tds2000b series data sheet,” Datasheet, 2016. [Online]. Available: <http://www.testequipmenthq.com/datasheets/TEKTRONIX-TDS1002B-Datasheet.pdf>
- [111] —, “Ac/dc current measurement systems - tcpa300, tcp312a, tcp305a, tcp303, tcpa400, tcp404xl datasheet,” Datasheet, 2016. [Online]. Available: http://www.farnell.com/datasheets/2239280.pdf?_ga=2.73376083.1188572977.1542210576-2146271758.1542210576